TITLE: HIGH PERMEABILITY TERNARY PALLADIUM ALLOY MEMBRANES WITH IMPROVED SULFUR AND HALIDE TOLERANCES

FINAL REPORT

REPORTING PERIOD START DATE: 5/02/07 (PROGRAM START)

REPORTING PERIOD END DATE: 12/31/10

PRINCIPLE AUTHOR(S): K. COULTER

DATE REPORT WAS ISSUED: MARCH 2011

DOE AWARD NUMBER: DE-FC26-07NT43056

SUBMITTING ORGANIZATION: SOUTHWEST RESEARCH INSTITUTE
6220 CULEBRA ROAD (78238-5166)
P.O. BOX 28510 (78228-0510)
SAN ANTONIO, TEXAS

OTHER TEAM MEMBERS: COLORADO SCHOOL OF MINES
GEORGIA TECH UNIVERSITY
TDA RESEARCH, INC.
IDATECH, LLC

SUBMIT TO: NETL AAD DOCUMENT CONTROL
BLDG. 921 U.S. DEPARTMENT OF ENERGY
NATIONAL ENERGY TECHNOLOGY LABORATORY
P.O. BOX 10940
PITTSBURGH, PA 15236-0940

TITLE: HIGH PERMEABILITY TERNARY PALLADIUM ALLOY MEMBRANES WITH IMPROVED SULFUR AND HALIDE TOLERANCES

FINAL REPORT

REPORTING PERIOD START DATE: 5/2/2007 (PROGRAM START)

REPORTING PERIOD END DATE: 12/31/10

PRINCIPLE AUTHOR(S): K. COULTER

DATE REPORT WAS ISSUED: MARCH 2011

DOE AWARD NUMBER: DE-FC26-07NT43056

SUBMITTING ORGANIZATION: SOUTHWEST RESEARCH INSTITUTE
6220 CULEBRA ROAD (78238-5166)
P.O. BOX 28510 (78228-0510)
SAN ANTONIO, TEXAS

OTHER TEAM MEMBERS: COLORADO SCHOOL OF MINES
GEORGIA TECH UNIVERSITY
TDA RESEARCH, INC.
IDATECH, LLC

SUBMIT TO: NETL AAD DOCUMENT CONTROL
BLDG. 921 U.S. DEPARTMENT OF ENERGY
NATIONAL ENERGY TECHNOLOGY LABORATORY
P.O. BOX 10940
PITTSBURGH, PA 15236-0940

APPROVED:

BEN H. THACKER, DIRECTOR
MATERIALS ENGINEERING DEPARTMENT

DISCLAIMER

ABSTRACT

The project team consisting of Southwest Research Institute® (SwRI®), Georgia Institute of Technology (GT), the Colorado School of Mines (CSM), TDA Research, and IdaTech LLC was focused on developing a robust, poison-tolerant, hydrogen selective free standing membrane to produce clean hydrogen. The project completed on schedule and on budget with SwRI, GT, CSM, TDA and IdaTech all operating independently and concurrently. GT has developed a robust platform for performing extensive DFT calculations for H in bulk palladium (Pd), binary alloys, and ternary alloys of Pd. Binary alloys investigated included $Pd_{96}M_4$ where M = Li, Na, Mg, Al, Si, Sc, Ti, V, Cr, Mn, Fe, Co, Ni, Cu, Zn, Ga, Y, Zr, Nb, Mo, Tc, Ru, Rh, Ag, Cd, In, Sn, Sb, Te, Hf, Ta, W, Re, Os, Ir, Pt, Au, Tl, Pb, Bi, Ce, Sm, Gd, Tb, Dy, Ho, Er, Tm, Yb, Lu. They have also performed a series of calculations on $Pd_{70}Cu_{26}Ag_4$, $Pd_{70}Cu_{26}Au_4$, $Pd_{70}Cu_{26}Ni_4$, $Pd_{70}Cu_{26}Pt_4$, and $Pd_{70}Cu_{26}Y_4$. SwRI deposited and released over 160 foils of binary and ternary Pd alloys. There was considerable work on characterizing and improving the durability of the deposited foils using new alloy compositions, post annealing and ion bombardment. The 10 and 25 µm thick films were sent to CSM, TDA and IdaTech for characterization and permeation testing. CSM conducted over 60 pure gas permeation tests with SwRI binary and ternary alloy membranes. To date the PdAu and PdAuPt membranes have exhibited the best performance at temperatures in the range of 423-773 ºC and their performance correlates well with the predictions from GT. TDA completed testing under the Department of Energy (DOE) WGS conditions on over 16 membranes. Of particular interest are the PdAuPt alloys that exhibited only a 20% drop in flux when sulfur was added to the gas mixture and the flux was completely recovered when the sulfur flow was stopped. IdaTech tested binary and ternary membranes on a simulated flue gas stream and experienced significant difficulty in mounting and testing the sputter deposited membranes. IdaTech was able to successfully test PdAu and PdAuPt membranes and saw similar sulfur tolerance to what TDA found.

The Program met all the deliverables on schedule and on budget. Over ten presentations at national and international conferences were made, four papers were published (two in progress) in technical journals, and three students (2 at GT and 1 at CSM) completed their doctorates using results generated during the course of the program. The three major findings of program were; 1) the DFT modeling was verified as a predictive tool for the permeability of Pd based ternary alloys, 2) while magnetron sputtering is useful in precisely fabricating binary and ternary alloys, the mechanical durability of membranes fabricated using this technique are inferior compared to cold rolled membranes and this preparation method is currently not ready for industrial environments, 3) based on both modeling and experimental verification in pure gas and mixed gas environments PdAu and PdAuPt alloys were found to have the combination of the highest permeability and tolerance to sulfur.

TABLE OF CONTENTS

LIST OF TABLES

LIST OF FIGURES

LIST OF FIGURES (Continued)

LIST OF FIGURES (CONTINUED)

LIST OF FIGURES (CONTINUED)

LIST OF FIGURES (CONTINUED)

LIST OF FIGURES (CONTINUED)

LIST OF FIGURES (CONTINUED)

LIST OF FIGURES (CONTINUED)

LIST OF FIGURES (CONTINUED)

HIGH PERMEABILITY TERNARY PALLADIUM ALLOY MEMBRANES WITH IMPROVED SULFUR AND HALIDE TOLERANCES

The objective of the proposed program was to develop and demonstrate an ultra-thin durable ternary Pd-alloy membrane with excellent resistance to sulfur and halogen attack while meeting or exceeding the hydrogen permeability performance established by the Department of Energy (DOE). The project can be summarized in three primary tasks of: 1) Materials modeling and composition selection 2) Fabrication of high-performance ternary alloy membranes, and 3) Membrane testing and evaluation. All milestones for the program have been met and the following Final Report outlines the completion of all the tasks.

1.0 MATERIALS MODELING

Carnegie Mellon University (CMU), and upon David Sholl's move, Georgia Institute of Technology performed detailed calculations for interstitial H in representative Pd alloys for the purpose of applying rigorous cluster expansion techniques to the derivation of lattice models for these alloys.

1.1 Binary Alloys $Pd_{96}M_4$

Sholl's group studied the bulk properties of these binary alloys via DFT while using the Vienna *Ab-Initio* Simulation Package (VASP). They construct a bulk material by using a supercell composed of 27 atoms which are periodically repeated in order to simulate an infinite material. Due to the supercell definition this meant that although Sholl's group proposed to begin their analysis with $Pd_{95}M_5$, they would best be able to describe the $Pd_{96}M_4$ by replacing a single Pd atom with an M atom in the cell. This was the closest and best representation of what they were looking for, which was attempting to understand how a trace amount of an additive metal would affect the properties of H in the bulk of these materials.

These binary alloys form random FCC bulk materials, and in FCC structures H can reside in 2 interstitial sites which are the 6-fold octahedral (O) sites and the 4-fold tetrahedral (T) sites. Since a random configuration of the metal atoms is expected, this means that there is a possibility that as H permeates through these materials, that it may encounter small gatherings of the additive metal atoms. By focusing on the O site and observing the nearest neighboring (NN) and next to nearest neighboring metal atoms (NNN) to the H it could now have more than 1 M atom in either shell and these in turn could be found at different distances from each other. By combining the most common occurrences of how the M atoms could surround an H in a particular O site Sholl's group developed a data set of 21 particular O sites. These 21 O sites make up about 99% of a randomly defined bulk material of composition $Pd_{96}M_4$. In FCC structures for every O site there are 8 possible T site, and for the 21 O sites of the rigorous DFT calculations, they have also calculated the corresponding T sites (and in turn the transition states (TS) between each O site to T site). Sholl's Group analyzed extensively binary alloys with M = Ag, Cu, and Rh and determined that even a small amount of Ag improves both the solubility as

well as the diffusion of H in these bulk materials throughout the entire temperature range of 400-1200 K. Rh as an additive metal atom causes a slight reduction in the permeability of H compared to pure Pd, yet it is still an improvement over the effects of using Cu as the additive metal atom. A preliminary data set for M = Ag, Au, Co, Cr, Cu, Fe, Hf, Ir, Mn, Mo, Nb, Ni, Os, Pt, Re, Rh, Ru, Ta, Tc, Ti, V, W, Y, and Zr was completed.

Previous work done by Kamakoti and Sholl on Pd-based alloys employed a lattice model that only looked at the number of Pd atoms in the NN and the NNN to define the binding energy of H in an O site. Using this simple model to describe the O site data set for the $Pd_{96}M_4$ it would only be able to identify 8 distinct O sites. The reason for this is that some of the O sites have the same NN and NNN definition but the placement of the M atoms to each other causes them to be different and also has an effect towards the binding energy. A more rigorous approach would be to use Cluster Expansion (CE). The cluster expansion provides a general mathematical framework for the problem outlined above based on a formally infinite series of characteristic figures such as pairs, triplets, four-body terms and so on that represent multiple body interactions that sum together to define the energy of a configuration. The limit to the CE is that you have to determine how many interactions you want to look at as well as to what distance from the H atom. For the O site definition the following 14 parameters were modeled:

Table 1. Modeling parameters

Parameter ID	Parameter Definition
1	# of Pd in NN (2xN)
2	# of Pd in NNN (3xN)
3	2 body interaction in NN shell (2.83 Å)
4	2 body interaction in NN shell (4.00 Å)
5	2 body interaction in NNN shell (4.00 Å)
6	2 body interaction in NNN shell (5.66 Å)
7	2 body interaction in NNN shell (6.93 Å)
8	2 body interactions between NN and NNN shell (2.83 Å)
9	3 body interactions in NN
10	3 body interactions in NNN (< 6.93 Å)
11	4 body interaction in NN
12	4 body interaction in NNN (faces of cube)
13	# of Pd in 4xN
14	# of Pd in 5xN

A similar approach was implemented to the T sites definition. Because the position of the TS is not symmetrically easy to identify such as the O and T site, yet a particular TS always occurs from one O site to a specific T site defined by the TS by using the a combination of the parameters used for the O and T sites of the particular TS. Using the CE model with all the parameters to define the binding site, Sholl's group checked if using a truncated parameter definition (any possible combination of the parameters) would in fact be better in describing the sites. This means that if 11 parameters are used to describe a site there are 2036 potential CE models. In order to determine which is the best-suited CE model the Leave-One-Out (LOO) method is used. LOO consists of performing a least squares minimization of the model being considered *X* independent times; where in each case one data point from the complete set of *X* values is left out. The model with the absolute lowest LOO error, essentially the model that best fits the data, is used for the macroscopic description of the alloys. It was observed for the $Pd_{96}Ag_4$, $Pd_{96}Cu_4$, and $Pd_{96}Rh_4$ alloys that the CE models perform well in describing the data collected for the O and T sites. For $Pd_{96}Cu_4$ and $Pd_{96}Rh_4$ the CE also performs well for the TS, yet scattering can be observed in the $Pd_{96}Ag_4$ alloy.

Sholl's group originally proposed to perform DFT calculations on $Pd_{60}Cu_{35}Rh_5$ and $Pd_{80}Cu_{15}Rh_5$, these compositions were based on previous Pd-based binary alloy analysis and preliminary ternary analysis performed by Kamakoti and Sholl. After obtaining the results from the detailed calculations on the binary alloys, they decided to analyze ternary alloys that would include Rh, but also Ag as the third metal additive. Due to lack of crystal structure data on these ternary compositions the alloys were kept in the FCC phase. With these additional influences, $Pd_{70}Cu_{26}M_4$ was analyzed. The compositions were determined by the supercell definition used, which is the same 27 atom definition used for the binary alloys. In the ternary alloys, 7 atoms were randomly chosen to be Cu, 1 to be M and the remaining atoms to be Pd. It is assumed that because the base binary alloys ($Pd_{70}Cu_{30}$ and $Pd_{96}M_4$) form random FCC structures that the same was true for the ternaries. Similarly to the binary alloys, because these are random structures, as H permeates through the bulk it could potentially encounter small gathering of a particular atom. In these cases, there are not only Pd 'clusters,' but also Cu and even M atoms forming small gatherings. This reduces the number of calculations needed in order to accurately describe the possible environments H could encounter within the bulk of the binary alloys and the ternary alloys respectively. Due to the substantial number of calculations performed, Sholl's group has developed a method based on binary alloy calculations to determine the TS, without having to perform nudged elastic band (NEB) calculations. This new approximated TS method has been checked with NEB calculations and the energy predictions as well as the position of the atoms are in excellent agreement with NEB predicted values. This new method reduced computational time substantially. Although a complete data set for the ternary alloys was not done, a CE model determination on the O sites with the limited data was performed.

In January 2008, David Sholl and his group moved to Georgia Institute of Technology (GT). They completed the data collection from the DFT calculations for $Pd_{70}Cu_{26}Ag_4$ (compositions in at.%) as well as $Pd_{70}Cu_{30}$. The reason for selecting PdCuAg as a ternary alloy was as a result of

detailed calculations on the $Pd_{96}M_4$ which concluded that even a small amount of Ag as an additive metal atom would improve both the diffusion and the solubility of H in the bulk of the membrane. They also calculated the $Pd_{70}Cu_{30}$ alloy in order to have similar detailed calculations for comparison with the current work that they have performed.

Upon completing all the calculations involving H in the distinct interstitial binding sites as well as the TS and the zero point energy corrections for each site, GT performed the CE-LOO analysis to obtain a model that would accurately define corresponding binding sites. Given that it is a ternary system they included additional CE parameters that would distinguish between which particular atom they were dealing with, which produced a total of 20 O site parameters and 23 T site parameters. The TS are defined by a linear combination of the O sites and T site parameters, meaning that there are a total of 43 parameters. Because they are searching for models with all possible combinations of 2 parameters up to the full parameter model, the number of potential models exponentially increases with each parameter used. In order to prevent this problem, after the O site and the T site models were selected, GT in turn then utilized the parameters from those models and performed CE-LOO analysis on the TS. In other words, they pre-selected which of the 43 parameters to use before performing the CE-LOO analysis by using the CE parameters best suited to define the O sites and the T sites.

Once all the models required to analyze the behavior of H in the bulk of these membranes were complete, GT performed both solubility and diffusion calculations on each of the systems. In the solubility analysis both the O site and the T site contributions were included in the analysis, although the contribution to the solubility from the T sites is very low in comparison to the O sites. In Figure 1.a the solubility results normalized with respect to pure Pd for the $Pd_{96}Ag_4$, $Pd_{96}Cu_4$, $Pd_{70}Cu_{26}Ag_4$ and $Pd_{70}Cu_{30}$ alloys are plotted. The ternary alloy has increased solubility relative to the binary $Pd_{70}Cu_{30}$ and the Cu content has reduced the solubility in comparison to that of pure Pd. Although the effects may seem minor when the ternary alloy is normalized with respect to the binary alloy as shown in Figure 1.b, adding 4 at.% Ag to the binary base dramatically improves the solubility of H (especially at lower temperatures) with improvements of 3.1 times greater solubility.

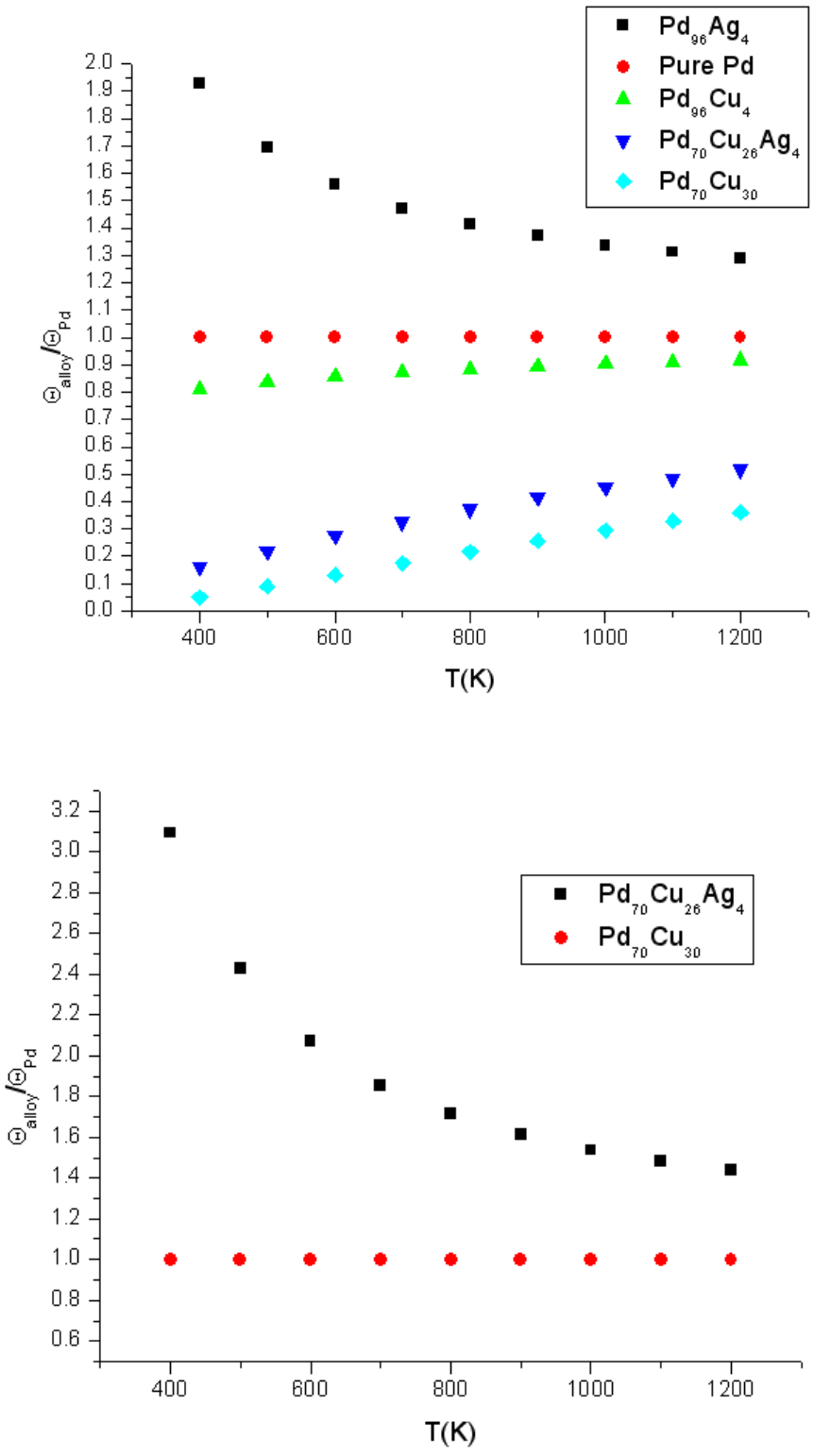

Figure 1. **Solubility results for the temperature range of 400 to 1200 K (a) normalized with respect to pure Pd and (b) normalized with respect to $Pd_{70}Cu_{30}$.**

In the diffusion analysis, GT has taken into account that the presence of Ag has an effect on some of the T sites causing them to no longer be energy minima. This has been implemented in all of the alloys and is only activated when an additive metal atom that is larger than Pd is included in the alloy which causes an expansion of the lattice. Figure 2.a shows the results of the diffusion analysis over the temperature range of 400 to 1200 K normalized with respect to pure Pd. Again a clear improvement is seen in the ternary alloy over the base binary alloy. What is most interesting is that at high temperatures the ternary alloy seems to have similar diffusion rates to the $Pd_{96}Cu_4$ alloy. In Figure 2.b the diffusion result is plotted (now normalized with respect to $Pd_{70}Cu_{30}$) and the presence of Ag has caused an average improvement in the diffusion of H of about 1.7 times that of $Pd_{70}Cu_{30}$.

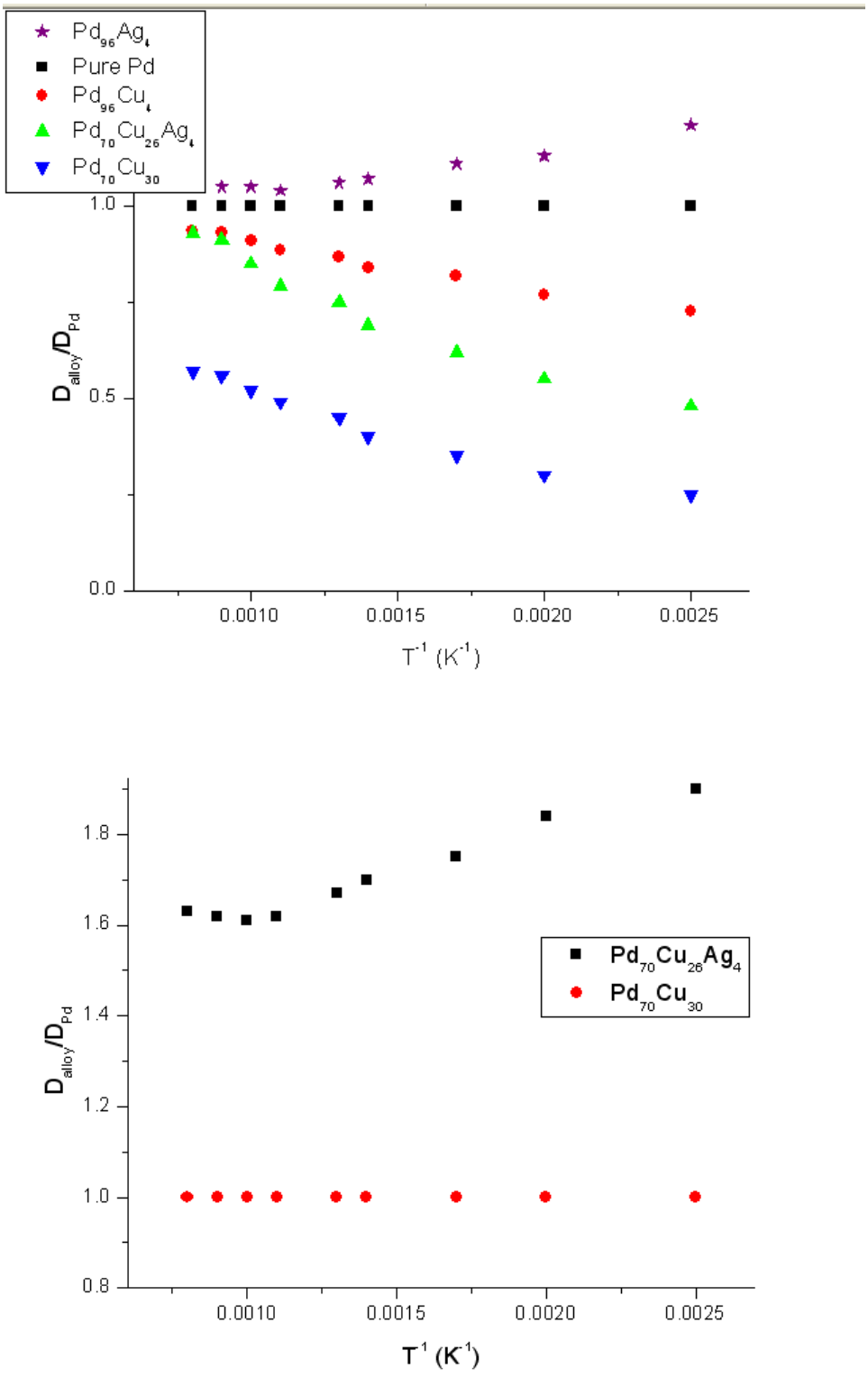

Figure 2. **Diffusion results for the temperature range of 400 to 1200 K (a) normalized with respect to pure Pd and (b) normalized with respect to $Pd_{70}Cu_{30}$.**

Finally GT performed permeability analysis on all the alloys and plotted the results in Figure 3. Figure 3.a has the results normalized with respect to pure Pd for all the alloys in question. The permeability of H is greater in the ternary system than in the binary base since both the diffusion and the solubility resulted in improved results. This suggests that this ternary alloy is a good target for an experimental study.

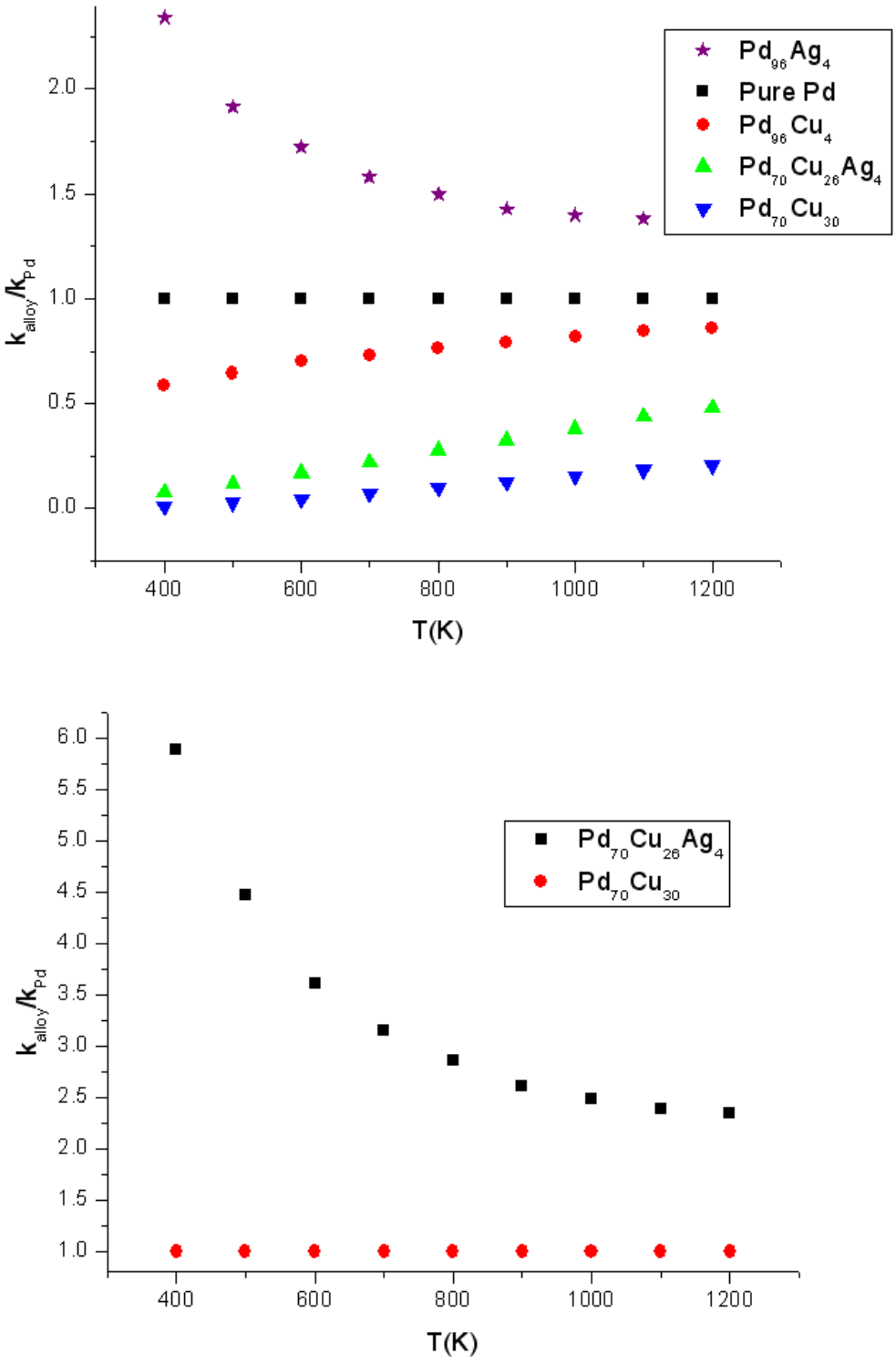

Figure 3. **Permeability results for the temperature range of 400 to 1200 K (a) normalized with respect to pure Pd and (b) normalized with respect to $Pd_{70}Cu_{30}$.**

Having performed detailed DFT calculations on $Pd_{96}M_4$ for M=Ag, Cu, and Rh, GT could combine this data with cluster expansion (CE) models in order to predict the properties of H in the bulk of these alloys in comparison to pure Pd behavior. From this analysis, GT was able to deduce that by adjusting the composition of the alloy with a small amount of an additive metal atom they could manipulate the properties of H in the bulk material to ultimately improve the permeability of the H. Keeping this in mind, the objective is to examine a membrane that has experimentally been shown to be resistant to deactivation in the presence of contaminants as the base of the alloy that could then be manipulated by the addition of a small amount of an additive metal atom. The selected candidates were PdCu alloys in the FCC crystal structure.

GT began analyzing $Pd_{70}Cu_{26}M_4$ for M = Ag and Cu. Silver as an additive metal atom was initially chosen due to the promising results in our detailed binary analysis. Copper was chosen as to have the $Pd_{70}Cu_{30}$ composition which was used to compare the properties of the H in bulk material with the ternary alloy. The compositions are determined by a supercell definition in our DFT calculations with the same 27 atom definition used for the binary alloys. In the ternary alloys, 2 distinct supercells were used to define the position of the atoms. In one of the supercells, 7 atoms were randomly chosen to be Cu, 1 to be M and the remaining atoms to be Pd. The assumption is that because the base binary alloys ($Pd_{70}Cu_{30}$ and $Pd_{96}M_4$) form random FCC structures that the same will be true for the ternaries. The other supercell was a random arrangement of 19 Pd atoms and 8 Cu atoms at the ternary alloy lattice constant. This arrangement of atoms has no M atoms, given that at the composition of the alloy, the majority of the bulk material which H will encounter will be a random assortment of Pd and Cu atoms therefore more Pd-Cu configurations were desired. The lattice constants were optimized for the ternary alloy composition for each individual alloy and utilized in all the corresponding calculations.

Similar to our detailed binary calculations, the binding energy and vibrational frequencies of H in the interstitial sites within the bulk of these alloys are critical. At high temperatures, it is known that H diffuses through the bulk of FCC membranes through a series of hops from interstitial site to interstitial site via what is known as the transition state (TS). With the supercell definition being used, there are 27 O sites, 54 T sites and 216 TS per supercell. Unlike our detailed binary analysis, the TS are not obtained by performing individual NEB calculations. This method would be unfeasible for screening through a series of ternary alloys. Given that several binary alloys were screened, a method of finding an initial estimate was developed, similar to that predicted by NEB, for the TS. In order to find the TS of a binary alloy the TS position of the pure metal membrane must be known; meaning, that from pure Pd the position of the TS for $Pd_{70}Cu_{30}$ can be estimated. Once the TS for the $Pd_{70}Cu_{30}$ alloy was identified, using the same concept the method to extrapolate an initial guess for the TS in the $Pd_{96}Cu_{26}M_4$ was utilized. This method gave the same position as an NEB calculation would for the ternary TS initial position with a difference of less than 0.001 Å in the position of the TS.

Once the DFT data collection procedure was established, the subsequent alloy calculations were sped up by using the optimized atom positions for any succeeding M atom that was identified to be analyzed. Because the addition of Ag expands the lattice constant (LC) in comparison to the base binary alloy, M atoms that would produce similar effects on the LC for comparison were kept. This meant that M = Au and Pt were used, which would also expand the LC of the ternary alloy in comparison to the binary could potentially, still form an FCC crystal structure. In total for each alloy 54 O sites, 108 T sites, 432 TS, and the corresponding zero point energy (ZPE) for $Pd_{70}Cu_{26}M_4$ for M = Ag, Au, Cu, and Pt were calculated.

In GT's work on detailed binary alloys, the idea of describing the binding sites with a series of well defined geometric configurations via a cluster expansion method was introduced. From the combination of the images selected to define a specific site a series of prospective models to accurately define the energy of H in a particular site was obtained. In order to select the best CE model, the Leave One Out (LOO) analysis was introduced. With the CE-LOO analysis, the DFT data sets were taken and models developed that could accurately define the binding sites, these models were then used in subsequent analysis of the solubility and diffusion of H in the bulk of the alloys.

In defining the geometric shapes in the ternary alloys, the same definitions implemented in the detailed binary analysis were taken and additional terms added that would aid in adding distinction to each of the binding sites. This was absolutely necessary, given that the complexity of the bulk environment is increased with the addition of the third component. The O site parameters used for the ternary alloys included 20 terms (compared to the 14 in the binary) that ranged from the shell composition up to 4 metal-body interactions. The T site parameters also increased to 30 parameters (compared to the 15 terms in the binaries), which also included up to 4 metal-body interactions. The idea of defining the TS as a linear combination of the O site parameters and the T site parameters was kept, but given the total number of terms used to define these sites (50 parameters) a new CE-LOO procedure had to be implemented given that the combination of the parameters (using 2 parameters up to the full parameter model) is a factorial problem (giving us $1.13´10^{15}$ possible CE models), making a complete analysis of these combinations unfeasible. The procedure consisted of taking the TS DFT data and performing 2 initial CE-LOO screenings. First a CE-LOO analysis was performed on the TS DFT data using only the O site parameters that were selected for the O CE model; the same procedure was done using the T site parameters. From each of these individual CE-LOO calculations a collection of parameters was obtained that were best suited to define the TS DFT data. A final CE-LOO was performed using the combination of the pre-screened parameters to obtain the final CE model for the TS data. These procedures were performed on all of the proposed ternary alloys for the classical binding energies and the ZPE independently. In Figures 4-7 the CE model predicted values are plotted for DFT data vs. DFT data for $Pd_{70}Cu_{30}$, $Pd_{70}Cu_{26}Ag_4$, $Pd_{70}Cu_{26}Au_4$, and $Pd_{70}Cu_{26}Pt_4$ respectively.

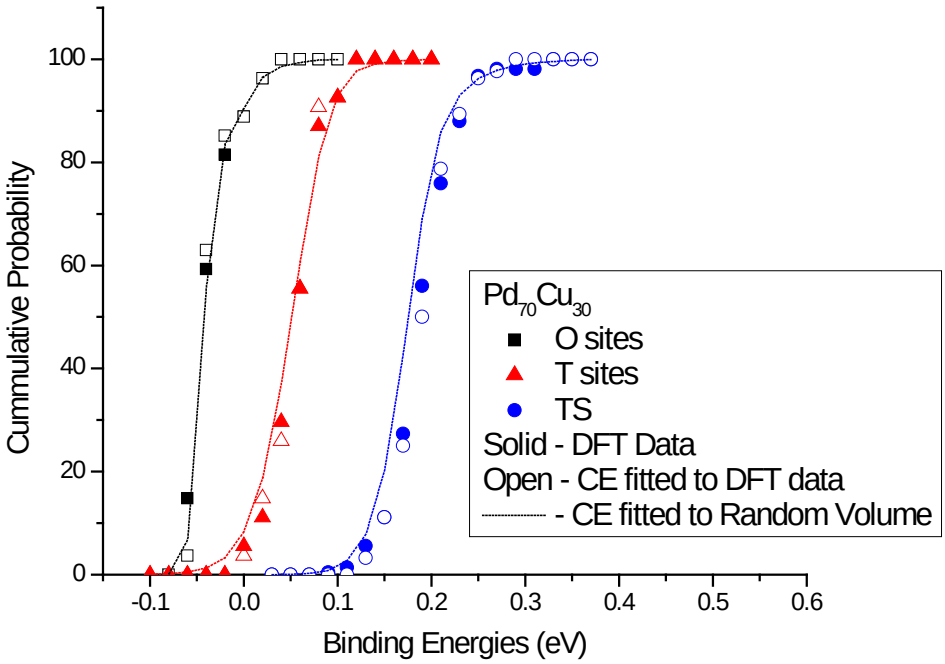

Figure 4. **CE analysis on binding sites of $Pd_{70}Cu_{30}$.**

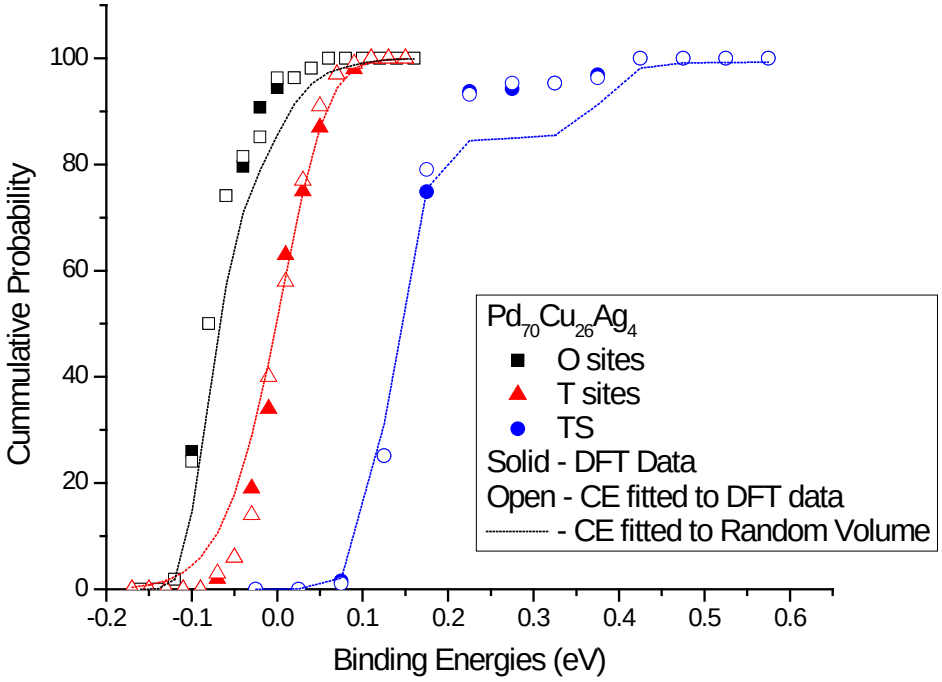

Figure 5. **CE analysis on binding sites of $Pd_{70}Cu_{26}Ag_4$.**

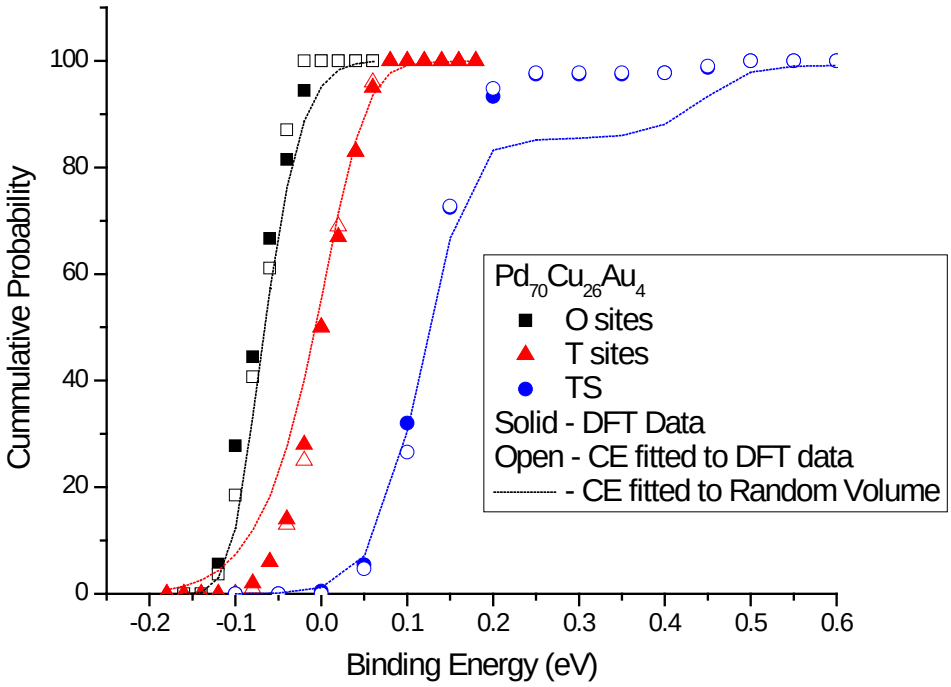

Figure 6. **CE analysis on binding sites of $Pd_{70}Cu_{26}Au_4$.**

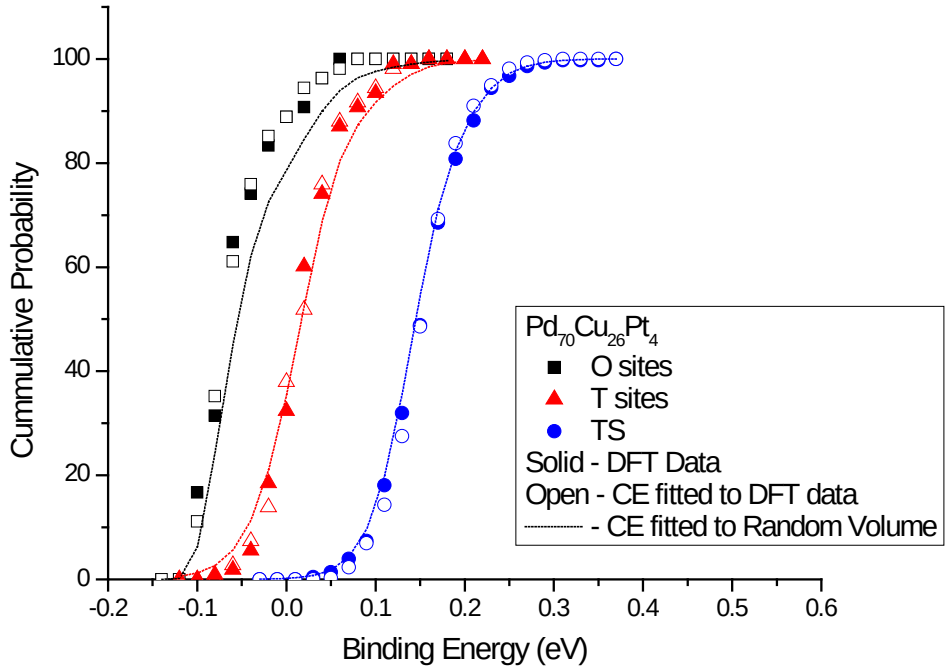

Figure 7. **CE analysis on binding sites of $Pd_{70}Cu_{26}Pt_4$.**

It should be noted that similar to the detailed binary alloys, there were some T sites that were no longer energy minimums when M was larger than a Pd atom. In addition, from careful observation of these figures, M = Ag and Au exhibit some inconsistencies in the T site prediction, particularly for $Pd_{70}Cu_{26}Au_4$, which seems to predict some T sites to be more soluble than some of the O sites. In addition, there seems to be some inconsistency with the TS prediction for both M = Ag and Au. In terms of the T site prediction, this means that there will be a slight under prediction for some T sites as well as for some of the TS.

Solubility analysis on these alloys was performed in a similar fashion as previous applied to the detailed binary alloys. This meant that Sievert's Law was used to calculate the solubility of H in the bulk of the membranes in the temperature range of T = 400 K – 1200 K. It has always been assumed that because the O sites are the favorable binding sites within the FCC structures that the solubility is dominated by these sites. To confirm this, in addition to the O site contribution to the solubility the T site contribution to solubility was calculated. When compared to the O site contribution, the T site contributions are minimal; therefore they have not been included in the solubility analysis. In Figure 8(a), the results have been plotted normalized with respect to pure Pd. It is clear that all the ternary alloys have lower H solubility than pure Pd. This was expected given that as the Cu content increased the solubility of H decreases. Yet similar to the detailed binary alloy results, by simply adding 4 at.% of M atoms the H solubility has been improved compared to the base binary alloys. This is clearly observed in Figure 8(b), which plots the solubility results normalized with respect to $Pd_{70}Cu_{30}$.

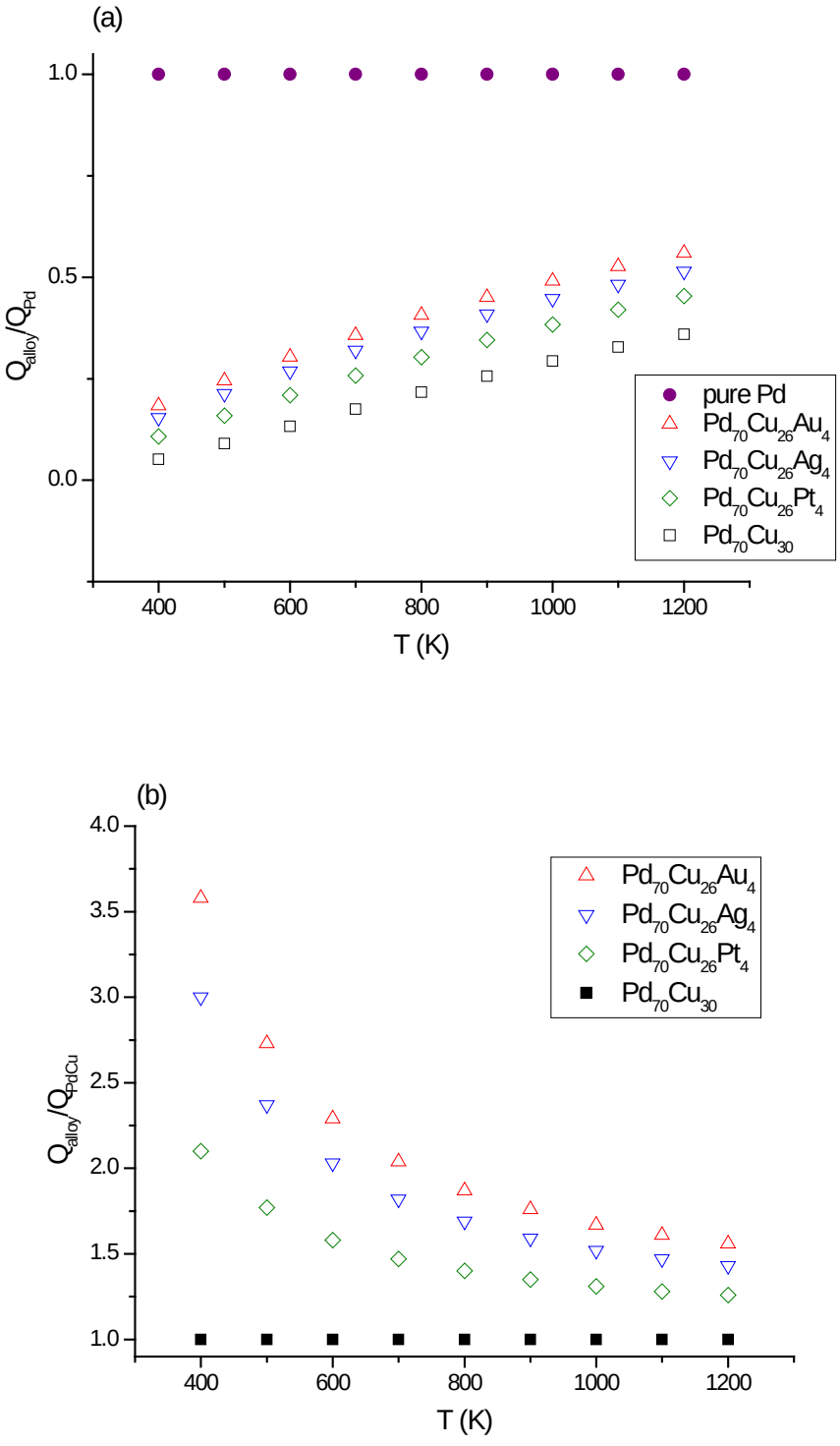

Figure 8. **Solubility results for the ternary alloys at our given compositions. (a) Results normalized with respect to pure Pd. (b) results normalized with respect to $Pd_{70}Cu_{30}$ excluding pure Pd.**

As with the solubility analysis, this was done using the same methods applied to the detailed binary alloys. There is an obvious exception, which is the number of M atoms were limited to one in on our analysis, unlike the binary analysis where clustering of the additive metal atoms up to clusters of 3 atoms were examined. In Figure 9, the diffusion results are plotted for the ternary alloys normalized with respect to $Pd_{70}Cu_{30}$.

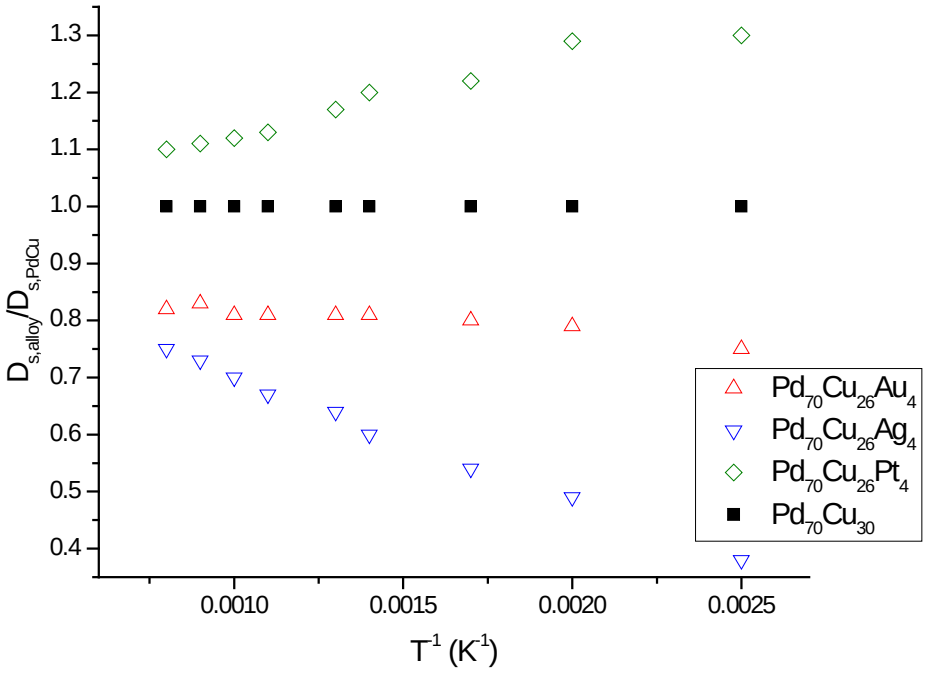

Figure 9. Diffusion results normalized with respect to $Pd_{70}Cu_{30}$.

It can be observed that by adding a small amount of M, when M = Ag and Au, the diffusion of H has been reduced. A possible reason for this is that these M atoms are known to produce trap sites, this is apparent from the solubility conclusions, yet these trap sites also slow down the diffusion. The reason this is not seen in the detailed binary analysis is that we also examined the consequences of having multiple M atoms in the bulk, which in fact become anti trap sites; these site are the ones that aid in increasing the diffusion of H in the bulk of these membranes. It can also be observed that this is not true when M = Pt, which in fact improves the diffusion of H in the bulk of the ternary alloy in comparison to the base binary.

Having both the solubility and the diffusion the permeability is calculated as $k = D_s \times K_s / 2$. Figure 10 shows the permeability predictions for the ternary alloys of the composition $Pd_{70}Cu_{26}M_4$ for M = Cu, Ag, Au and Pt.

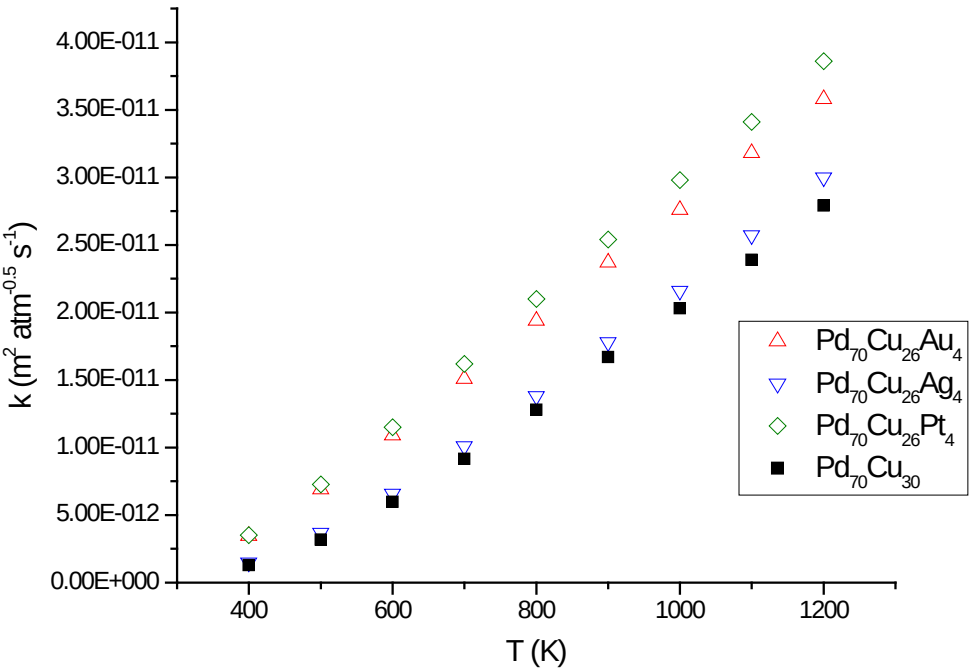

Figure 10. Permeability results for the ternary alloys at our compositions of study.

It can be observed that the permeability for the all ternary alloys studied have greater permeability for H than the $Pd_{70}Cu_{30}$ alloy. In Figure 11 the same permeability results have been plotted, but now they are normalized with respect to $Pd_{70}Cu_{30}$.

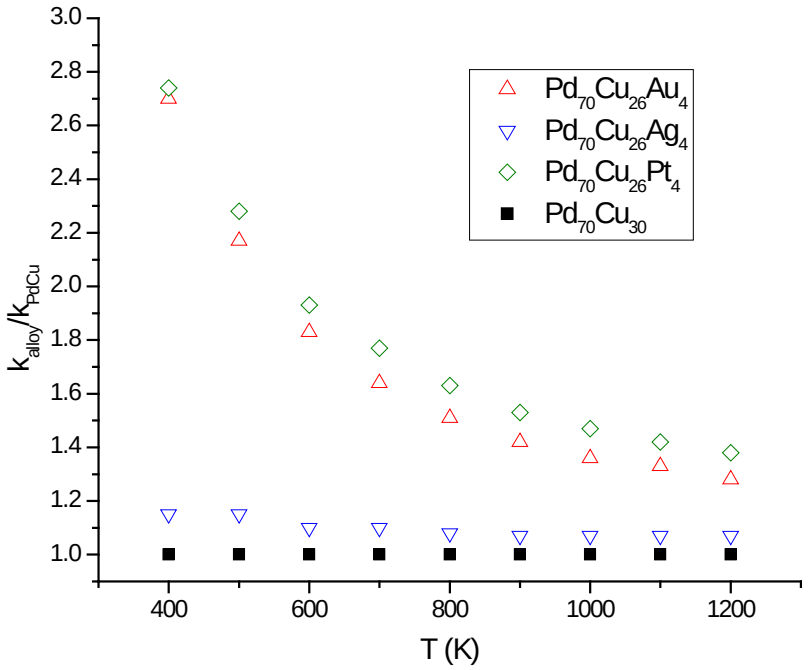

Figure 11. Permeability results for the ternary alloys at our compositions of study normalized with respect to $Pd_{70}Cu_{30}$.

The permeability of H in the ternary alloy when M = Ag is relatively consistent throughout the entire temperature range, while there is a much larger improvement when M = Au or Pt.

The work performed on the ternary alloys $Pd_{70}Cu_{26}M_4$ for M = Ag, Au, Cu and Pt was based on the additive metal atoms that were selected from some of the conclusions from the detailed binary calculations as well as from binary phase diagrams for Pd-M and Cu-M. Atoms which formed FCC crystals in binary compositions with both Pd and Cu independently were selected. The results are consistent with the detailed binary calculations, that the properties of a membrane can be tweaked by "doping" it to form a ternary alloy. From the M atoms, all of the LC studied were slightly expanded from the PdCu LC, which can be a simple explanation for the improvement in the solubility. This improvement in solubility is due to more favorable binding in the bulk, which results in a reduction in the diffusion for M = Ag and Au. For M = Pt, as clearly seen from Figure 7 that the binding energies have slightly shifted towards more favorable binding sites, yet the it seems that improvement of the binding energy was not great enough to form trap sites that would affect the diffusion of the H in these bulk materials. Ultimately the conclusions are that an M atom such as Pt would be best suited as a doping/additive metal atom in these PdCu alloys for improvement in terms of permeability. It should be noted that due to the over/under prediction errors in the CE of M = Ag and Au, the results are likely to shift slightly,

there is a high degree of confidence in the results for the ternary alloy M = Pt based on the accuracy of the CE models.

GT continued developing models to determine whether sufficient data points had been sampled within the bulk of the ternary alloys in order to make predictions of the properties of hydrogen in the bulk of the materials. In Figure 12, the solubility of H in the bulk of these ternary alloys has been plotted as well as the results for pure Pd and $Pd_{70}Cu_{30}$. It can be clearly seen that the high percentage of Cu greatly reduces the solubility of H in comparison to pure Pd. By forming ternary alloys the amount of Cu has been reduced and replaced with the additive metal atom of interest. For the additive metal atoms M = Ag, Au and Pt the solubility of H is improved. This is not as surprising given that all of these additive metal atoms expand the lattice of the ternary alloy in comparison to PdCu alloy. Yet, the surprising result is that the when Ni, which is smaller than Cu in atomic size and reduces the lattice, is used as the additive metal atom in the ternary system, the solubility of H is improved over that of PdCu binary alloy.

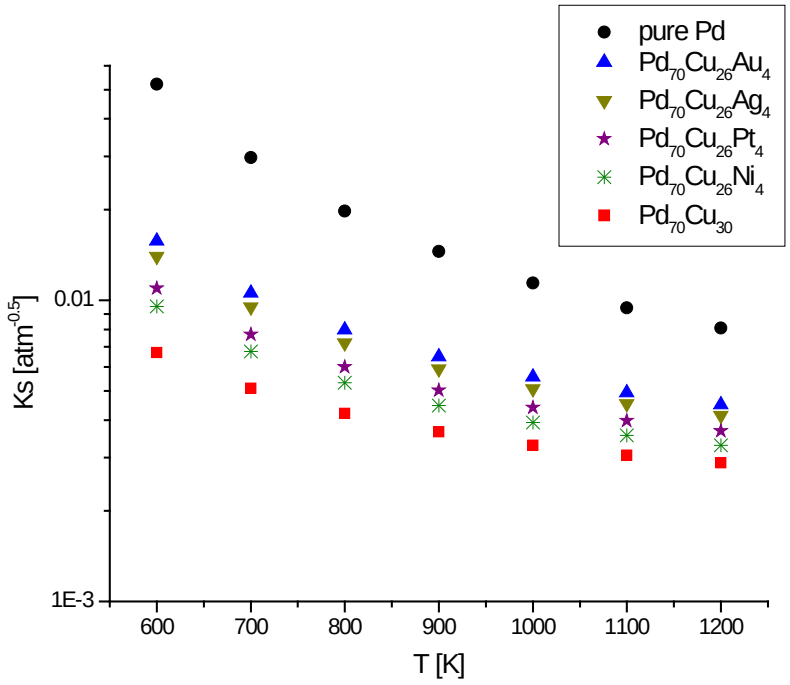

Figure 12. Hydrogen solubility results for Pd based and PdCu based alloys for temperature range of 600-1200 K.

Continuing the analysis of the properties of H in the bulk of these materials, the diffusion in the bulk of these materials was analyzed. In Figure 13, the results for $Pd_{70}Cu_{26}M_4$ (M = Ag, Au, Pt and Cu) are plotted and compared to the diffusion of H in pure Pd. It is clearly seen that by adding Cu to pure Pd the diffusion is also reduced in comparison to the diffusion of H in pure Pd.

By forming the ternary alloys a slight variation in the diffusion of H is seen. The Ag additive has little effect on the diffusion in comparison to the PdCu, which is relatively surprising given that since the solubility of H is improved it would be expected that the diffusion should be reduced. On the other hand, the addition of Au, as expected seemed to reduce the diffusion of H; which can be rationalized with the knowledge of the increase in solubility if H. In the case of Pt as the additive metal atom it can be observed that the diffusion of H is in fact improved over that in the PdCu alloy. The effective activation energy was calculated and the results are as follows:

Table 2. Hydrogen activation Energy

System	Ea, effective [eV]
Pure Pd	0.19
$Pd_{70}Cu_{26}Au_4$	0.24
$Pd_{70}Cu_{26}Ag_4$	0.23
$Pd_{70}Cu_{26}Pt_4$	0.22
$Pd_{70}Cu_{30}$	0.24

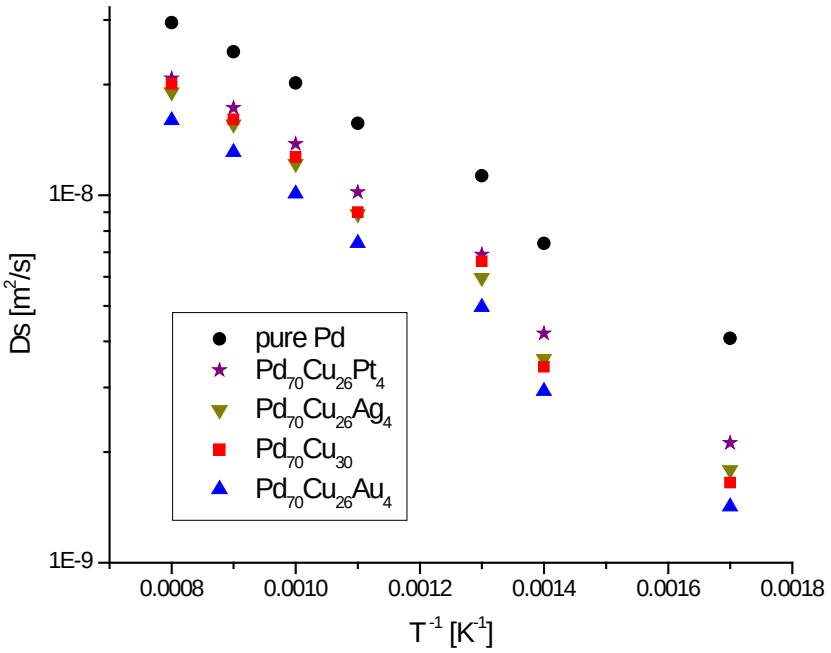

Figure 13. Hydrogen diffusion results for Pd and PdCu based alloys for the temperature range 600-1200 K.

Having both the solubility and the diffusion, the permeability of H in the bulk of these metal membranes was calculated. The permeability of H is greatly reduced with the presence of Cu. The addition of any of the additives metal atoms M = Ag, Au, or Pt improve the permeability. In the case of Ag and Au as the additives, the solubility seems to be the strong factor improving the permeability. Pt as the additive improved both the solubility and the diffusion, hence improving the permeability. It is clear that these ternary alloys are still in no way as good in performance in comparison to pure Pd. Yet the improvement over the PdCu-base alloy is an indication that we can tune a binary alloy by developing ternary alloys that could potentially be used for H purification at comparable performance to pure Pd.

In Figure 14, the solubility results for the binary alloys are plotted. As expected the addition of additive metal atoms larger than Pd such as Ag and Au have improved solubility of H over pure Pd. Rh as an additive metal atom is similar in size to Pd, not changing much the lattice of the alloy in comparison to pure Pd. Given that the change in the binary when using Rh was not substantial, the solubility is not greatly affected by the presence of Rh. Cu and Ni as additive metal atoms reduce the lattice of the alloys in comparison to pure Pd. As expected when Cu is introduced to the binary system the solubility is reduced. Surprisingly, the introduction of Ni to form the binary has an initial expected result of reduction of solubility at lower temperatures. At higher temperatures, however, there is a slight improvement of solubility over pure Pd.

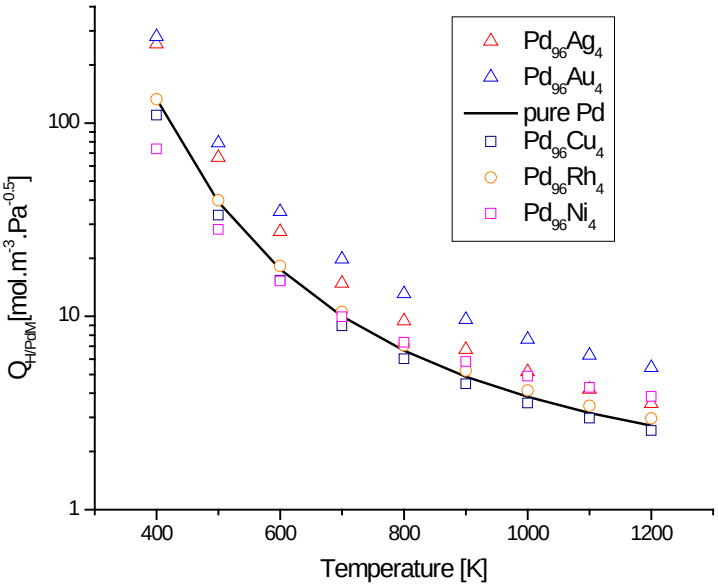

(a)

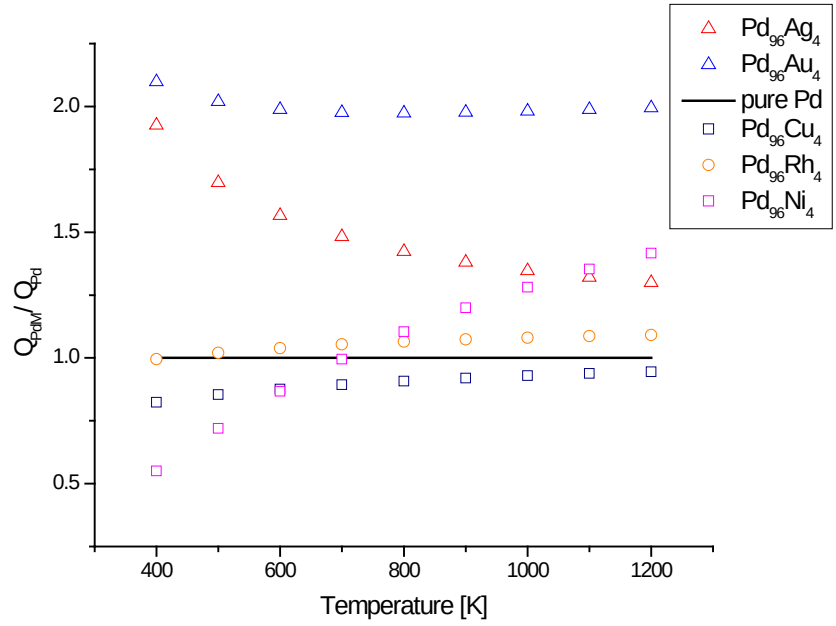

(b)

Figure 14. **Hydrogen Solubility results for the binary systems (open symbols) compared to the solubility of H in pure Pd (solid line). (a) Shows the solubility in $\mathrm{mol} \times \mathrm{m}^{-3} \times \mathrm{Pa}^{-0.5}$ and (b) shows the results normalized with respect to pure Pd for the temperature range of 400 K – 1200 K.**

Diffusion calculations were performed using a modified Kinetic Monte Carlo (KMC) scheme similar to the one previously employed by Kamakoti and Sholl. Our KMC results for the binary systems are shown in Figure 15. Unlike in the solubility analysis, the addition of Ag and Au do not have the same favorable effects on diffusion. The addition of Ag improves the diffusion at higher temperatures, while Au reduces the diffusion throughout the entire temperature range when compared to pure Pd. All the other additives (Cu, Ni, Pt and Rh) reduce the diffusion of H in the bulk of these alloys when compared to pure Pd, as expected.

Because the permeability is directly related to both the solubility and the diffusion, based on the results the permeability of H in each of the systems was calculated. The permeability results are shown in Figure 16. Regardless of the reduction of diffusion, given that the solubility had such great improvement over pure Pd in the $Pd_{96}Ag_4$ alloy the permeability is also improved. This is not so for all the other additive metal atoms, including the additive of Au. This is mainly due to the reduction of diffusion in the systems.

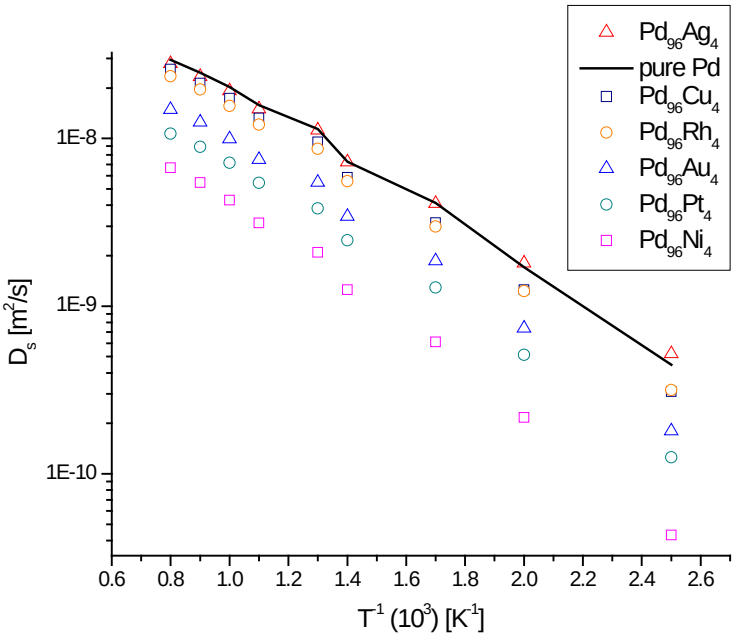

(a)

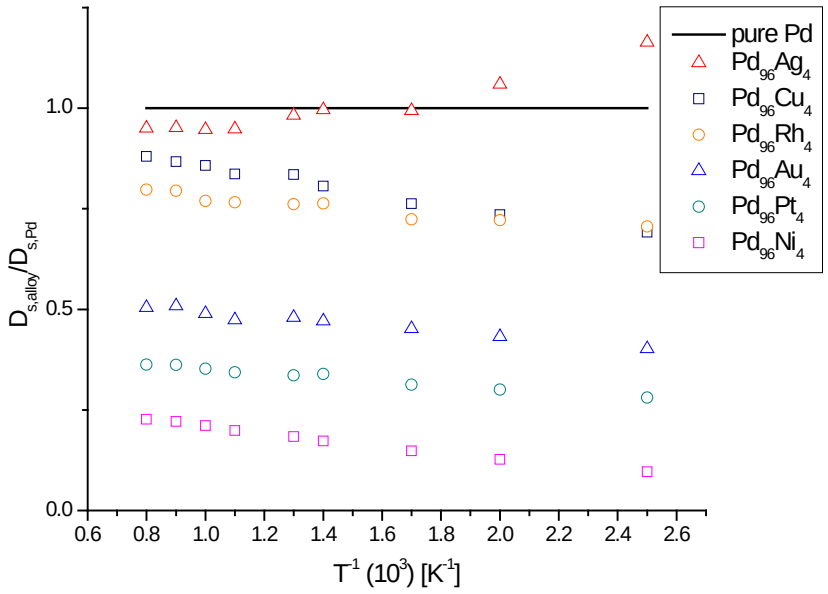

(b)

Figure 15. **Hydrogen diffusion results for the binary systems (open symbols) compared to the diffusion of H in pure Pd (solid line). (a) Shows the diffusion in $m^2 \times s^{-1}$ and (b) shows the results normalized with respect to pure Pd for the temperature range of 400 K – 1200 K.**

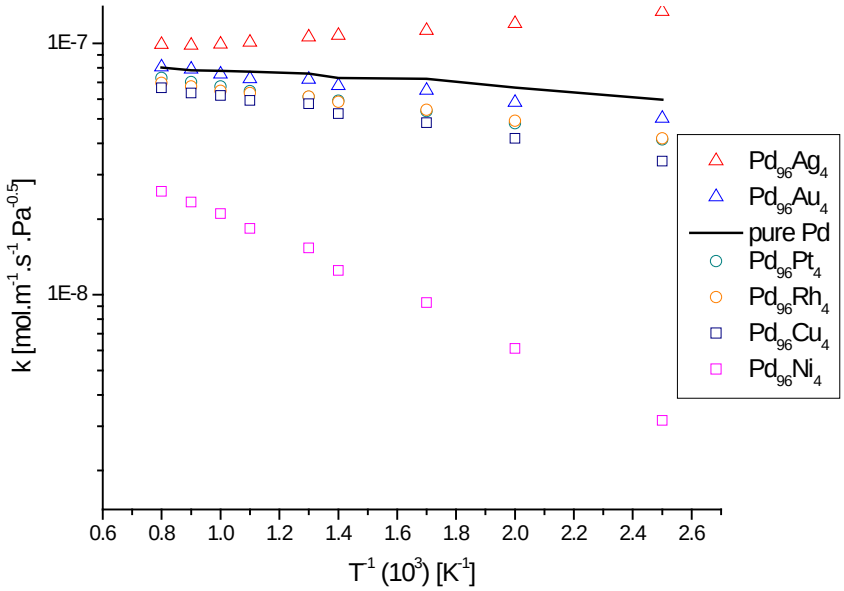

(a)

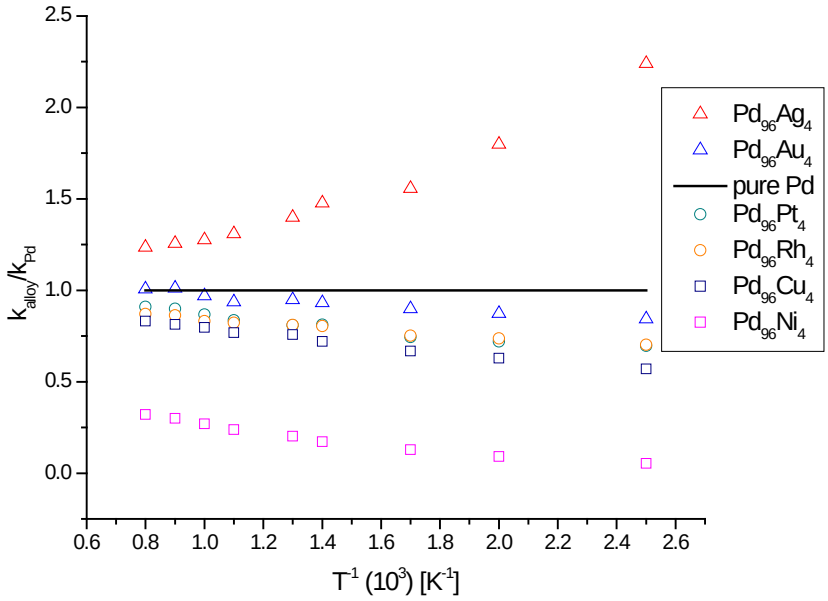

(b)

Figure 16. Hydrogen permeability results for the binary systems (open symbols) compared to the permeability of H in pure Pd (solid line). (a) Shows the permeability in $\mathrm{mol \times m^{-1} \times s^{-1} \times Pa^{-0.5}}$ and (b) shows the results normalized with respect to pure Pd for the temperature range of 400 K – 1200 K.

The solubility, diffusion, and permeability calculations for the ternary alloys are performed in the same manner as the binary alloys described above, but the material used for comparison with the ternary alloys is different. Previously all the results for ternary alloys were normalized with respect to a base binary, in this case the $Pd_{70}Cu_{30}$ system. An alternative basis for comparison would be to compare the ternary alloys to a $Pd_{74}Cu_{26}$ binary alloy. This concept has now been incorporated into the analysis. Figure 17 (a) shows the solubility results for all ternaries of interest normalized with respect to the $Pd_{70}Cu_{30}$ alloy, while (b) shows the same results normalized with respect to the $Pd_{74}Cu_{26}$ alloy.

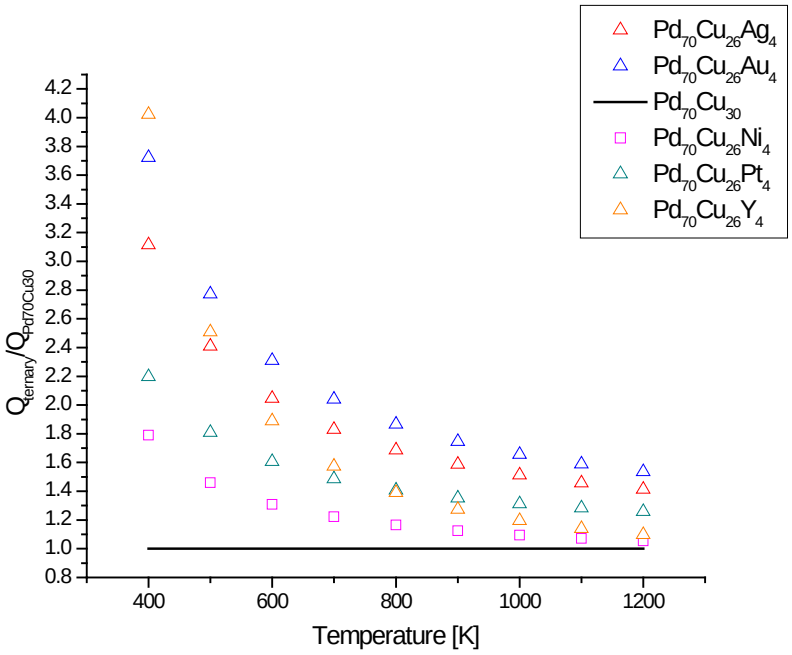

(a)

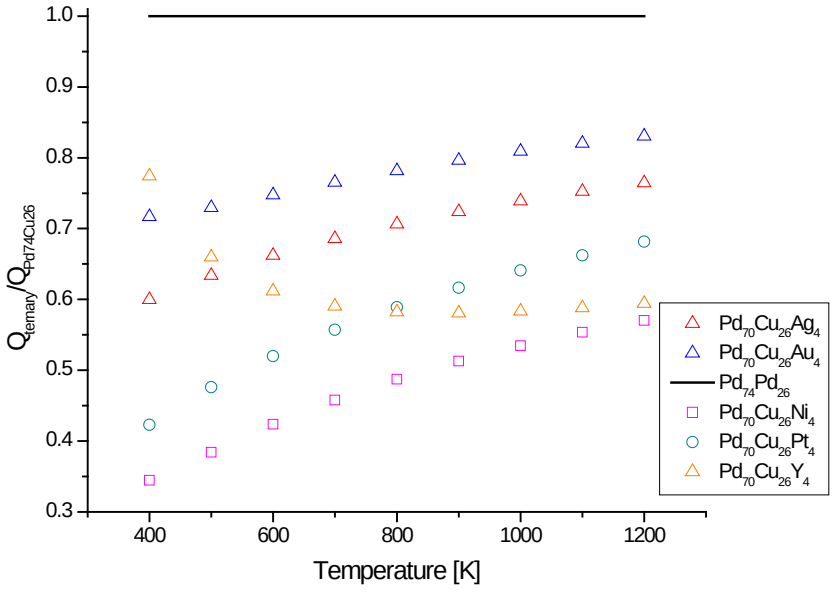

(b)

Figure 17. Solubility results for the ternary systems of interest (a) normalized with respect to $Pd_{70}Cu_{30}$ and (b) normalized with respect to $Pd_{74}Cu_{26}$.

By comparing the results with the two distinct base binaries, qualitatively different conclusions can be obtained (even though the absolute quantities calculated for the ternary alloys are identical in the two calculations). If the ternary alloy is described relative to $Pd_{70}Cu_{30}$, the ternary component can viewed as replacing a fraction of the Cu in the binary alloy. If the ternary alloy is described relative to $Pd_{74}Cu_{26}$, however, the third component can be thought of as replacing part of the Pd in the binary alloy. In the former case, the ternary components effectively increase the overall solubility, which in the latter case the opposite is true.

In Figure 18, the diffusion results for the ternaries have been plotted in the same fashion as for the solubility. Unlike the solubility results, in the diffusion all the additive metal atoms seem to improve over the base binary regardless of the one used for comparison, although as expected there is greater improvement when compared to the $Pd_{70}Cu_{30}$ binary system.

Finally the permeability results for the ternary systems are shown in Figure 19. Given that the solubility was not greatly improve when compared to the $Pd_{74}Cu_{26}$, the only additive metal atom that shows improvement in the addition of Ag to form a ternary alloy. Yet when compared to the $Pd_{70}Cu_{30}$ binary system all the additive metal atoms could be considered as improvement to form ternary alloys. It is clear from these results that clearly identifying the “base binary” to which a ternary alloy is compared is important in understanding the implications of different ternary additives on the permeability of hydrogen through these alloys.

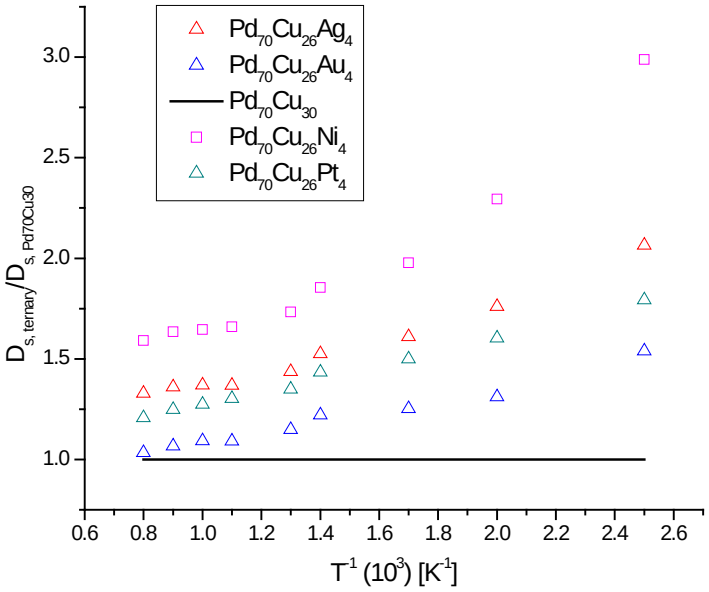

(a)

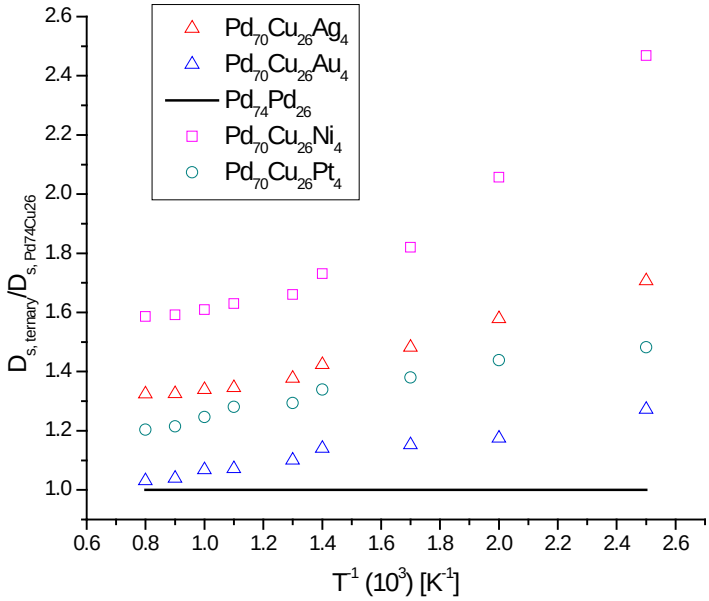

(b)

Figure 18. Diffusion results for the ternary systems of interest (a) normalized with respect to $Pd_{70}Cu_{30}$ and (b) normalized with respect to $Pd_{74}Cu_{26}$.

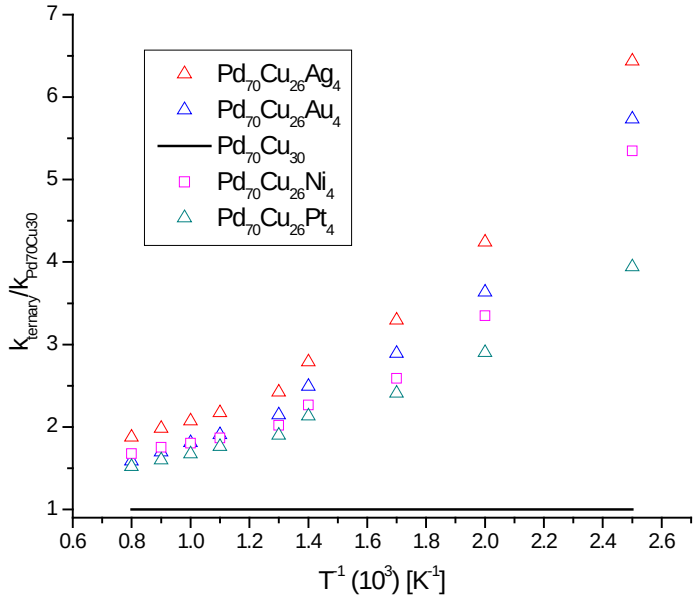

(a)

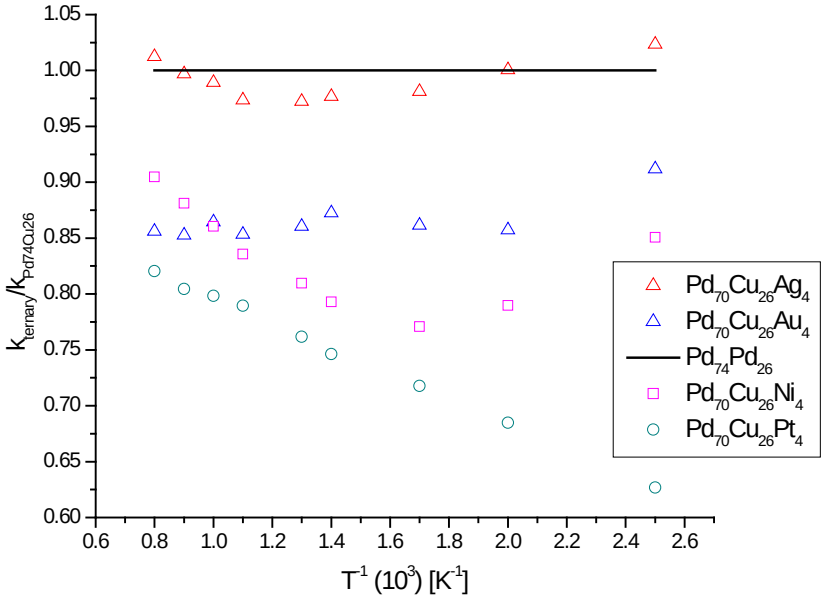

(b)

Figure 19. Permeability results for the ternary systems of interest (a) normalized with respect to $Pd_{70}Cu_{30}$ and (b) normalized with respect to $Pd_{74}Cu_{26}$.

We emphasize here that all the alloys examined previously only include a small amount (3.7 at.%) of the additive element, M. As the membranes examined experimentally usually include a large variety of compositions, we began analyzing alloys with a larger composition of M elements to predict how the properties of H changes with the M composition. The ideal candidates were PdCuAg alloys as we have previously finished the examination of different PdCuAg alloys including $Pd_{96}Cu_4$, $Pd_{96}Ag_4$ and $Pd_{70}Cu_{26}Ag_4$.

The first alloy we examined was $Pd_{66.7}Cu_{25.9}Ag_{7.4}$. Here and below, our compositions are defined in at.%. This composition is determined by a supercell definition in our DFT calculations with 27 metal atoms, including 18 Pd, 7 Cu and 2 Ag atoms. Two distinct supercells were used in our calculations with different placement of two Ag atoms. In the first supercell, two Ag atoms were separated far from each other while in the second supercell they were next to each other, which represented the possible Ag clusters at this composition.

Similar to previous calculations, we need to know both the binding energy and vibrational frequencies of H in the interstitial sites within the bulk of these alloys, which includes 27 octahedral (O) sites and 54 tetrahedral (T) sites in one supercell. Here we only showed the final comparison between binding energies given by DFT calculations and predicted by CE method in Figure 20. It is clear that for all the O sites, T sites and TSs, the CE model gives a good prediction compared with DFT calculations. To further confirm that CE model predicts not only the accurate value of binding energies, but also an accurate distribution of binding energies, we connected the cumulative probability of the binding energies as shown in Figure 21. The comparison between the cumulative probability given by DFT and CE model showed that for both O sites and T sites, CE model fits well with the DFT data, while for TS we slightly overweighted those sites with energies 0.15-0.2 eV in our DFT calculations. This does not point to a problem with our CE, but additional numerical tests will be performed in the near future to further address this issue.

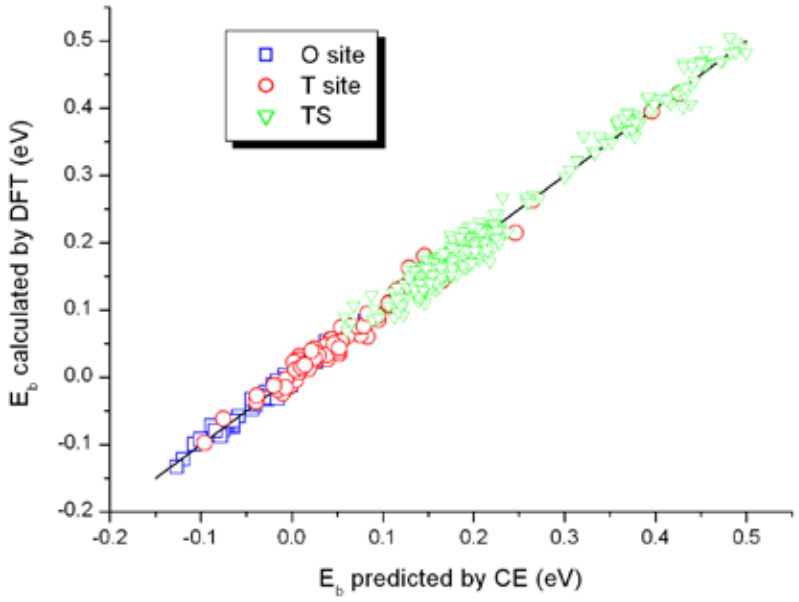

Figure 20. **Comparison between DFT calculated binding energies and CE predicted binding energies.**

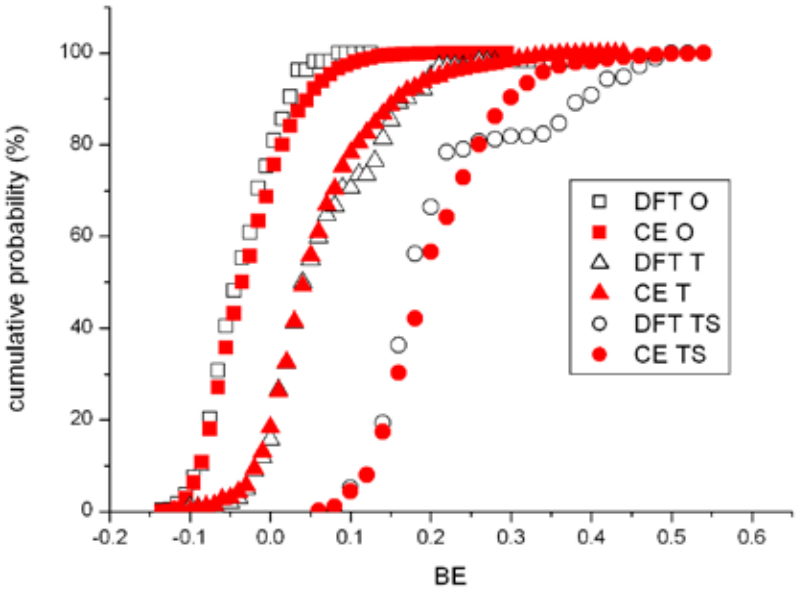

Figure 21. **Comparison between the cumulative probability of binding energies given by DFT calculations and CE predictions.**

After obtaining all CE models for O site, T site and TS, we performed the solubility analysis on these alloys in a similar fashion as previous applied to $Pd_{96}M_4$ and $Pd_{70}Cu_{26}M_4$. The detailed description of this procedure is also given in our previous reports. Here we showed the solubility of hydrogen in $Pd_{70}Cu_{30}$, $Pd_{70}Cu_{26}Ag_4$ and $Pd_{66.7}Cu_{25.9}Ag_{7.4}$, normalized with the solubility in $Pd_{70}Cu_{30}$ in Figure 22. The results showed that substituting Ag for either Pd or Cu atom will increase the solubility of hydrogen. This is consistent with our previous observations. As Ag has a larger atom size than both Pd and Cu, increasing Ag content in the alloy expands the size of the lattice, which favors the existence of interstitial hydrogen atoms.

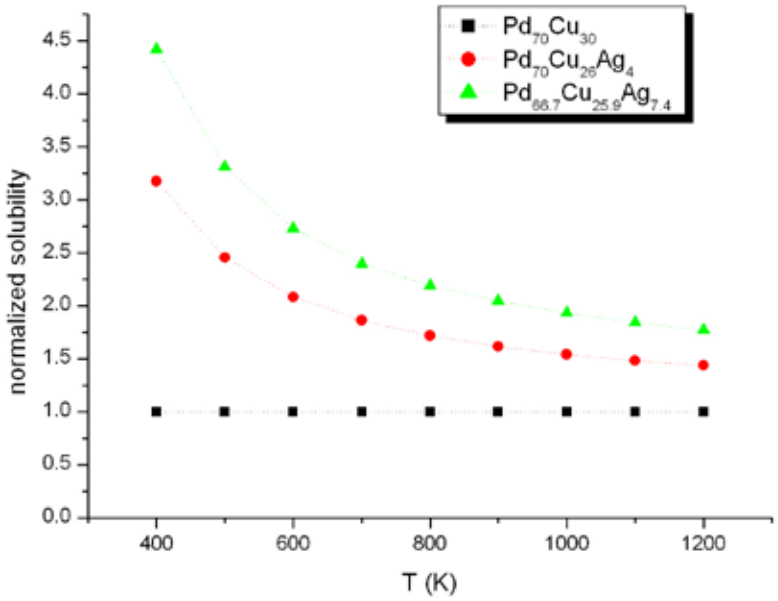

Figure 22. Normalized solubility of hydrogen in $Pd_{70}Cu_{30}$, $Pd_{70}Cu_{26}Ag_4$ and $Pd_{66.7}Cu_{25.9}Ag_{7.4}$.

Similarly, we applied the same method to obtain the diffusivity of hydrogen in $Pd_{66.7}Cu_{25.9}Ag_{7.4}$ alloys. Figure 23 showed us the calculated diffusivity for those three alloys above and for pure Pd. We notice that increasing Ag content in $Pd_{70}Cu_{30}$ also favors the hopping of hydrogen through the lattice. However, in all three alloys we examined the diffusivity is still lower than in pure Pd.

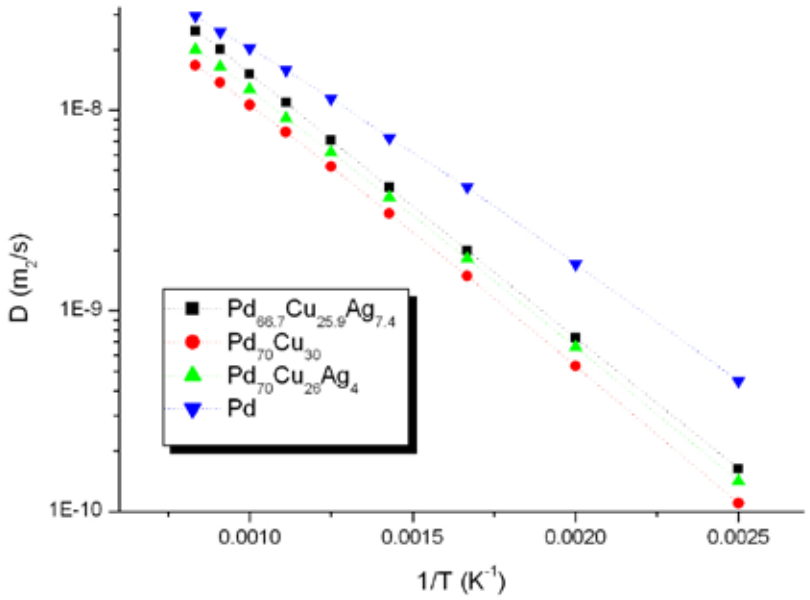

Figure 23. **Normalized diffusivity of hydrogen in $Pd_{70}Cu_{30}$, $Pd_{70}Cu_{26}Ag_4$, $Pd_{66.7}Cu_{25.9}Ag_{7.4}$ and pure Pd.**

Having both the solubility and the diffusivity we calculated the permeability as the product of solubility and diffusivity. Figure 24 shows the permeability predictions for the three alloys we discussed above. It can be observed that the alloy with higher Ag content has the higher permeability. At 400 K, the permeability in $Pd_{66.7}Cu_{25.9}Ag_{7.4}$ is 6 times larger than in $Pd_{70}Cu_{30}$.

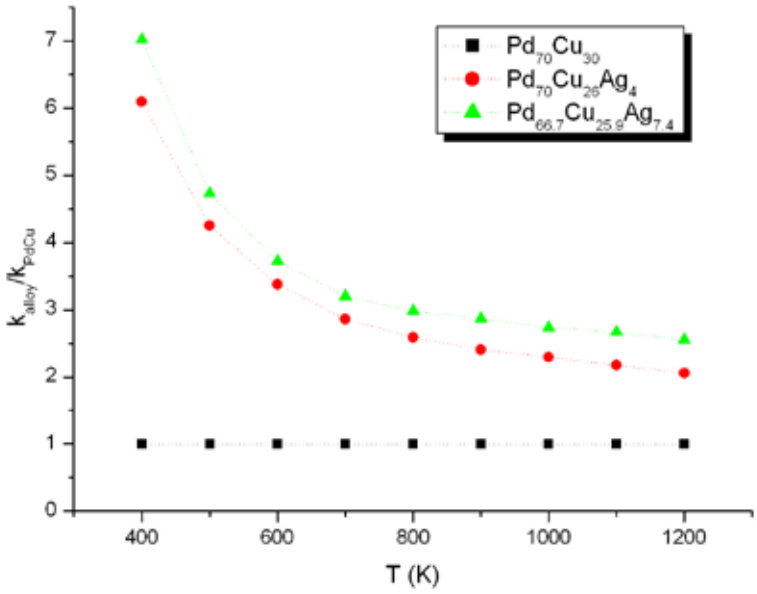

Figure 24. Normalized permeability of hydrogen in $Pd_{70}Cu_{30}$, $Pd_{70}Cu_{26}Ag_4$ and $Pd_{66.7}Cu_{25.9}Ag_{7.4}$.

We find that increasing Ag content in $Pd_{70}Cu_{30}$ results in the increasing of both solubility and diffusivity.

We have finished the analysis of several PdCuAg alloys as well as PdAg binary alloys. Specifically, we have examined four series of PdCuAg alloys, $Pd_{100-x}Ag_x$, with x=3.7, 7.4 and 18.2; $Pd_{96.3-x}Cu_{3.7}Ag_x$ with x=3.7 and 7.4; $Pd_{88.9-x}Cu_{11.1}Ag_x$ with x=18.5 and $Pd_{74.1-x}Cu_{25.9}Ag_x$ with x=3.7 and 7.4. Figure 25 gives a map of the location of those alloys in the ternary phase diagram.

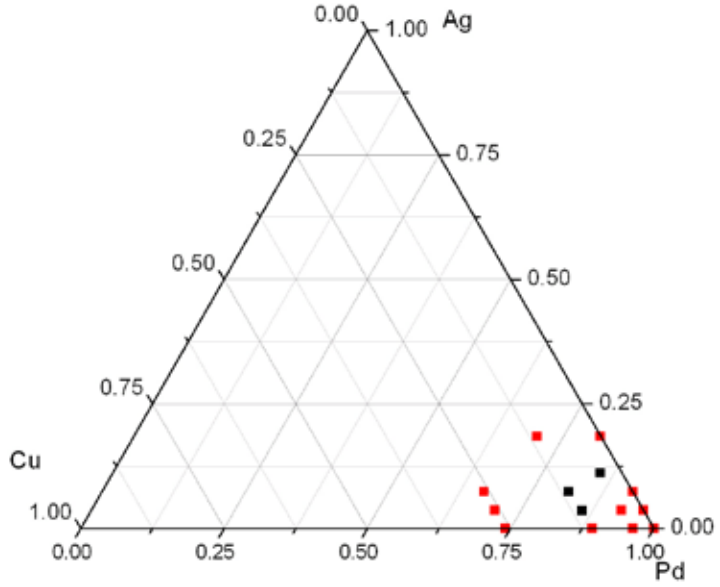

Figure 25. Illustration of the composition of PdCuAg we studied in a ternary phase diagram. Red color: alloys we have examined; black color: alloys we are examining in continuing work.

Figure 26 shows the calculated solubility in PdAg binary alloys normalized by the solubility in pure Pd. For comparison, experimental results from Holleck's report [1] are also shown in the same graph. The results show that substituting Ag for Pd atom will increase the solubility of hydrogen. This is consistent with the experimental observations. As Ag has a larger atom size than both Pd and Cu, increasing Ag content in the alloy expands the size of the lattice, which favors the existence of interstitial hydrogen atoms.

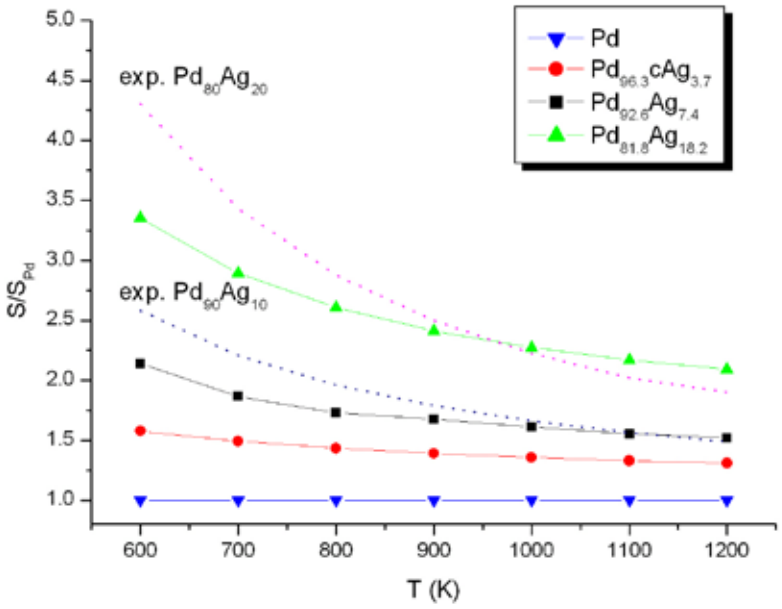

Figure 26. The calculated solubility in PdAg binary alloys normalized by the value in pure Pd. The experimental data comes from ref. 1.

Figure 27 shows the normalized solubility in PdCuAg alloys. A similar trend was found in the ternary alloys; substituting Ag for Pd increases the solubility of hydrogen. However, as we already know that PdCu alloys have lower solubility than pure Pd, in $Pd_{70.4}Cu_{25.9}Ag_{3.7}$ and $Pd_{66.7}Cu_{25.9}Ag_{7.4}$, the net solubilities are still lower than for pure Pd due to the high concentration of Cu in these two alloys.

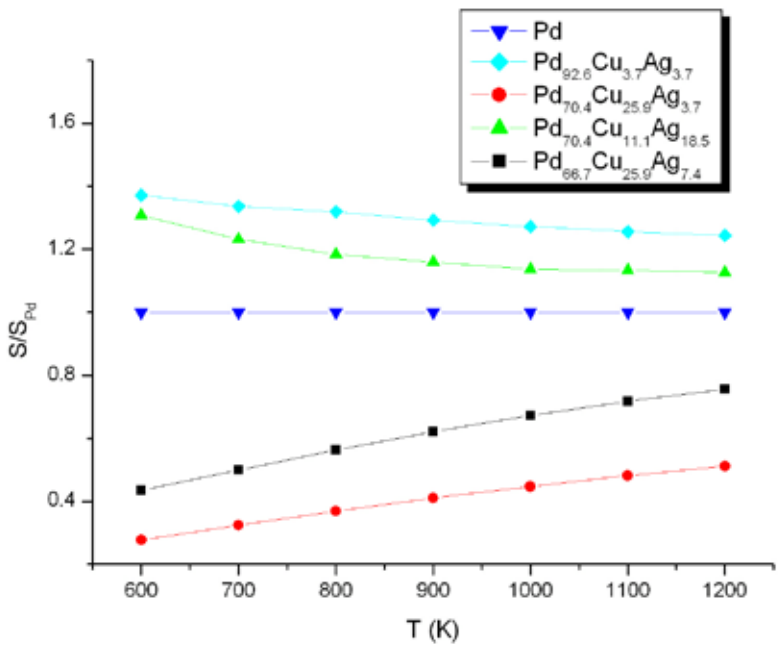

Figure 27. The calculated solubility in PdCuAg ternary alloys, normalized by the value in pure Pd.

Figure 28 shows the calculated diffusivity in PdAg normalized by the diffusivity in pure Pd, as well as the experimental results from Holleck's report.[1] We notice that adding Ag usually decreases the diffusivity in PdAg alloys. The overall permeability in PdAg alloys as a product of the diffusivity and solubility were also shown in Figure 29, normalized by the permeability in pure Pd. Although the additive of Ag has an opposite effect on the solubility and diffusivity, the improvement of the solubility is, however, the dominant effect, and PdAg binary alloys have higher permeability than pure Pd, which is also consistent with experimental observations. These results further prove that our method gives reliable result in screening Pd based alloys, as it does for PdCu alloys.

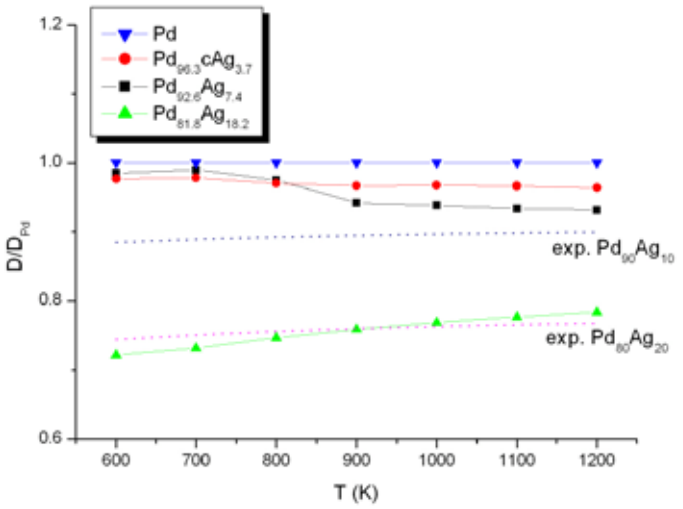

Figure 28. The calculated diffusivity in PdAg binary alloys, normalized by the value in pure Pd. The experimental data comes from ref. 1.

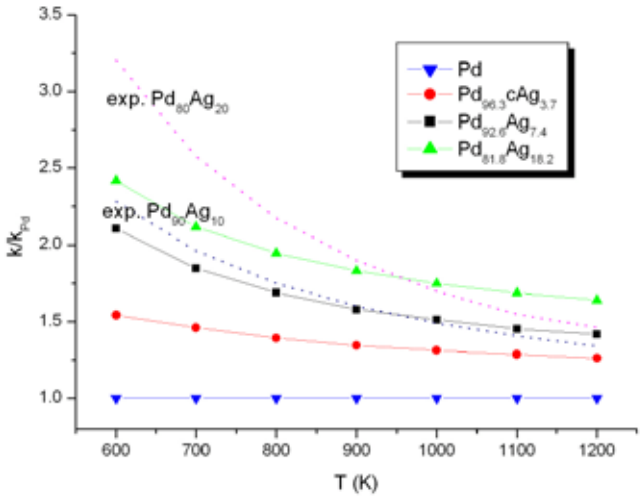

Figure 29. The calculated permeability in PdAg binary alloys, normalized by the value in pure Pd. The experimental data comes from ref. 1.

Finally we calculated diffusivity in PdCuAg ternary alloys that are shown in Figure 30. We found that substituting either Ag or Cu atoms for Pd decreases the diffusivity. The overall permeabilities were also shown in Figure 30. Similar to what we observed in PdAg binary alloys, adding more Ag increases the permeability indicating the improvement of the solubility is greater than the decrease of the diffusivity. However, due to the high Cu content in $Pd_{70.4}Cu_{25.9}Ag_{3.7}$ and $Pd_{66.7}Cu_{25.9}Ag_{7.4}$, the permeabilities of these two alloys are still far below the value for pure Pd.

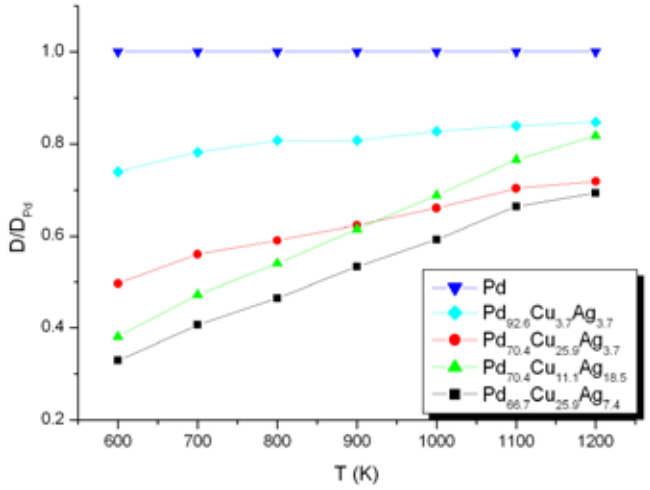

Figure 30. The calculated diffusivity in PdCuAg ternary alloys, normalized by the value in pure Pd.

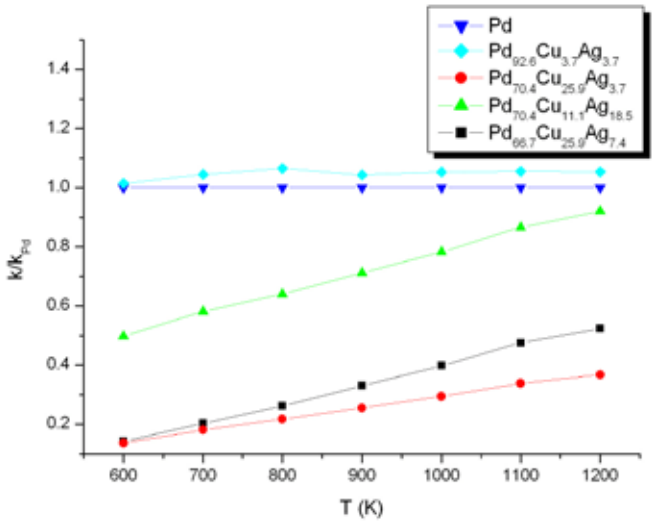

Figure 31. The calculated permeability in PdCuAg ternary alloys, normalized by the value in pure Pd.

We have shown the work performed on several PdCuAg ternary alloys as well as PdAg binary alloys. We find that increasing Ag content in PdCuAg will result in increasing solubility and decreasing diffusivity. The overall permeability, however, shows an improvement.

In October 2010, both Lymarie Semidey-Flecha and Chen Ling successfully defended their PhD theses at Georgia Tech (GT). GT has shown previously that extensive quantum chemistry calculations can be used to make accurate predictions of the hydrogen permeance of metal alloys. The level of work required to make these predictions is still large, with our

computational throughput limited to ~10 distinct materials per year. GT has used their extensive DFT data to explore simplified models that could potentially be used to screen large numbers of alloys more rapidly with the idea that promising alloys from an approximate screening of this kind could then be examined in more detail using the described earlier methods. The core concept in this simplified approach is to examine a model with a minimal number of adjustable parameters so that these parameters can be determined from a very small number of quantum chemistry calculations for materials of interest. In the model we are currently exploring, the site energies and hopping energies for interstitial H are described using a two parameter model where the two parameters represent the effects of lattice expansion/contraction and localized chemical interactions between H and non-Pd atoms. Some details associated with this heuristic model remain to be resolved, but our preliminary results are encouraging.

Another aspect of GT's previous work that made calculations somewhat time consuming was the use of Kinetic Monte Carlo (KMC) simulations to simulate H diffusion. We have examined the use of a semi-analytical approach known as the Average Jump Rate Theory (AJRT) which gives predictions of diffusivities much more rapidly than KMC. The main assumption in using the AJRT is that no spatial correlations exist between the distribution of binding energies for interstitial sites and the binding energies of transition states for site to site hops. This assumption cannot be exactly correct, but our initial calculations suggest that invoking this assumption does not introduce a large level of uncertainty. Used in combination with the heuristic binding site model outlined above, this approach may make it possible for us to rapidly predict the permeation of H through a very large set of alloys at an approximate level with the aim of identifying promising materials for more detailed study.

The exploratory calculations with the approximation methods outlined above have suggested a number of binary Pd-based alloys for more detailed study. These include alloys of Pd with Zr, Hf, and Ir. We are currently performing detailed DFT calculations to assess these alloys more precisely.

The absorption and diffusion of carbon in Pd and Pd-based alloys can be important in applications of these materials as catalysts or membranes, but little is known about these processes. We used first principles calculations to characterize the absorption of C in pure Pd and PdM alloys with M=Ag, Au, and Cu. Our calculations show that the preferred configuration of C in Pd is as an interstitial atom; effects from Pd vacancies are minimal and substitutional sites are much less favorable. When the effects of thermal lattice expansion are included, our calculations predict C diffusivities in good agreement with experimental data, which is only available at elevated temperatures. Characterizing the binding energy and hopping energies of interstitial C in terms of lattice expansion or contraction is also a useful way to understand the effect of small amounts of M=Ag, Au, or Cu in PdM alloys. We also examined the properties of interstitial C in $Pd_{77.7}Ag_{22.3}$. Our calculations predict that the diffusivity of C in this alloy is two to three orders of magnitude lower than in pure Pd.

The focus of the GT work to date is in understanding the effects of dilute amounts of additive metals which have not been studied before in Pd-rich binary membranes. Specifically Zr, Hf, Ta, Ir, Nb, and Ru were chosen as additive metals. Zr is known to contribute to the hydrogen sorption process. PdZr alloys are known to become active and selective in the hydrogenation of compounds after HF treatment and oxidation in experiment [2]. Pure Ta and Nb exhibit higher hydrogen permeability than Pd [3-5]. Ir is known as a gas selective metal, and it is also chiefly known for its catalytic activity [6]. Way et al. demonstrated experimentally that adding Ru helps the membranes exhibit high hydrogen flux (greater than one mol/m^2/s) at 673 K [7]. The phase diagrams of binary metal alloys are well known experimentally [8]. We analyzed the binary phase diagrams of Pd and Zr, Hf, Ta, Ir, Nb, and Ru to ensure the addition of small atomic percent of the additive metal atoms would result in an fcc crystal structure.

The predicted H solubilities in the binary alloys we examined are shown in Figure 32. In each case, the solubility is normalized with the DFT-predicted results for pure Pd under the same conditions. Our DFT results for pure Pd are in good agreement with experimental data. For instance, with $\Theta = K_s\sqrt{P_{H_2}}$ our calculations give Θ_{Pd} = 0.011 $atm^{-0.5}$ at 1000 K and 1 atm pressure, while an experimental value of Θ_{Pd} = 0.009 $atm^{-0.5}$ was observed under the same conditions [9]. Here, Θ is the H/M ratio in the alloy. Including Ir, Nb or Ru in a binary alloy increases H solubility in the alloy relative to pure Pd. For $Pd_{96}Ru_4$, the predicted solubility of H in the alloy relative to pure Pd is approximately independent of temperature. $Pd_{89}Zr_{11}$, $Pd_{89}Hf_{11}$, and $Pd_{89}Ta_{11}$ are all predicted to have lower solubility for H than pure Pd.

It is commonly considered that H solubility in Pd alloys is largely affected by the lattice expansion or contraction of the alloy relative to pure Pd, with lattice expansion corresponding to increased solubility. Semidey-Flecha showed that Au and Ag expand the metal, and Cu contracts the metal [10]. Of course, a non-geometric effect which is actually associated with the specific interactions between interstitial H and M atoms can also play an important role in controlling solubility. For instance, if the predictions were made solely based on lattice parameters, $Pd_{96}Ir_4$ would be expected to show the lowest solubility among the alloys we examined. In contrast, in Figure 33, the calculated solubility for this alloy is higher than all other materials except for the alloy with Ru. The behavior of PdZr, PdHf, and PdTa alloys also illustrate the role of these chemical effects. Alloying with Zr, Hf and Ta increases the material's lattice constant, but there is a reduction in H solubility. These results are consistent with the experimental results of Sakamoto *et al*. who reported that the palladium-tantalum and palladium-zirconium lattice expands, but the alloys behave as contracted alloys with respect to solubility [12]. Experimentally, the solubility of hydrogen decreases in PdTa alloys, even though the lattice is expanded by alloying with Ta [12].

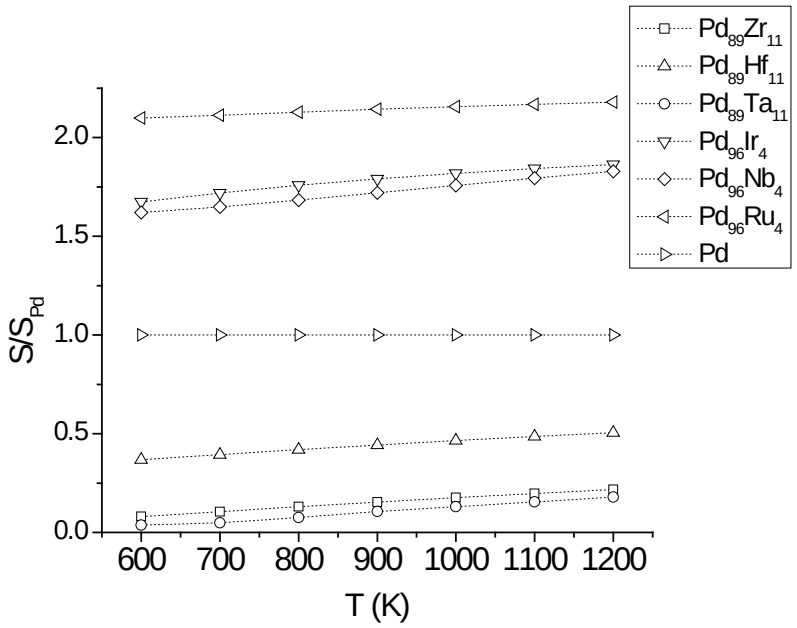

Figure 32. Hydrogen solubility predictions for $Pd_{100-x}M_x$ for M = Zr, Hf, Ta, Ir, Nb, and Ru normalized with respect to Pd.

Figure 33 shows the results for normalized diffusivity of each alloy for T = 600 – 1200 K. The most obvious effect is that the additive metal predicted to have the highest solubility shows the lowest diffusivity. From the Arrhenius diffusion equation, we determined the diffusion pre-exponential factor with the effective activation energy barrier. Both Zr and Hf as an additive have reduced the solubility of H, but in turn they have improved the diffusion. Ta is the only metal additive to have been predicted to reduce both H solubility and diffusion relative to H behavior in pure Pd. We observe that the remaining $Pd_{96}M_4$ alloys (M = Ir, Nb, Ru) have enhanced the solubility of H, but in turn they have reduced the diffusion.

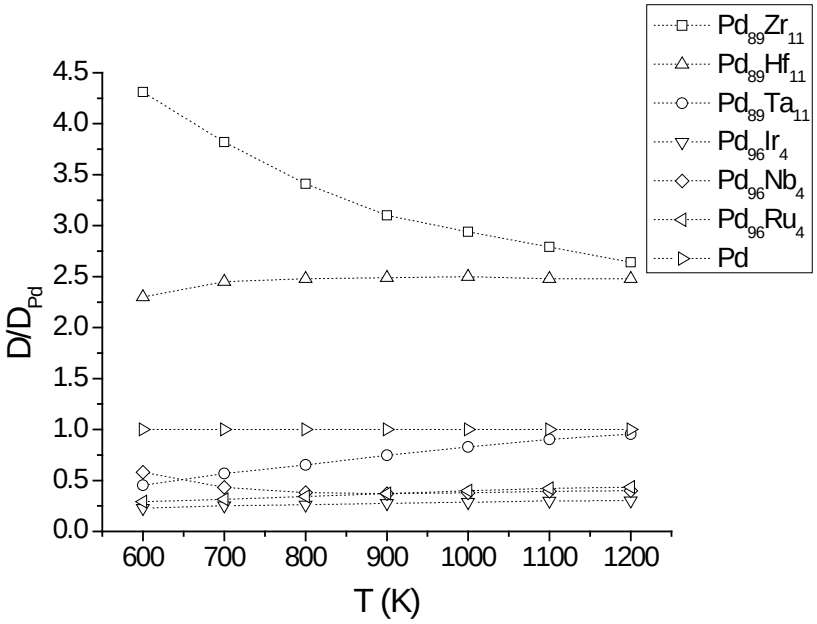

Figure 33. Hydrogen diffusivity predictions for $Pd_{100-x}M_x$ for M = Zr, Hf, Ta, Ir, Nb, and Ru normalized with respect to Pd.

The permeability results normalized with respect to pure Pd's permeability are shown in Figure 34. Permeability is directly proportional to both solubility and diffusion. Even though there was a high H solubility in the $Pd_{96}Ir_4$, the diffusion of H was quite slow. This low diffusivity reduces the H permeability. The resulting permeability of H in $Pd_{96}Ir_4$ was on average only 49 % of the H permeability in pure Pd. For the $Pd_{89}Zr_{11}$ alloy, we observe improved performance only in H diffusivity, and the overall result was reduced H permeability in $Pd_{89}Zr_{11}$. The $Pd_{89}Hf_{11}$ alloy shows reduced H solubility with great improvement in H diffusion relative to pure Pd. The enhancement in H diffusion overwhelms the reduction in solubility of H in the bulk material. As a result, it makes H permeability improved above T = 750 K. This improvement is because of the increased H solubility and diffusivity at elevated temperatures. Tantalum negatively affects the permeability of H in comparison to pure Pd. The $Pd_{89}Ta_{11}$ alloy is predicted to have the lowest permeability of all the systems we studied. This is not surprising if we take into account the reduction in both solubility and diffusion of H for the $Pd_{89}Ta_{11}$ alloys. For the Ir, Nb, and Ru alloys, they show improved H solubility with reduction in H diffusion.

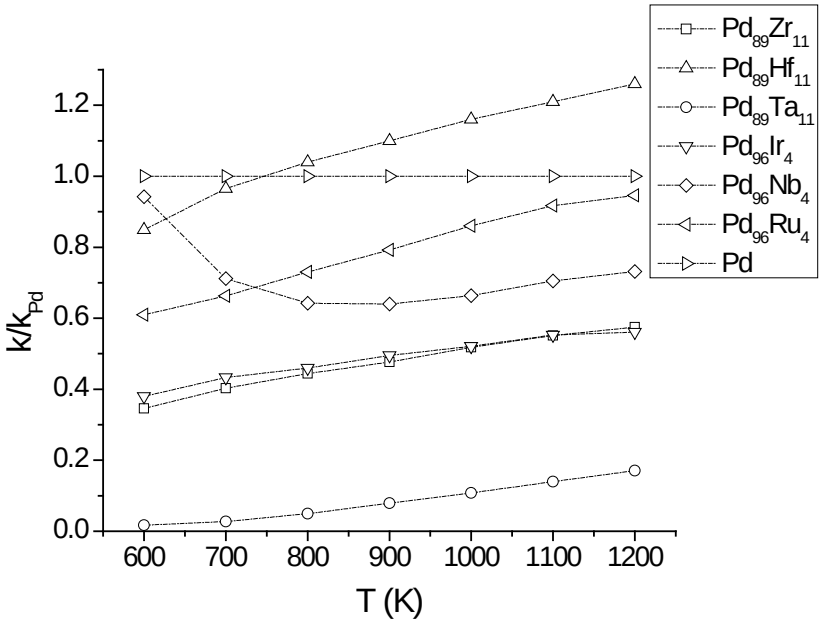

Figure 34. Hydrogen permeability predictions for $Pd_{100-x}M_x$ for M = Zr, Hf, Ta, Ir, Nb, and Ru normalized with respect to pure Pd.

As shown in Figure 35, there is a good agreement in terms of hydrogen permeability, solubility, and diffusivity between the accurate CE models and new method. The heuristic lattice model enables us to use smaller numbers of DFT calculations to predict whether a binary alloy is an interesting candidate as H purification membrane that merits detailed study in a rapid time.

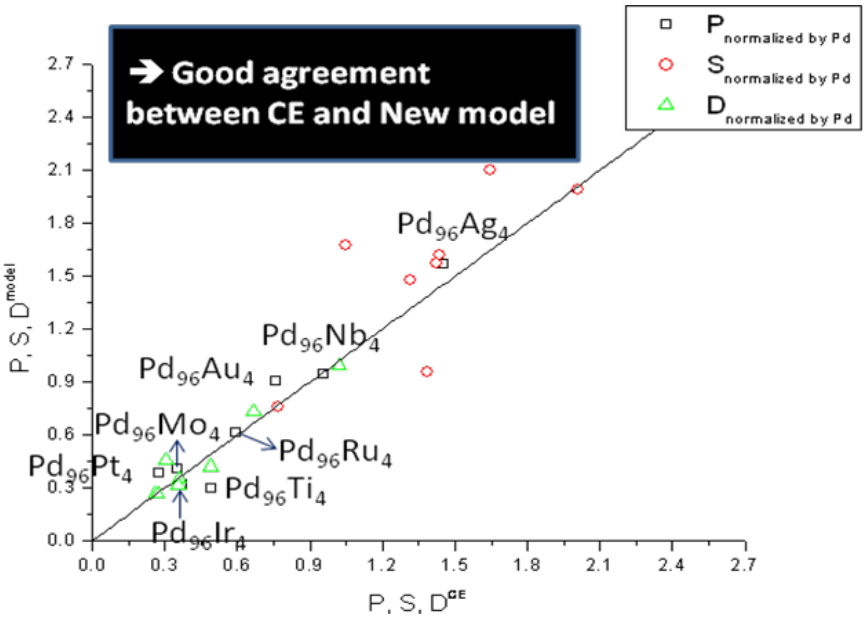

Figure 35. Comparison of solubility, diffusivity, and permeability between CE method and new method.

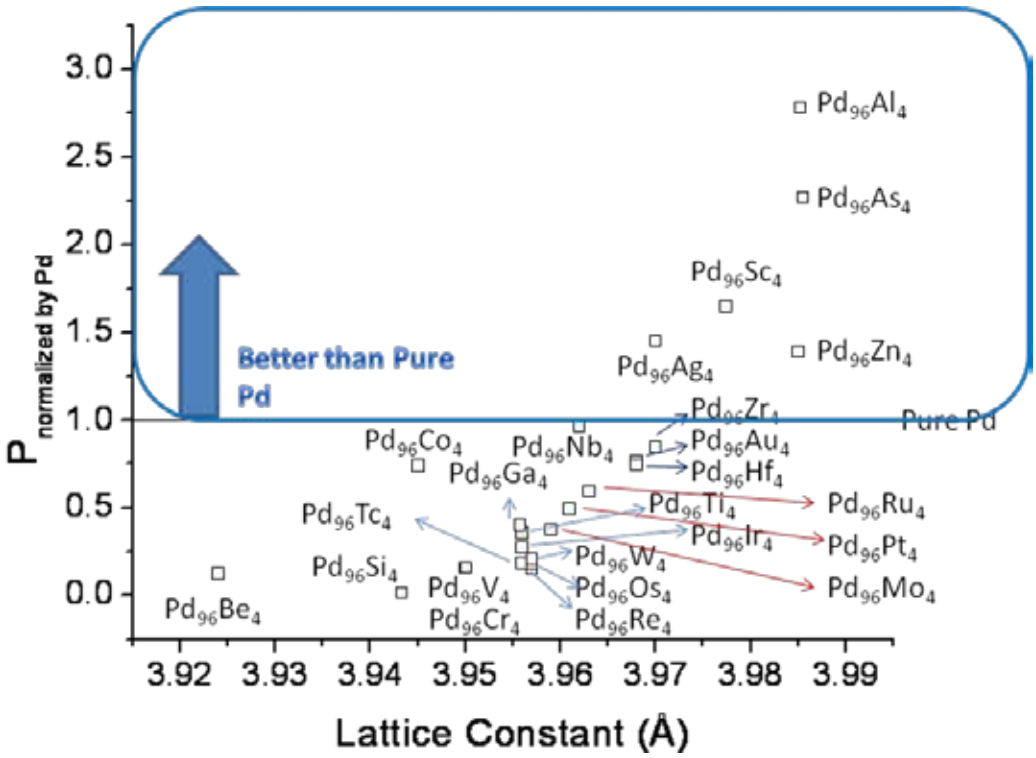

Figure 36. Hydrogen permeability normalized by pure Pd at each alloy.

From the binary phase diagrams we know that Pd forms FCC alloys with many metals, including M = Ag, Al, As, Au, Be, Co, Cr, Ga, Hf, Ir, Mo, Nb, Os, Pt, Re, Sc, Si, Ru, Tc, Ti, V, W, Zn, Zr. We have analyzed binary alloys of composition $Pd_{96}M_4$ with all of these metals at 600 K. We find an initial lattice constant estimate using Vegard's Law. This initial lattice constant is used to find the DFT optimized lattice constant while allowing all the metal atoms to relax as the cell volume changes. As shown in Figure 36, there is a general trend of an increase of hydrogen permeability as lattice constant increases. In order to further examine the materials with the highest predicted hydrogen permeability (namely $Pd_{96}Al_4$, $Pd_{96}As_4$, $Pd_{96}Sc_4$, and $Pd_{96}Zn_4$) detailed calculation using our original method were performed. We are aware of no reports on these materials in the literature, so it is interesting to elucidate their performance with respect to hydrogen permeability.

Shortly prior to this report being completed, we realized that the lattice constant used in the calculations for $Pd_{96}Al_4$ in Figure 36 was erroneous. This implies that the very high permeability predicted for this alloy is incorrect. The results for the other high permeability alloys in Figure 36, however, were not affected by the problem that led to this error.

The calculations introduced by Semidey-Flecha [10] provided detailed predictions about which alloys are best suited for H purification relative to other dense metal membranes. The solubility of H is associated with the lattice expansion in an alloy compared to the host lattice. However, lattice expansion or contraction is not enough for crystalline alloys to show high hydrogen permeability, since the permeability of hydrogen is determined by the product of the solubility and diffusivity. Accordingly, we also have to consider the chemical effects that come from the local surrounding environment of the hydrogen in the interstitial sites on the diffusion of H in alloys. It can be more challenging to understand chemical effects on the diffusion of H. We have developed a heuristic lattice model that is appropriate for rapidly characterizing H solubility and diffusion in alloys for the search of new promising materials for membranes. This approach is not as precise as the detailed models of Semidey-Flecha and Sholl, but can be used as an initial tool for screening materials prior to using more detailed models on promising materials. We analyzed Pd-based binary alloys to demonstrate the capability of our new model that makes screening more efficient and quick by comparison with the cluster expansion approach. Using our model, we predicted the hydrogen permeability of the $Pd_{96}M_4$ where M = Li, Na, Mg, Al, Si, Sc, Ti, V, Cr, Mn, Fe, Co, Ni, Cu, Zn, Ga, Y, Zr, Nb, Mo, Tc, Ru, Rh, Ag, Cd, In, Sn, Sb, Te, Hf, Ta, W, Re, Os, Ir, Pt, Au, Tl, Pb, Bi, Ce, Sm, Gd, Tb, Dy, Ho, Er, Tm, Yb, Lu. This is a far greater range of materials than has been examined in previous modeling or experimental studies.

Figure 37 shows the predicted solubility of H in a large number of alloys, normalized by the solubility in pure Pd. In general, H solubility is related to the alloy's lattice constant, which means that the alloys that have larger lattice constant show higher solubility. The palladium-rare earth alloys have been considered to be good candidates for use in hydrogen purification membranes [4]. Since the lattice constants of the most of the lanthanides are large, this suggests solubility of their alloys will be high. The range of solubilities seen at a fixed value of the lattice constant in Figure 37 demonstrates the chemical effects that also contribute to H solubility.

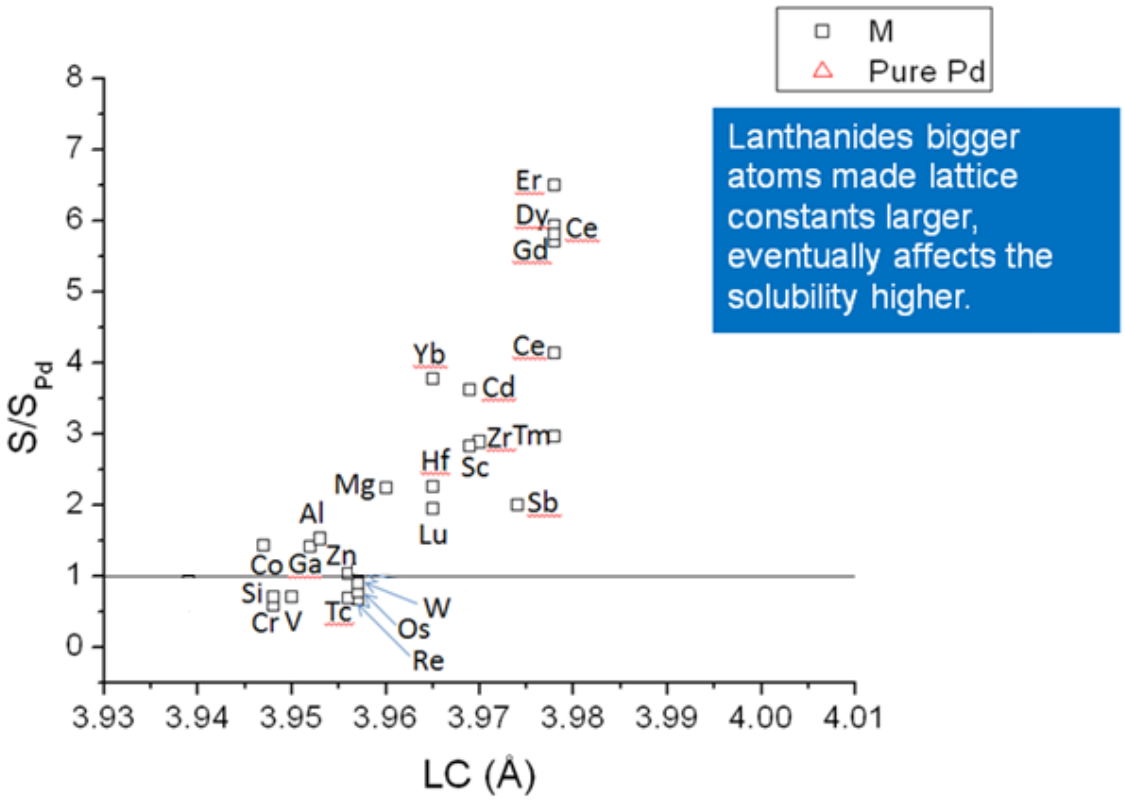

Figure 37. Solubility in $Pd_{96}M_4$ alloys predicted using a DFT-based heuristic model.

The predicted H diffusivity (again normalized by the result for pure Pd) in a large number of alloys is summarized in Figure 38. Most of the materials that showed high solubility have lower diffusivity than pure Pd. However, for Tm, our simplified model predicts higher diffusivity and higher solubility than pure Pd. For this material, we performed detailed DFT-based calculations using the methods of Semidey-Flecha and Sholl. These calculations confirm the predictions of our initial model.

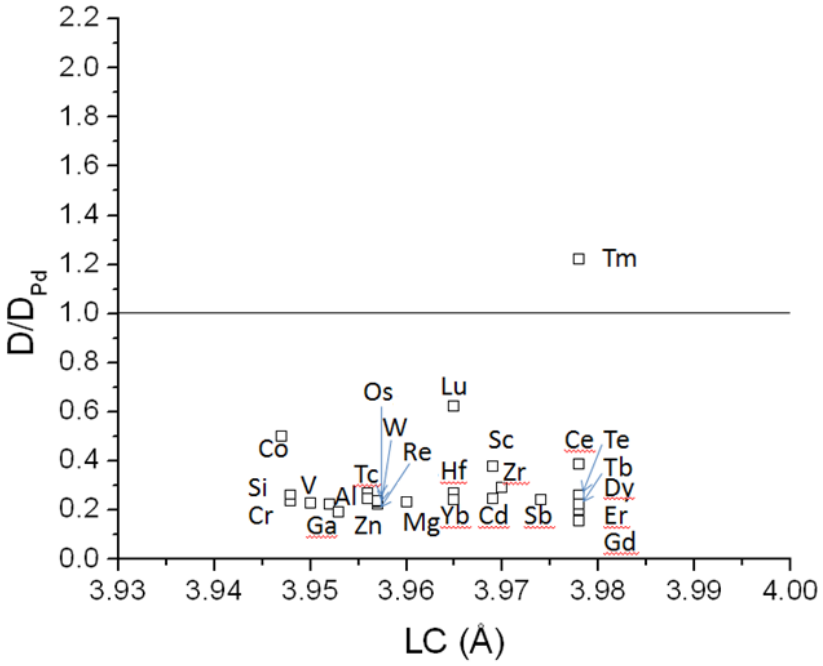

Figure 38. Diffusivity in $Pd_{96}M_4$ alloys predicted using a DFT-based heuristic model.

Once we know the diffusivity and solubility, we could predict the permeability of hydrogen in the alloys as shown in Figure 39. The orange curve in this figure shows the result that would be found for pure Pd if the lattice constant was simply expanded or contracted relative to the equilibrium value. Deviations for specific materials away from this curve indicate the presence of chemical effects in the solubility and diffusion of H. Our calculations identify multiple alloys that are predicted to have permeability higher than pure Pd. In particular, the permeability of $Pd_{96}Tm_4$ is predicted to be far larger than pure Pd. As mentioned above, this prediction was also made by more detailed DFT-based calculations we performed for this same alloy. These predictions suggest that experimental testing of this novel alloy would be worthwhile.

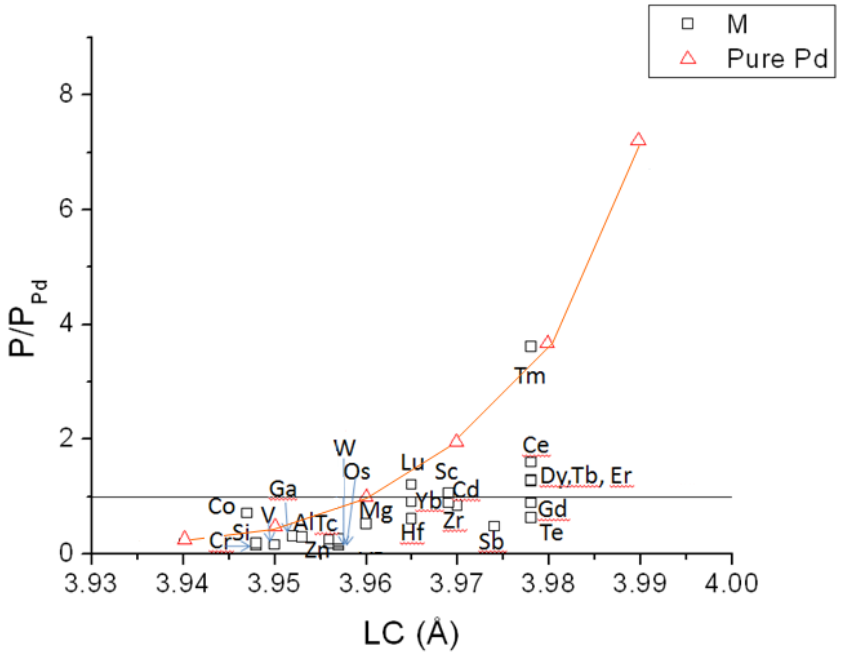

Figure 39. Permeability in $Pd_{96}M_4$ alloys predicted using a DFT-based heuristic model.

2.0 MEMBRANE DEPOSITION, COMPOSITION AND MICROSTRUCTURE OPTIMIZATION

The development of thin Pd-alloy membranes using physical vapor deposition methods including magnetron sputtering have proceeded over the last 36 months. The following table shows all (>160) of the deposition runs with the vacuum processing conditions.

Table 3. Deposition conditions

Run #	Target	Base press (torr)	Substrate	Run time	Sputtering		
					watts	volts	amps
Pd-14	Pd	1.80E-06	1x6 Si wafer witness	50 min	1,500	411	3.6
Pd-15	Pd	1.30E-06	1x6 witness, 6"wafer	5 hr 10 min	1,500	404	3.6
Pd-17	Pd	9.00E-07	6" wafer	5 hr	1,500	410	3.5
Pd-18	Pd	8.00E-07	6" wafer	5 hr	1,500	403	3.6
Pd-19	Pd	1.10E-06	6" wafer	5 hr	780	480	1.6
Pd-20	Pd	1.10E-06	6" wafer	2.5 hr	780	480	1.6
Pd-21	Pd	1.00E-06	1x6 Si wafer witness	30 min	780	480	1.6
Pd-22	Pd/Cu 5%	1.10E-06	6" wafer	3 hr 40 mn	780	488	1.6
Pd-23	Pd/Cu 20%	1.00E-06	6" wafer	1 hr 50 min		497	

Run #	Target	Base press (torr)	Substrate	Run time	Sputtering watts	volts	amps
					780		1.5
Pd-24	Pd/Ag 5%	6.50E-07	6" wafer	1 hr 50 min	780	471	1.6
Pd-25	Pd/Ag 20%	9.00E-07	6" wafer	1 hr 50 min	780	498	1.5
Pd-26	Pd/Ag 20%	7.30E-07	1x6 witness	30 min	780	507	1.5
Pd-27	Pd	1.00E-06	12" wafer	19 min	780	490	1.5
Pd-28	Pd/Cu /Ag 75/20/5%	7.20E-07	6" wafer	1 hr 50 min	780	490	1.5
Pd-29	Pd	3.60E-06	None	30 min	780	487	1.7
Pd-30	Pd/Cu /Ag 75/20/5%	1.30E-06	6" wafer	3hrs 21min	780	485	1.7
Pd-31	Pd/Cu /Ag 75/20/5%	1.40E-06	6" wafer	3hrs 21min	780	496	1.7
Pd-32	Pd/Cu /Ag 75/20/5%	1.20E-06	6" wafer	3hrs 21min	780	493	1.7
Pd-33	Pd/Cu /Ag 75/20/5%	1.60E-06	6" wafer	3hrs 21min	780	501	1.7
Pd-34	Pd/Cu /Ag 75/20/5%	1.70E-06	6" wafer	3hrs 21min	780	541	1.5
Pd-35	Pd	1.10E-06	None	30 min	780	484	1.7
Pd-36	Pd/Cu 60%	1.00E-06	2- 1" coated wafers	2hrs 15min	780	483	1.7
Pd-37	Pd	8.00E-07	2x6" taped wafer	30 min	780	475	1.7
Pd-38	Pd/ Cu 60/40%	2.00E-06	2x6" taped wafer	30 min	780	479	1.7
Pd-39	Pd/ Cu 60/40%	3.00E-06	6" wafer	1hrs 56min	780	479	1.7
Pd-40	Pd/ Cu 60/40%	2.90E-07	6" wafer	1hrs 25min	780	485	1.7
Pd-41	Pd	3.10E-06	1.5"x5" taped wafer	30 min	780	468	1.7
Pd-42	Pd/Au 90/10%	1.60E-06	2"x 6" taped wafer	30 min	780	467	1.8
Pd-43	Pd/Au 90/10%	2.40E-07	6" wafer	3hrs 44min	780	465	1.7
Pd-44	Pd/Au 90/10%	1.50E-07	6" wafer	3hrs 44min	780	464	1.8
Pd-45	Pd/Au 90/10%	1.90E-07	6" wafer	3hrs 44min	780	467	1.8
Pd-46	Pd/Au 90/10%	1.50E-07	6" wafer	4hrs 24min	780	485	1.7
Pd-47	Pd/Au 90/10%	2.10E-07	6" wafer	4hrs 24min	780	481	1.7
Pd-48	Pd/Au 90/10%	2.50E-07	6" wafer	4hrs 24min	780	487	1.7

Run #	Target	Base press (torr)	Substrate	Run time	Sputtering watts	volts	amps
Pd-49	Pd/Cu/Au 75/17/8%	4.00E-07	2"x 6" taped wafer	30 min	780	494	1.7
Pd-50	Pd/Cu/Au 75/17/8%	2.50E-07	6" wafer	4hrs 24min	780	495	1.7
Pd-51	Pd/Cu/Au 75/17/8%	1.30E-07	6" wafer	4hrs 24min	780	498	1.7
Pd-52	Pd/Cu/Pt 75/17/8%	4.80E-07	1"x 6" taped wafer	30 min	780	515	1.6
Pd-53	Pd/Cu/Pt 75/17/8%	1.10E-07	6" wafer	4hrs 24min	780	511	1.7
Pd-54	Pd/Cu/Pt 75/17/8%	2.00E-07	6" wafer	4hrs 24min	780	520	1.6
Pd-55	Pd	2.00E-05	None	30 min	780	498	1.7
Pd-56	Pd/Cu/y 79/17/4%	3.50E-06	2"x 6" taped wafer	30 min	780	491	1.7
Pd-57	Pd/Cu/y 79/17/4%	4.60E-07	2"x 6" taped wafer	30 min	780	493	1.7
Pd-58	Pd/Cu/y 79/17/4%	2.20E-07	6" wafer	4hrs 24min	780	488	1.7
Pd-59	Pd/Cu/y 79/17/4%	1.90E-07	6" wafer	4hrs 24min	780	496	1.7
Pd-60	Pd	9.00E-08	None	30 min	780	498	1.7
Pd-61	Pd/Cu 75/25%	2.50E-06	1.5"x 6" taped wafer	30 min	780	520	1.6
Pd-62	Pd/Cu 75/25%	2.30E-07	6" wafer	4hrs 24min	780	510	1.4
Pd-63	Pd/Cu 75/25%	2.10E-07	6" wafer	5hrs 33 min	780	515	1.4
Pd-64	Pd/Cu/Pt 70/17/13%	3.60E-06	1.5"x 6" taped wafer	30 min	780	520	1.4
Pd-65	Pd/Cu/Pt 70/17/13%	2.10E-07	6" wafer	5hrs 33 min	780	515	1.4
Pd-66	Pd/Cu/Pt 70/17/13%	9.00E-07	1.5"x 6" taped wafer	30 min	780	521	1.6
Pd-67	Pd/Cu/Pt 70/17/13%	1.60E-07	6" wafer	5hrs 33 min	780	535	1.5
Pd-68	Pd/Cu/Pt 70/17/13%	2.10E-07	6" wafer	5hrs 33 min	780	508	1.5
Pd-69	Pd/Cu/Pt 70/17/13%	2.10E-07	6" wafer	5hrs 33 min	780	498	1.7
Pd-70	Pd	1.70E-07	None	30min	780	461	1.8
Pd-71	Pd/Cu/Au 70/17/13%	1.80E-06	1.5"x 6" taped wafer	40min	780	491	1.7
Pd-72	Pd/Cu/Au 70/17/13%	1.40E-07	6" wafer	5hrs 33 min	780	515	1.6
Pd-73	Pd/Cu/Au 70/17/13%	1.60E-07	6" wafer	5hrs 33 min	780	478	1.8
Pd-74	Pd/Cu/Au 70/17/13%	9.00E-08	6" wafer	5hrs	780	477	1.7
Pd-75	Pd/Cu/Au	2.00E-07	6" wafer	5hrs 10min		475	

Run #	Target	Base press (torr)	Substrate	Run time	Sputtering watts	volts	amps
	70/17/13%				780		1.7
Pd-76	Pd	1.00E-06	None	30min	780	470	1.7
Pd-77	Pd/Cu/Ni 75/17/8%	1.90E-07	1.5"x 6" taped wafer	40min	780	466	1.8
Pd-78	Pd/Cu/Ni 75/17/8%	1.40E-07	6" wafer	3hrs 30min	780	476	1.7
Pd-79	Pd/Cu/Ni 75/17/8%	9.00E-08	6" wafer	5hrs 10min	780	476	1.7
Pd-80	Pd/Cu/Ni 75/17/8%	1.60E-06	6" wafer	5hrs 10min	780	475	1.7
Pd-81	Pd/Cu/Ni 75/17/8%	2.00E-07	6" wafer	5hrs 10min	780	489	1.7
Pd-82	Pd	1.60E-06	None	40 min	780	497	1.7
Pd-83	Pd-Ru 90/10%	2.00E-07	1.5"x 6" taped wafer	40min	780	489	1.7
Pd-84	Pd-Ru 90/10%	1.40E-07	6" wafer	3hrs 51 min	780	476	1.7
Pd-85	Pd-Ru 90/10%	9.00E-08	6" wafer	3hrs 51 min	780	469	1.7
Pd-86	Pd-Ru 90/10%	1.30E-06	6" wafer	3hrs 51 min	780	488	1.7
Pd-87	Pd-Ru 90/10%	2.40E-07	6" wafer	4hrs 56min	780	488	1.7
Pd-88	Pd/Cu/Ru 85/5/10%	1.30E-07	1.5"x 6" taped wafer	40 min	780	483	1.7
Pd-89	Pd/Cu/Ru 85/5/10%	2.50E-07	6" wafer	3hrs 36min	780	492	1.7
Pd-90	Pd/Cu/Ru 85/5/10%	2.40E-07	6" wafer	4hrs 56min	780	486	1.7
Pd-91	Pd	3.70E-07	None	30	780	465	1.8
Pd-92	Pd/Cu/Au 85/5/10%	3.00E-06	1.5"x 6" taped wafer	40 min	780	505	1.7
Pd-93	Pd/Cu/Au 85/5/10%	2.00E-07	6" wafer	5hrs 10min	780	485	1.7
Pd-94	Pd/Cu/Au 85/5/10%	2.00E-07	6" wafer	4hrs 53min	780	484	1.7
Pd-95	Pd/Cu/Au 85/5/10%	2.10E-07	6" wafer	4hrs 53min	780	484	1.7
Pd-96	Pd/Cu/Au 85/5/10%	2.50E-07	6" wafer	4hrs 53min	780	488	1.7
Pd-97	Pd	2.50E-07	None	30 min	780	448	1.8
Pd-98	Pd/Cu/Au 65/35/5%	1.00E-07	1.5"x 6" taped wafer	40 min	780	496	1.7
Pd-99	Pd/Cu/Au 65/35/5%	9.00E-08	6" wafer	4hrs 53min	780	520	1.6
Pd-100	Pd/Cu/Au 65/35/5%	2.00E-07	6" wafer	5hrs 10min	780	520	1.6

Run #	Target	Base press (torr)	Substrate	Run time	Sputtering watts	volts	amps
Pd-101	Pd/Cu/Au 65/35/5%	2.40E-07	6" wafer	5hrs 20min	780	515	1.6
Pd-102	Pd/Cu/Au 65/35/5%	1.40E-07	6" wafer	5hrs 15min	780	516	1.7
Pd-103	Pd	2.50E-07	None	30 min	780	450	1.9
Pd-104	Pd-Cu 60/40%	2.50E-07	1.5"x 6" taped wafer	40 min	780	491	1.7
Pd-105	Pd-Cu 60/40%	9.00E-08	6" wafer	3hrs 10min	780	506	1.7
Pd-106	Pd-Cu 60/40%	9.00E-08	6" wafer	3hrs 10min	780	512	1.7
Pd-107	Pd-Cu 60/40%	2.40E-07	6" wafer	3hrs 10min	780	514	1.7
Pd-108	Pd-Cu 60/40%	9.00E-08	6" wafer	3hrs 10min	780	516	1.7
Pd-109	Pd-Cu 60/40%	1.20E-07	6" wafer	3hrs 55min	780	522	1.6
Pd-110	Pd-Cu 60/40%	2.60E-07	1.5"x6" wafer	40 min	780	500	1.6
Pd-111	Pd-Cu 60/40%	1.20E-07	6" wafer	3hrs 55min	780	513	1.7
Pd-112	Pd-Cu 60/40%	3.00E-07	6" wafer	3hrs 55min	780	522	1.6
Pd-113	Pd-Cu 60/40%	4.50E-07	6" wafer	3hrs 55min	780	531	1.6
Pd-114	Pd-Cu 60/40%	2.80E-07	6" wafer	3hrs 55min	780	527	1.6
Pd-115	Pd-Cu 60/40%	4.50E-07	1.5"x6" wafer	40 min	780	524	1.6
Pd-116	Pd-Cu 60/40%	2.90E-07	6" wafer	3hrs 55min	780	527	1.6
Pd-117	Pd-Cu 60/40%	3.30E-07	6" wafer	3hrs 55min	780	546	1.5
Pd-118	Pd-Cu 60/40%	1.60E-07	6" wafer	3hrs 55min	780	546	1.5
Pd-119	Pd-Cu 60/40%	3.20E-07	6" wafer	3hrs 55min	780	550	1.5
Pd-120	Pd-Cu 60/40%	3.00E-07	6" wafer	3hrs 55min	780	548	1.5
Pd-121	Pd-Cu 60/40%	1.30E-07	6" wafer	3hrs 55min	780	544	1.5
Pd-122	Pd	5.30E-06	None	40 min	780	472	1.7
Pd-123	Pd-Au 90/10%	6.20E-06	1.5"x 6" wafer	40 min	780	484	1.7
Pd-124	Pd-Au 90/10%	5.40E-06	1.5"x 6" wafer	40 min	780	495	1.7
Pd-125	Pd-Au 90/10%	1.20E-07	6" wafer	14 hrs 50 min	780	465	1.7
Pd-126	Pd-Au 90/10%	2.60E-07	6" wafer	12 hrs 25 min	780	463	1.8

Run #	Target	Base press (torr)	Substrate	Run time	Sputtering watts	volts	amps
Pd-127	Pd-Au 90/10%	1.40E-07	6" wafer	12 hrs 10 min	780	457	1.8
Pd-128	Pd-Au 90/10%	1.00E-06	6" wafer	11 hrs 10 min	780	461	1.8
Pd-129	Pd	1.80E-06	None	40 min	780	442	1.9
Pd-130	Pd-Au-Ag 90/5/5%	2.40E-07	1.5" x 6" wafer	40 min	780	457	1.9
Pd-131	Pd-Au-Ag 90/5/5%	4.00E-07	1.5" x 6" wafer	40 min	780	504	1.7
Pd-132	Pd-Au-Ag 90/5/5%	1.40E-07	6" wafer	5hrs 15 min	780	478	1.7
Pd-133	Pd	3.40E-07	none	30 min	780	466	1.7
Pd-134	Pd-Au-Ag 90/5/5%	6.00E-06	1" x 6" wafer	40 min	780	512	1.7
Pd-135	Pd-Au-Ag 90/5/5%	1.70E-07	6" wafer	40 min	780	496	1.7
Pd-136	Pd-Au-Ag 90/5/5%	3.20E-07	6" wafer	5hrs 10 min	780	471	1.7
Pd-137	Pd-Au-Ag 90/5/5%	2.90E-07	6" wafer	5hrs	780	473	1.8
Pd-138	Pd-Au-Ag 90/5/5%	2.00E-07	6" wafer	5hrs	780	486	1.7
Pd-139	Pd	1.40E-07	None	40min	780	458	1.8
Pd-140	Pd-Au-Pt 85/10/5%	5.00E-06	1" x 6" wafer	40min	780	464	1.7
Pd-141	Pd-Au-Pt 85/10/5%	1.30E-07	6" wafer	5hrs	780	470	1.7
Pd-142	Pd-Au-Pt 85/10/5%	2.90E-07	6" wafer	4hrs 40 min	780	463	1.8
Pd-143	Pd-Au-Pt 85/10/5%	1.00E-07	6" wafer	4hrs 40 min	780	465	1.8
Pd-144	Pd-Au-Pt 85/10/5%	2.50E-07	6" wafer	4hrs 40 min	780	464	1.7
Pd-145	Pd-Au-Pt 85/10/5%	1.40E-07	6" wafer	4hrs 40 min	780	472	1.7
Pd-146	Pd-Au-Pt 80/10/10%	9.50E-07	1/2" x 6" wafer	40min	780	496	1.7
Pd-147	Pd-Au-Pt 80/10/10%	1.20E-07	6" wafer	4hrs 45 min	780	481	1.7
Pd-148	Pd-Au-Pt 80/10/10%	1.30E-07	6" wafer	5hrs 5 min	780	475	1.7
Pd-149	Pd-Au-Pt 80/10/10%	2.40E-07	6" wafer	5 hrs 25 min	780	478	1.7
Pd-150	Pd-Au-Pt 80/10/10%	2.50E-07	6" wafer	5 hrs 20 min	780	485	1.7
Pd-151	Pd-Au-Pt 80/10/10%	2.60E-07	1/2" x 6" wafer	40min	780	513	1.7
Pd-152	Pd-Au-Pt 80/10/10%	1.20E-07	6" wafer	12 hrs 10 min	780	485	1.7

Run #	Target	Base press (torr)	Substrate	Run time	Sputtering watts	volts	amps
Pd-153	Pd-Au-Pt 80/10/10%	1.00E-07	6" wafer	12 hrs 10 min	780	495	1.7
Pd-154	Pd-Au-Pt 80/10/10%	1.90E-07	6" wafer	12 hrs 10 min	780	500	1.7
Pd-155	Pd-Au-Pt 80/10/10%	2.80E-07	6" wafer	12 hrs 10 min	780	498	1.7
Pd-156	Pd-Au-Pt 80/10/10%	2.00E-06	1/2" x 6" wafer	1 hr	780	502	1.7
Pd-157	Pd-Au-Pt 80/10/10%	2.90E-07	6" wafer	12 hrs 10 min	780	482	1.7
Pd-158	Pd-Au-Pt 80/10/10%	4.20E-07	6" wafer	13 hrs	780	487	1.7
Pd-159	Pd	3.66E-05	None	40min	780	493	1.7
Pd-160	Pd-Au-Ru 80/10/10%	5.60E-07	1/2" x 6" wafer	1 hr	780	525	1.6
Pd-161	Pd-Au-Ru 80/10/10%	3.20E-07	6" wafer	12 hrs 10 min	780	511	1.7
Pd-162	Pd-Au-Ru 80/10/10%	4.40E-07	6" wafer	14 hrs 10 min	780	502	1.7
Pd-163	Pd	7.00E-07	None	40 min	780	442	2.0
Pd-164	Pd-Au-Pt 80/10/10%	2.60E-06	1/2"x 6"wafer	1hr	780	498	1.7
Pd-165	Pd-Au-Pt 80/10/10%	3.60E-07	6"wafer	13 hrs	780	480	1.7
Pd-166	Pd-Au-Pt 80/10/10%	4.80E-07	6"wafer	13 hrs	780	475	1.8
Pd-167	Pd-Au-Pt 80/10/10%	4.80E-07	6"wafer	13 hrs	780	478	1.7
Pd-168	Pd-Au-Pt 80/10/10%	3.40E-07	6"wafer	13 hrs	780	489	1.7
Pd-169	Pd	3.40E-06	None	40 min	780	474	1.7
Pd-170	Pd	3.80E-06	None	30	780	516	1.7
Pd-171	Pd-Ru 90-10%	1.60E-06	1/2" x 6" wafer	1hr	780	501	1.7
Pd-172	Pd-Ru 90-10%	5.70E-07	6" wafer	13 hrs	780	480	1.7
Pd-173	Pd-Ru 90-10%	7.00E-07	6" wafer	12hrs	780	465	1.7
Pd-174	Pd	5.00E-06	None	30min	780	510	1.7
Pd-175	Pd-Cu-Au 80/10/10%	5.60E-07	1/2"x 6"wafer	1 hr	780	548	1.6
Pd-176	Pd-Cu-Au 80/10/10%	5.30E-07	6"wafer	11hrs 10 min	780	535	1.6
Pd-177	Pd-Cu-Au 80/10/10%	2.80E-07	6"wafer	13hrs 15min	780	544	1.5
Pd-178	Pd	6.60E-06	None	30 min	780	504	1.7

Run #	Target	Base press (torr)	Substrate	Run time	Sputtering		
					watts	volts	amps
Pd-179	Pd-Tm 95/5%	4.80E-07	1/2" x 6" wafer	1 hr	780	489	1.7
Pd-180	Pd-Tm 95/5%	4.30E-07	6"wafer	11hrs 30 min	780	479	1.7
Pd-181	Pd-Tm 95/5%	2.80E-07	6"wafer	11hrs 30 min	780	475	1.7

The initial foils exhibited a distinct ‘handedness’ regarding the side next to the silicon wafer and the air. In Figure 40, a photograph of a piece of released foil is shown below.

Figure 40. Released palladium foil.

Instead of having a specular reflection, the air side was dull. Initial concerns about a leak in the chamber proved unfounded and subsequent SEM analysis showed a distinct surface texture difference. The wafer side was atomically smooth but the 'air' side was composed of nodules. Images of the two sides of the foils at increasing magnifications are shown below.

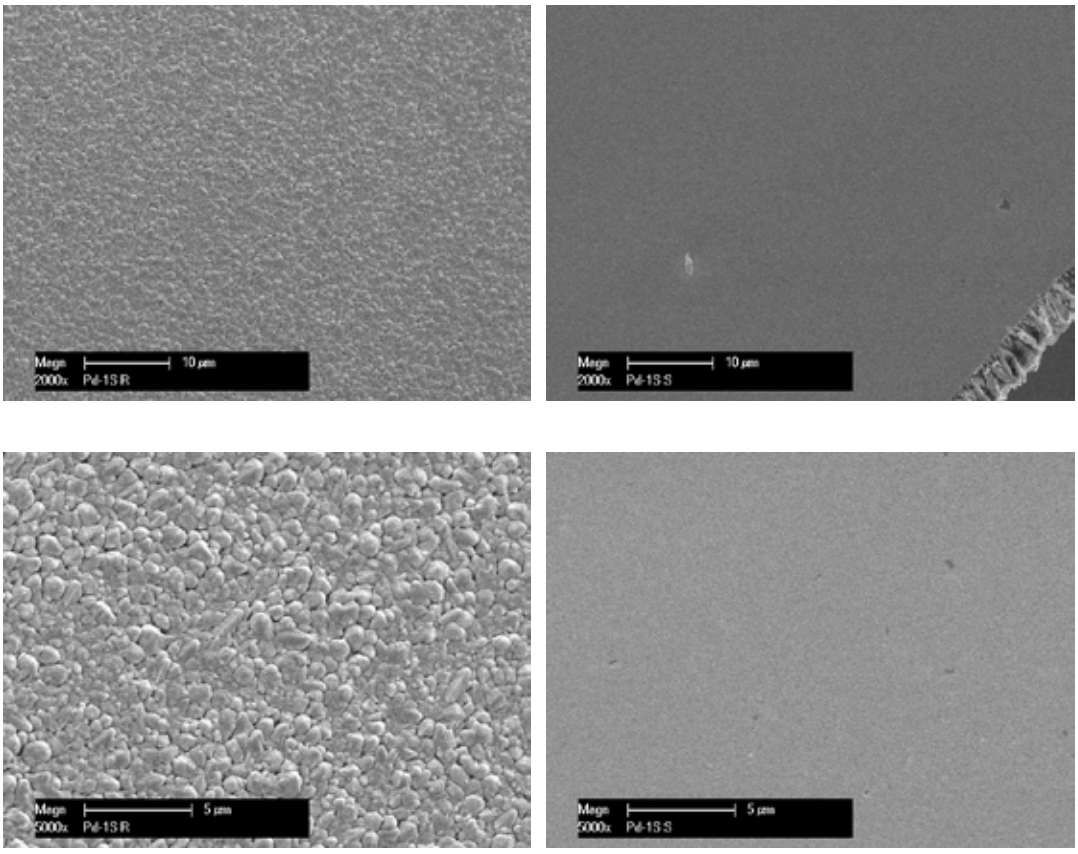

Figure 41. Surface images of released foils.

A review of the processing parameters comparing the foils fabricated as part of a previous DOE study and these Pd films found that the earlier films were run at a significantly lower base pressure. Upon replicating the base pressure conditions, the coated films and subsequent free standing foils exhibited a high specular reflectance as shown in Figure 42.

Figure 42. Photographs of deposited films exhibiting high specular reflectance.

A unique feature of the sputtering technique is the ability to rapidly produce membranes of almost any alloy composition with good uniformity and large areas (up to 100 square inches). The development of thin Pd-alloy membranes using magnetron sputtering continued with the deposition of binary and ternary Pd alloy samples. In the following table the comments related to the deposition of each foil is summarized.

Table 4. Deposition observations

Run #	Target	Comments
Pd-14	Pd	Shut off early planetary fail, film shiny easy release, slight comp
Pd-15	Pd	Press flucs, planetary probs, run abort, film very oxidized
Pd-17	Pd	Film rough, cloudy looking. Planetary gone, using simple rotation
Pd-18	Pd	Film rough, cloudy looking
Pd-19	Pd	Film shiny, excellent, full release neutral stress
Pd-20	Pd	Lowered substrate to 3" above cathode, film excellent, full release
Pd-21	Pd	Tooling run for tk/uniformity
Pd-22	Pd/Cu 5%	1st test Pd/Cu 5%, sample sent for EDS, full release mod tens
Pd-23	Pd/Cu 20%	Full release/mildly tensile/4 pinhole. Sample to EDS/thickness
Pd-24	Pd/Ag 5%	Full release/mildly tensile/10+ pinholes. Sample to EDS/thickness
Pd-25	Pd/Ag 20%	Full release/slightly tensile, 1 pinhole, delicate easy to tear
Pd-26	Pd/Ag 20%	Test for thickness uniform, pg 83 in lab book, center ~2k A thicker
Pd-27	Pd	Run to clean target, Cu and Ag chips removed
Pd-28	Pd/Cu 20%/ Ag/ 5%	Pd target with 72 Cu chips/11 Ag chips
Pd-29	Pd	Run to clean target, Cu and Ag chips removed
Pd-30	Pd/Cu20%/Ag5%	Pd target with 56 Cu chips/ 11 Ag chips. Full release/low stress

Run #	Target	Comments
Pd-31	Pd/Cu20%/Ag5%	Pd target with 56 Cu chips/ 11 Ag chips. Full release/High Stress
Pd-32	Pd/Cu20%/Ag5%	Pd target with 56 Cu chips/ 11 Ag chips. Full release/ High stress
Pd-33	Pd/Cu20%/Ag5%	Full release high tensile too many pinholes to further testing.
Pd-34	Pd/Cu20%/Ag5%	Full release moderate stress, few pinholes(5),
Pd-35	Pd	Run to clean target, Cu and Ag chips removed
Pd-36	Pd/Cu 60%	Films rough. samples sent to source for further testing
Pd-37	Pd	Run to clean target, Cu and Ag chips removed, dep rate test
Pd-38	Pd/ Cu 60/40%	Tooling run for Pd-Cu composition
Pd-39	Pd/ Cu 60/40%	Shiny mirror-like, full release medium to high stress
Pd-40	Pd/ Cu 60/40%	Shiny mirror-like full release medium to high stress
Pd-41	Pd	Run to clean target, Cu chips removed.
Pd-42	Pd/Au 90/10%	Tooling run for thickness and composition.
Pd-43	Pd/Au 90/10%	1st test Pd/Au 90/10% EDS, full release med to high tens, appears cloudy, 2 pin holes
Pd-44	Pd/Au 90/10%	Full release, med to high stress. film cloudy at outer edge, EDS, mirror like at center. (2ph)
Pd-45	Pd/Au 90/10%	Full release, med to high stress. Very similar to previous film
Pd-46	Pd/Au 90/10%	Full release, med to high stress mirror like at center, cloudy at edge. No pin holes
Pd-47	Pd/Au 90/10%	Full release, med to high stress mirror like at center, cloudy at edge. 2 pin holes
Pd-48	Pd/Au 90/10%	Full release, med to high stress mirror like at center, cloudy at edge. No pinholes
Pd-49	Pd/Cu/Au 75/17/8%	Tooling run for Pd-Cu-Au composition
Pd-50	Pd/Cu/Au 75/17/8%	Full release, low to medium stress mirror-like cloudy at center 2 pin holes
Pd-51	Pd/Cu/Au 75/17/8%	Full release, medium stress. Many pit and divets from Cu debris. mirror-like 2 pin holes
Pd-52	Pd/Cu/Pt 75/17/8%	Tooling run, 110 Cu chips added and 16 pt chips added
Pd-53	Pd/Cu/Pt 75/17/8%	Full release, mirror like-low stress. 2 pin holes 82Cu chips 14.5Pt chips
Pd-54	Pd/Cu/Pt 75/17/8%	Full release, mirror like-low stress. 3 pin holes at outer edge 57Cu chips 15 Pt chips
Pd-55	Pd	Run to clean target
Pd-56	Pd/Cu/y 79/17/4%	Tooling run, 57 Cu chips added and 10 Y chips added
Pd-57	Pd/Cu/y 79/17/4%	2nd tooling run, EDS results on previous run inconclusive added ten Cu chips and 15 Y chips
Pd-58	Pd/Cu/y 79/17/4%	Full release, mirror like-high stress 12 pin holes 67 Cu chips and 25 Y chips
Pd-59	Pd/Cu/y 79/17/4%	Full release, mirror like- high stress film 11 pin holes at outer edge 67 Cu chips and 25Y chips
Pd-60	Pd	Run to clean target
Pd-61	Pd/Cu 75/25%	Tooling run, 89 Cu chips added along race track
Pd-62	Pd/Cu 75/25%	Full release, medium stress mirror like with cloudy center ring. 4 pin holes detected.
Pd-63	Pd/Cu 75/25%	Full release, medium stress mirror like with cloudy center ring. 5 pin holes detected.
Pd-64	Pd/Cu/Pt 70/17/13%	Tooling run, 60 Cu chips added and 25 Pt chips added along race track.
Pd-65	Pd/Cu/Pt 70/17/13%	Full release, medium stress and mirror like, 5 pin holes detected

Run #	Target	Comments
Pd-66	Pd/Cu/Pt 70/17/13%	Retooling run for EDS results
Pd-67	Pd/Cu/Pt 70/17/13%	Full release, low to medium stress. Divets from Pt debris. mirror-like cloudy center, 1 pin hole
Pd-68	Pd/Cu/Pt 70/17/13%	Full release, medium stress and mirror-like. 1 pin hole detected
Pd-69	Pd/Cu/Pt 70/17/13%	Full release, low to medium stress, slight cloudiness at 2.5"dia, 1 pin hole detected.
Pd-70	Pd	Run to clean target
Pd-71	Pd/Cu/Au 70/17/13%	Tooling run, 60 Cu chips added and 25 Au chips added along race track.
Pd-72	Pd/Cu/Au 70/17/13%	Full release, low stress 1 pin hole detected cloudy at center1.5" dia
Pd-73	Pd/Cu/Au 70/17/13%	Full release, low stress no pin holes detected, slightly cloudy at center1.5" dia
Pd-74	Pd/Cu/Au 70/17/13%	Full release' medium stress; three pin holes detected. Cloudy at center.
Pd-75	Pd/Cu/Au 70/17/13%	Full release' medium to high stress; three pin holes detected. Cloudy at center 2"dia.
Pd-76	Pd	Run to clean target
Pd-77	Pd/Cu/Ni 75/17/8%	Tooling run, 65 Cu chips added and 20 Ni chips added along race track.
Pd-78	Pd/Cu/Ni 75/17/8%	Full release, mirror like medium stress, 3 pin holes detected
Pd-79	Pd/Cu/Ni 75/17/8%	Full release, mirror-like medium stress, 2 pin holes detected
Pd-80	Pd/Cu/Ni 75/17/8%	Full release, mirror-like medium stress, 2 pin holes detected
Pd-81	Pd/Cu/Ni 75/17/8%	Full release, mirror-like medium stress, 2 pin holes detected
Pd-82	Pd	Run to clean target
Pd-83	Pd-Ru 90/10%	Tooling run, 16 Ru chips added along racetrack
Pd-84	Pd-Ru 90/10%	Full release, high tensile too many pinholes to count, able to cut small section for testing
Pd-85	Pd-Ru 90/10%	Full release, medium to high stress. Mirror like appearance, 12 pin holes detected
Pd-86	Pd-Ru 90/10%	Full release, medium to high stress. Mirror like appearance, 1 pin hole detected
Pd-87	Pd-Ru 90/10%	Full release, low to med stress, mirror like appearance, 1 pin hole detected
Pd-88	Pd/Cu/Ru 85/5/10%	Tooling run for Pd-Cu-Ru composition 20 Cu chips and 16 Ru chips
Pd-89	Pd/Cu/Ru 85/5/10%	Full release, mirror-like. delamination rings noticed on outer edge, film intact. Low stress. 11 pin holes
Pd-90	Pd/Cu/Ru 85/5/10%	Full release, mirror-like. 3 pin holes, medium stress
Pd-91	Pd	Run to clean target.
Pd-92	Pd/Cu/Au 85/5/10%	Tooling run for Pd-Cu-Au composition 26 Cu chips and 32 Au chips
Pd-93	Pd/Cu/Au 85/5/10%	Full release, mirror-like low stress. Film lays flat on surface, no pin holes
Pd-94	Pd/Cu/Au 85/5/10%	Full release low to medium stress mirror-like, 1 pin hole
Pd-95	Pd/Cu/Au 85/5/10%	Full release, mirror-like pits detected possible from chip reduction lift off. Low to med stress 2 pin holes
Pd-96	Pd/Cu/Au 85/5/10%	Full release, mirror-like few pits low to medium stress, 1 pin hole
Pd-97	Pd	Run to clean target.
Pd-98	Pd/Cu/Au 65/35/5%	Tooling run for Pd-Cu-Au composition 106 Cu chips and 12 Au chips 60%-35%-5%
Pd-99	Pd/Cu/Au 65/35/5%	Full release low stress, mirror-like slightly cloudy. 5 pinholes
Pd-100	Pd/Cu/Au 65/35/5%	Full release, low to medium stress slightly cloudy, 1 pinhole
Pd-101	Pd/Cu/Au 65/35/5%	Full release, medium stress, slightly cloudy 1 pinhole detected

Run #	Target	Comments
Pd-102	Pd/Cu/Au 65/35/5%	Full release, medium stress slightly cloudy, 2 pinholes detected, divets on surface
Pd-103	Pd	Run to Clean target
Pd-104	Pd-Cu 60/40%	Tooling run for Pd-Cu, composition 120 Cu chips 60%-40%
Pd-105	Pd-Cu 60/40%	Full release mirror-like low stress no pinholes. Removed 13 chips prior to dep as per EDS results
Pd-106	Pd-Cu 60/40%	Full release medium to high stress, 6 pinholes detected, mirror-like.
Pd-107	Pd-Cu 60/40%	Full release, high stress, mirror-like finish 3 pinholes detected
Pd-108	Pd-Cu 60/40%	Full release, low to medium stress, mirror-like 2 pinholes detected, added 25 Cu chips prior to dep
Pd-109	Pd-Cu 60/40%	Full release, medium to high stress, 3 pin holes detected 132 Cu chips along racetrack
Pd-110	Pd-Cu 60/40%	Tooling run with 107 fresh cu chips
Pd-111	Pd-Cu 60/40%	Full release, low to medium stress. Mirror-like finish, 2 pinholes. 113 Cu chips
Pd-112	Pd-Cu 60/40%	Full release, medium stress mirror-like finish, no pin holes detected 130 Cu chips
Pd-113	Pd-Cu 60/40%	Full release, mirror like finish, med to high stress 4 pinholes. 130 Cu chips
Pd-114	Pd-Cu 60/40%	Full release, mirror-like, medium stress, no pin holes. 140 Cu chips
Pd-115	Pd-Cu 60/40%	Tooling run with 200 Cu chips
Pd-116	Pd-Cu 60/40%	Full release, mirror-like, low to medium stress, no pin holes. 172 Cu chips
Pd-117	Pd-Cu 60/40%	Full release, mirror-like, medium stress, 4 pin holes. 195 Cu chips
Pd-118	Pd-Cu 60/40%	Full release, mirror-like, low to medium stress 2 pinholes 195 Cu chips
Pd-119	Pd-Cu 60/40%	Full release, low to medium stress, mirror-like finish 2 pinholes
Pd-120	Pd-Cu 60/40%	Full release, low to med stress, mirror like appearance, 1 pin hole detected. Small divets detected
Pd-121	Pd-Cu 60/40%	Full release, low stress mirror-like finish, few divets no pinholes
Pd-122	Pd	Run to clean target
Pd-123	Pd-Au 90/10%	Tooling run with 7 Au chips
Pd-124	Pd-Au 90/10%	2nd tooling run, EDS results on previous run inconclusive added 2 Au chips
Pd-125	Pd-Au 90/10%	Full release, cloudy on deposition side clear on substrate side, low stress no pinholes
Pd-126	Pd-Au 90/10%	Full release, cloudy on deposition side clear on substrate side, low stress no pinholes
Pd-127	Pd-Au 90/10%	Full release, cloudy on deposition side clear on substrate side, medium stress no pinholes
Pd-128	Pd-Au 90/10%	Full release, cloudy on deposition side clear on substrate side, medium stress no pinholes
Pd-129	Pd	Run to clean target
Pd-130	Pd-Au-Ag 90/5/5%	Tooling run with 6 Au chips and 6 Ag chips
Pd-131	Pd-Au-Ag 90/5/5%	Tooling run with 6 Au chips and 25Ag chips to differ Pd peak from Ag peak on EDS
Pd-132	Pd-Au-Ag 90/5/5%	Full release, low to medium stress slightly cloudy in outer circumference, 0 pinholes
Pd-133	Pd	Run to clean new target. AJA international 5" x 12" Pd target. 99.95%
Pd-134	Pd-Au-Ag 90/5/5%	Tooling run with new target. 7Au chips and 20Ag chips loaded
Pd-135	Pd-Au-Ag 90/5/5%	Retooling run for EDS results 7Au chips and 16Ag chips loaded

Run #	Target	Comments
Pd-136	Pd-Au-Ag 90/5/5%	Full release, mirror-like with 3 pin holes at outer edge. Medium to high stress
Pd-137	Pd-Au-Ag 90/5/5%	Full release, mirror-like with slightly spotty appearance medium to high stress and 0 pinholes
Pd-138	Pd-Au-Ag 90/5/5%	Full release, mirror-like with medium to high stress and 0 pinholes
Pd-139	Pd	Run to clean target
Pd-140	Pd-Au-Pt 85/10/5%	Tooling run for Pd-Au-Pt 85/10/5%
Pd-141	Pd-Au-Pt 85/10/5%	Full release, low stress mirror-like finish no pinholes
Pd-142	Pd-Au-Pt 85/10/5%	Full release, medium stress, mirror-like and slightly cloudy in center
Pd-143	Pd-Au-Pt 85/10/5%	Full release, high stress, mirror-like finish no pinholes detected small lift off area, reason unknown
Pd-144	Pd-Au-Pt 85/10/5%	Full release, high stress, mirror-like 1 pinhole
Pd-145	Pd-Au-Pt 85/10/5%	Full release high stress slightly cloudy at center, mirror like finish no pinholes
Pd-146	Pd-Au-Pt 80/10/10%	Tooling run for Pd-Au-Pt 80/10/10% (11)Au chips and (12) Pt chips
Pd-147	Pd-Au-Pt 80/10/10%	Full release, Medium to high stress no pin holes mirror-like finish
Pd-148	Pd-Au-Pt 80/10/10%	Full release, high stress cloudy at center, no pin holes detected added one Au and one Pt chip to target
Pd-149	Pd-Au-Pt 80/10/10%	Full release, high stress slightly cloudy at center 1 pin hole detected at outer edge of film
Pd-150	Pd-Au-Pt 80/10/10%	Full release, med to high stress slightly cloudy at center 2 pinholes detected.
Pd-151	Pd-Au-Pt 80/10/10%	Tooling run for Pd-Au-Pt 80/10/10% (12)Au chips and (13) Pt chips
Pd-152	Pd-Au-Pt 80/10/10%	Full release mirror-like low stress 1pinhole, slightly cloudy at center small divets on surface
Pd-153	Pd-Au-Pt 80/10/10%	Full release, mirror-like finish slightly cloudy small area lifted off, few divets low stress no pin holes
Pd-154	Pd-Au-Pt 80/10/10%	Full release, cloudy at center yet mirror like, no pin holes and few divets
Pd-155	Pd-Au-Pt 80/10/10%	Full release, slightly cloudy near center, low to medium stress, no pin holes few divets
Pd-156	Pd-Au-Pt 80/10/10%	Tooling for Pd-Au-Pt 80/10/10% (17 Pt chips and (12) Pt chips to target racetrack
Pd-157	Pd-Au-Pt 80/10/10%	Full release, mirror-like and slightly cloudy at center few divets, low to medium stress no pin holes
Pd-158	Pd-Au-Pt 80/10/10%	Full-release many divets mirror-like and cloudy at center no pin holes, low to medium stress
Pd-159	Pd	Run to clean target
Pd-160	Pd-Au-Ru 80/10/10%	Tooling run for Pd-Au-Ru
Pd-161	Pd-Au-Ru 80/10/10%	Full release, low stress, mirror-like finish with no pin holes
Pd-162	Pd-Au-Ru 80/10/10%	Full release, mirror-like finish low stress and 1 pin hole
Pd-163	Pd	Run To clean Target
Pd-164	Pd-Au-Pt 80/10/10%	Tooling run for Pd-Au-pt
Pd-165	Pd-Au-Pt 80/10/10%	Full release, low to medium stress, cloudy at center. Many divets on film, no pinholes
Pd-166	Pd-Au-Pt 80/10/10%	Full release, low to medium stress, cloudy at center. Divets on film, no pinholes
Pd-167	Pd-Au-Pt 80/10/10%	Full release, no stress lays flat on surface, cloudy at center with some divets on film, no pin holes
Pd-168	Pd-Au-Pt 80/10/10%	Full release low stress, mirror-like slightly cloudy with few divets. 1 pinhole
Pd-169	Pd	Run to clean target

Run #	Target	Comments
Pd-170	Pd	Run to clean target and test target Rebuilt and cleaned magnetron
Pd-171	Pd-Ru 90-10%	Tooling run for Pd-Ru 21 Ru chips along center of target racetrack
Pd-172	Pd-Ru 90-10%	Full release low stress, lays flat on table, mirror-like finish, 1 pinhole
Pd-173	Pd-Ru 90-10%	Full release mirror-like finish, low to med stress no pinholes. Slightly hazy in center
Pd-174	Pd	Run to clean target
Pd-175	Pd-Cu-Au 80/10/10%	Tooling for Pd-Au-Cu, 40Cu chips and 18 Au chips along racetrack
Pd-176	Pd-Cu-Au 80/10/10%	Full release low to medium stress, mirror-like finish no pinholes and slightly hazy in center
Pd-177	Pd-Cu-Au 80/10/10%	Full release low to medium stress, slightly hazy center mirror-like finish, no pinholes
Pd-178	Pd	Run to clean target
Pd-179	Pd-Tm 95/5%	Tooling run for Pd-Tm, 14 Tm chips along racetrack
Pd-180	Pd-Tm 95/5%	Full release, mirror-like finish, few divets, no pinholes and low stress
Pd-181	Pd-Tm 95/5%	Full release, low to med stress, mirror-like finish, few divets and no pinholes

The foils were subsequently released from the silicon wafer and characterized for composition. The following table provides the measured composition and thickness.

Table 5. Membrane composition

			Average						
Run #	**Target**	**Thickness**	**Pd**	**Cu**	**Ru**	**Au**	**Ag**	**Ni/Tm**	**Pt**
Pd-18	Pd	12.9	100.0	-	-	-	-	-	-
Pd-22	Pd/Cu 5%	7	95.3	4.7	-	-	-	-	-
Pd-23	Pd/Cu 20%	5.3	86.0	14.0	-	-	-	-	-
Pd-24	Pd/Ag 5%	5.6	93.0	-	-	-	7.0	-	-
Pd-25	Pd/Ag 20%	6.2	85.4	-	-	-	14.6	-	-
Pd-28	Pd/Cu/Ag 80/20/5%	5	68.0	28.0	-	-	4.0	-	-
Pd-31	Pd/Cu/Ag 80/20/5%	6	89.6	10.4	-	-	-	-	-
Pd-32	Pd/Cu/Ag 80/20/5%	6	82.0	16.8	-	-	1.3	-	-
Pd-34	Pd/Cu/Ag 80/20/5%	6	79.6	16.5	-	-	3.9	-	-
Pd-44	Pd/Au 90/10%	9	91.9	-	-	8.2	-	-	-
Pd-46	Pd/Au 90/10%	10	90.8	-	-	9.3	-	-	-
Pd-50	Pd/Cu/Au 75/17/8%	10	79.0	13.6	-	7.4	-	-	-
Pd-51	Pd/Cu/Au 75/17/8%	10	79.3	12.7	-	8.1	-	-	-

			Average						
Run #	**Target**	**Thickness**	**Pd**	**Cu**	**Ru**	**Au**	**Ag**	**Ni/Tm**	**Pt**
Pd-53	Pd/Cu/Pt 75/17/8%	10	67.6	24.6	-	-	-	-	7.8
Pd-54	Pd/Cu/Pt 75/17/8%	10	78.7	17.6	-	-	-	-	3.8
Pd-62	Pd/Cu 75/25%	10	74.8	25.2	-	-	-	-	-
Pd-67	Pd/Cu/Pt 70/17/13%	11	76.8	12.0	-	-	-	-	11.2
Pd-68	Pd/Cu/Pt 70/17/13%	11	75.2	11.6	-	-	-	-	13.3
Pd-69	Pd/Cu/Pt 70/17/13%	11	75.8	11.7	-	-	-	-	12.5
Pd-74	Pd/Cu/Au 70/17/13%	10	72.5	12.4	-	15.1	-	-	-
Pd-75	Pd/Cu/Au 70/17/13%	10	77.0	12.0	-	11.0	-	-	-
Pd-79	Pd/Cu/Ni 75/17/8%	10	78.7	14.1	-	-	-	7.3	-
Pd-84	Pd/Ru 90/10%	8	94.1	-	6.0	-	-	-	-
Pd-85	Pd/Ru 90/10%	8	93.2	-	6.8	-	-	-	-
Pd-89	Pd/Cu/Ru 85/5/10%	8	88.1	4.4	7.5	-	-	-	-
Pd-93	Pd/Cu/Au 85/5/10%	11.1	82.4	5.6	-	12.1	-	-	-
Pd-94	Pd/Cu/Au 85/5/10%	10	81.6	5.3	-	13.1	-	-	-
Pd-95	Pd/Cu/Au 85/5/10%	10	82.7	4.9	-	12.5	-	-	-
Pd-96	Pd/Cu/Au 85/5/10%	10	84.0	4.8	-	11.2	-	-	-
Pd-99	Pd/Cu/Au 65/35/5%	10	61.9	31.1	-	7.1	-	-	-
Pd-100	Pd/Cu/Au 65/35/5%	10	62.5	28.7	-	8.9	-	-	-
Pd-101	Pd/Cu/Au 65/35/5%	10	63.2	28.3	-	8.5	-	-	-
Pd-102	Pd/Cu/Au 65/35/5%	10	65.5	27.9	-	6.6	-	-	-
Pd-105	Pd-Cu 60/40%	7	64.2	35.8	-	-	-	-	-
Pd-106	Pd-Cu 60/40%	7	68.1	32.0	-	-	-	-	-
Pd-107	Pd-Cu 60/40%	7	68.7	31.3	-	-	-	-	-
Pd-108	Pd-Cu 60/40%	7	61.2	38.8	-	-	-	-	-
Pd-109	Pd-Cu 60/40%	7	65.5	34.5	-	-	-	-	-
Pd-111	Pd-Cu 60/40%	7	65.6	34.4	-	-	-	-	-

			Average						
Run #	**Target**	**Thickness**	**Pd**	**Cu**	**Ru**	**Au**	**Ag**	**Ni/Tm**	**Pt**
Pd-112	Pd-Cu 60/40%	7	60.4	39.6	-	-	-	-	-
Pd-113	Pd-Cu 60/40%	7	62.8	37.2	-	-	-	-	-
Pd-114	Pd-Cu 60/40%	7	74.3	25.7	-	-	-	-	-
Pd-116	Pd-Cu 60/40%	7	53.5	46.5	-	-	-	-	-
Pd-117	Pd-Cu 60/40%	7	60.1	39.9	-	-	-	-	-
Pd-118	Pd-Cu 60/40%	7	61.7	38.3	-	-	-	-	-
Pd-119	Pd-Cu 60/40%	7	60.4	39.6	-	-	-	-	-
Pd-120	Pd-Cu 60/40%	7	59.7	40.3	-	-	-	-	-
Pd-121	Pd-Cu 60/40%	7	58.3	41.7	-	-	-	-	-
Pd-125	Pd-Au 90/10%	29	91.0	-	-	9.0	-	-	-
Pd-126	Pd-Au 90/10%	27	90.0	-	-	10.1	-	-	-
Pd-128	Pd-Au 90/10%	24	90.0	-	-	10.0	-	-	-
Pd-132	Pd-Au-Ag 90/5/5%	10.4	92.5	-	-	5.5	2.0	-	-
Pd-136	Pd-Au-Ag 90/5/5%	11.8	86.0	-	-	6.7	7.3	-	-
Pd-137	Pd-Au-Ag 90/5/5%	11.3	84.7	-	-	7.7	7.7	-	-
Pd-138	Pd-Au-Ag 90/5/5%	11.2	88.0	-	-	6.2	5.8	-	-
Pd-141	Pd-Au-Pt 85/10/5%	11.1	85.7	-	-	9.4	-	-	4.9
Pd-142	Pd-Au-Pt 85/10/5%	10	83.6	-	-	12.1	-	-	4.3
Pd-143	Pd-Au-Pt 85/10/5%	10	85.0	-	-	10.7	-	-	4.3
Pd-144	Pd-Au-Pt 85/10/5%	10	87.2	-	-	8.8	-	-	4.0
Pd-145	Pd-Au-Pt 85/10/5%	10	86.8	-	-	9.1	-	-	4.1
Pd-147	Pd-Au-Pt 80/10/10%	9.4	83.6	-	-	7.4	-	-	9.0
Pd-148	Pd-Au-Pt 80/10/10%	9.6	84.3	-	-	8.1	-	-	7.6
Pd-149	Pd-Au-Pt 80/10/10%	11.2	81.9	-	-	9.7	-	-	8.5
Pd-150	Pd-Au-Pt 80/10/10%	11.2	83.3	-	-	9.2	-	-	7.5
Pd-152	Pd-Au-Pt 80/10/10%	25	80.4	-	-	10.7	-	-	8.9

			Average						
Run #	**Target**	**Thickness**	**Pd**	**Cu**	**Ru**	**Au**	**Ag**	**Ni/Tm**	**Pt**
Pd-153	Pd-Au-Pt 80/10/10%	25	79.4	-	-	12.9	-	-	7.7
Pd-154	Pd-Au-Pt 80/10/10%	25	80.2	-	-	12.5	-	-	7.3
Pd-155	Pd-Au-Pt 80/10/10%	25	81.4	-	-	10.9	-	-	7.7
Pd-156	Pd-Au-Pt 80/10/10%	25	75.4	-	-	11.8	-	-	12.8
Pd-157	Pd-Au-Pt 80/10/10%	25	80.8	-	-	8.8	-	-	10.4
Pd-158	Pd-Au-Pt 80/10/10%	25	77.9	-	-	11.6	-	-	10.6
Pd-161	Pd-Au-Ru 80/10/10%	25	77.8	-	9.9	12.4	-	-	-
Pd-162	Pd-Au-Ru 80/10/10%	25	79.9	-	9.3	10.8	-	-	-
Pd-165	Pd-Au-Pt 80/10/10%	25	81.3	-	-	9.1	-	-	9.6
Pd-166	Pd-Au-Pt 80/10/10%	25	83.6	-	-	8.6	-	-	7.8
Pd-167	Pd-Au-Pt 80/10/10%	25	80.7	-	-	11.6	-	-	7.7
Pd-168	Pd-Au-Pt 80/10/10%	25	75.8	-	-	11.3	-	-	12.9
Pd-172	Pd-Ru 90-10%	29.9	94.6	-	5.4	-	-	-	-
Pd-173	Pd-Ru 90-10%	26	96.3	-	3.7	-	-	-	-
Pd-176	Pd-Cu-Au 80/10/10%	26.6	77.5	8.6	-	13.9	-	-	-
Pd-180	Pd-Tm 95/5%	25	94.0	-	-	-	-	7.5	-
Pd-181	Pd-Tm 95/5%	33.6	93.0	-	-	-	-	7.0	-

In addition, the released foils were characterized by SEM to check thickness. Following are images of Pd-22 through Pd-25 samples.

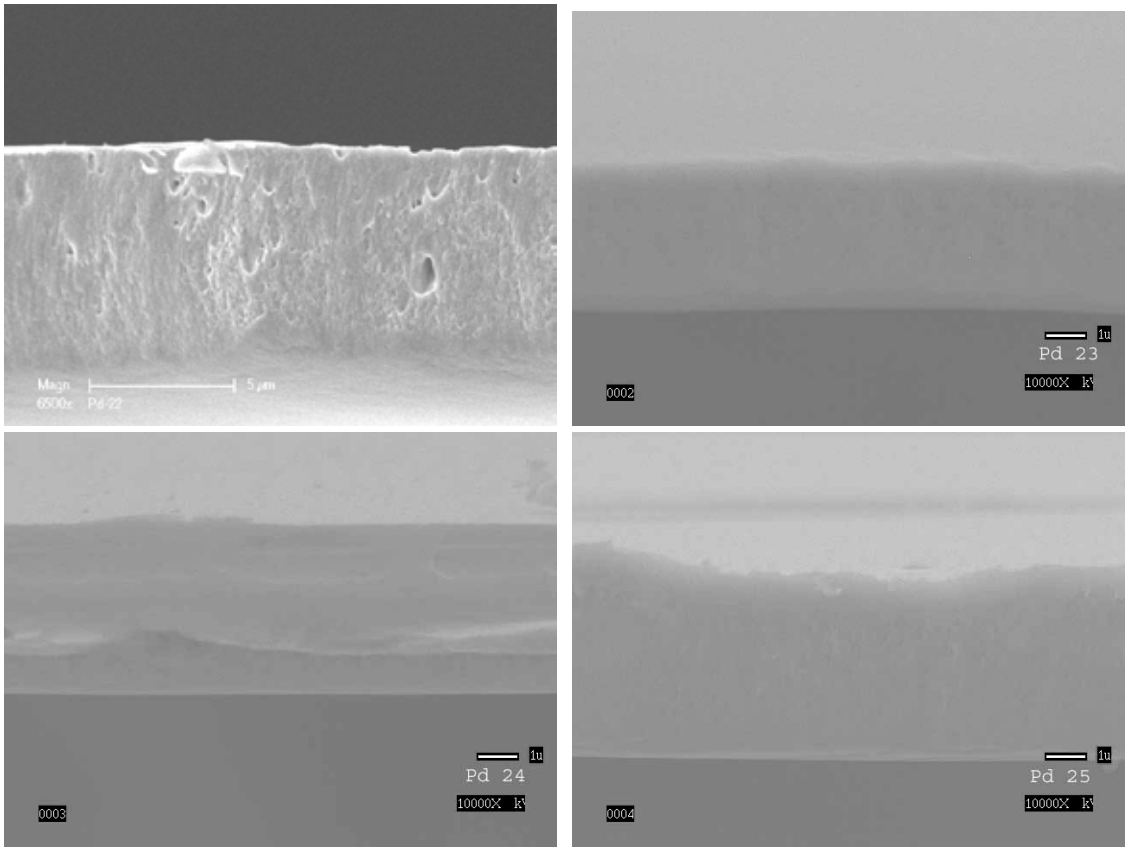

Figure 43. SEM images of PdCu & PdAg foils.

Sample Pd-40 was sent to Dave Edlund at Protonex. Dave placed the foils in their standard one inch test apparatus shown below.

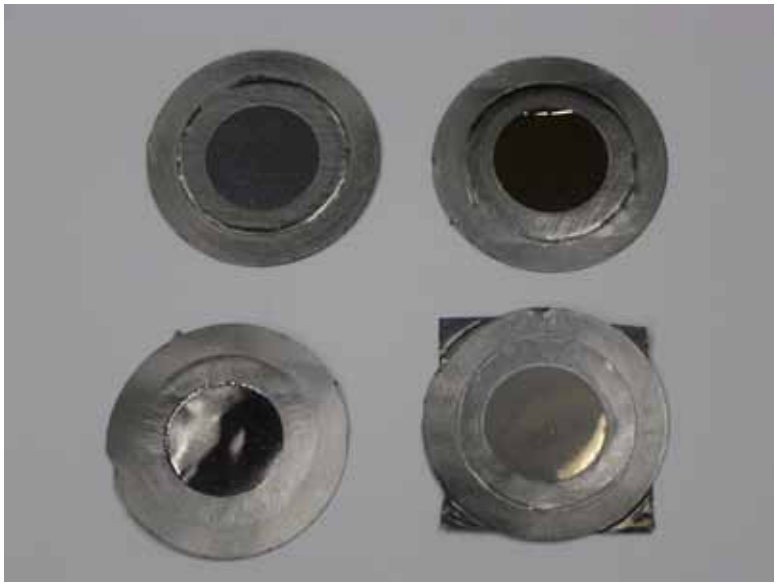

Figure 44. PdCu foils tested by Protonex.

The PdCu alloy measured 50 mL/min*cm^2 @ 400 ºC and 50 psig H_2. These values are consistent for a 5.3 µm binary alloy at this composition. The encouraging result was that the foil could be relatively easily incorporated into a commercial test apparatus and operated without the formation of pinholes or significant support engineering. In addition, a PdAu foil was supplied to Proton Energy Systems for evaluation in their hydrogen generators. The preliminary results on a 2" X 2" sample were promising and they requested a 6" in diameter sample.

2.1 Comparison of Cold Rolled versus PVD Fabricated Membranes

The ternary and binary membranes fabricated using physical vapor deposition (PVD) techniques all catastrophically fail upon exposure to DOE test condition #2a. This occurred at both TDA and IdaTech. It was also found that for PdCu foils of the same stoichiometry and thickness that while the cold rolled foils exhibited a loss in flux with exposure to H_2S, they did not fail and the PVD films did fail.

In order to compare the mechanical strength of the foils samples of each were exposed to air and H_2S in air at 400 ºC for 1 hour. The foils were then loaded into a test frame as shown below.

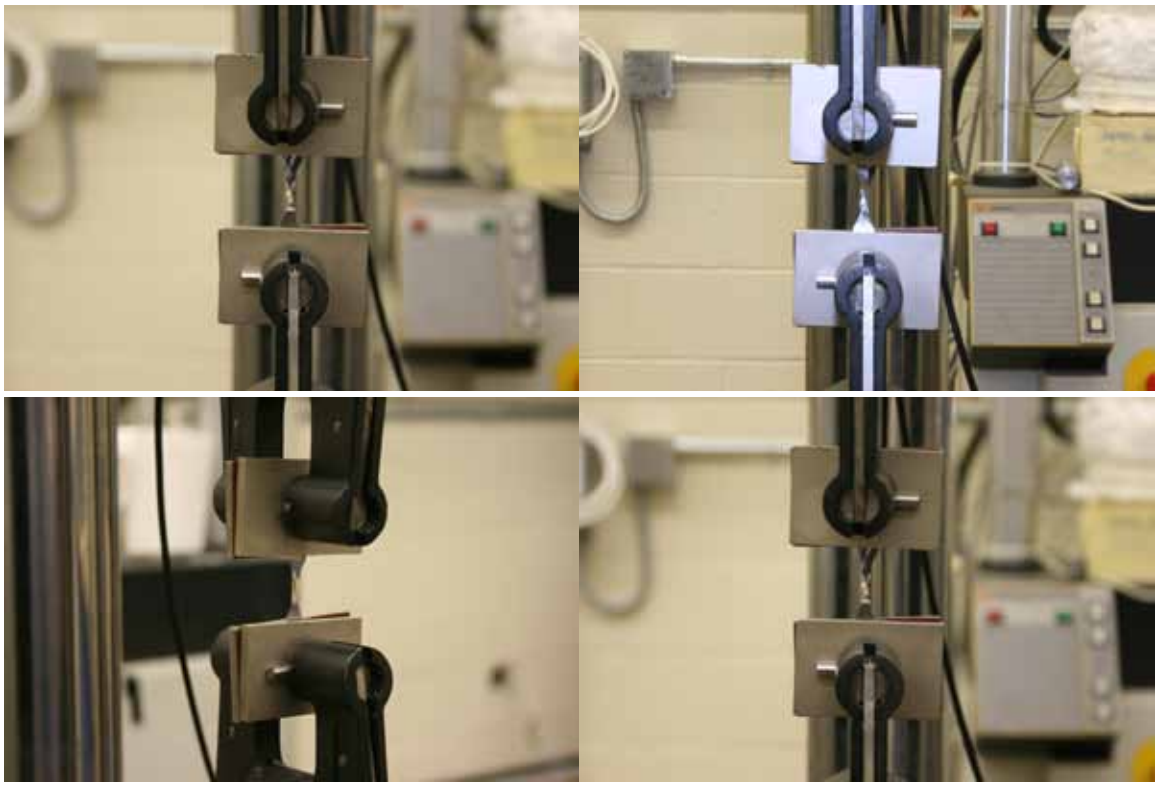

Figure 45. Tensile test apparatus.

The tensile test results are summarized below.

Table 6. Tensile test results.

Specimen Description	Specimen No.	Peak Load (lbf)	Break Extension (in)	Air	H_2s
	1-1	4.217	0.022	ü	
	1-2	3.745	0.044	ü	
	1-3	4.143	0.014		ü
Pd40Cu, 5mm	1-4	3.967	0.027		ü
	2-1	5.714	0.030	ü	
	2-2	3.554	0.036	ü	
	2-3	5.757	0.015		ü
Pd40Cu, 7.5mm	2-4	5.938	0.014		ü
	3-1	7.346	0.048	ü	
	3-2	7.840	0.021	ü	
	3-3	7.513	0.016		ü
Pd40Cu, 10mm	3-4	7.690	0.016		ü
	4-1	10.821	0.010	ü	
	4-2	10.803	0.018	ü	
	4-3	10.591	0.015		ü
Pd40Cu, 12.5mm	4-4	10.444	0.018		ü
	5-1	12.304	0.030	ü	
	5-2	12.014	0.028	ü	
	5-3	12.010	0.030		ü
Pd40Cu, 15mm	5-4	11.937	0.021		ü
Pd-114 Pd-Cu 71.34 wt% 28.66 wt%	6-1	10.069	0.015	ü	
	6-2	9.041	0.021	ü	
	6-3	8.038	0.017		ü
	6-4	10.649	0.020		ü
Pd-111 Pd-Cu 65.65 wt% 34.36 wt%	7-1	9.565	0.019	ü	
	7-2	10.591	0.037	ü	
	7-3	9.064	0.013		ü
	7-4	10.793	0.015		ü
Pd-118 Pd-Cu 61.71 wt% 38.29 wt%	8-1	8.938	0.020	ü	
	8-2	9.309	0.030	ü	
	8-3	9.036	0.015		ü
	8-4	7.887	0.031		ü

There is no discernible difference between the cold rolled & PVD foils following annealing in either air or H_2S. The next evaluation was x-ray diffraction (XRD) of the foils to see if there was any crystal structure difference. The following plots are for the cold rolled foil.

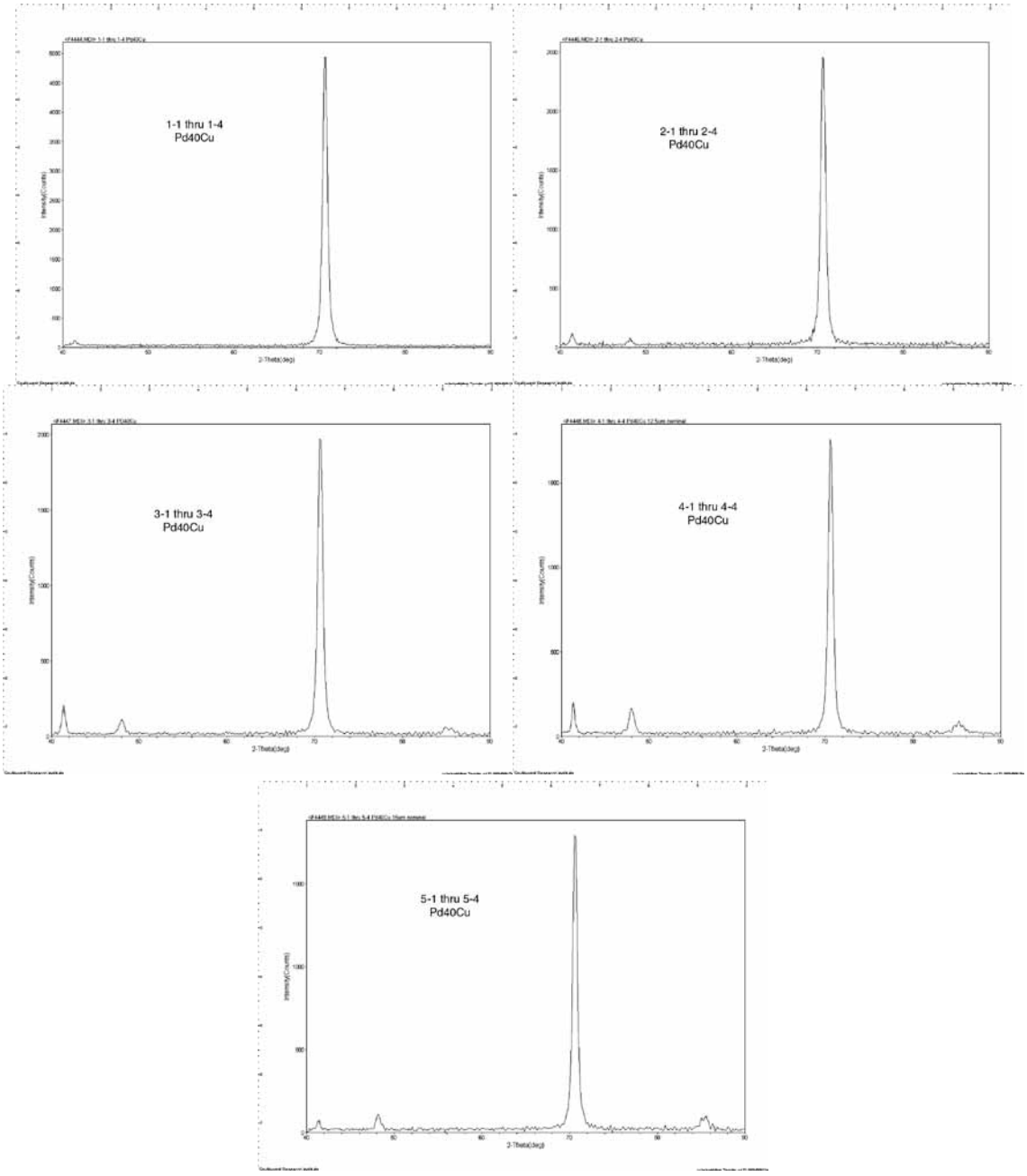

Figure 46. XRD plots of cold rolled foil.

These plots suggest a dominant fcc structure PdCu across all the membrane thicknesses. The following plots are for the PVD foils.

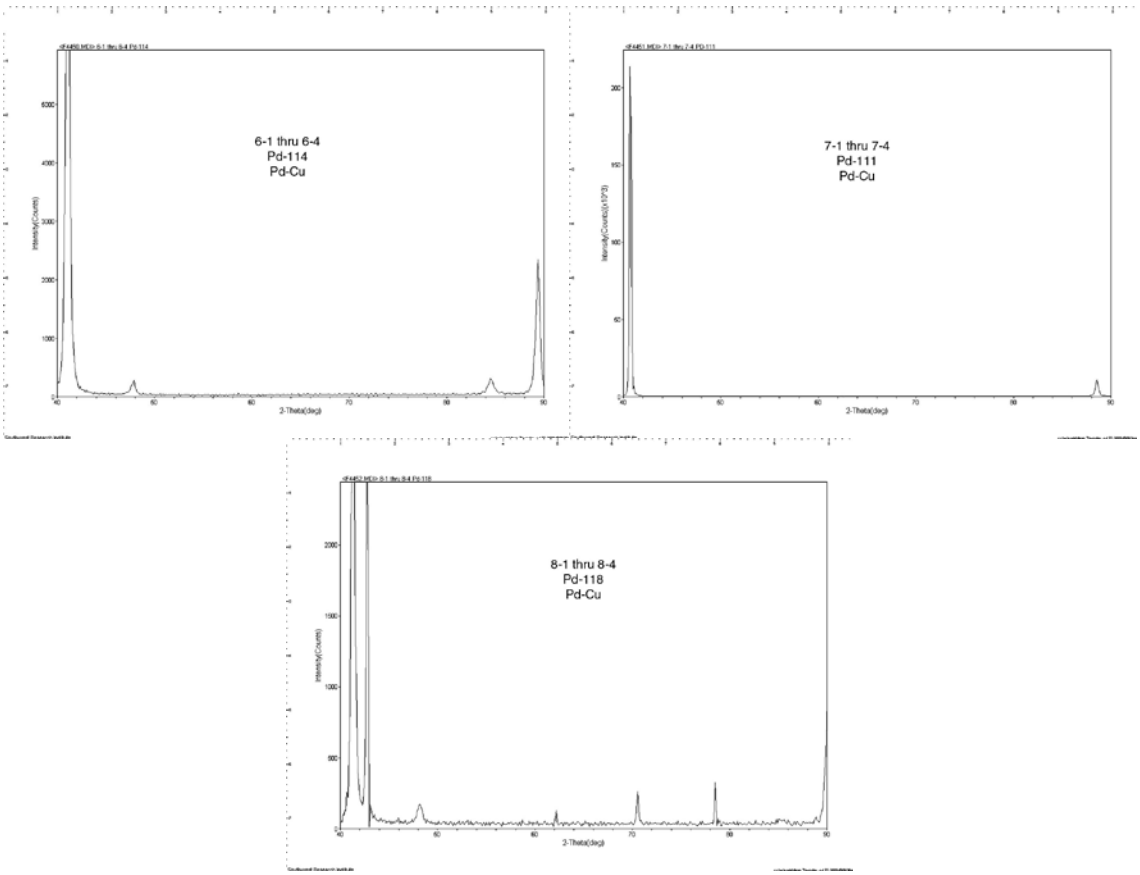

Figure 47. XRD plots of PVD foils.

These plots suggest the PVD foils are a combination of bcc & fcc lattice structures. There is obviously a difference between the cold rolled and PVD foils which may explain the failure of the PVD upon exposure to H_2S. A series of annealing tests were completed to further determine if this issue could be overcome, but none were found to reproducibly solve the problem.

3.0 CHARACTERIZATION AND PERMEATION TESTING IN CONTROLLED ENVIRONMENTS

In total 62 membranes were tested for hydrogen permeability in either pure gas or mixed gas environments. The following table summarizes all the permeation testing results from CSM, TDA and IdaTech.

Table 7. Permeability results

Run #	Target	CSM @ 400 ºC H_2 Permeability x 10^5 ($SCCM/cm/s/Hg^{0.5}$)	CSM 80 psi $SCFH/ft^2$	TDA DOE#1 $SCFH/ft^2$	IdaTech H_2 Permeability x 10^5 ($SCCM/cm/s/Hg^{0.5}$)
Pd-18	Pd	9.6			
Pd-22	Pd/Cu 5%	3.4			
Pd-23	Pd/Cu 20%	1.3			
Pd-24	Pd/Ag 5%	7.5			
Pd-25	Pd/Ag 20%	13.5			
Pd-28	Pd/Cu/Ag 80/20/5%	2.0			
Pd-31	Pd/Cu/Ag 80/20/5%	0.4			
Pd-32	Pd/Cu/Ag 80/20/5%	1.8			
Pd-34	Pd/Cu/Ag 80/20/5%	1.5			
Pd-44	Pd/Au 90/10%	13.7	182.1		
Pd-46	Pd/Au 90/10%	13.8	213.1		
Pd-50	Pd/Cu/Au 75/17/8%	3.1			
Pd-51	Pd/Cu/Au 75/17/8%	3.1			
Pd-53	Pd/Cu/Pt 75/17/8%	3.4			
Pd-54	Pd/Cu/Pt 75/17/8%	3.2			
Pd-62	Pd/Cu 75/25%	1.6			
Pd-67	Pd/Cu/Pt 70/17/13%	3.4			
Pd-68	Pd/Cu/Pt 70/17/13%	4.3			
Pd-69	Pd/Cu/Pt 70/17/13%	4.3			
Pd-74	Pd/Cu/Au 70/17/13%	5.9			
Pd-75	Pd/Cu/Au 70/17/13%	4.5			
Pd-79	Pd/Cu/Ni 75/17/8%	1.4			
Pd-84	Pd/Ru 90/10%	6.5			
Pd-85	Pd/Ru 90/10%	2.7			
Pd-89	Pd/Cu/Ru 85/5/10%	2.36			
Pd-93	Pd/Cu/Au 85/5/10%	8.5	106.5	140.0	
Pd-94	Pd/Cu/Au 85/5/10%	9.4			9.2/ 2.46*
Pd-95	Pd/Cu/Au 85/5/10%	6.34			
Pd-99	Pd/Cu/Au 65/35/5%	0.78			
Pd-101	Pd/Cu/Au 65/35/5%	1.03			
Pd-102	Pd/Cu/Au 65/35/5%	1.34			
Pd-105	Pd-Cu 60/40%	1.2			
Pd-107	Pd-Cu 60/40%	1.5			
Pd-112	Pd-Cu 60/40%	0.5			
Pd-119	Pd-Cu 60/40%	0.37			
Pd-120	Pd-Cu 60/40%	2.79			
Pd-121	Pd-Cu 60/40%	0.457			
Pd-125	Pd-Au 90/10%	5.59			
Pd-126	Pd-Au 90/10%	11.3	84	90.0	12.8
Pd-128	Pd-Au 90/10%	14.85			14.8
Pd-132	Pd-Au-Ag 90/5/5%	5.5	104		
Pd-136	Pd-Au-Ag 90/5/5%	7.1	100		

		CSM @ 400 ºC	CSM	TDA	IdaTech
		H_2 Permeability x 10^5	80 psi	DOE#1	H_2 Permeability x 10^5
Run #	**Target**	**(SCCM/cm/s/$Hg^{0.5}$)**	**SCFH/ft^2**	**SCFH/ft^2**	**(SCCM/cm/s/$Hg^{0.5}$)**
Pd-137	Pd-Au-Ag 90/5/5%	4.5	84		
Pd-138	Pd-Au-Ag 90/5/5%	3.9	84		
Pd-141	Pd-Au-Pt 85/10/5%	7.7		100.0	
Pd-142	Pd-Au-Pt 85/10/5%	6.3			
Pd-143	Pd-Au-Pt 85/10/5%	5.18			5.2
Pd-147	Pd-Au-Pt 80/10/10%	9.2			
Pd-148	Pd-Au-Pt 80/10/10%	5.94			
Pd-149	Pd-Au-Pt 80/10/10%	6.17			
Pd-153	Pd-Au-Pt 80/10/10%	9.66			
Pd-154	Pd-Au-Pt 80/10/10%	11.5			
Pd-155	Pd-Au-Pt 80/10/10%	9.33			
Pd-157	Pd-Au-Pt 80/10/10%				3.2/ 0.97*
Pd-158	Pd-Au-Pt 80/10/10%	8.5		20.0	
Pd-161	Pd-Au-Ru 80/10/10%	6			
Pd-165	Pd-Au-Pt 80/10/10%	5.02			
Pd-166	Pd-Au-Pt 80/10/10%				3.13*
Pd-167	Pd-Au-Pt 80/10/10%	6.73			1.91*
Pd-168	Pd-Au-Pt 80/10/10%	5.53			
Pd-176	Pd-Cu-Au 80/10/10%	4	22		
Pd-181	Pd-Tm 95/5%	15	110		

3.1 Pure Gas Permeation Measurements

Single Element Pd Membranes

In order to establish baseline performance, pure gas permeation experiments were performed with the pure Pd foils. The support was a Mott porous stainless steel disk, oxidized at 600 ºC for 12 hours to produce an oxide film. This technique works fine for short duration testing and is simple experimentally. A nominal 25 mm diameter disk was cut from Pd foil sample #18. Although the thickness reported for this sample was 4.3 microns, CSM's mass measurements suggested that the thickness of this sample was actually 12.9 microns. This thickness measurement was very consistent with previous measurements from CSM and the literature. This is shown in Figure 48, where flux is plotted versus reciprocal thickness at a constant temperature of 400 ºC and a feed pressure of 32 psia = 220.6 kPa. If diffusion of atomic hydrogen is the rate limiting step, then a plot of flux versus reciprocal thickness should be linear. In Figure 48, CSM data for a series of membranes fabricated by Sabina Gade by electroless plating, a cold-rolled Pd foil from Alfa Aesar of 25 microns thickness, and the data point for Pd-18 are plotted. The line on this plot is the flux predicted by the correlation for the pure hydrogen permeability from the literature. This plot supports CSM's claim that the thickness of Pd-18 is approximately 13 microns because at that thickness, the measured flux agrees very well with previous measurements and the literature.

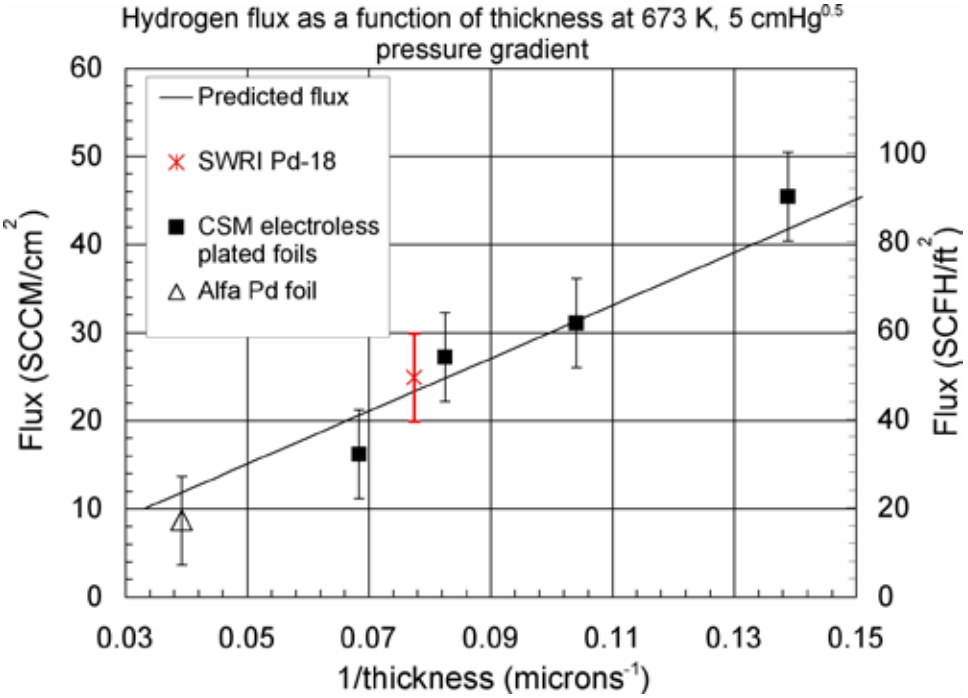

Figure 48. The influence of reciprocal thickness on the pure hydrogen flux at 400 ºC and 32 psia hydrogen feed pressure. Data for CSM electroless Pd membranes.

The ideal selectivity of membrane Pd-18 was perfect throughout the week-long permeation test. This means that the flow of N_2 was below the detection limit of 1 µL/min; therefore the minimum ideal H_2/N_2 selectivity was 58,000. The influence of temperature and driving force on the pure hydrogen flux is shown in Figure 49. The data obey Sievert's law, where the driving force for hydrogen permeation is the difference between the square root of feed and permeate hydrogen partial pressures.

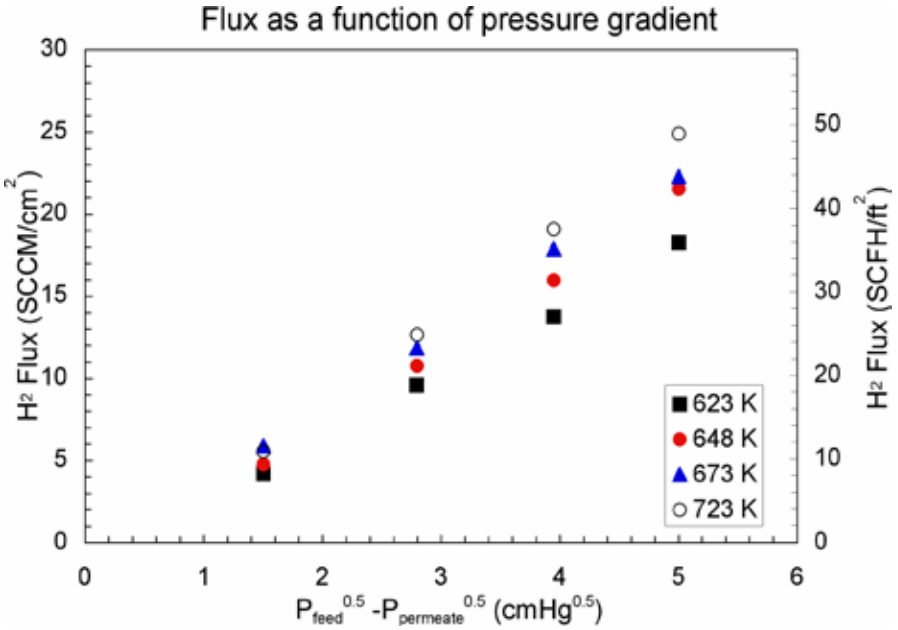

Figure 49. The influence of hydrogen partial pressure and temperature on hydrogen flux for pure Pd membrane #Pd-18.

3.2 Binary Pd Membranes

All membranes tested had no detectable nitrogen leak rate (<0.001 SCCM/cm2 @ 20 psi) prior to testing. This was only possible with membranes that were annealed prior to testing, as unannealed films had significant residual stress and tended to tear during the mounting process. The thinner films developed detectable leak rates during the heating process, but remained stable thereafter, including over multiple brief air exposures.

After Testing an SEM analysis showed significant variation in surface morphologies. Figure 50a is a feed-side surface image of PdCu-1 at 2000x magnification, showing a distinctly pebbled surface structure. In contrast, the newer membranes Pd-22 and Pd-25 had no visible surface features, appearing significantly smoother up to 7000x magnification (Figure 50b). Upon standardless EDS analyses, these newer membranes also had much better correspondence to the SwRI predicted compositions.

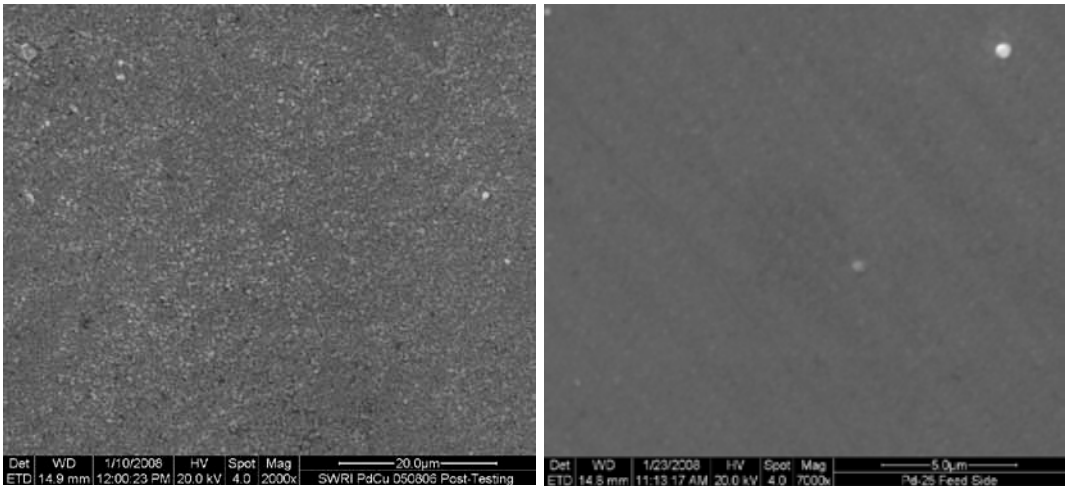

Figure 50. (a) SEM image of PdCu-1 (05/08/06) after testing at 2000x magnification; (b) SEM image of Pd-25 after testing at 7000x magnification.

The influence of temperature and driving force on the pure hydrogen fluxes of Pd-22 and Pd-25 is shown in Figure 51. Neither film was strongly affected by temperature in the range between 350-400 ºC. The H_2 permeability of membrane Pd-25 [1.3 x 10^{-4} cm^3(STP).cm/ cm^2.s.$cmHg^{0.5}$ at 350 ºC] is 10% lower than the predicted literature value for a 15 wt% silver film [1], well within measurement error for a film of this size. Film Pd-22, on the other hand, has a H_2 permeability of 3.1 x 10^{-5} cm^3(STP).cm/ cm^2.s.$cmHg^{0.5}$ at 350 ºC, approximately 1/3 of the expected value. The reason for this discrepancy is unknown. Both films were tested under identical conditions with the same support materials.

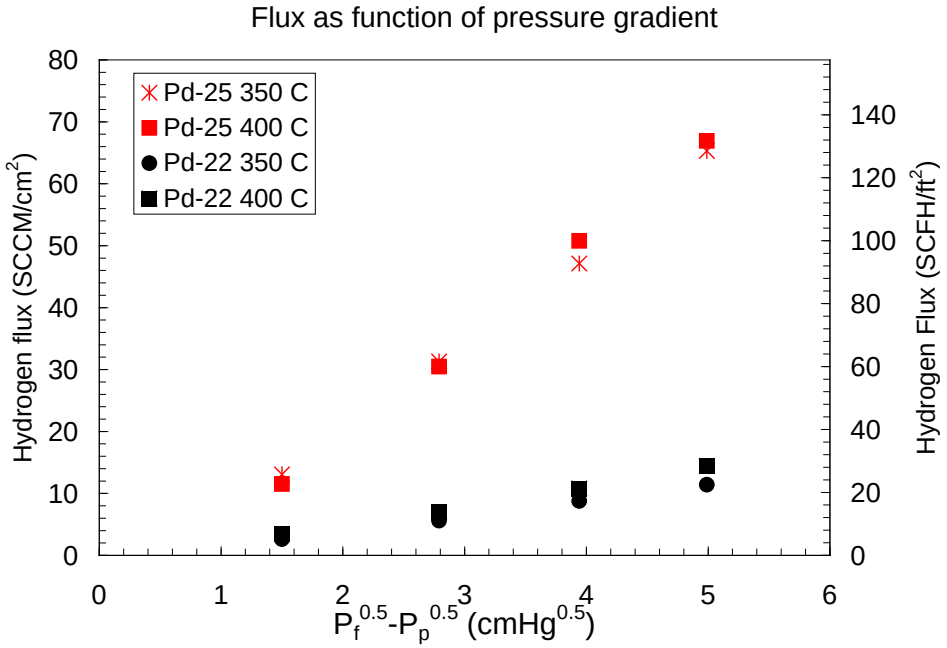

Figure 51. The influence of hydrogen partial pressure and temperature on hydrogen flux.

The binary PdAg alloy membrane Pd-24a had a modest N_2 leak from the beginning of the test after the foil was mounted in the permeation cell at room temperature. The hydrogen pure gas permeability at 400 ºC was 7.7 x 10^{-5} cm^3(STP).cm/ cm^2.s.$cmHg^{0.5}$. This is probably lower than expected from the literature as SwRI membrane Pd-25 had an H_2 permeability of over 10^{-4} cm^3(STP).cm/ cm^2.s.$cmHg^{0.5}$. Flux versus time and flux versus feed pressure plots are shown in Figures 52 and 53.

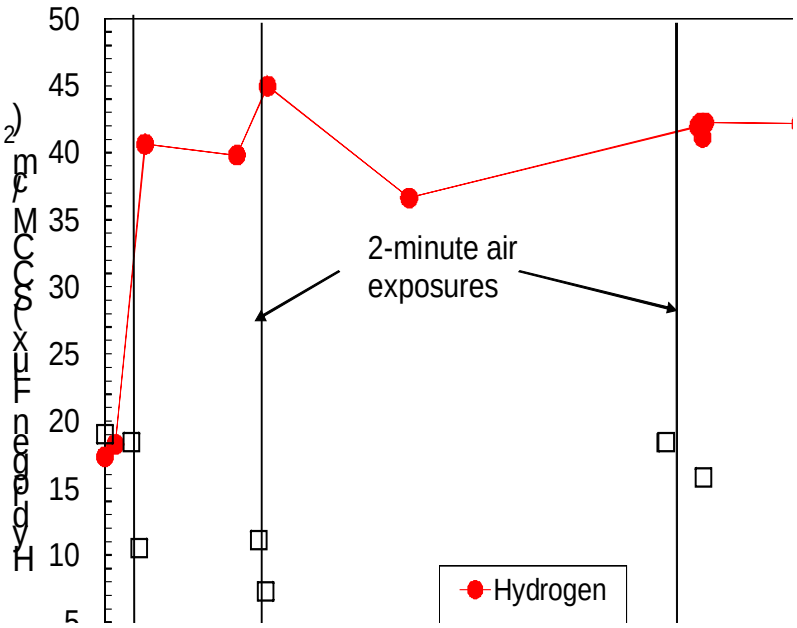

Figure 52. **The influence of time on the pure hydrogen and nitrogen fluxes for $Pd_{93}Ag_7$ membrane Pd-24a at 673 K and 32 psia feed pressure (2.2 bar absolute).**

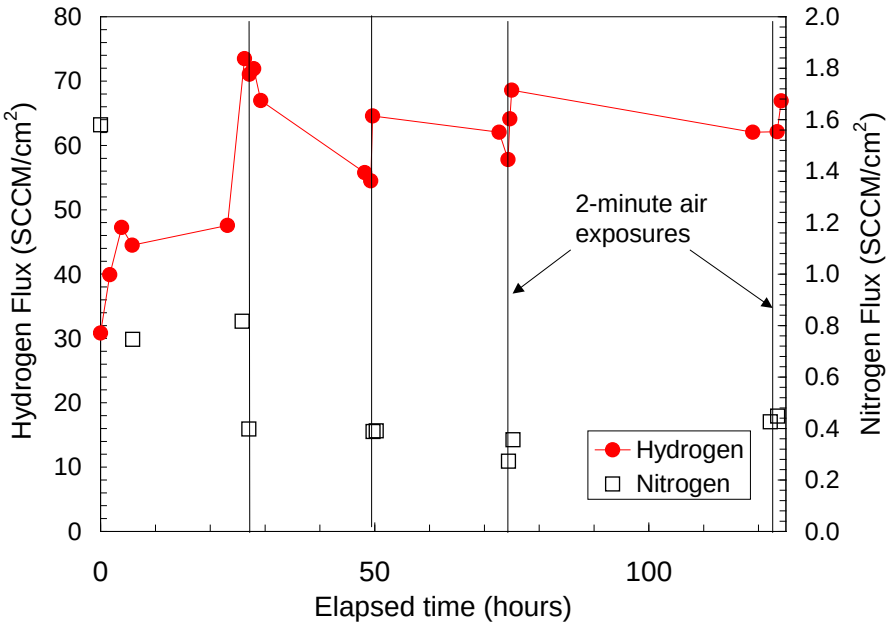

Figure 53. **The development of flux as a function of time at 400ºC and 20 psi feed pressure for membrane Pd-25.**

The influence of partial pressure driving force on the pure hydrogen flux through $Pd_{93}Ag_7$ membrane Pd-24a is shown in Figure 54.

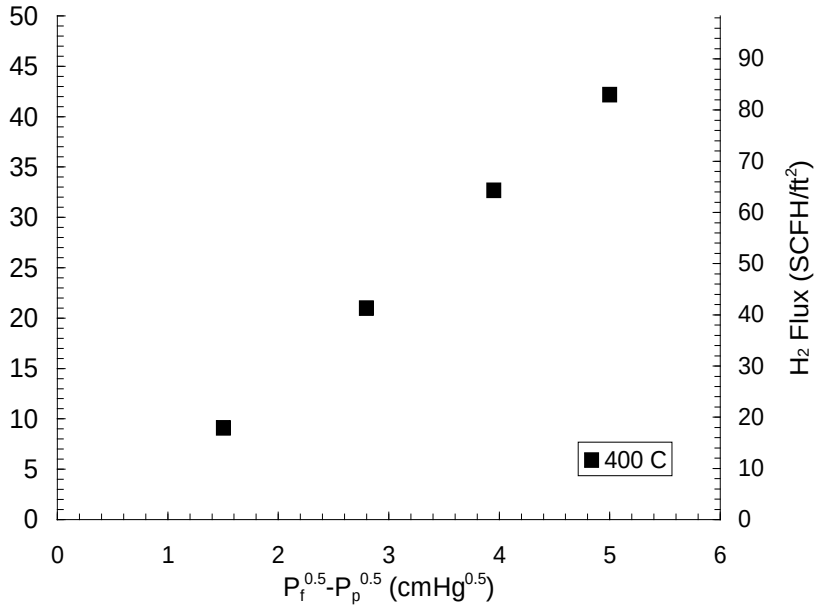

Figure 54. The influence of feed pressure and temperature on the pure hydrogen flux for $Pd_{93}Ag_7$ membrane Pd-24a. Tests were performed at feed pressures of 5, 10, 15, and 20 psig.

Pure gas permeation experiments were performed with Pd-31. An intermediate layer of ceramic paper was used to prevent intermetallic diffusion. A 25 mm diameter section of membrane was cut and weighed, and the SwRI composition was used to calculate a density and to estimate thickness. The operating conditions were over the temperature range from 200 ºC to 400 ºC with hydrogen and nitrogen. Feed pressures varied from 5 to 20 psig. Results of these tests are summarized in the table below

Table 8. PdCu performance data

Foil	T, K	Thickness from SwRI (µm)	Composition (SwRI, wt%)	Composition (standardless EDS, wt%)	H_2 Permeability (cm^3(STP).cm/ cm^2.s.$cmHg^{0.5}$)	H_2/N_2 Ideal Selectivity
Pd-31	473	8.6	$Pd_{89.4}Cu_{10.6}$	$Pd_{76.4}Cu_{23.6}$		•
				feed side	4.24E-07	
	523	8.6	$Pd_{89.4}Cu_{10.6}$	$Pd_{89}Cu_{11}$		•
				perm side	1.20E-06	
	573	8.6	$Pd_{89.4}Cu_{10.6}$		2.31E-06	•
	623	8.6	$Pd_{89.4}Cu_{10.6}$		2.76E-06	•
	673	8.6	$Pd_{89.4}Cu_{10.6}$		4.35E-06	•

Membrane Pd-31 was tested for approximately 200 hours as a function of both temperature (200 – 400 ºC) and feed pressure (5 to 20 psig). A two minute oxidation treatment was performed at each temperature, shown as dotted lines in Figure 55. The thermal history of the membrane is that it was heated in N_2 to 400 ºC, and then the permeation tests began. Compared to other higher permeability foil samples, air oxidations had a relatively small effect on the hydrogen permeability of this membrane. As might be expected, there was a monotonic drop in hydrogen flux as temperature decreased from 400 to 200 ºC. No nitrogen leak was detected during the permeation testing of membrane Pd-31, until the membrane was cooled to 158 ºC in H_2, at which point it developed a significant leak, presumably due to formation of a hydride phase. This is shown as the high flux at 39 ºC.

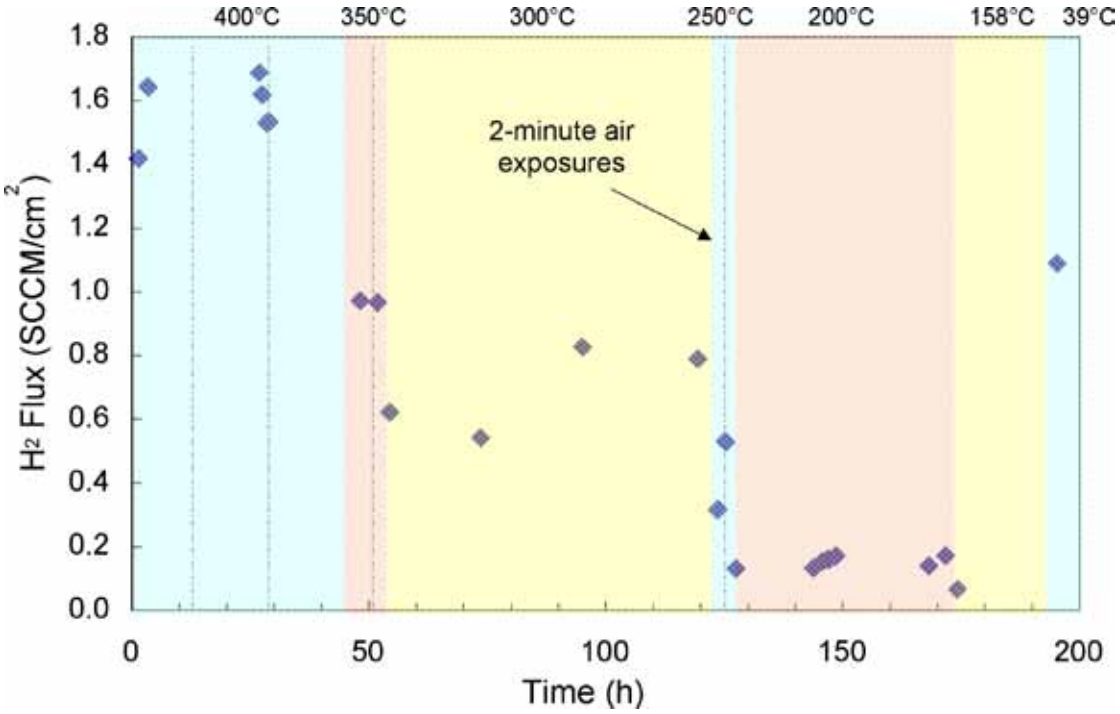

Figure 55. The influence of time and temperature on the pure hydrogen and nitrogen fluxes for $Pd_{89.4}Cu_{10.6}$ binary alloy membrane Pd-31 at 673 K and 32 psia feed pressure (2.2 bar absolute).

The influence of partial pressure driving force on the pure hydrogen fluxes of $Pd_{89.4}Cu_{10.6}$ binary alloy membrane Pd-31 is shown in Figure 56 at three measurement temperatures. Surprisingly, the best fit of hydrogen flux versus partial pressure driving force is linear for these data. There could be several possible explanations for this. First, these fluxes are very small and there is significant error in measuring flows that are less than 1 cm^3(STP)/min. However, measurement error cannot fully explain why the flux is linear with pressure, particularly with a low flux alloy. Usually when we see this behavior for a very thin membrane on a porous support, the most likely explanation is that Knudsen diffusion in the porous support is rate-limiting. That certainly does not apply here. Another possibility is some kind of "surface rate process," which could be

hydrogen desorption, or the rate of hydrogen entering the bulk from the surface. A surface resistance that is probably not a candidate is dissociative adsorption which is essentially instantaneous on pure Pd. If these foils are extremely smooth, the resistance associated with hydrogen moving from the surface to the bulk may be responsible. Usually, air oxidations roughen up the surface and can increase the flux by up to a factor of two. That didn't work in this case, but perhaps we needed to use more aggressive conditions.

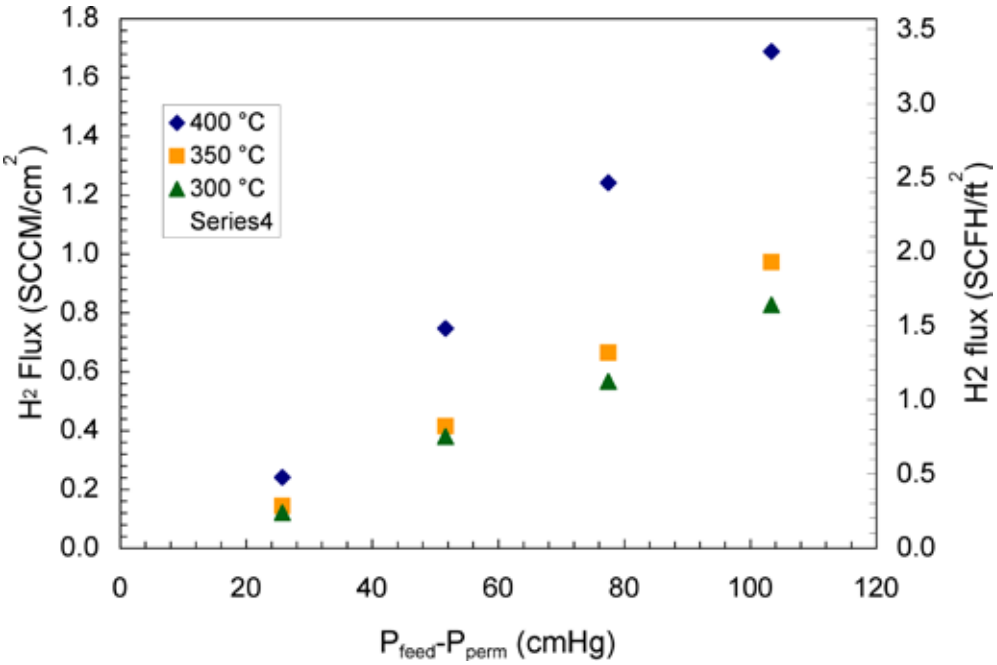

Figure 56. The influence of feed pressure and temperature on the pure hydrogen pressure for $Pd_{89.4}Cu_{10.6}$ binary alloy membrane Pd-31. Tests were performed at 5, 10, 15, and 20 psig feed pressure at three temperatures.

The permeability of this membrane at 350 ºC (623 K) is quite low; approximately an order of magnitude less than the value for the $Pd_{90}Cu_{10}$ alloy reported in the McKinley patent. However, given that the Cu composition is this foil may be non-homogeneous, and is higher than 10 mass % on one side, the low permeability is not surprising. The EDAX compositions in the table above are before testing. The EDAX compositions of the Pd-31 sample after testing are very close to the values reported above: feed side: 22.7 mass % Cu; permeate side: 10.2 mass % Cu.

Pure gas permeation experiments were performed with Pd binary alloy foil sample PdAu-2 with a composition of 90% Pd and 10% Au. An intermediate layer of ceramic paper was used to prevent intermetallic diffusion between the foil and the porous stainless steel disk support. This foil was fabricated using conventional metallurgical techniques (cold rolling) by the Wilkinson Company of Post Falls, ID. A 47 mm diameter section of membrane was cut and weighed, and

the composition from synthesis was used to calculate a density and used to estimate thickness, which compared well to the thickness measured by a micrometer.

Membrane PdAu-2 was tested for approximately 250 hours as a function of both temperature (300 – 500 ºC) and feed pressure (5 to 20 psig). Results of these tests are summarized in the table below.

Table 9. PdAu performance data

Foil	T, K	Thickness (μm)	Composition (wt%)	Composition (standardless EDS, wt%)	H_2 Permeability (cm^3(STP).cm/ cm^2.s.$cmHg^{0.5}$)	H_2/N_2 Ideal Selectivity
PdAu-2	573	28	$Pd_{90}Au_{10}$	$Pd_{87.5}Au_{12.5}$	8.11E-05	•
	623	28	$Pd_{90}Au_{10}$	$Pd_{87.5}Au_{12.5}$	1.03E-04	•
	673	28	$Pd_{90}Au_{10}$	$Pd_{87.5}Au_{12.5}$	1.15E-04	•
	723	28	$Pd_{90}Au_{10}$	$Pd_{87.5}Au_{12.5}$	1.35E-04	•
	773	28	$Pd_{90}Au_{10}$	$Pd_{87.5}Au_{12.5}$	1.50E-04	•

The influence of temperature on the pure hydrogen permeability is shown in Figure 57. The thermal history of the membrane is that it was heated in N_2 to 300 ºC, and then the permeation tests began. After reaching steady-state at each temperature, the temperature was increased. CSM measured permeability for both increasing and decreasing temperature. As might be expected, there was a monotonic increase in hydrogen permeability as temperature increased from 300 to 500 ºC. No nitrogen leak was detected during the permeation testing of membrane. Some hysteresis was observed as the permeabilities upon cooling are lower than those measured during the heating cycle. The data agrees with data provided by Tanaka Precious Metals of Japan for their own PdAu foils. McKinley reports a hydrogen permeability of 1.06×10^{-4} cm^3(STP).cm/ cm^2.s.$cmHg^{0.5}$ for a 5 mass % Au alloy foil at 350 ºC. From the table above, our value at 350 ºC for the 10% Au alloy is 1.03×10^{-4} cm^3(STP).cm/ cm^2.s.$cmHg^{0.5}$. Our data, along with the literature, provides a basis for comparison with the PdAu samples fabricated by SwRI.

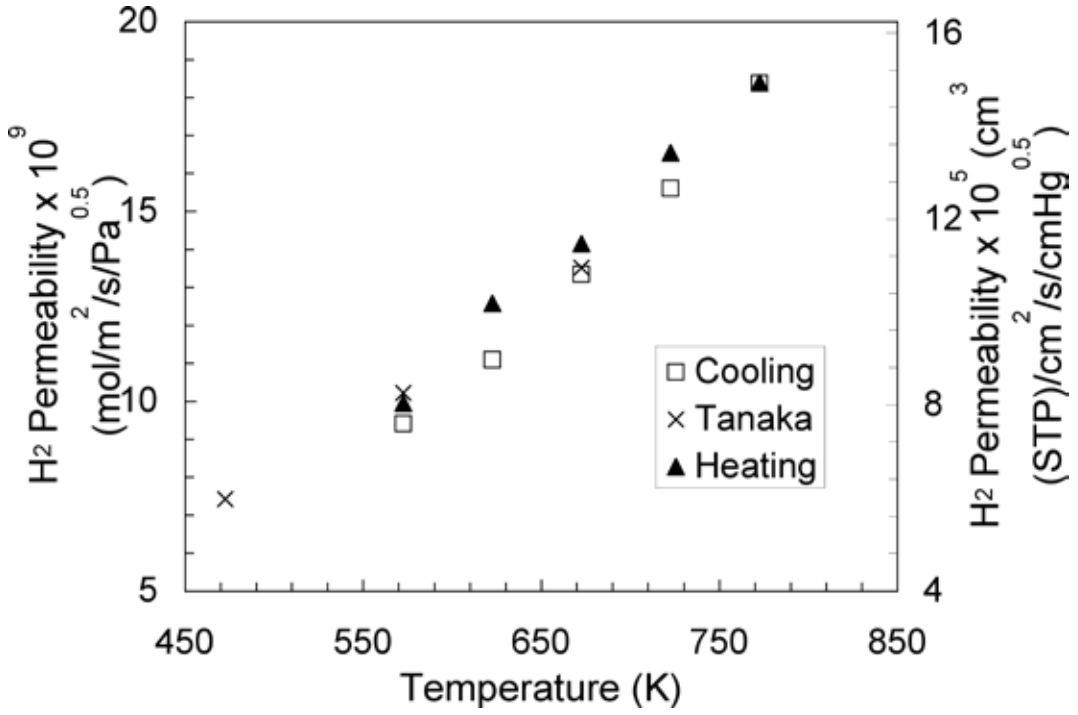

Figure 57. The influence of temperature on the pure hydrogen and nitrogen fluxes for $Pd_{90}Au_{10}$ binary alloy membrane PdAu-2 at 32 psia feed pressure (2.2 bar absolute).

The H_2 permeability data for membrane PdAu-2 between 573 and 773 K was fit with the Arrhenius relationship. The Arrhenius equation fits the data well (R_2>0.99 for both heating and cooling) and the relevant constants are listed in the following table.

Table 10. Thermodynamic values for PdAu

	E_a (J/mol)	**k_0 (mol H_2/m ^{2}/s/Pa $^{0.5}$)**
Heating	11,465	$9.59*10^{-8}$
Cooling	12,559	$1.11*10^{-7}$

X-ray diffraction was used to distinguish pure Pd, pure Au, and Pd-Au alloy phases (Figure 58). The sampling depth for the Cu-K• x-rays used in our XRD system is a maximum of 4.0 microns. In addition to qualitative phase results, Vegard's law, which states that lattice parameter in certain solid solutions is directly proportional to composition, is known to apply to the Pd-Au system. Thus, quantitative gold content can be determined from Pd-Au peak shift.

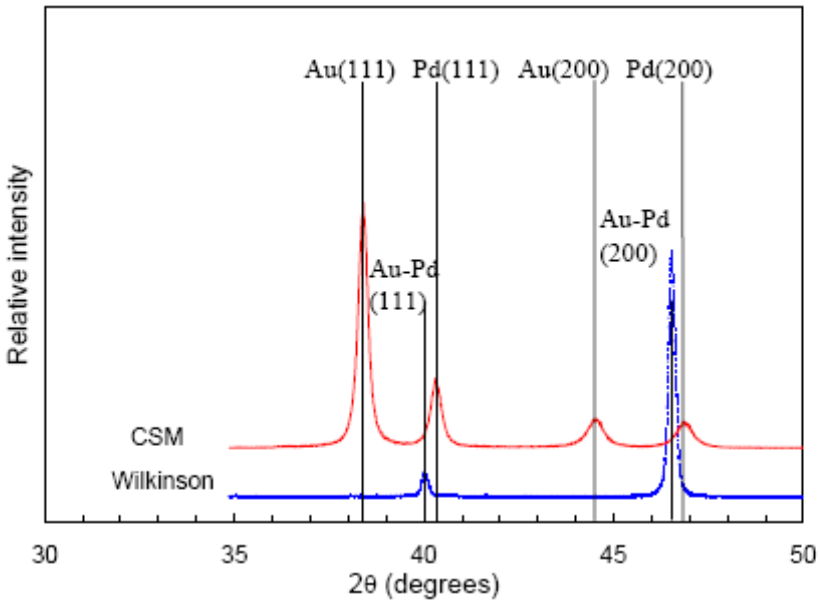

Figure 58. X-ray diffraction patterns for sequentially plated Au on Pd (CSM) and cold rolled fully annealed $Pd_{90}Au_{10}$ by weight (Wilkinson (PdAu-2).

The following table shows a comparison of analytical techniques for foil PdAu2.

Table 11. Wilkinson composition

	Composition (by weight)		
Sample	**Nominal**	**Standardless EDS**	**XRD**
Wilkinson PdAu-2	$Pd_{90}Au_{10}$	$Pd_{87.5}Au_{12.5}$	$Pd_{90.9}Au_{9.1}$

In previous permeation tests, CSM had used an alumina ceramic paper between the sputtered foil and the stainless steel support. While this arrangement is simple and provides negligible resistance to flow, SEM imaging of the ceramic paper shows that it contains needlelike structures which can damage foils and lower membrane selectivity. To obviate this, a technique was developed in which the metallic supports were dip-coated with an aqueous zirconia slurry. This technique does not significantly increase resistance to flow in the support, and the dip-coated supports were used during permeation tests on membranes Pd-44 and Pd-46. The tests ran for 180 hours under operating temperatures, and in that time the membrane permeabilities showed no signs of intermetallic diffusion introducing contaminants. When testing was complete, the membranes detached readily from the dip-coated supports without any evidence of adhesion. This suggests that dip-coating can produce viable diffusion barriers.

Membranes were characterized prior to testing by SEM/EDS and XRD. XRD showed the membranes consisted of a single FCC crystalline phase, and that composition was fairly constant

across membrane thickness. Similar results were observed with EDS, although both analysis techniques imply slightly different compositions and thicknesses than the nominal values.

Two binary Pd-Au membranes, Pd-44 and Pd-46 were permeation tested simultaneously and under identical conditions, and the results are summarized in the following table. The maximum temperature tested was 773 K, after which the membranes were cooled and retested in 50 K increments until failure. Both membranes had leak rates below the detection limit (0.01 SCCM) at all temperatures at or above 523 K. Membrane Pd-44 developed a slight leak between 523 K and 473 K, and both membranes failed catastrophically upon hydrogen exposure at 423 K.

Hydrogen permeabilities, P, were fit with a linear Arrhenius relationship, and the resulting activation energies (E_a) and pre-exponential factors (k_o) are given. Permeabilities were calculated using:

$$P(T) = k_o e^{-\frac{E_a}{RT}}$$

Summary of experimental results for membranes Pd-44 and Pd-46 are shown in Table 12.

Table 12. PdAu permeability data

	SwRI Pd-44			**SwRI Pd-46**		
Temperature (K)	**Best n-value**	**H_2/N_2 ideal selectivity**	**Flux @ 32 psia feed, 12 psia permeate (cm^3/cm^2.min)**	**Best n-value**	**H_2/N_2 ideal selectivity**	**Flux @ 32 psia feed, 12 psia permeate (cm^3/cm^2.min)**
473	1.02	206	14.97	0.87	>3800	13.17
523	0.52	>5710	19.75	1.01	>4650	16.08
573	0.71	>6390	22.16	0.68	>5650	19.60
623	0.57	>8370	29.07	0.6	>7030	24.41
673	0.59	>10200	35.36	0.65	>8630	29.92
723	0.43	>11500	39.92	0.52	>10800	37.49
773	0.55	>13200	45.82	0.53	>13200	42.35
Ea (J/mol)	11417			12159		
k_0 (mol/m/s/$Pa^{0.5}$)	9.05E-08			1.32E-07		

The permeabilities agree well with those in the literature for binary Pd-Au alloys. For example, Tanaka Precious Metals of Japan shared some of their data for PdAu foils with us, just prior to the ICIM 10 meeting in the spring of 2008. At 400 ºC, the Tanaka 10 mass % Au Pd alloy had a hydrogen permeability of 1.5 x 10^{-8} mole.m/m^2.s.Pa $^{0.5}$, essentially the same as we observed for SwRI Pd-46. Membranes generally had n-values between 0.5 and 0.7, suggesting that the most rate-limiting step in hydrogen transport was bulk diffusion, except at low temperatures.

The compositions of the PdCu binary alloy membranes by EDAX analysis are shown in the table below. The pure gas permeation tests are summarized in Figure 59.

Table 13. PdCu compositions

Membrane	SwRI-105	SwRI-107	SwRI-112	SwRI-121
Side A	$Pd_{55}Cu_{45}$	$Pd_{70}Cu_{30}$	$Pd_{50}Cu_{50}$	$Pd_{55.4}Cu_{44.6}$
Side B	$Pd_{62}Cu_{38}$	$Pd_{64}Cu_{36}$	$Pd_{60}Cu_{40}$	$Pd_{61.3}Cu_{38.7}$
Thickness (microns)	6.7	7.9	7	8

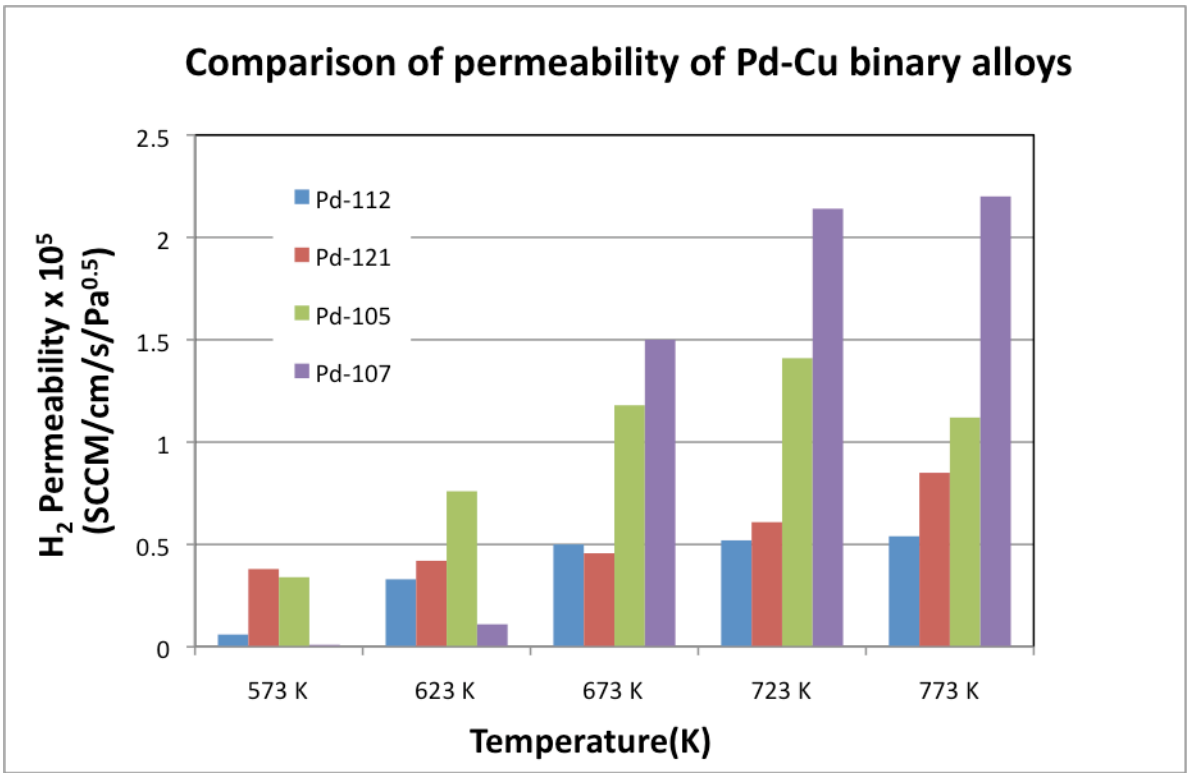

Figure 59. Comparison of hydrogen permeabilities for different Pd-Cu alloys at 20 psi feed pressure across a range of membrane compositions.

The pure hydrogen permeability data in Figure 59 are quite surprising. First, the permeabilities are all very low, at most about 15% of pure Pd at 673 K = 400 ºC. Membrane Pd-107 has the highest permeability, followed by sample #Pd-105. The differences in the permeabilities are very likely due to differences in the phase structure, shown in Figure 60. The BCC phase is known to have higher permeability due to the more open BCC structure, resulting in a higher hydrogen diffusivity. However, unless the composition is exactly 40 mass % Cu (within 0.5%), the permeability will be much lower than the maximum value of about 1.4 times pure palladium. Side B of membrane Pd-107 corresponds to the mixed FCC/BCC phase, while side A of this membrane is probably solely FCC. A similar situation probably exists for membrane Pd-105. Since the permeabilities of all of this batch of binary PdCu alloys is so low, no further analyses, such as XRD were performed.

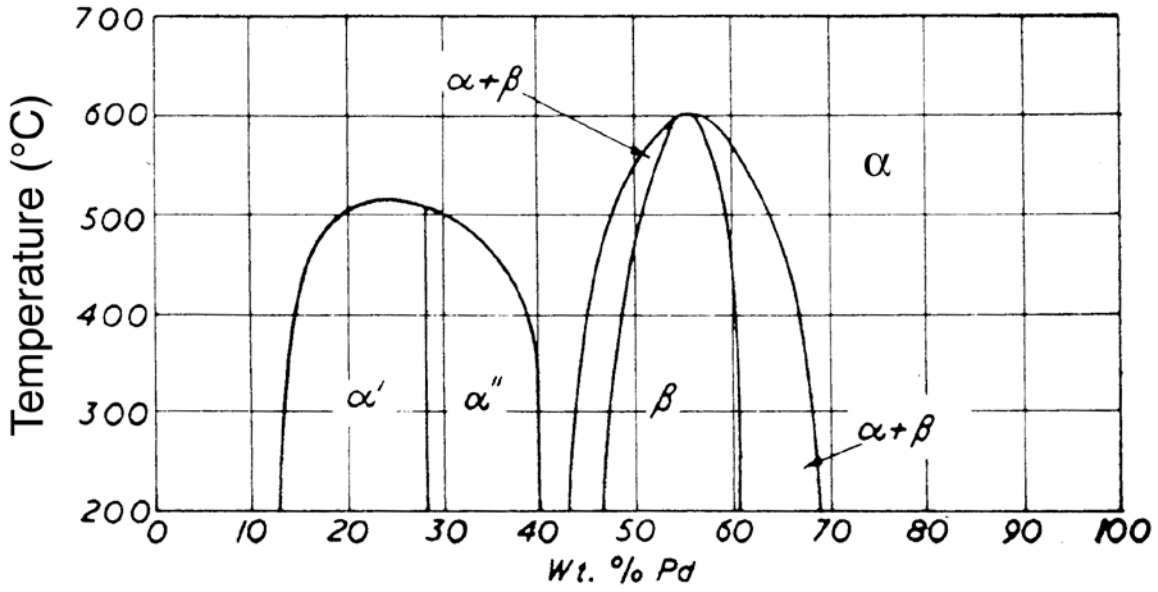

Figure 60. Palladium copper binary alloy phase diagram. The alpha phase is FCC, while the beta phase is BCC [15].

The composition of the PdAu binary alloys by EDAX analysis is shown in the table below. The pure hydrogen permeability data are given in Figure 61, which compares two SwRI membranes to a cold-rolled $Pd_{90}Au_{10}$ foil membrane from Tanaka Precious Metals of Japan.

Table 14. PdAu compositions

Membranes	SwRI-125	SwRI-126	TKK ~10% Au
Side A	$Pd_{90.7}Au_{9.3}$	$Pd_{90}Au_{10}$	$Pd_{89}Au_{11}$
Side B	$Pd_{91.3}Au_{8.7}$	$Pd_{89.9}Au_{10.1}$	$Pd_{89}Au_{11}$
Thickness (Microns)	37.2	31.2	25

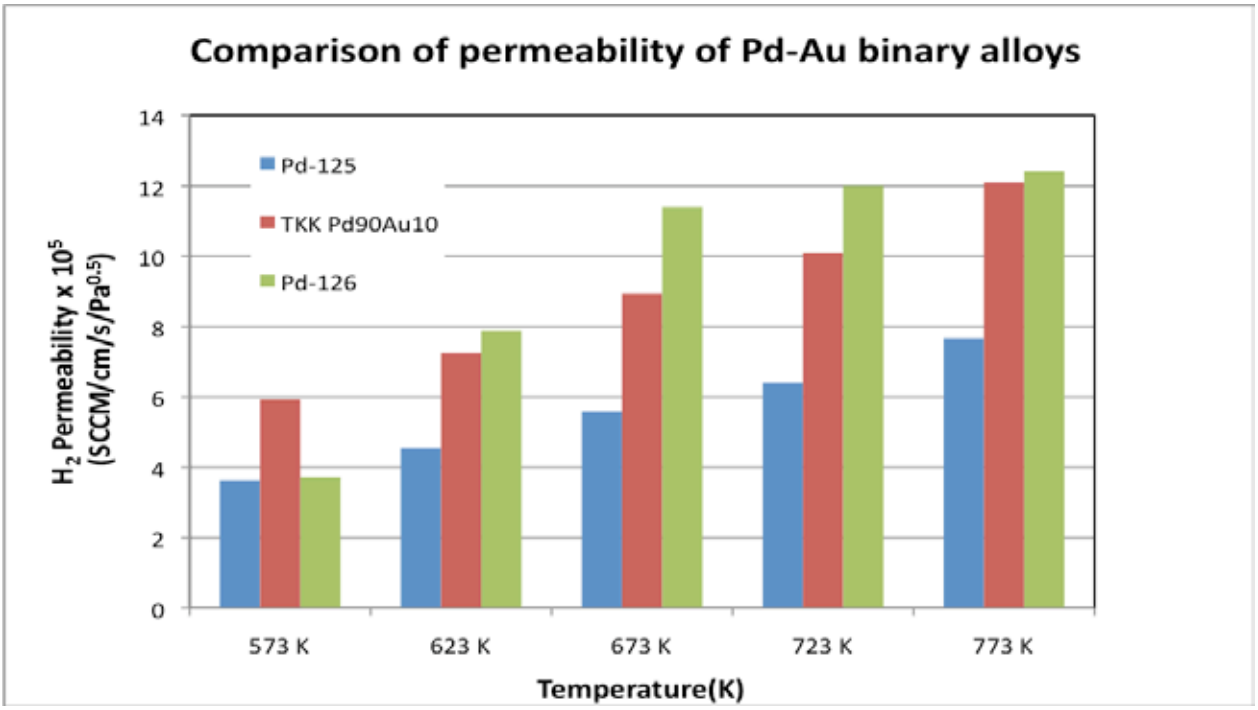

Figure 61. Comparison of hydrogen permeabilities for different Pd-Au alloys at 20 psi feed pressure across a range of membrane compositions.

In general, the permeabilities of the PdAu binary alloy membranes are high. Membrane Pd-126 has a permeability that is slightly higher than pure Pd. All of these palladium-gold alloys have almost the same composition (90% Pd, 10%Au); still the permeability of hydrogen through them was found to differ by up to almost a factor of two. The Pd-125 and Pd-126 membranes were made by sputtering while the TKK membrane was manufactured by a cold-working technique. XRD analysis shows that the preferential orientation of the sputtered membranes is quite different from those made by cold-working.

Table 15. Membrane compositions as measured by standardless EDS analysis

Membrane	Pd-119	Pd-120	Pd-121	Pd-125	Pd-126
Side A	$Pd_{60}Cu_{40}$	$Pd_{56}Cu_{44}$	$Pd_{52}Cu_{48}$	$Pd_{91}Au_{9}$	$Pd_{90}Au_{10}$
Side B	$Pd_{55}Cu_{45}$	$Pd_{56}Cu_{44}$	$Pd_{58}Cu_{42}$	$Pd_{91}Au_{9}$	$Pd_{90}Au_{10}$
Mean	$Pd_{58}Cu_{42}$	$Pd_{56}Cu_{44}$	$Pd_{55}Cu_{45}$	$Pd_{91}Au_{9}$	$Pd_{90}Au_{10}$
Thickness (micron)	6.32	7.42	7.5	37.2	31.2

The membrane compositions were within experimental error of the nominal values (Table 15) for the Pd-Au membranes, but the Pd-Cu membranes had significant variations across the thickness, and were as much as 5% away from the nominal composition. Permeability data for the PdCu membranes are shown in Figure 62. Since the PdCu alloy compositions were significantly different from optimum 40 mass % Cu, the hydrogen permeabilities were quite low, ranging from 3-15% that of pure Pd at 623 K. The Pd-Au membranes, having compositions close to the optimum for PdAu alloys, had superior hydrogen permeabilities.

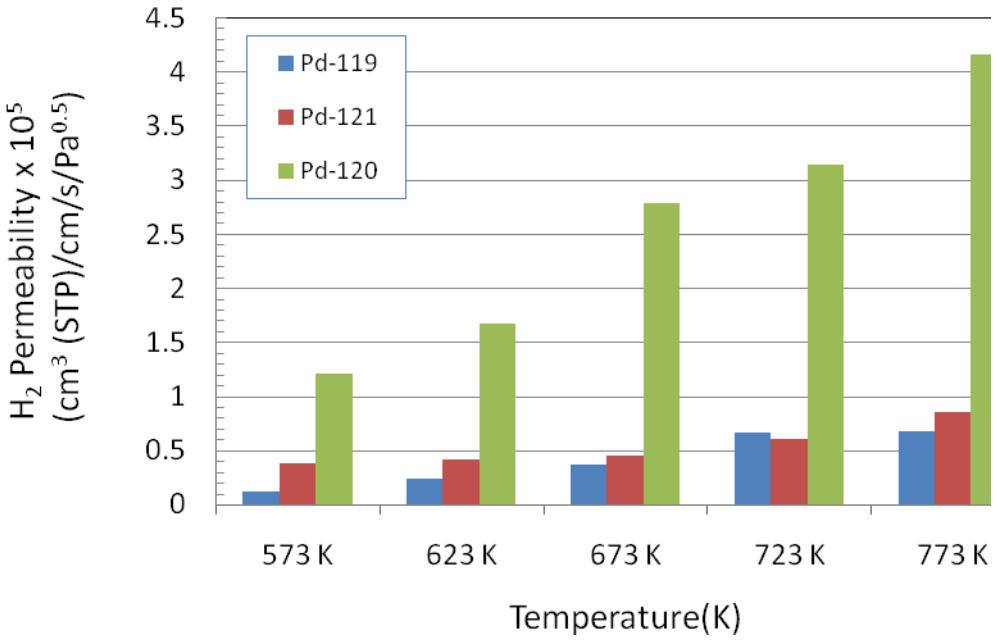

Figure 62. Comparison of hydrogen permeabilities for Pd-Cu alloys at 20 psi feed pressure.

As shown in Figure 63, membrane Pd-125 had significantly lower permeability than Pd-126, a result not explained by the trivial difference in their compositions.

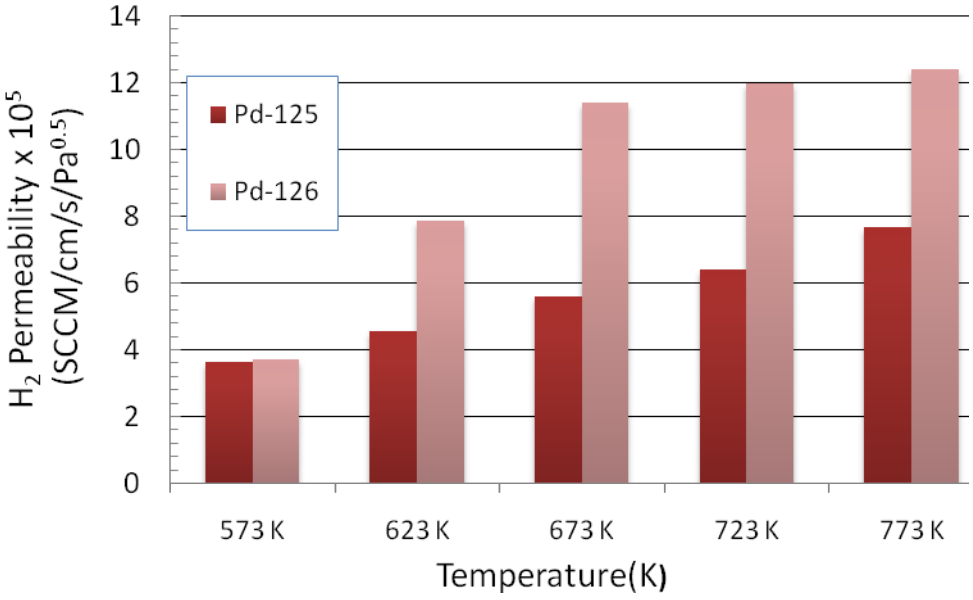

Figure 63. Comparison of hydrogen permeabilities for $Pd_{90}Au_{10}$ (by weight) alloys at 20 psi feed pressure.

The cold-worked 10 wt% Au foil tested at TDA research under DOE 2a mixture gas conditions with 20 ppm H_2S was retrieved from its housing and subjected to analysis by XRD and SEM/EDS. Several phenomena were notable. The feed side of the membrane had been significantly roughened from its smooth, polished as-received state (Figure 64).

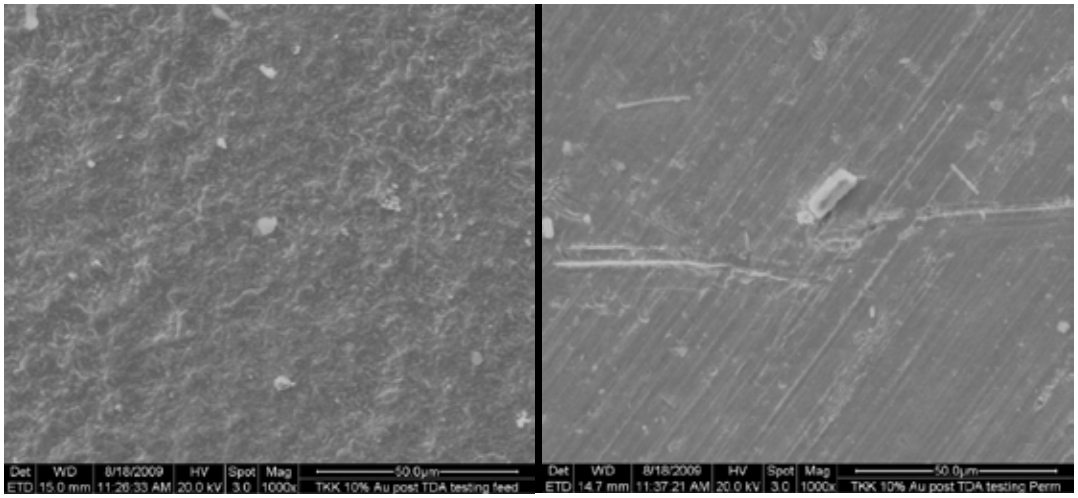

Figure 64. 1000x SEM images of a 10% Au cold-worked foil after mixture gas testing showing feed side (left) and permeate side (right).

The feed side also appears to have some significant segregation, with feed compositions by standardless EDS ranging from 0.4-1.5 wt% Au, while the permeate side ranged from 12-16 wt% Au. No surface sulfur was detectable. We have previously observed some evidence of permeation-driven segregation in pure-gas experiments, but the extent of segregation in those cases was far less.

XRD analysis of the membrane (Figure 65) showed minimal peak shift after testing, but the feed side developed several new peaks. The d-values of these peaks correspond to sulfides of palladium, in particular, Pd_4S and $Pd_{2.8}S$. A single small palladium hydride peak (relative intensity 1%) is also noticeable, which was most probably formed after the membrane had been completely tested and was cooling.

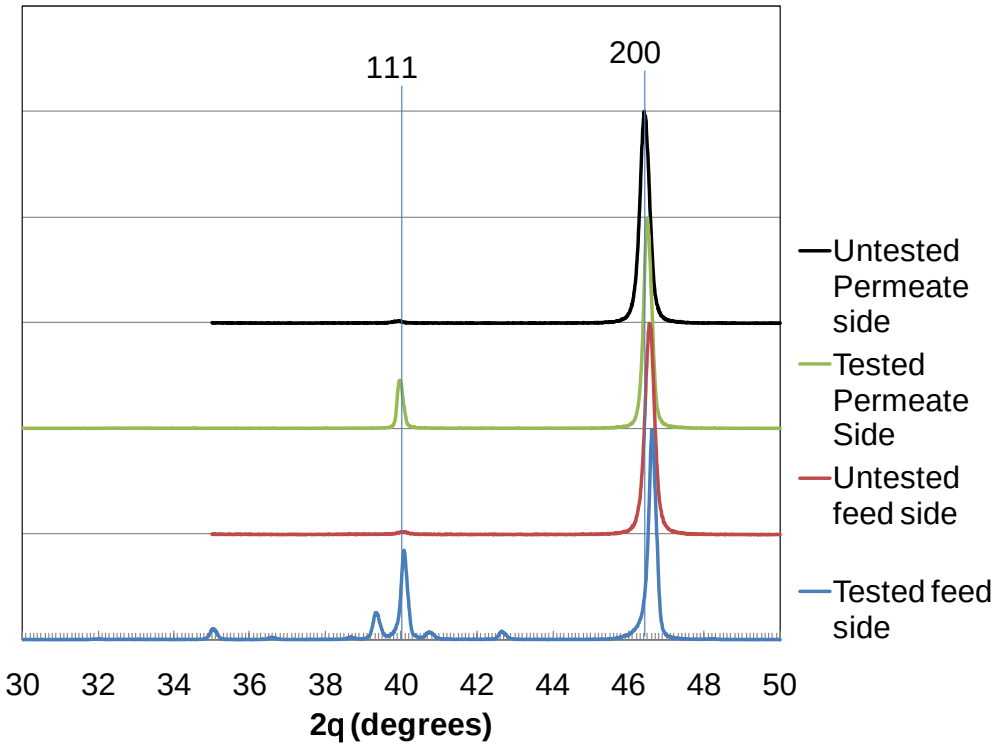

Figure 65. X-ray diffractograms for a 10 wt% Au cold-worked foil before and after mixture gas testing.

CSM purchased and installed a Micromeritics ASAP™ (Accelerated Surface Area and Porosimetry) 2020. This instrument will perform automated chemisorption and physisorption experiments over a range of temperatures from 77 to 800 K. Previous research has determined hydrogen permeability at a range of temperatures for both cold-worked and sputtered Pd-Au foils, but we have not yet determined the relative contributions of diffusivity and solubility, or how these properties compare to other materials. The ability to conduct hydrogen sorption measurements made these studies possible.

Measurements presented in this report were obtained using the high-temperature chemisorption mode. Adsorbed surface contaminants were removed from the foil surfaces by heating under vacuum, and the sample was cooled to the desired temperature under vacuum. An adsorptive, in this case hydrogen, was added to the sample in doses at a given pressure, and the drop in pressure as the sample adsorbed the hydrogen was measured. Using the known sample weight, the concentration of adsorbed hydrogen was calculated, as shown in Figure 66.

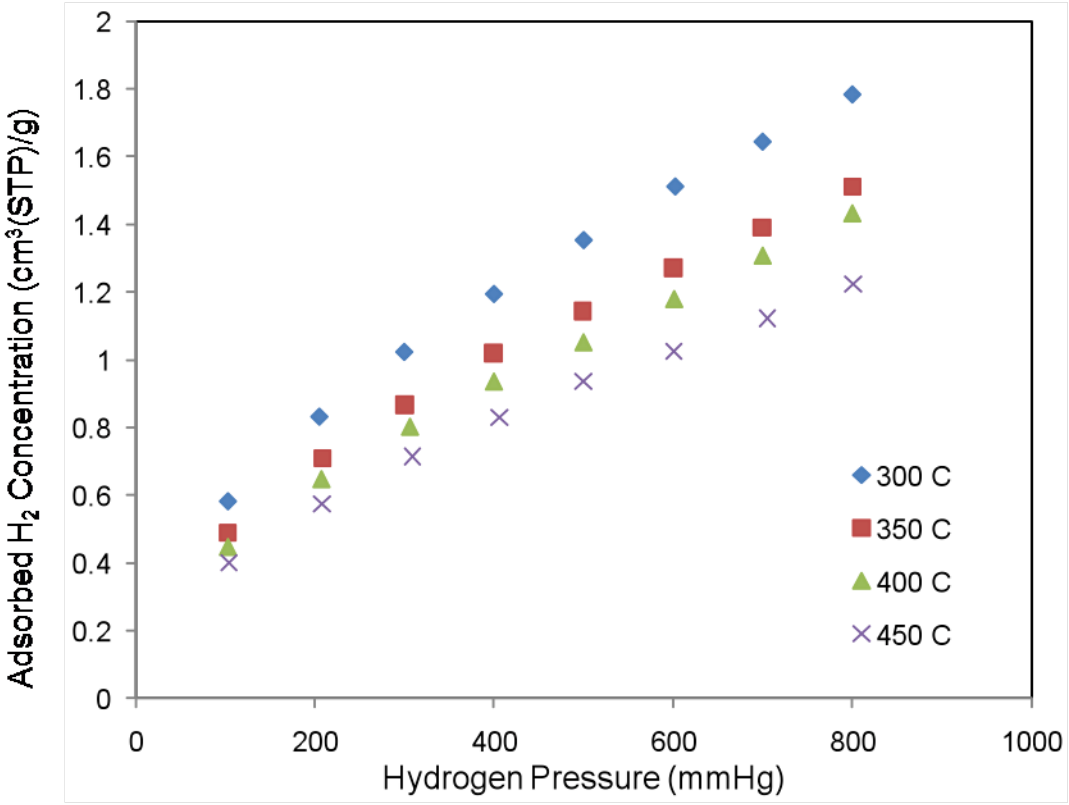

Figure 66. Concentration of adsorbed hydrogen as a function of pressure for a $Pd_{90}Au_{10}$ (by weight) cold-worked foil sample.

The concentration of hydrogen in the lattice is linearly proportional to $P^{0.5}$, in agreement with Sievert's law, and the slope of this line is the solubility coefficient *S*. Using the relationship

$$\mathbb{P} = \mathcal{D}\, x\, S$$

where P is the hydrogen permeability, the diffusivity coefficient *D* can also be calculated. The results of these calculations, using previously-measured hydrogen permeabilities, are shown in Figures 67 and 68.

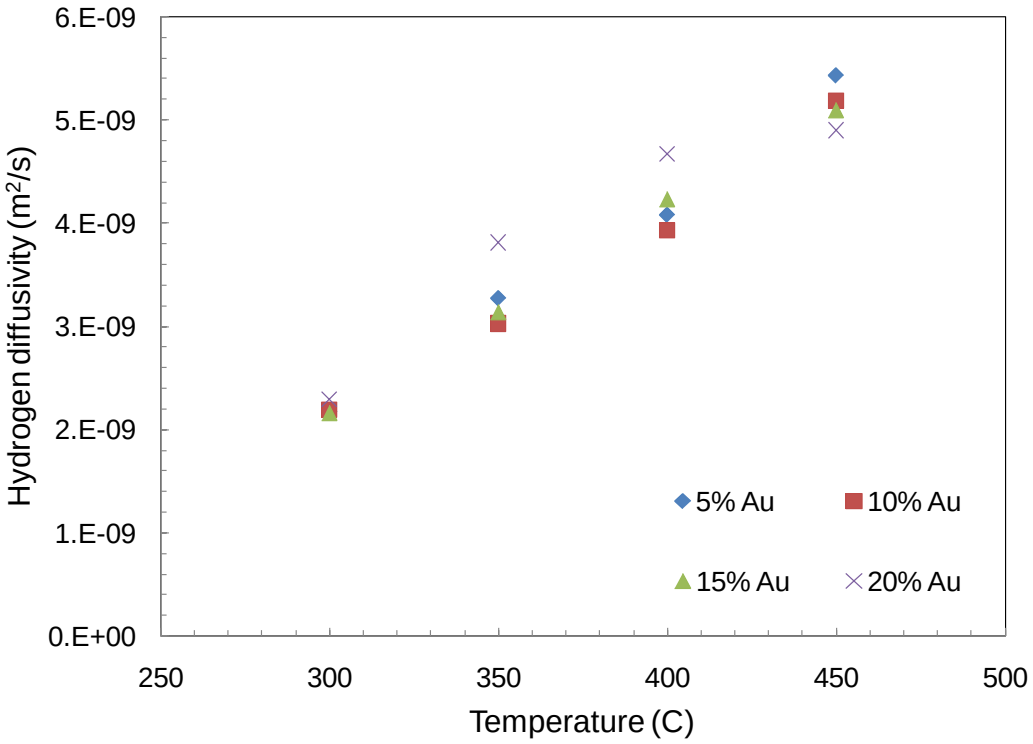

Figure 67. Hydrogen diffusivity as a function of temperature for Pd-Au cold-rolled foils.

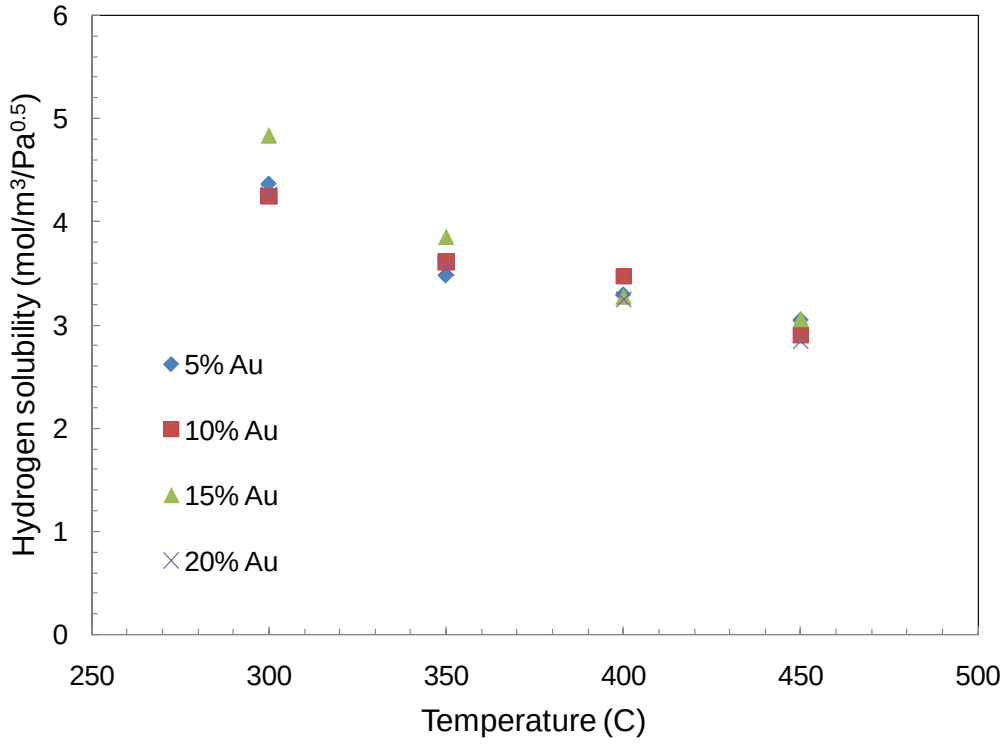

Figure 68. Hydrogen solubility as a function of temperature for cold-rolled Pd-Au foils.

From these preliminary results, it appears that variations in gold content have a more significant effect on diffusivity at higher temperatures, and on solubility at lower temperatures. Overall, the two effects tend to cancel each other out, as permeabilities are generally similar across this range of gold contents. As shown in Figure 67, the diffusivities calculated from experimental permeabilities and solubilities range from about 3.5 to 5 x 10^{-9} m^2/s at 400 ºC for a range of Au compositions. These are slightly higher than those predicted from DFT simulations. Wilcox and coworkers predicted diffusivities at 400 ºC ranging from 2 - 4 x 10^{-9} m^2/s for these compositions. This is surprisingly good agreement between theory and experiment. However, the trend of the simulated diffusion coefficients at constant temperature was one of decreasing diffusivity with increasing Au composition. This is seen in our data at 450 ºC but not at lower temperatures.

CSM has observed that oxidation at temperature or heating a Pd alloy membrane up to temperature in air increases the pure hydrogen permeability compared to samples that were not oxidized. Preliminary experiments to investigate whether oxidation can increase the rate of hydrogen sorption were performed and whether oxidation under the same conditions would increase pure hydrogen permeability.

As shown in Figure 69, Uchikawa and coworkers [13] reported that both oxidation and mechanical roughening increased the rate of hydrogen sorption in cold-worked, pure Pd foils, compared to an as-received foil sample. Oxidation for several minutes at 600 ºC increased the sorption rate at 25 ºC by over 100 times. This observation showed that the catalyst absorption rate could be changed by oxidation. The other key observation from our own work and the literature is that the degree of permeability improvement is inversely proportional to membrane thickness. In other words, the H_2 permeability of a thinner membrane is increased more than a thicker membrane. Therefore, it is likely that oxidation changes one of the rate processes in series associated with hydrogen permeation.

In high temperature chemisorption mode, equilibrium H_2 sorption isotherms can be measured as shown in Figures 70 and 71 for 25 micron thick, as-received and oxidized, cold-rolled, $Pd_{75}Ag_{25}$ foils.

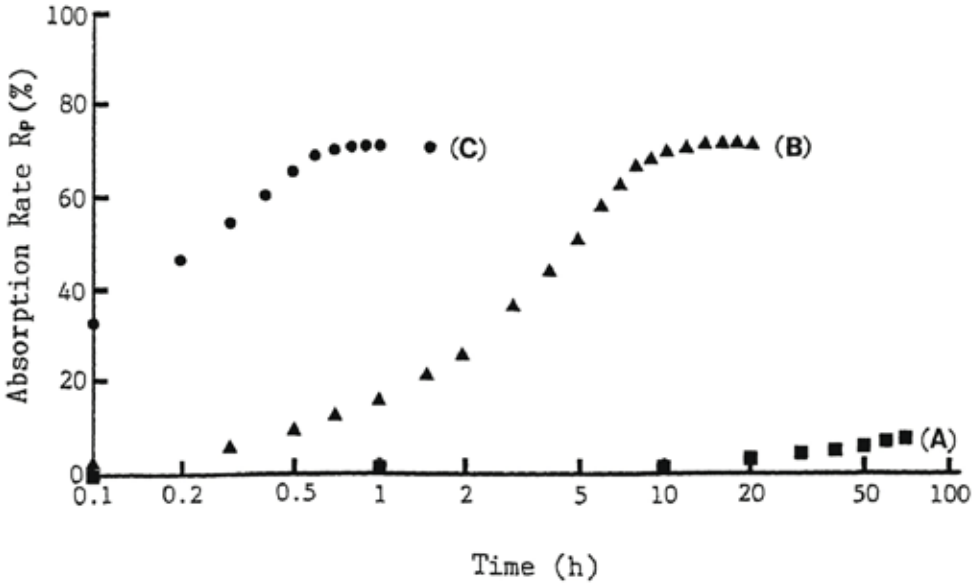

Figure 69. Hydrogen absorption rate measured using TGA for three identical cold-worked Pd foils, sample a was "as-received", sample b was polished with an abrasive paper, and sample c was oxidized [13].

In Figure 70, the equilibrium sorption for oxidized and as-received foils is compared as a function of temperature. The hydrogen sorption was measured as a function of temperature for the as-received PdAg foils starting at 450 ºC and repeating the isotherm as the temperature decreased in 50 ºC increments to 300 ºC. The same foil membrane was then oxidized at 300 ºC for 20 hours and the sorption experiments were repeated over the same temperature ranges. Within error, the equilibrium hydrogen sorption amounts are essentially the same for both as-received and oxidized foils. In Figure 71, the sorption isotherms were repeated for the oxidized foils. The agreement between the two sorption experiments is quite good at all measurement temperatures.

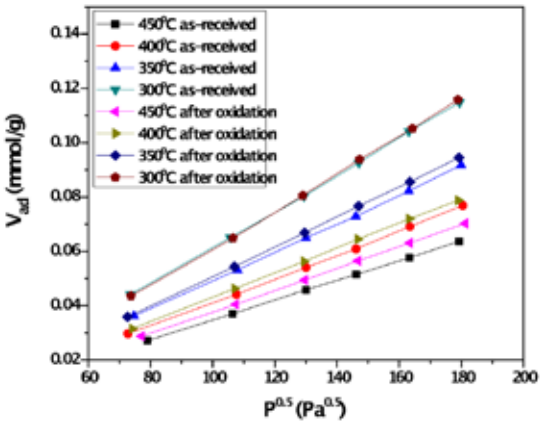

Figure 70. The influence of temperature (300 – 450 °C) on the equilibrium H_2 absorption isotherms for PdAg membranes before and after air oxidation at 300 °C.

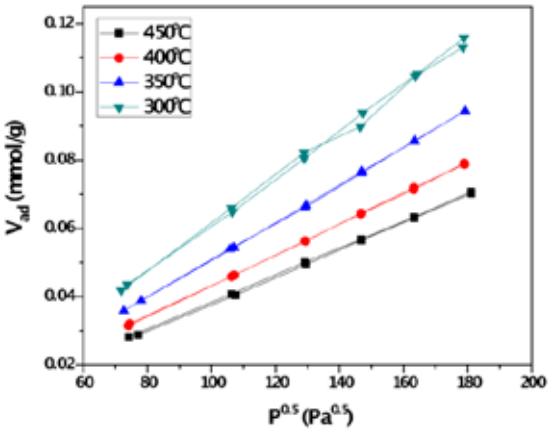

Figure 71. Repeat measurements of hydrogen sorption isotherms for the oxidized PdAg foil membrane.

The data in Figures 70 and 71 suggest that the equilibrium solubility is not changed by oxidation of the PdAg foil. However, in agreement with Uchikawa, the H_2 sorption rate was increased by oxidation. This can be seen in Figures 72 and 73 below. In Figure 72, the initial sorption rate at 160 Pa for a PdAg foil oxidized at 300 ºC for 20 hours is compared to an as-received PdAg foil. The steady-state value is reached much more quickly for the oxidized sample. However, in Figure 73, the sorption rate measurement is repeated for the oxidized foil. Note that in this case, the steady-state absorbed volume is the same for both samples, but the oxidized sample reaches the steady-state value much faster. The difference may be due to consumption of hydrogen from reaction with adsorbed oxygen on the membrane surface, in addition to the hydrogen absorbed into the PdAg foil. A summary of the absorption rate experiments is given in Table 16. Note that the increase in sorption rate is the greatest (~74%) at the lowest pressure of 160 Pa. At an equilibrium pressure of over 1 atm, the sorption rate increase due to oxidation was 25%.

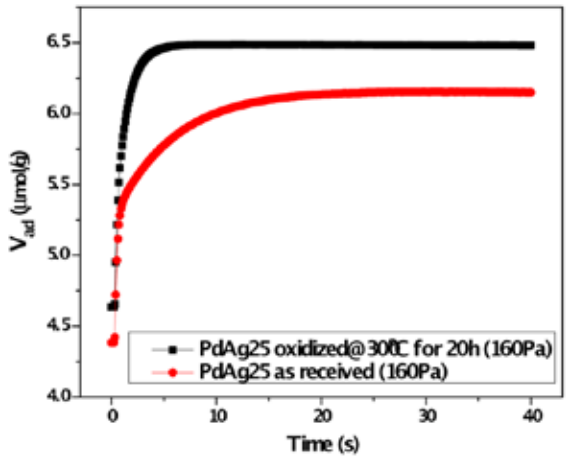

Figure 72. Hydrogen sorption rate for as-received and oxidized PdAg foil membrane.

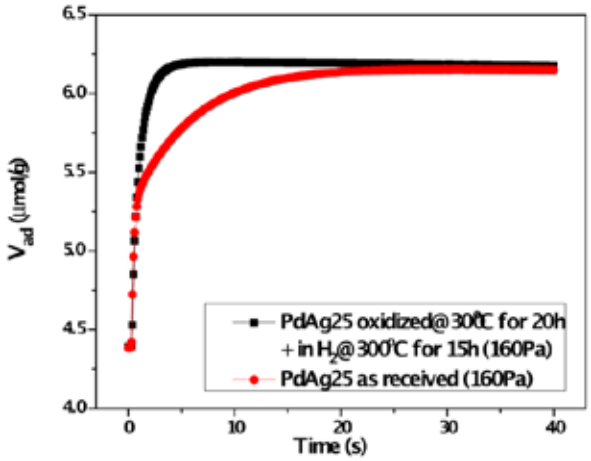

Figure 73. Repeat sorption rate measurement for the PdAg foil membrane oxidized at 300 °C compared to the as-received foil

Table 16. Summary of hydrogen absorption rate data

Equilibrium Pressure (kPa)		0.16	14.1	28.5	42.7	57.1	71.5	85.9
Time to equilibrium (s)	Before oxidation (t_1)	23.0	4.6	2.7	1.8	1.6	1.4	1.2
	After oxidation (t_2)	6.0	2.6	1.6	1.2	1.1	1.0	0.9
Enhancement for kinetics [(t1-t2)/t1] (%)		73.9	43.5	40.7	33.3	31.3	28.6	25.0

Figure 74 compares the hydrogen fluxes measured at 300 ºC for another $Pd_{75}Ag_{25}$ foil membrane sample from the same batch of cold-rolled foil with and without oxidation for 24 hours at 300 ºC. The as-received foil membrane was first at a series of feed pressures, and then oxidized and the pure H_2 permeation tests were repeated. Although not clear from Figure 74, the detailed data in Table 17 show that the greatest enhancement in flux/permeability was observed at the lowest feed pressure. This correlates extremely well with the sorption kinetics data. The pure H_2 permeability calculated for the highest feed pressure of 772 kPa was 1.49 x 10^{-8} mol.m/m^2.s.$Pa^{0.5}$. This permeability compares well to the value of 1.56 x 10^{-8} mol.m/m^2.s.$Pa^{0.5}$ reported for a 30 mass % Ag alloy by the Tanaka Precious Metals Corporation of Japan at 300 ºC [4].

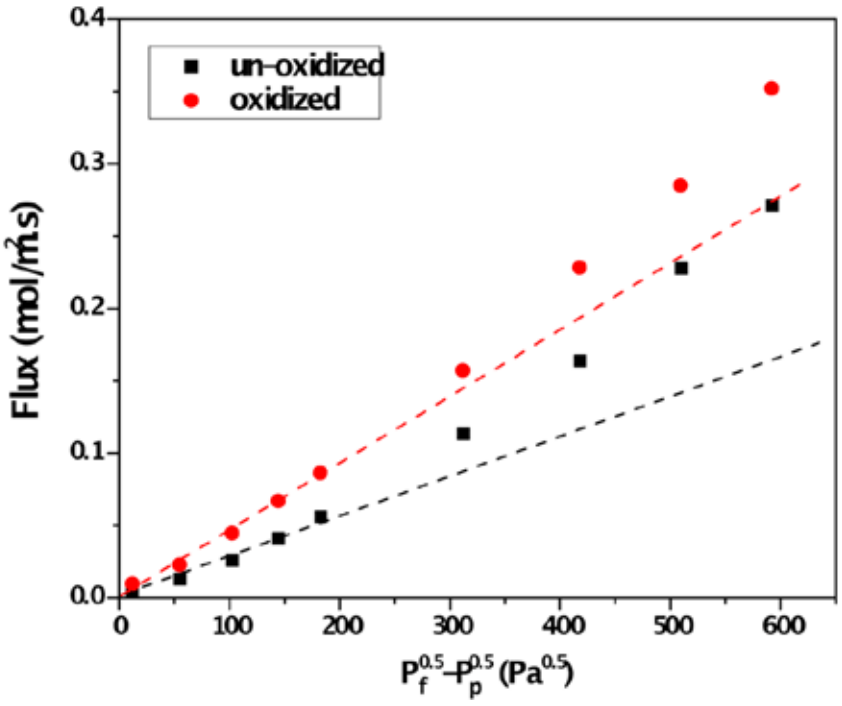

Figure 74. The influence of feed pressure and 300 ºC oxidation for 24 hours on the permeability of a 25 micron thick, $Pd_{75}Ag_{25}$ cold-rolled membrane.

Table 17. Summary of pure H_2 permeation tests at 300 ºC with the $Pd_{75}Ag_{25}$ foil membrane

Feed Pressure (Pa)	Permeate Pressure (Pa)	Pressure difference ($Pa^{0.5}$)	Permeance ($mol/m^2.s.Pa^{0.5}$) × 10^{-4}		Permeability ($mol/m.s.Pa^{0.5}$) × 10^{-9}		Permeability increase (%)
			Before oxidation	After oxidation	Before oxidation	After oxidation	
8.90E+04	**82000**	**12**	4.34	8.25	10.9	20.6	90
1.17E+05	**82000**	**55**	2.36	4.19	5.91	10.5	77
1.51E+05	**82000**	**102**	2.53	4.38	6.32	11	73
1.85E+05	**82000**	**144**	2.84	4.66	7.11	11.6	64
2.19E+05	**82000**	**182**	3.08	4.73	7.69	11.8	54
3.58E+05	**82000**	**312**	3.63	5.05	9.09	12.6	39
4.95E+05	**82000**	**417**	3.92	5.47	9.8	13.7	40
6.33E+05	**82000**	**509**	4.47	5.6	11.2	14	25
7.72E+05	**82000**	**592**	4.58	5.95	11.5	14.9	30

The effect of heat treatment in N_2 on H_2 absorption kinetics and membrane surface morphology of Pd-Ag25 (wt%) foils is compared to heat treatment in air at 300 °C.

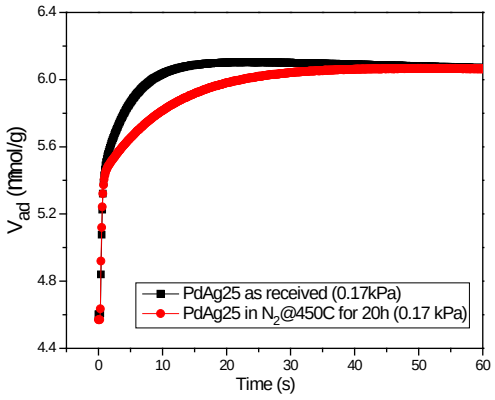

Figure 75. H_2 adsorption kinetics for the Pd-Ag membranes before and after N_2 heat treatment at 450 ºC for 20 h.

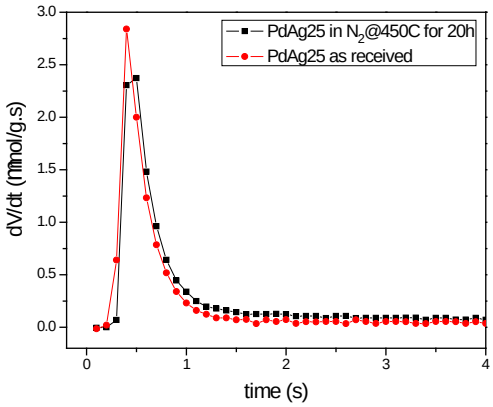

Figure 76. The rate of H_2 absorption for the Pd-Ag membranes before and after N_2 heat treatment at 450 ºC for 20 h.

Figure 75 shows the H_2 adsorption kinetics for the Pd-Ag membranes before and after N_2 heat treatment at 450 °C for 20 h with the equilibrium pressure of 170 Pa. All the kinetic tests were performed at 350 °C in this report. The equilibrium sorption amounts indicate that the H_2 solubility does not change after the N_2 heat treatment. However, the heat treatment slows down the sorption kinetics significantly. The time needed to reach equilibrium is about 40 seconds for the membrane after N_2 heat treatment, which is nearly doubled, compared to that of the as-received sample (Figure 75). The rate of absorption for the Pd-Ag membranes before and after N_2 heat treatment, as shown in Figure 76, demonstrates that the N_2 heat treatment affects the initial H_2 sorption rate on the membrane surface. The maximum hydrogen absorption rate of the N_2 heat-treated membrane is not as high as that of the as-received one. This indicates that the most significant difference for kinetics is at the very beginning of the absorption. The effect of N_2 heat treatment on sorption kinetics for Pd-Ag membranes is actually going in the opposite direction as the effect of heat treatment in air. The air oxidation accelerates the H_2 absorption kinetics rather than slowing it down (Figure 77). Moreover, for the membranes before and after air oxidation, the rate of absorption reached to the same highest value within the first 0.5 second. After reaching the highest point, the sorption rate decreases (absolute sorption amounts still increase), but the trend of the decline is different. Note that the sorption rate values after the decrease in rate are not zero, but small as the system moves toward absorption equilibrium. In Figure 78 (also in Figure 76), only the rate data of the first 4 seconds are shown to make a clear view for comparison. For the oxidized membrane, the sorption takes place at a higher rate than that of the as-received one for sorption time before 2.5 seconds. In other words, H_2 uptake increases more quickly for oxidized membrane toward final equilibrium within this time range.

For the oxidized membrane, the sorption rates are lower than the as-received one after 2.5 seconds since the equilibrium is almost reached.

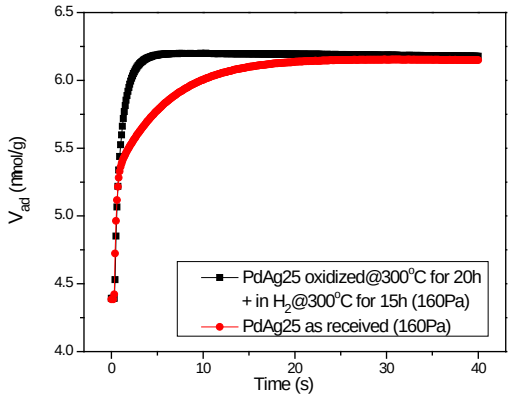

Figure 77. H_2 adsorption kinetics for the Pd-Ag membranes before and after air oxidation at 300 ºC for 20 h.

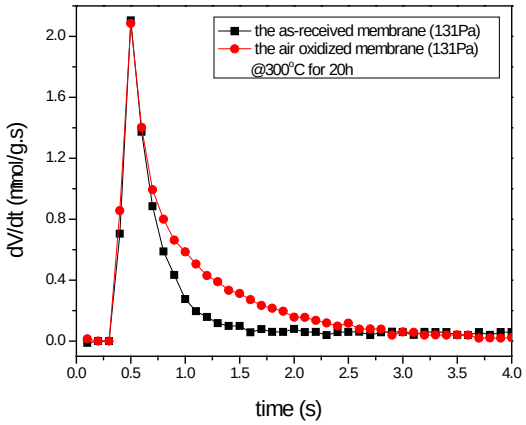

Figure 78. The rate of absorption for the Pd-Ag membranes before and after air oxidation at 300 °C for 20 h.

The similarity between heat treatment in air and nitrogen is that neither method changes the H_2 solubility in the Pd-Ag membranes. On the other hand, the change of H_2 absorption kinetics for the membranes does not vary with the following exposure of H_2. For the air oxidation, the heat treatment enhances both the sorption amounts and kinetics (Figure 79). The increase of sorption amounts is not permanent and can be recovered by H_2 exposure following the air oxidation (Figure 78), while the change of sorption kinetics is invariable. Similar kinetic results are also found for the membranes after N_2 heat treatment followed by an extended H_2 exposure at the same temperature (450 °C). There is little if any recovery of the kinetics for the membrane with the additional H_2 exposure. So the depression of H_2 absorption rate caused by N_2 heat-treatment at 450 °C (or the acceleration of H_2 absorption rate by air oxidation at 300 °C) is relatively stable.

Figure 81 shows SEM micrographs of the surface morphology for the as-received and heat treated membranes. There are some surface defects and rolling lines for the as-received Pd-Ag membrane (Figure 81a). After heat treatment in N_2 followed by H_2 exposure at 450 °C for 20 h, the membrane exhibits a relatively smoother and continuous surface as shown in Figure 81b. It seems that the surface defects, such as the pits and holes shown in Figure 81a, have been filled up by the heat treatment. On the contrary, for the membranes heat treated in air, a rougher surface is obtained and the size and density of surface defects are increased (Figure 81c). The surface morphology of the oxidized membrane actually develops into a pitted surface (Figure 81d) after exposure to hydrogen.

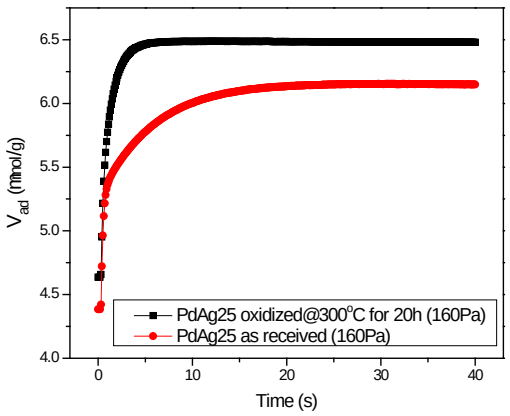

Figure 79. H_2 adsorption kinetics for the Pd-Ag membranes before and after air oxidation at 300 ºC for 20 h.

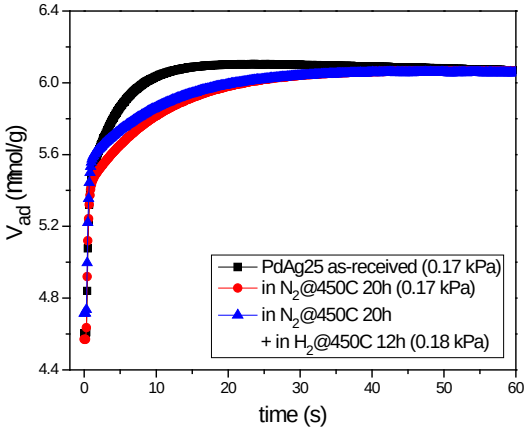

Figure 80. H_2 adsorption kinetics for the Pd-Ag membranes before and after N_2 heat treatment and further H_2 exposure.

Therefore, the absorption kinetics are thought to be the inherent reason for the H_2 permeation change after heat treatment in different atmospheres. For the oxidized membrane, the much quicker sorption equilibrium implies higher hydrogen diffusivity at the Pd-Ag membrane surface and higher transfer rate of atomic hydrogen from the surface/sub-surface to the membrane bulk that may be derived from the introduction of surface defects from oxidation that increase the sorption rate into the membrane. For the membranes heat treated in N_2, the depressed sorption kinetics and equilibrium lead to the lower transfer rate of atomic hydrogen and lower hydrogen diffusivity at the membrane surface, due possibly to the filling of the surface defects. The effect of N_2 may simply be due to annealing of the surface.

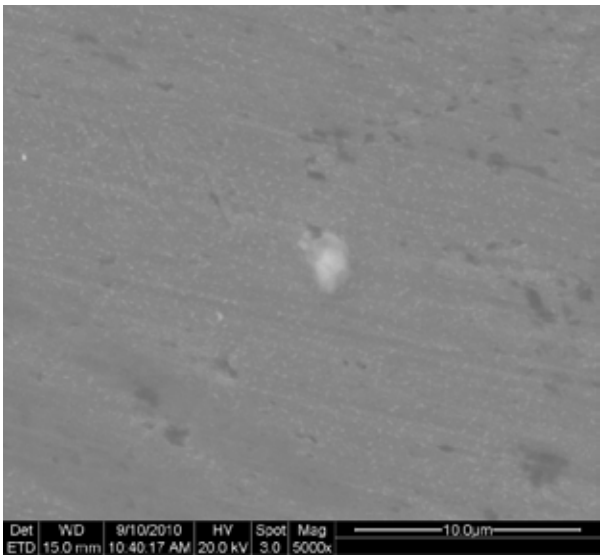

Fig.81a

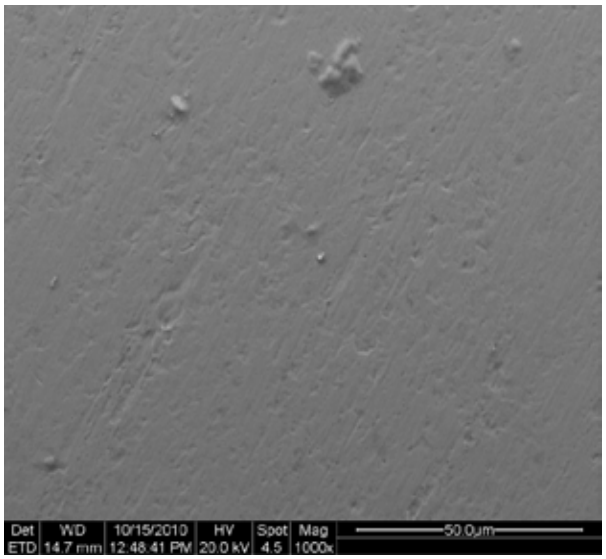

Fig.81b

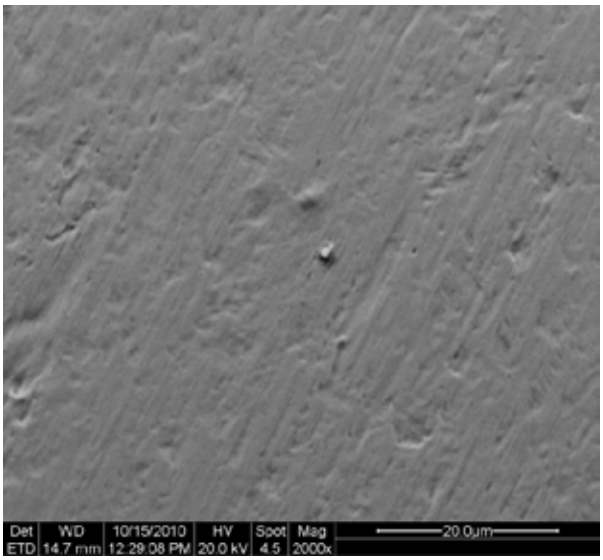

Fig 81c

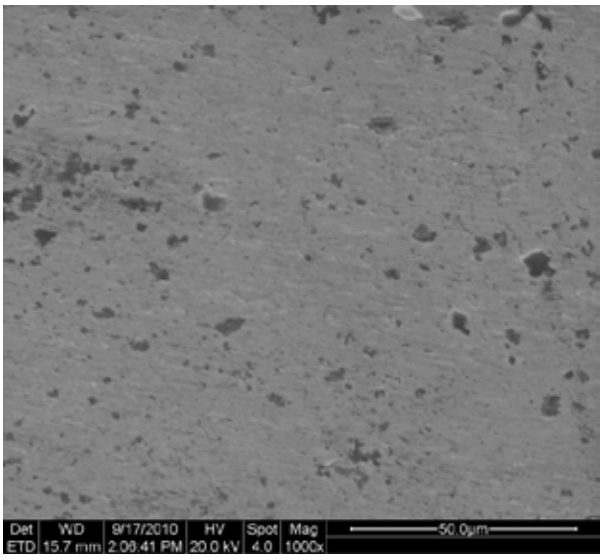

Fig.81d

Figure 81. SEM images of the cold-rolled PdAg25 membranes. The as-received foil is shown in 81a, after heat treatment in N_2 in 81b, 81c shows the foil after oxidation, and 81d is the surface of the oxidized foil after exposure to H_2.

Three sputtered foils, Pd-172, Pd-176, and Pd-181 were examined by EDS to determine their compositions. Thickness was then calculated using measured compositions, areas, and the weights of films. The compositions are listed in Table 18.

Table 18. Alloy compositions of sputtered foils as measured by EDS

Membrane	Side A composition (wt%)	Side B composition (wt%)	Mean composition (wt%)	Thickness (μm)
Pd-172	$Pd_{93}Ru_7$	$Pd_{91}Ru_9$	$Pd_{92}Ru_8$	29.9
Pd-176	$Pd_{72}Cu_{14}Au_{14}$	$Pd_{72}Cu_7Au_{21}$	$Pd_{72}Cu_{11}Au_{17}$	26.6
Pd-181	$Pd_{93}Tm_7$	$Pd_{93}Tm_7$	$Pd_{93}Tm_7$	33.6

The Pd-Tm alloy was unusually sensitive to low-temperature hydrogen embrittlement, rupturing when high pressure hydrogen was applied at 350 or 300°C, as well as when kept under high H_2 pressures at 773 K for significant amounts of time, such as overnight. One plausible explanation for this would be the presence of incompletely alloyed or segregated thulium, which forms a hydride phase at temperatures substantially greater than the 567 K of palladium (Figure 82). This hydride phase, TmH_2, has a lattice parameter of 5.0915 Å compared to 3.589 Å for thulium, 3.895 Å for palladium, and 4.03 Å for palladium hydride.

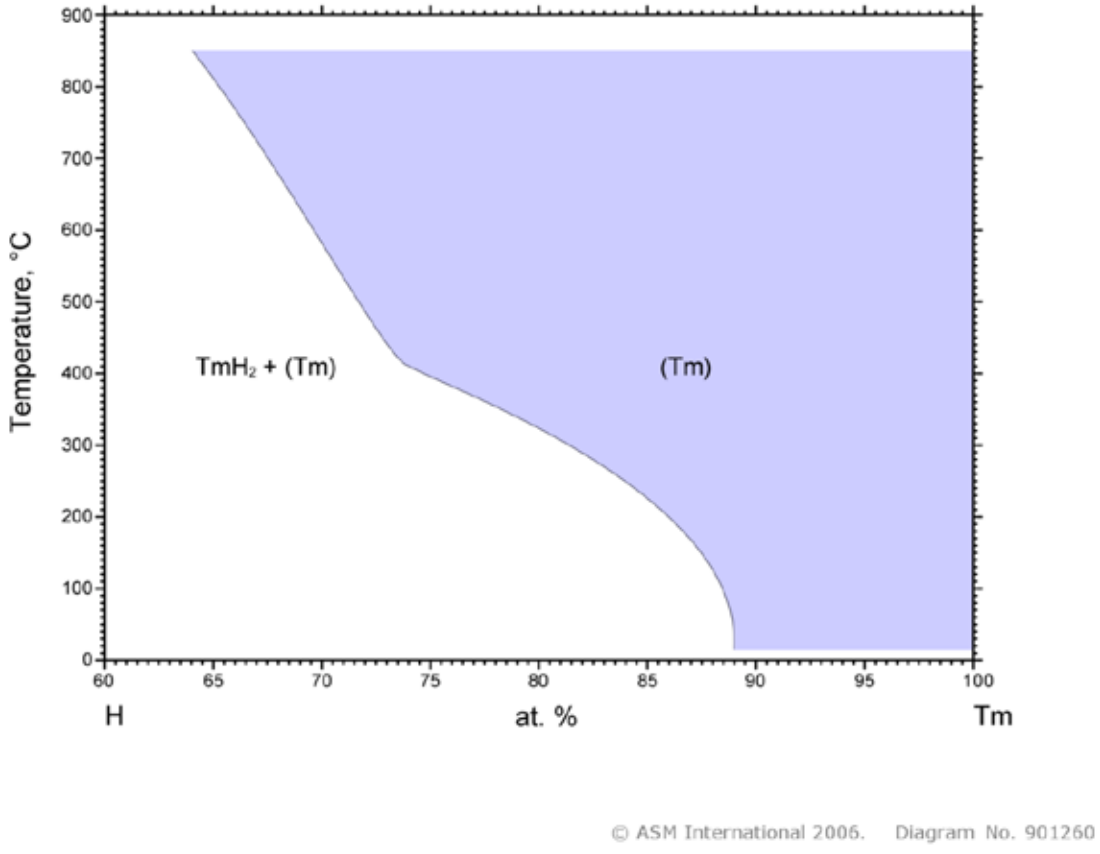

Figure 82. Phase diagram for the thulium-hydrogen system from ASM International [14].

Despite this, it was possible to take some hydrogen measurements in a leak-free regime between 673-773 K. In this temperature region, the Pd-Tm membrane was extremely hydrogen permeable, having approximately 140% of the permeability of pure palladium at 673 K.

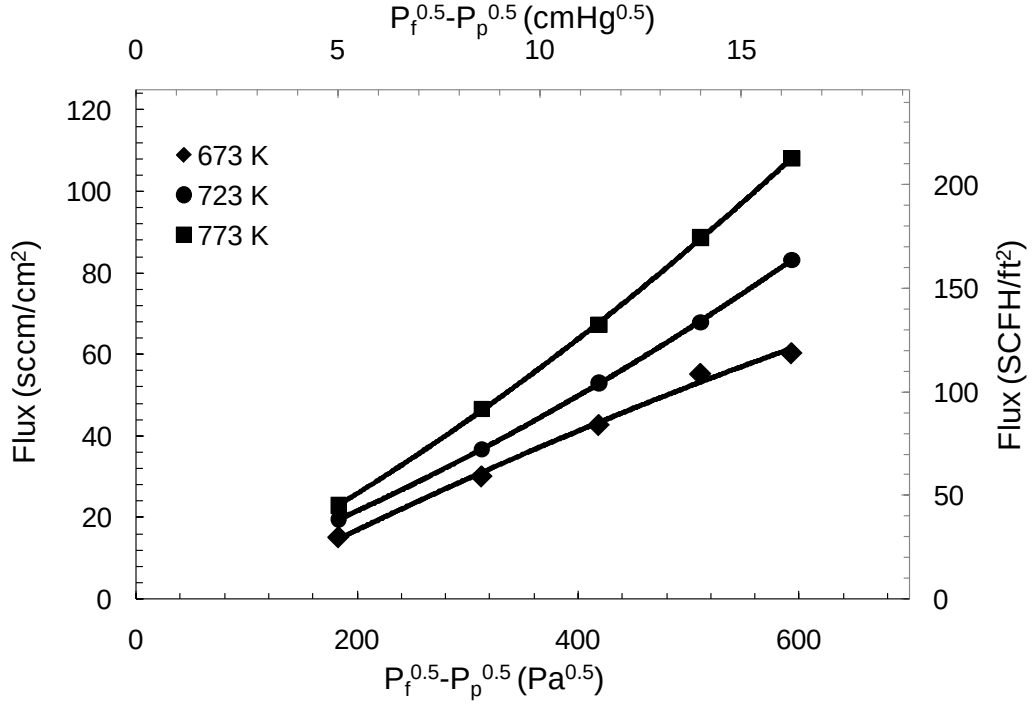

Figure 83. Hydrogen flux as a function of pressure gradient for a 33.6 μm thick $Pd_{93}Tm_7$ membrane (Pd-181).

Conversely, the PdCuAu ternary alloy tended to fail at higher temperatures (723-773 K), for more opaque reasons not immediately apparent from the phase diagram. However, it was successfully tested in the temperature range from 573-723 K (Figure 84).

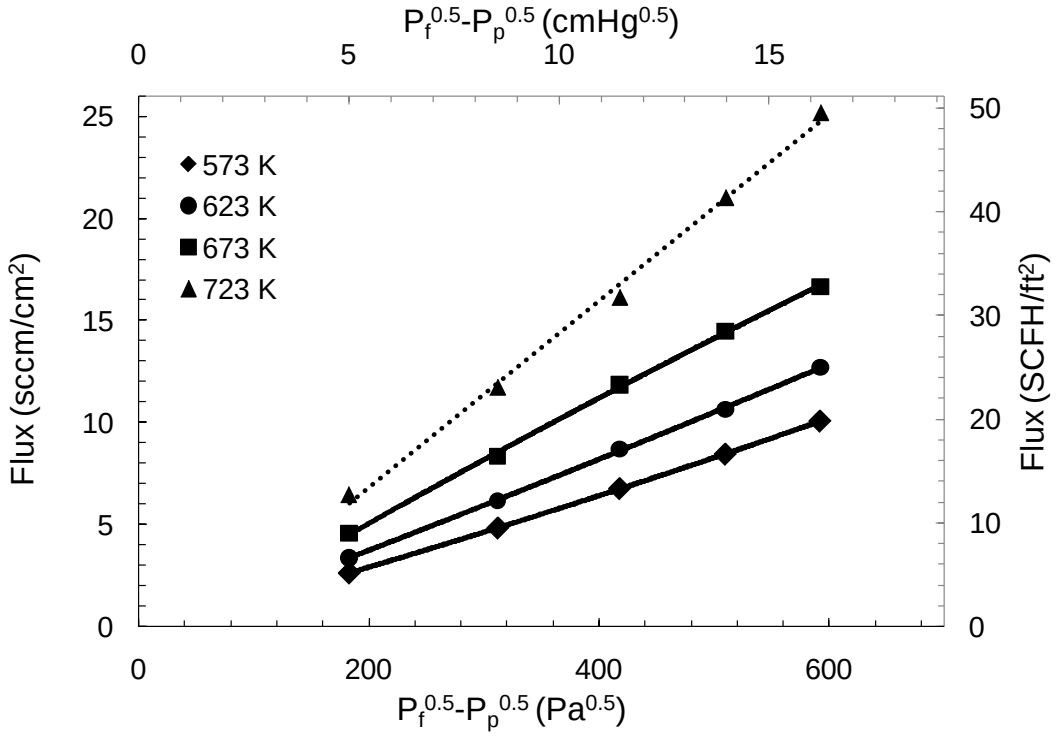

Figure 84. Hydrogen flux as a function of pressure gradient for a 26.6 μm thick $Pd_{72}Cu_{11}Au_{17}$ membrane (Pd-176).

This ternary alloy membrane performed very similarly to Pd-95, the previous best ternary alloy (Figure 84). Its permeability was approximately 1/3 of the pure Pd permeability at 673 K. In Figure 85, the permeability of the PdTm sample is compared to the PdCuAu alloys.

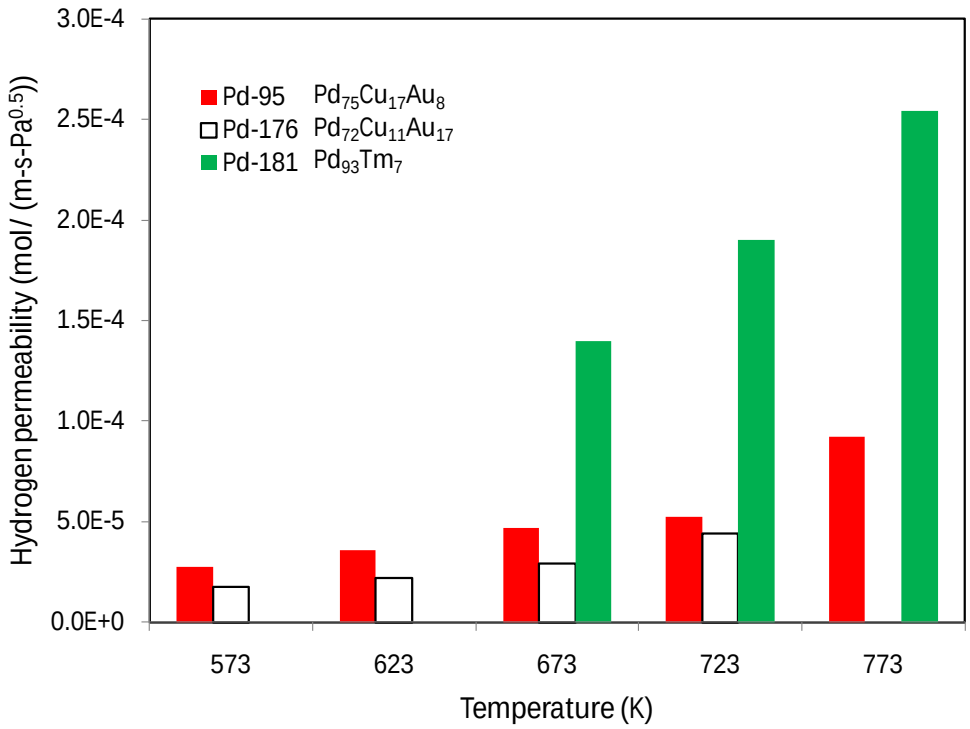

Figure 85. Hydrogen permeability as a function of temperature for sputtered alloy membranes.

3.3 Ternary Pd Membranes

The first ternary alloys fabricated were PdCuAg and CSM designed an experiment to investigate whether the addition of Ag to PdCu would increase the hydrogen permeability. Given potential questions about temperature, support effects, feed gas, etc., a side by side test was determined to provide the most persuasive test. Consequently, a side by test pure gas permeation test of $Pd_{86}Cu_{14}$ binary alloy Pd-23 and $Pd_{80}Cu_{16}Ag_4$ ternary alloy Pd-34 was initiated. This means that both samples were run at the same time, in the same furnace, with the same support, the same feed gases. The preliminary results, shown as a function of time, are shown in Figures 86. Essentially, the ternary PdCuAg alloy membrane Pd-34 has twice the hydrogen permeability as the PdCu binary. It is common for fluxes to decline somewhat after air oxidations, so this ratio could change over time.

Permeability normalizes the flux for the partial pressure gradient, which is the driving force divided by the membrane thickness. So, as you would expect, the flux for both membranes is about the same, but the thickness of the ternary alloy is twice that of the binary alloy foil.

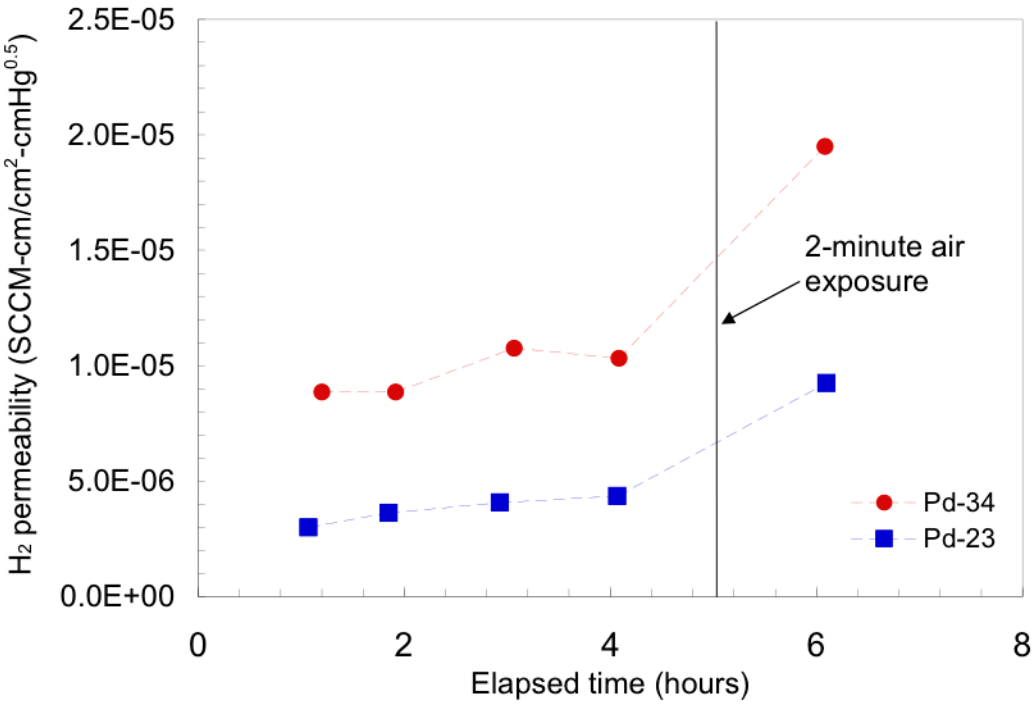

Figure 86. The influence of time on the pure hydrogen permeabilities of ternary alloy Pd-34 and binary alloy Pd-23 at 673 K and 32 psia feed pressure (2.2 bar absolute).

CSM conducted pure gas permeation tests with ternary membrane Pd-32 over the temperature range from 200 ºC to 400 ºC with hydrogen and nitrogen. Feed pressures varied from 5 to 20 psig (17 to 32 psia in Golden, CO where the ambient pressure is ~12 psia). Results of these tests are summarized in the table below.

Table 19. PdCuAg permeability

Foil	T.K	H_2 Permeability (cm^3(STP).cm/ cm^2.s.$cmHg^{0.5}$)
Pd-32	473	4.25×10^{-6}
	523	6.75×10^{-6}
	573	9.66×10^{-6}
	623	1.36×10^{-5}
	673	1.79×10^{-5}

The permeability of a binary $Pd_{86}Cu_{14}$ foil and a ternary $Pd_{80}Cu_{16}Ag_4$ foil were measured at 200, 250, 300, 350, and 400 ºC. The following table shows the data collected for each system.

Table 20. PdCu and PdCuAg permeability

	SWRI Pd-23a ($Pd_{86.2}Cu_{13.8}$)					SWRI Pd-34a ($Pd_{79.6}Ag_{3.9}Cu_{16.5}$)				
	Permeability (cm^3(STP)-cm/cm^2-s-$cmHg^{0.5}$)					Permeability (cm3(STP)/cm/cm2-s-cmHg0.5)				
T	H_2	N_2	Leak-corrected H_2 (Knudsen)	best n-value	Ideal H_2/N_2 selectivity	H_2	N_2	best n-value	Ideal H_2/N_2 selectivity	Permeability ratio (Pd-34/Pd-23)
200 C	3.34E-06	1.16E-07	2.90E-06	0.89	29	3.50E-06	0	1.11	>420	1.21
250 C	4.68E-06	1.04E-07	4.29E-06	0.72	45	5.30E-06	0	0.56	>640	1.24
300 C	7.41E-06	1.01E-07	7.03E-06	0.57	74	7.60E-06	0	0.98	>920	1.08
350 C	9.22E-06	7.27E-08	8.94E-06	0.66	127	1.09E-05	0	1.12	>1320	1.22
400 C	1.25E-05	9.34E-08	1.22E-05	0.81	134	1.48E-05	0	0.66	>1790	1.21
Ea (J/mol)	19044.7					20637.65425				
Pre-exponential factor (mol/m-s-Pa0.5)	4.43E-08					3.84E-08				

Adding a small amount of Ag appears to improve the permeability of the PdCu binary alloy, although the observed increase is less dramatic than predicted by theory for similar compositions. Theory suggests that the permeability ratio will increase as T is lowered – this was not observed experimentally.

Extended duration pure gas permeation experiments were performed with the ternary PdCuAg alloy foil sent to CSM from SwRI. The support was a Mott porous stainless steel disk that was oxidized at 600 ºC for 12 hours to produce an oxide film which helps prevent intermetallic diffusion. Samples of 25 mm diameter were cut and weighed, and the SwRI composition was used to estimate thickness.

The ternary alloy membrane Pd-28 had no detectable N_2 leak at the beginning of the test after the foil was mounted in the permeation cell at room temperature. However, as soon as the cell was heated to the test temperature of 400 ºC, it had developed a significant leak. Unfortunately, this is a common observation for very thin foils. In general, the average ideal H_2/N_2 selectivity at 400 ºC was quite low, approximately 37. Given the high leak rate, the permeabilities should be viewed as preliminary. Assuming all of the N_2 permeated via a Knudsen diffusion mechanism, the corrected H_2 permeability at 400 ºC would be 1.6 x 10^{-5} cm^3(STP).cm/ cm^2.s.$cmHg^{0.5}$ = 2 x 10^{-9} mole.m/m^2.s.$Pa^{0.5}$. This value is roughly 16% of the permeability previously measured for pure Pd foils at 400 ºC. An estimate of the corrected hydrogen permeability at 350 ºC is 8 x 10^{-6} cm^3(STP).cm/ cm^2.s.$cmHg^{0.5}$.

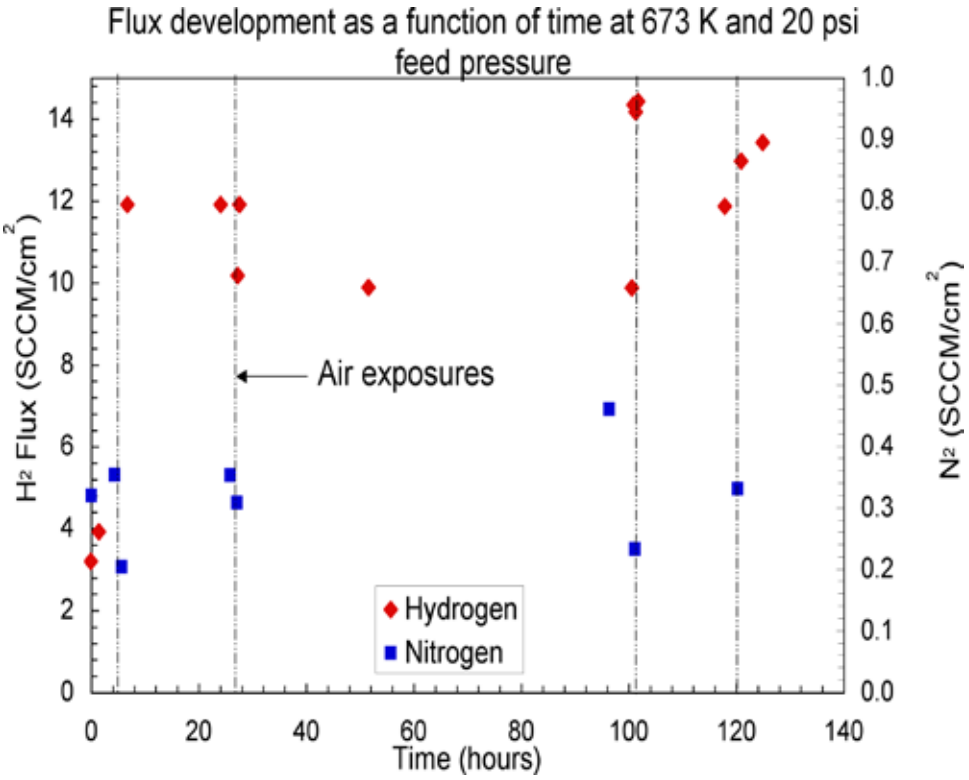

Figure 87. The influence of time on the pure hydrogen and nitrogen fluxes for PdCuAg membrane Pd-28 at 673 K and 32 psia feed pressure (2.2 bar absolute).

The H_2 permeability value at 673 K for the $Pd_{70}Cu_{30}$ membrane (PdCu-1) was 2.3 x 10^{-5} cm^3(STP).cm/ cm^2.s.$cmHg^{0.5}$ so the permeability of the ternary foil is less, and that difference is probably greater than the error in the measurements. The ternary foil has about 10% of the hydrogen permeability of $Pd_{85}Ag_{15}$ membrane Pd-25.

Historically CSM has found that free-standing foil membranes become much easier to handle, cut, and mount in permeation cells when their thickness is greater than or equal to 7 microns. It

is quite difficult to handle foil membranes that are less than 5 microns in thickness. A decision was therefore made to increase film thickness in future experiments.

The influence of temperature and driving force on the pure hydrogen fluxes of Pd-28 is shown in Figure 88. The fluxes were a reasonably strong function of temperature, with the values at 673 K, approximately 1.7 times larger than at the lower temperature.

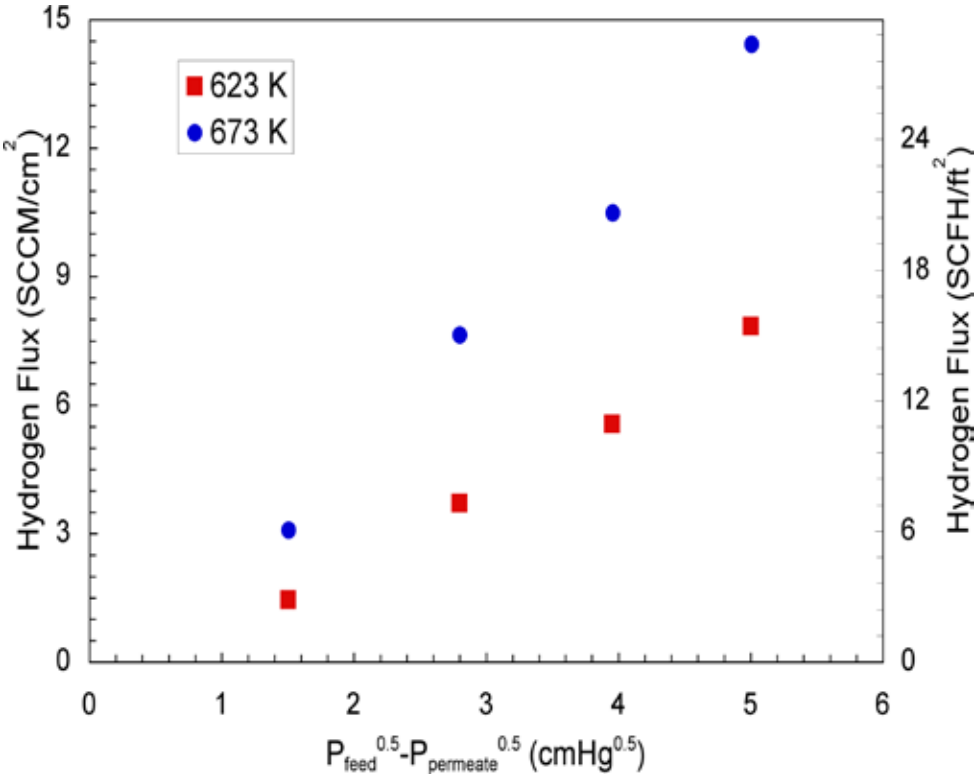

Figure 88. The influence of feed pressure and temperature on the pure hydrogen pressure for PdCuAg membrane Pd-28. Tests were performed at 5, 10, 15, and 20 psig feed pressure.

For the increased thickness of the subsequent batch of PdCuAg ternary alloy foil samples, the selectivity of the 8.5 micron thick PdCuAg sample Pd-34 was much higher than those recently reported for thinner samples.

Pure gas permeation experiments were performed with Pd ternary alloy foil sample Pd-32. Membrane Pd-32 was tested for approximately 100 hours as a function of both temperature (200 – 400 ºC) and feed pressure (5 to 20 psig). The permeation data are shown in Figure 89. A two minute oxidation treatment was performed at each temperature. The thermal history of the membrane is that it was heated in N_2 to 400 ºC, and then the permeation tests began. At this initial temperature of 400 ºC, the air oxidation had a small effect. However, upon cooling to 350 ºC, the H_2 flux essentially doubled after the oxidation. No other flux increases were observed after oxidations at other temperatures. To check for any temperature hysteresis, the membrane was once again heated to 400 ºC and at the end of the experiment and the flux was

about twice that originally measured. As might be expected, there was a monotonic drop in hydrogen flux as temperature decreased from 350 to 200 ºC. No nitrogen leak was detected during the permeation testing of membrane Pd-32.

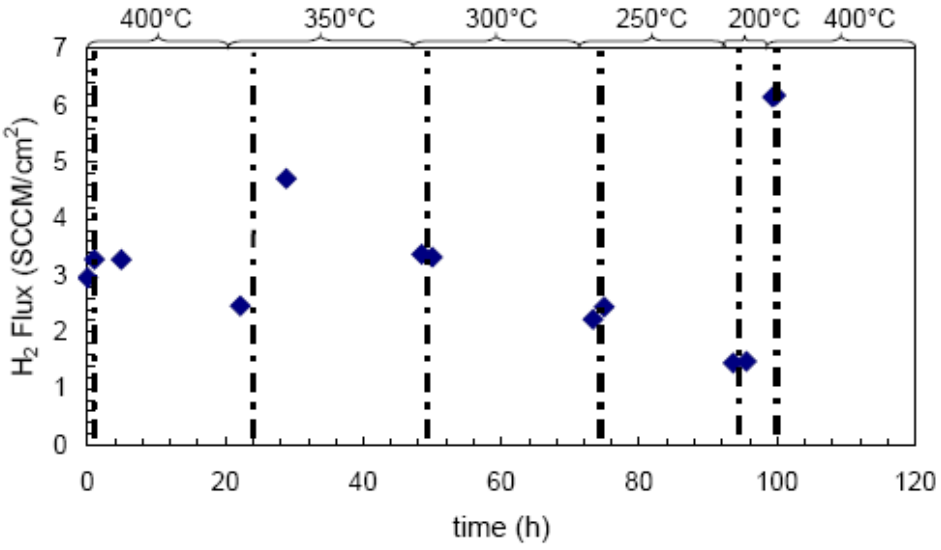

Figure 89. The influence of time and temperature on the pure hydrogen and nitrogen fluxes for ternary alloy membrane Pd-32 at 673 K and 32 psia feed pressure (2.2 bar absolute).

The influence of partial pressure driving force on the pure hydrogen flux through ternary alloy membrane Pd-32 is shown in Figure 90 at the five measurement temperatures. A pressure exponent, or n-value of 0.5 appears to give a good linear correlation of the flux.

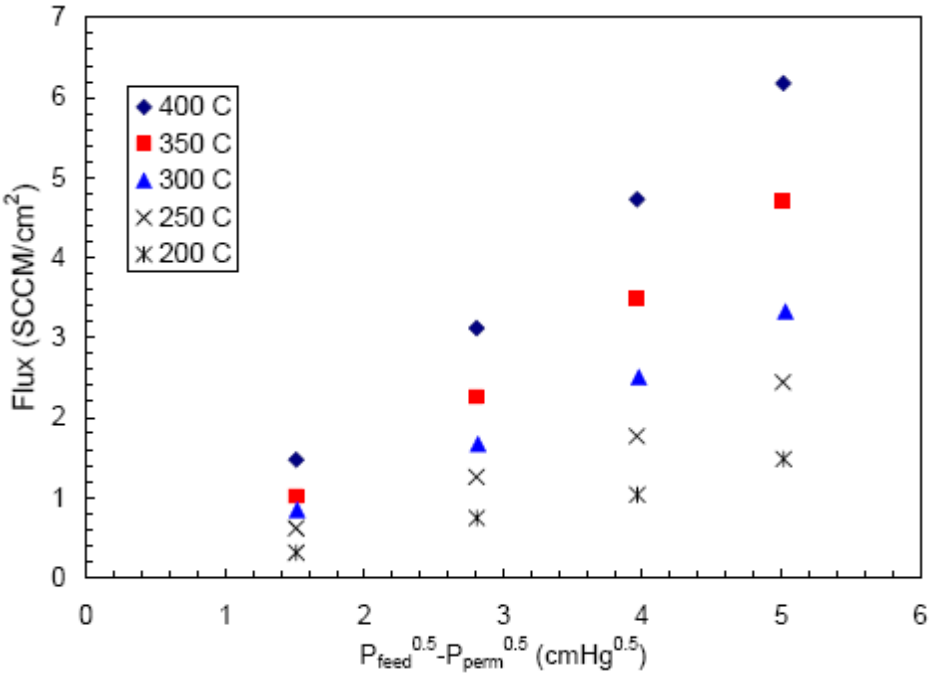

Figure 90. The influence of feed pressure and temperature on the pure hydrogen pressure for ternary alloy membrane Pd-32. Tests were performed at 5, 10, 15, and 20 psig feed pressure at five temperatures.

A total of four ternary alloy membranes, Pd-50, Pd-51, Pd-53, and Pd-54 were examined prior to permeation testing by XRD and standardless EDS. The membranes were generally 1-2 microns thicker than their nominal thickness, and somewhat enriched in palladium from their nominal composition. There was, particularly in the PdCuPt membranes, a significant variation in composition across the membrane thickness.

Table 21. Ternary alloy compositions

Membrane	Pd-50	Pd-51	Pd-53	Pd-54
Thickness (nominal, mm)	10	10	Not given	10
Thickness (gravimetric, mm)	11.5	11.5	11.6	12.0
Composition (nominal, wt%)	$Pd_{75}Cu_{17}Au_{8}$	$Pd_{75}Cu_{17}Au_{8}$	$Pd_{67.6}Cu_{24.4}Pt_{8}$	$Pd_{78.7}Cu_{17.6}Pt_{3.7}$
Composition (EDS, Side A, wt%)	$Pd_{79.5}Cu_{12.2}Au_{8.3}$	$Pd_{81.2}Cu_{10.3}Au_{8.5}$	$Pd_{78.3}Cu_{16.7}Pt_{5}$	$Pd_{86.4}Cu_{12.8}Pt_{0.8}$
Composition (EDS, Side B, wt%)	$Pd_{75.3}Cu_{17.8}Au_{6.9}$	$Pd_{77.3}Cu_{15.1}Au_{7.6}$	$Pd_{85.6}Cu_{10}Pt_{4.4}$	$Pd_{89.7}Cu_{7.68}Pt_{2.58}$
Lattice Parameter (FCC, side A, Å)	3.8313	3.8518	3.8589	3.8397
Lattice Parameter (FCC, side B, Å)	3.8282	3.8446	3.8471	3.8579

A total of four ternary alloy membranes, Pd-50, Pd-51, Pd-53, and Pd-54 were examined. All four membranes consisted primarily of an FCC lattice with lattice parameters slightly less than that of pure palladium (Cu[3.6148 Å]<Pd[3.8908 Å]<Pt[3.9240 Å] <Au[4.0786 Å]). The diffractograms were all dominated by the <111> reflection, with no other reflection having even 5% of its intensity. This points to significant preferential orientation within the foil. Membranes Pd-53 and Pd-54 also contained a single additional peak corresponding to the Pt-<111> position, suggesting that some metallic platinum is incompletely incorporated into the lattice. This peak is small, and occurs on only one side of each membrane, perhaps implying a surface phase.

Membranes were mounted in a stainless-steel test housing with porous stainless supports and alumina paper diffusion barriers, and tested under single-gas N_2 and H_2 at feed pressures ranging from 12-92 psia, with ambient pressure (12 psia in Golden, Colorado) on the permeate side. Membrane Pd-51 failed during heating. The maximum temperature tested was 773 K, after which the membranes were cooled and retested in 50 K increments until failure. H_2 flux vs. T is shown in Figure 91.

Membranes 50, 53, and 54 were all leak-free at temperatures above 423 K, and membrane 54 remained leak-tight for a full two hours at room temperature with 40 psig H_2 on its feed side. Hydrogen permeabilities, P, were fit with a linear Arrhenius relationship, and the resulting activation energies (E_a) and pre-exponential factors (k_o) shown below.

Table 22. Ternary alloy thermodynamic values

Membrane	E_a (J/mol)	k_0 (mol/m/s/$Pa^{0.5}$)
Pd-50	20165	$1.46*10^{-7}$
Pd-53	22814	$2.38*10^{-7}$
Pd-54	18082	$9.94*10^{-8}$

All three tested membranes had hydrogen permeabilities in the range of 35% of that of pure palladium. N-values, relating H_2 flux to pressure gradient, were between 0.5 and 0.7 for all temperatures above 473ºK, indicating that the rate-limiting step in hydrogen transport is bulk diffusion in this temperature regime.

CSM tested Membrane Pd-51 for a total of 163 hours under operating conditions. The maximum temperature tested was 773 K, after which the membranes were cooled and retested in 50 K increments until failure.

Table 23. PdCuAu and PdCuPt compositions

Membrane	Pd-50	Pd-51	Pd-53	Pd-54
Thickness (nominal, mm)	10	10	Not given	10
Thickness (gravimetric, mm)	11.5	11.5	11.6	12.0
Composition (nominal, wt%)	$Pd_{75}Cu_{17}Au_8$	$Pd_{75}Cu_{17}Au_8$	$Pd_{67.6}Cu_{24.4}Pt_8$	$Pd_{78.7}Cu_{17.6}Pt_{3.7}$
Composition (Side A, wt%)	$Pd_{79.5}Cu_{12.2}Au_{8.3}$	$Pd_{81.2}Cu_{10.3}Au_{8.5}$	$Pd_{78.3}Cu_{16.7}Pt_5$	$Pd_{86.4}Cu_{12.8}Pt_{0.8}$
Composition (Side B, wt%)	$Pd_{75.3}Cu_{17.8}Au_{6.9}$	$Pd_{77.3}Cu_{15.1}Au_{7.6}$	$Pd_{85.6}Cu_{10}Pt_{4.4}$	$Pd_{89.7}Cu_{7.68}Pt_{2.58}$
Lattice Parameter (FCC, side A, Å)	3.8313	3.8518	3.8589	3.8397
Lattice Parameter (FCC, side B, Å)	3.8282	3.8446	3.8471	3.8579

Membranes 50, 51, 53, and 54 were all leak-free at temperatures above 423 K. Pd-51 remained leak-free until it had cooled to approximately 394 K. Membrane Pd-54 remained leak-tight for a full two hours at room temperature with 40 psig H_2 on its feed side, suggesting this alloy is quite resistant to hydrogen embrittlement. Hydrogen permeabilities, P, were fit with the previously mentioned linear Arrhenius relationship, and the resulting activation energies (E_a) and pre-exponential factors (k_o) are given below.

Table 24. Ternary alloy thermodynamic values #2

Membrane	E_a (J/mol)	K_0 (mol/m/s/$Pa^{0.5}$)
Pd-50	20165	$1.46*10^{-7}$
Pd-51	20206	$1.33*10^{-7}$
Pd-53	22814	$2.38*10^{-7}$
Pd-54	18082	$9.94*10^{-8}$

N-values, relating H_2 flux to pressure gradient, were between 0.5 and 0.7 for all temperatures above 473 K, indicating that the rate-limiting step in hydrogen transport is bulk diffusion in this temperature regime. However, the n-values increased sharply to 0.93 at 423 K, suggesting that significant surface limitations to flux arise at this low temperature.

Figure 91 compares the hydrogen fluxes of the latest Pd-Cu-Au (50 and 51) and Pd-Cu-Pt (53 and 54) membranes. All of the ternary alloys are fairly similar in permeation performance with H_2 permeabilities about 30% that of pure Pd. Gade et al. compared free-standing Pd foils prepared by both electroless plating and cold-rolling over the thickness range of 7 to 25 μm[7]. The agreement between Gade's permeation measurements and the predictions made by Morreale et al. from the literature was excellent. At 673 K, the flux through a 10 micron pure Pd foil at 220 kPa H_2 feed pressure was ~ 30 cm^3/cm^2.min, compared to about 8 cm^3/cm^2.min for the four foil samples tested.

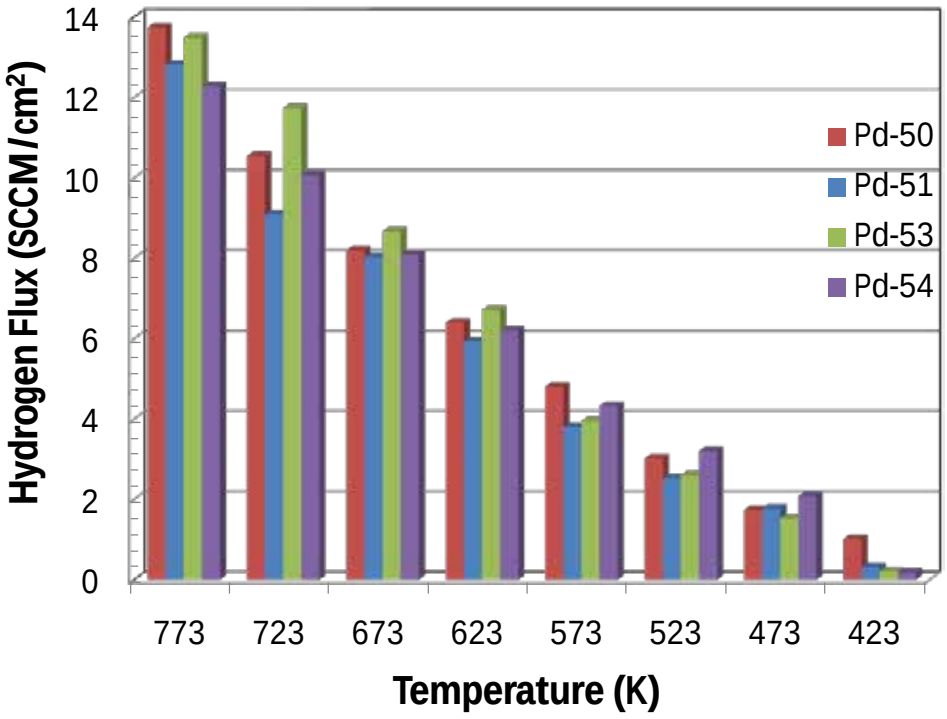

Figure 91. Hydrogen flux at 220 kPa (32 psia) feed, 83 kPa (12 psia) permeate pressure, as a function of temperature for Pd-Cu-Au (50 and 51) and Pd-Cu-Pt (53 and 54) membranes.

SwRI fabricated and shipped samples including PdCu binary and PdCuY and PdCuPt ternary alloys. None of the membranes had any detectable nitrogen leakage under the conditions tested. The n-values relating pressure to hydrogen flux were generally between 0.5 and 0.75, suggesting that the rate limiting step in transport was bulk diffusion. Hydrogen permeability as a function of temperature is summarized in Figure 92. Membrane Pd-62 is the first binary PdCu membrane tested by CSM in the composition range of 70-80 wt% Pd, and it had significantly lower hydrogen permeability than ternary alloys with either Au or Pt. Membrane Pd-75, which contained 13% Au, had higher permeability than any previously tested ternary alloy membrane: approximately 45% that of pure Pd at 673 K and 38% that of pure Pd at 623 K[1]. Membrane Pd-79, which contained 8% Ni, had H_2 permeability very similar to the PdCu binary system.

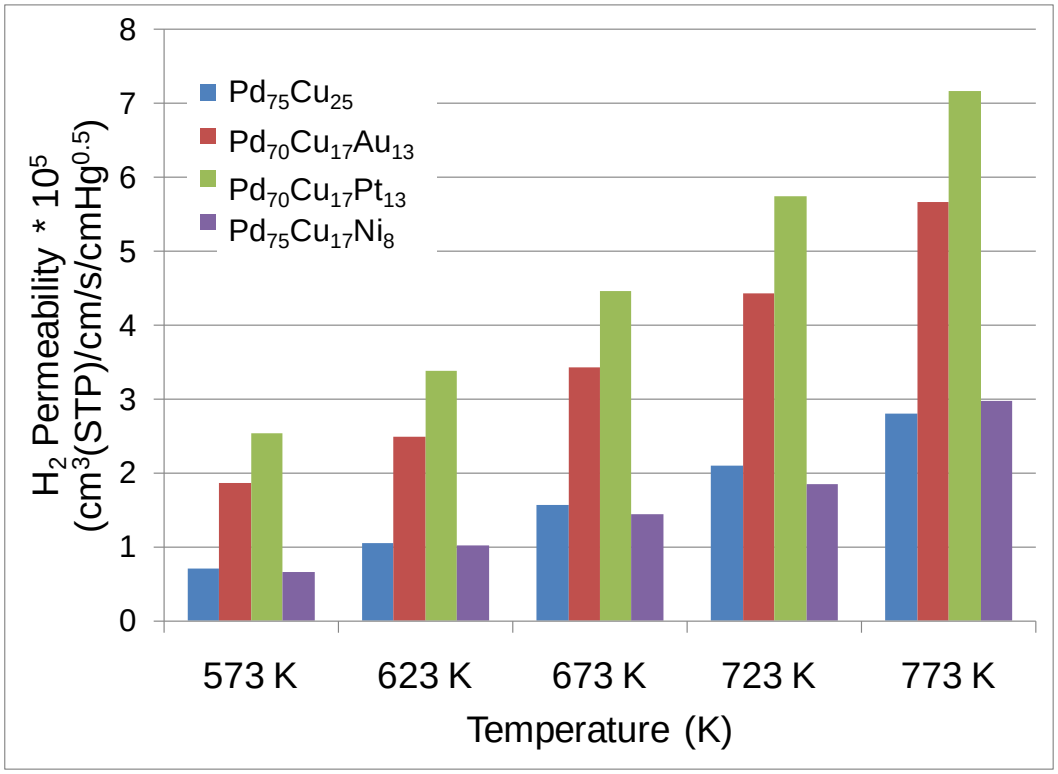

Figure 92. Hydrogen permeability at as a function of temperature for binary $Pd_{75}Cu_{25}$ (Pd-62) and ternary $Pd_{70}Cu_{17}Pt_{13}$ (Pd-67), $Pd_{70}Cu_{17}Au_{13}$ (Pd-75), and $Pd_{75}Cu_{17}Ni_8$ (Pd-79) foils.

The H_2 permeabilities, were fit with a linear relationship which was used to calculate the Arrhenius activation energies and preexponential factors. The results are summarized in the following table:

Table 25. Activation energies and preexponential factors for hydrogen permeability.

Membrane	$\mathbb{P}_0$ (Mol/m/s/Pa$^{0.5}$)	Ea (J/mol)
Pd-62	$1.82 * 10^{-7}$	25565
Pd-67	$1.70 * 10^{-7}$	20673
Pd-75	$1.72 * 10^{-7}$	19215
Pd-79	$2.06 * 10^{-7}$	26497

In the next batch, the binary Pd-Ru membrane (Pd-84) had the highest H_2 permeability in the temperature range from 573-673 K, but at higher temperatures the low-copper ternary $Pd_{83}Cu_5Au_{12}$ (Pd-95) surpassed it. Membrane Pd-95 is approximately 57% of the permeability

of Pure Pd at 673 K and 45% at 623 K. Pd-89, the ternary alloy with Cu and Ru ($Pd_{88}Cu_4Ru_8$), was the first sample of this alloy tested at CSM. Its permeability was found to be lower than ternary alloys of gold or platinum, but higher than nickel alloys. A comparison of the highest-permeability materials for ternary systems is shown in Figure 93.

Table 26. Activation energies and preexponential factors for hydrogen permeability.

Membrane	$\mathbb{P}_0$ (Mol/m/s/Pa$^{0.5}$)	Ea (J/mol)
Pd-74	$1.23 * 10^{-7}$	15681
Pd-84	$1.12 * 10^{-7}$	14764
Pd-89	$8.43 * 10^{-8}$	18789
Pd-95	$3.55 * 10^{-7}$	20759

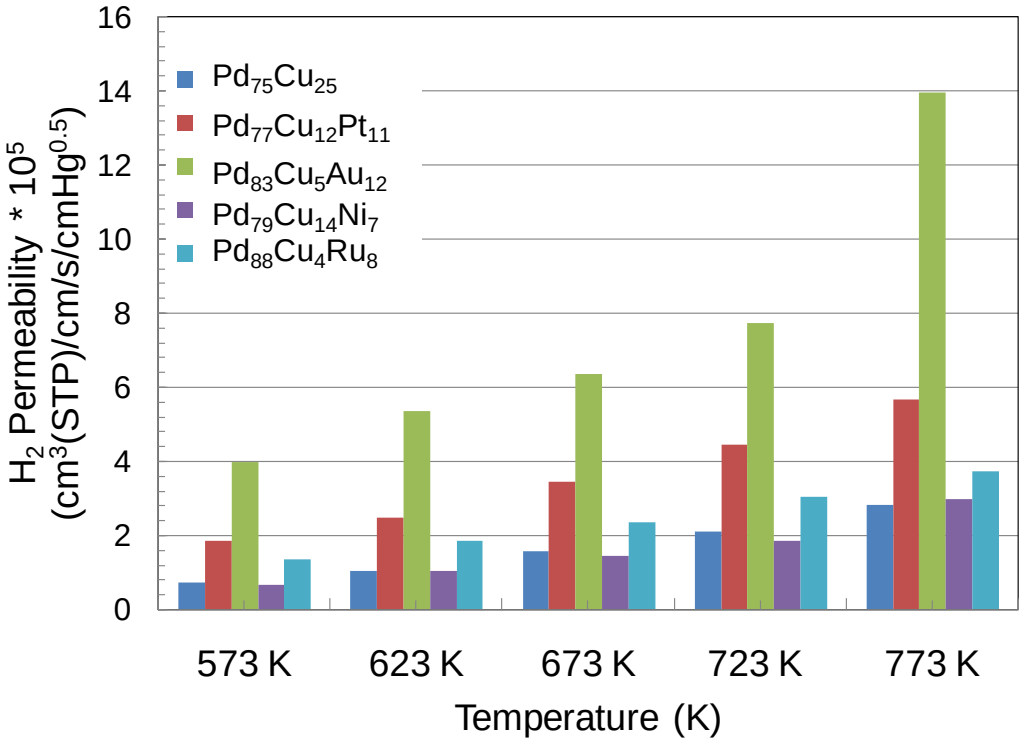

Figure 93. Hydrogen permeability at as a function of temperature for binary $Pd_{75}Cu_{25}$ (Pd-62) and ternary $Pd_{77}Cu_{12}Pt_{11}$ (Pd-67), $Pd_{83}Cu_5Au_{12}$ (Pd-75), $Pd_{79}Cu_{14}Ni_7$ (Pd-79), and $Pd_{88}Cu_4Ru_8$ (Pd-89) foils.

Ternary alloys of PdCu with Au have consistently demonstrated higher hydrogen permeabilities than systems with Pt, Ni, and Ru. Figure 94 summarizes the results of experiments on PdCuAu alloy materials. As a general trend, higher gold content and lower copper content lead to higher hydrogen permeability.

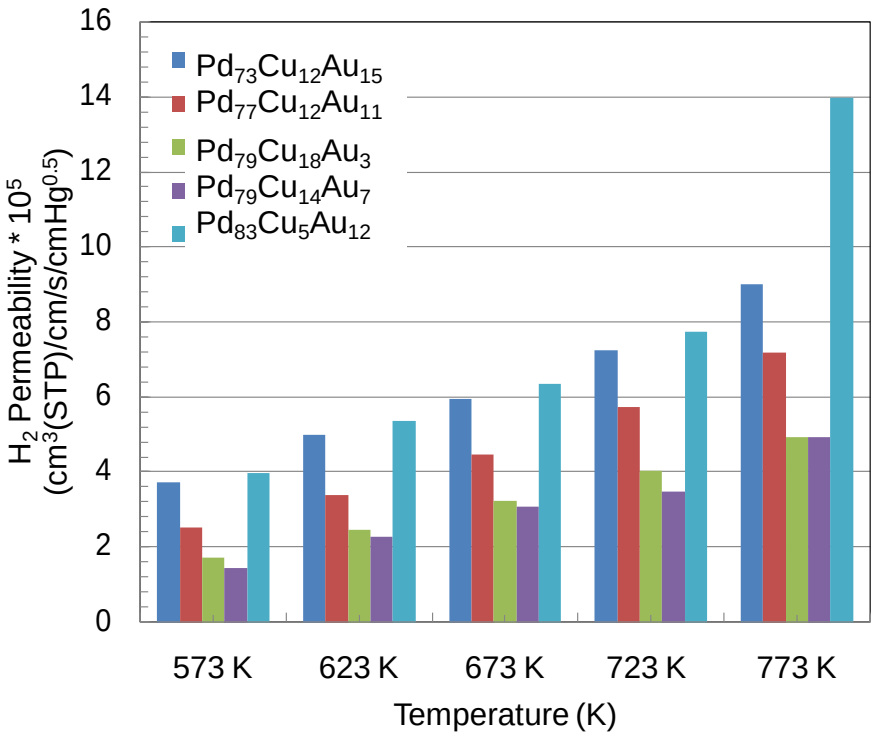

Figure 94. Hydrogen permeabilities as a function of temperature for PdCuAu ternary alloys (compositions given in wt%)

CSM characterized the ternary alloy membrane Pd-93 by EDAX to determine composition which is shown in the table below.

Table 27. PdAuCu compositions

Membrane	SwRI-93
Side A	$Pd_{85}Au_{12.5}Cu_{2.5}$
Side B	$Pd_{85.5}Au_{12.2}Cu_{2.3}$

Membrane Pd-93 is approximately 70% of the permeability of pure Pd at 673 K and 67% at 623 K. A summary of ternary PdCuAu alloy pure hydrogen permeabilities is given in Figure 95.

Table 28. Activation energies and preexponential factors for hydrogen permeability.

Membrane	P_0 (Mol/m/s/$Pa^{0.5}$)	Ea (J/mol)
Pd-85	$1.80 * 10^{-8}$	9411
Pd-93	$2.81 * 10^{-7}$	18891
Pd-99	$4.24 * 10^{-7}$	34355
Pd-101	$2.25 * 10^{-7}$	29666
Pd-102	$3.54 * 10^{-8}$	18365

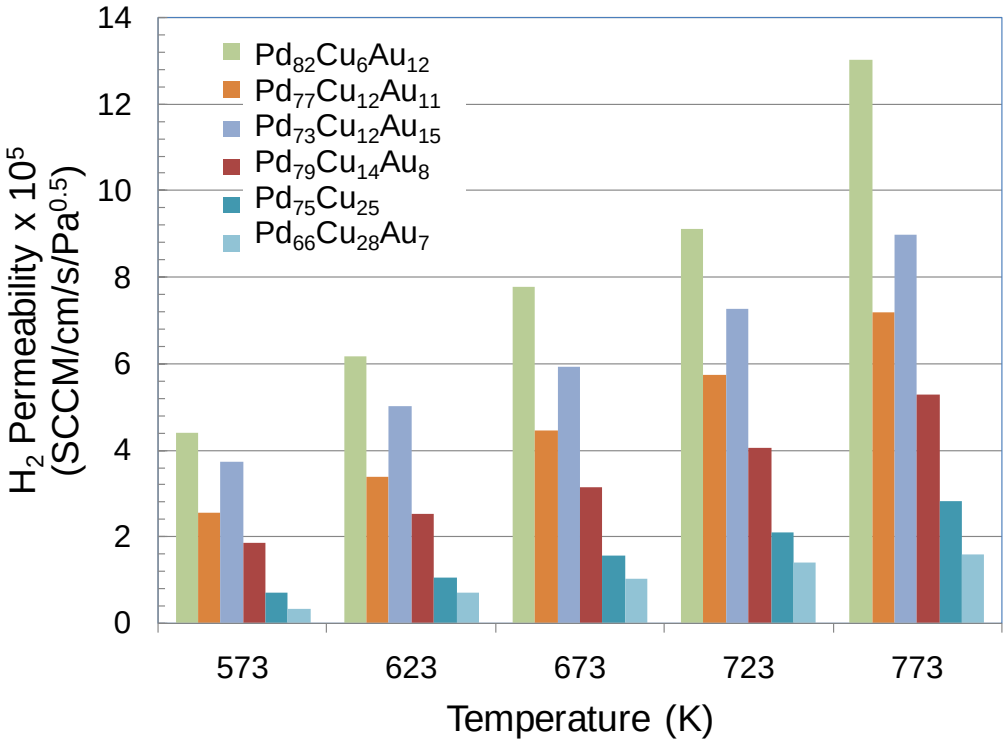

Figure 95. Comparison of hydrogen permeabilities for binary PdCu and ternary PdCuAu alloys at 20 psi feed pressure across a range of membrane compositions. The best performing of these alloys is Pd-93 with a composition of $Pd_{82}Cu_6Au_{12}$.

Membranes Pd-99 through Pd-101 contained the highest copper contents of any alloy yet tested. The results for these membranes are shown in Figure 96. The membranes have low hydrogen permeabilities, approximately 10-15% that of pure Pd. Membrane Pd-102 is unique in that it had a drop in hydrogen permeability when heating from 673 K to 723 K, a behavior consistent with a phase change taking place.

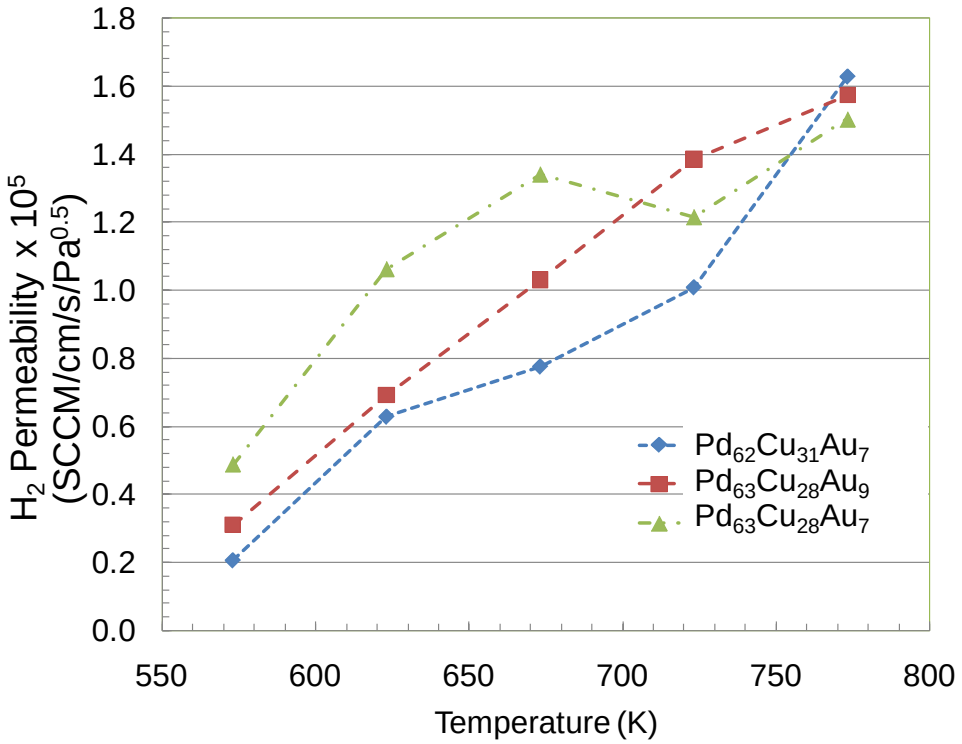

Figure 96. Comparison of hydrogen permeabilities for ternary $Pd_{60}Cu_{35}Au_5$ (nominal composition, actual compositions listed on chart) at 20 psi feed pressure across a range of membrane compositions.

The PdAuAg membranes had significant variations in compositions across the thickness, and were as much as 7-8% away from the nominal composition as it can be seen in Table 29.

Table 29. Membrane compositions as measured by standardless EDS analysis

Membrane	Pd-132	Pd-136	Pd-137	Pd-138
Side A composition	$Pd_{94}Au_5Ag_1$	$Pd_{83}Au_8Ag_9$	$Pd_{81}Au_9Ag_{10}$	$Pd_{86}Au_7Ag_7$
Side B composition	$Pd_{91}Au_6Ag_3$	$Pd_{89}Au_5Ag_6$	$Pd_{88}Au_7Ag_5$	$Pd_{90}Au_6Ag_4$
Mean composition	$Pd_{92}Au_6Ag_2$	$Pd_{86}Au_7Ag_7$	$Pd_{85}Au_8Ag_7$	$Pd_{88}Au_7Ag_5$
Thickness (micron)	10.2	13.1	15	9.7

The hydrogen fluxes through all these alloy membranes were almost same for all the temperatures as shown in Figure 97. Slight changes in the flux at different temperatures were

probably due to variation in the composition across the membrane and differences in the thickness between each membrane.

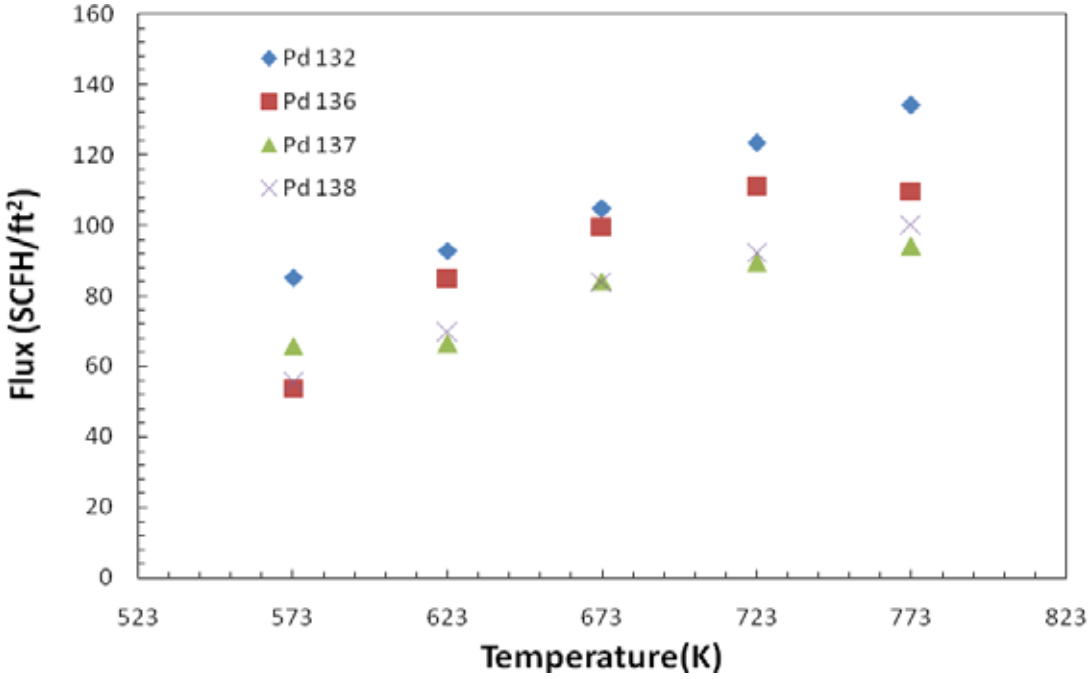

Figure 97. Comparison of hydrogen flux for PdAuAg alloys at 80 psi feed pressure.

The PdCuPt membranes had significant variations in compositions across the thickness, and were as much as 7-8% away from the nominal composition, as can be seen in Table 30.

Table 30. Membrane compositions as measured by standardless XRF analysis

Membrane	Pd-68	Pd-69
Mean composition	$Pd_{70.5}Pt_{18.5}Cu_{11}$	$Pd_{71.5}Pt_{17.5}Cu_{11}$
Thickness (micron)	*10*	*11*

Hydrogen fluxes of all these alloy membranes were almost equal for all the temperatures as shown in Figure 98. Slight changes in the flux at different temperatures were possibly due to variation in the membrane composition and differences in the thickness of each membrane. The hydrogen permeability of the membranes is 3.25×10^{-5} cm^3-cm/cm^2-s-$cmHg^{0.5}$; 33% of the pure palladium value at 400 ºC.

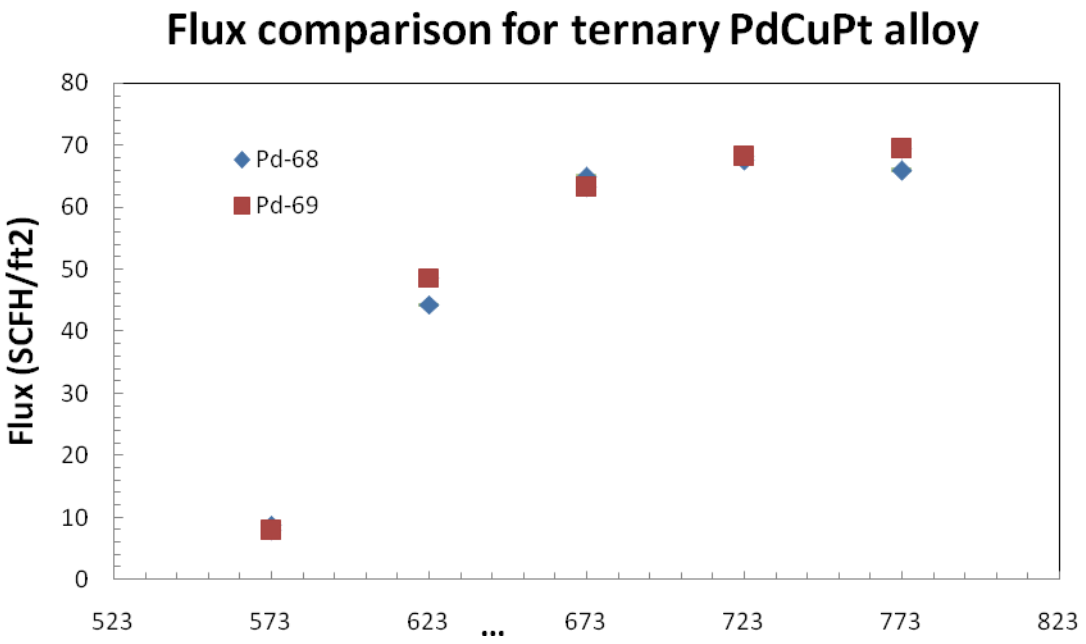

Figure 98. Comparison of Hydrogen flux for PdCuPt alloys at 80 psi feed pressure.

Composition by EDAX analysis is shown in the following table;

Table 31. CSM EDS characterization

Membrane	Pd-132	Pd-136	Pd-137	Pd-138
Side A composition	$Pd_{94}Au_5Ag_1$	$Pd_{83}Au_8Ag_9$	$Pd_{81}Au_9Ag_{10}$	$Pd_{86}Au_7Ag_7$
Side B composition	$Pd_{91}Au_6Ag_3$	$Pd_{89}Au_5Ag_6$	$Pd_{88}Au_7Ag_5$	$Pd_{90}Au_6Ag_4$
Mean composition	$Pd_{92}Au_6Ag_2$	$Pd_{86}Au_7Ag_7$	$Pd_{85}Au_8Ag_7$	$Pd_{88}Au_7Ag_5$
thickness (micron)	10.2	13.1	10	9.7

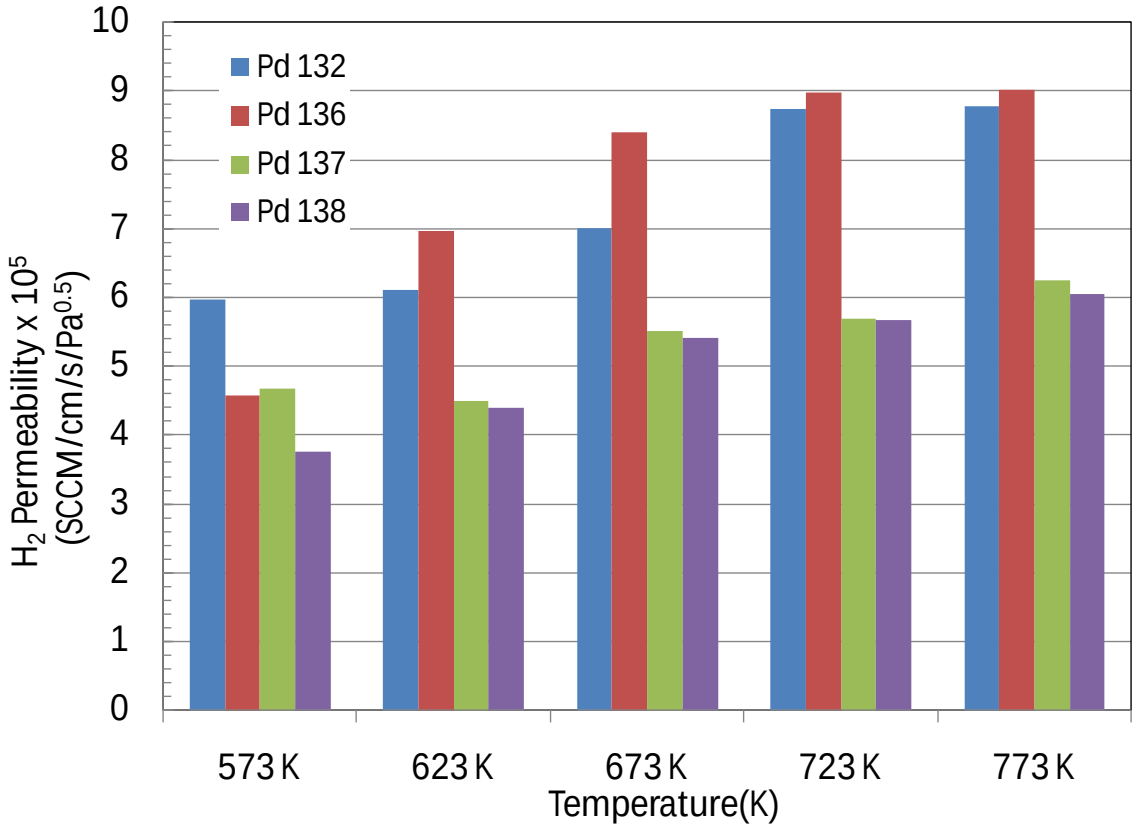

Figure 99. Comparison of hydrogen permeabilities for different Pd-Ag-Au alloys across a range of temperatures.

Since the 90%Pd-10%Au binary alloy has a high hydrogen permeability compared to pure Pd, ternary alloy membranes with palladium (90%) and equal percentages of Ag and Au (5%) were prepared in order to study the permeability of these membranes. Pd-132 and Pd-136 seem to have higher permeability (80% of that of pure palladium), compared to Pd-137 and Pd-138. This result is puzzling since the differences in composition are slight. Possible reasons include differences in pretreatment such as heating up in air rather than inert gas, as well as compositional variation across the foil. Heating the membranes up in air may contribute to higher hydrogen permeabilities. Membrane Pd-136 was heated up in air while Pd-132 was heated to temperature in inert gas.

The other surprising observation was that permeability had only minimal change from 723 K to 773 K. This may be indicative of unexpected annealing behaviors such as phase change, or unusual sensitivity to poisoning of the films. We have previously observed evidence of seal decomposition causing permeability to be depressed at higher temperatures (823 K), but further investigation is necessary to confirm this theory.

Composition by XRF analysis is shown in the following table:

Table 32. CSM composition analysis of Pd-68 and Pd-69.

Membrane	SwRI-68	SwRI-69
Mean composition	$Pd_{70.5}Cu_{18.5}Pt_{11}$	$Pd_{71.5}Cu_{17.5}Pt_{11}$
Thickness (Micron)	10	11

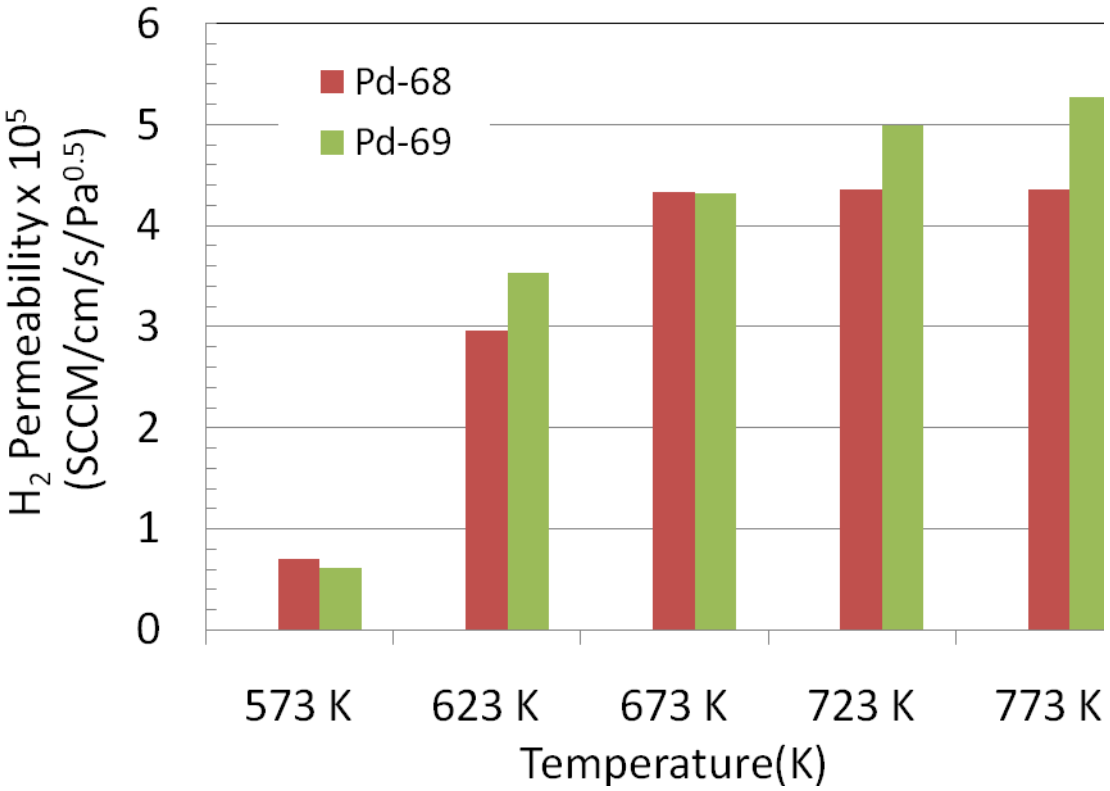

Figure 100. Comparison of hydrogen permeabilities for different Pd-Cu-Pt alloys across a range of temperatures.

The PdCuPt ternary alloy has low hydrogen permeability (30-40% of pure palladium). Furthermore, comparing membranes 68 and 69 to a binary $Pd_{90}Cu_{10}$ alloy, the ternary alloys have about 60% of the hydrogen permeability of the binary alloy at 350 ºC. Making the same comparison for a binary Pd-Cu alloy with 30 mass % Cu, the ternary Pd-Cu-Pt alloy has about three times the pure H_2 permeability of a $Pd_{70}Cu_{30}$ binary foil.

Composition by EDAX analysis is shown in the following table:

Table 33. CSM elemental composition analysis.

Membrane	Pd-141	Pd-142
Side A composition	$Pd_{80}Au_{19}Pt_1$	$Pd_{78}Au_{20}Pt_2$
Side B composition	$Pd_{84}Au_{13}Pt_3$	$Pd_{77}Au_{22}Pt_1$
Mean composition	$Pd_{82}Au_{16}Pt_2$	$Pd_{78}Au_{21}Pt_1$
thickness (micron)	9.80	9.62

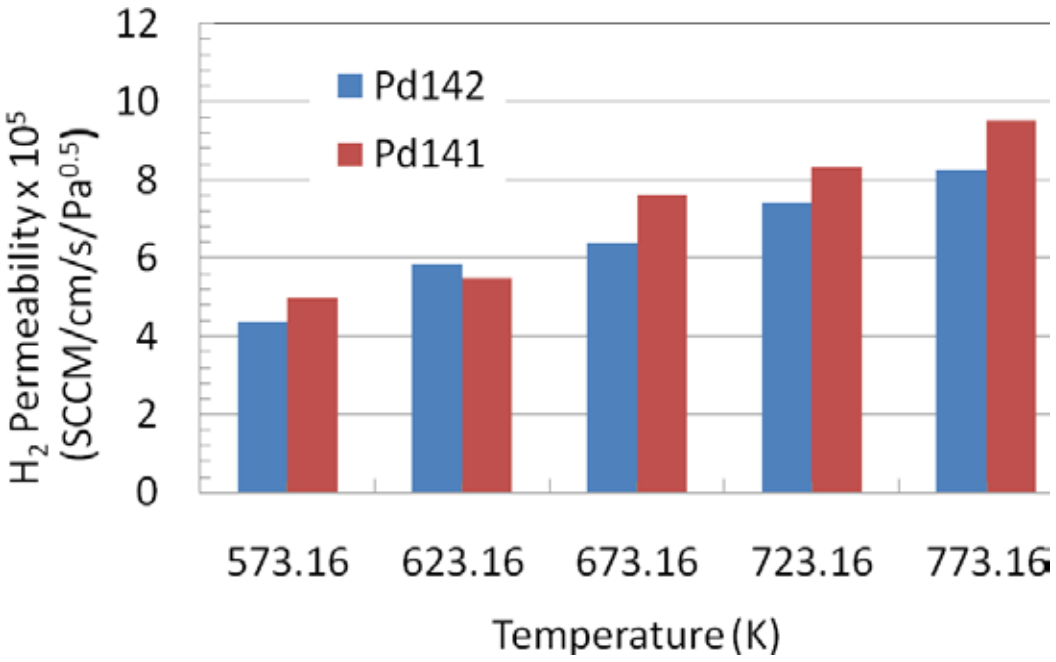

Figure 101. Comparison of hydrogen permeabilities for different Pd-Au-Pt alloys across a range of temperatures.

Surprisingly, addition of a small amount of platinum to a PdAu binary alloy significantly reduces the pure hydrogen permeability of the resulting ternary alloy. At 400 ºC, the $Pd_{80}Au_{20}$ alloy has slightly higher hydrogen permeability (5-7%) compared to pure Pd. Therefore, it is curious that the addition of only one to three mass % of Pt would reduce the hydrogen permeability at 400 ºC by about 40%.

Table 34. Membrane compositions as measured by EDAX analysis (Nominal thickness = 12 µm)

Membrane	Pd-147	Pd-148	Pd-149
Side A composition	$Pd_{78.2}Au_{12.5}Pt_{9.3}$	$Pd_{78}Au_{13}Pt_{9}$	$Pd_{75.7}Au_{17.7}Pt_{6.6}$
Side B composition	$Pd_{76.4}Au_{13.8}Pt_{9.8}$	$Pd_{84}Au_{13.4}Pt_{2.4}$	$Pd_{77.7}Au_{14.5}Pt_{7.8}$
Mean composition	$Pd_{77.3}Au_{13.2}Pt_{9.5}$	$Pd_{81}Au_{13.2}Pt_{5.8}$	$Pd_{76.7}Au_{16.1}Pt_{7.2}$
thickness (micron)	11	12.2	12.6

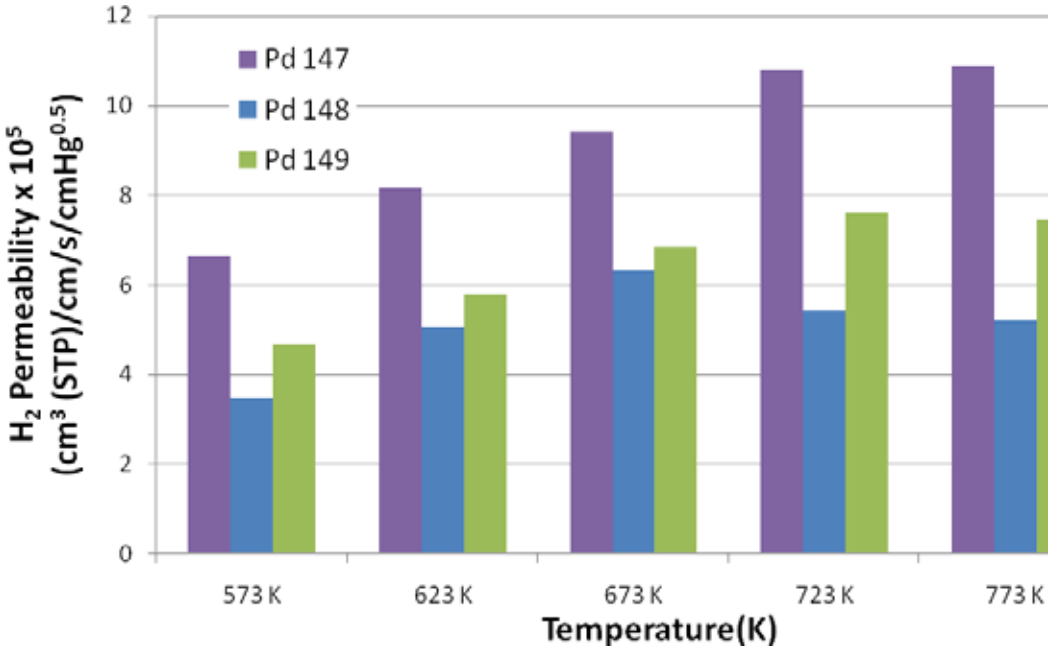

Figure 102. Comparison of hydrogen permeabilities for thinner Pd-Au-Pt alloys across a range of temperatures.

As shown in Figure 102, thinner (~12 µm) ternary alloy films of palladium, gold, platinum showed hydrogen permeability almost half to that of pure palladium. Based on these data, thicker membranes with a nominal palladium composition of 80 mass% were fabricated at SwRI.

Table 35. Membrane compositions as measured by EDAX analysis (Nominal thickness = 25 µm)

Membrane	Pd-153	Pd-154	Pd-155
Side A composition	$Pd_{74.5}Au_{19.6}Pt_{5.8}$	$Pd_{80.4}Au_{14.3}Pt_{5.3}$	$Pd_{78}Au_{16}Pt_{6}$
Side B composition	$Pd_{74.5}Au_{19.7}Pt_{5.8}$	$Pd_{74.5}Au_{20.5}Pt_{5}$	$Pd_{74.8}Au_{19.2}Pt_{6}$
Mean composition	$Pd_{74.5}Au_{19.7}Pt_{5.8}$	$Pd_{77.5}Au_{17.4}Pt_{5.2}$	$Pd_{76.5}Au_{17.5}Pt_{6}$
thickness (micron)	26.8	27.8	30.8

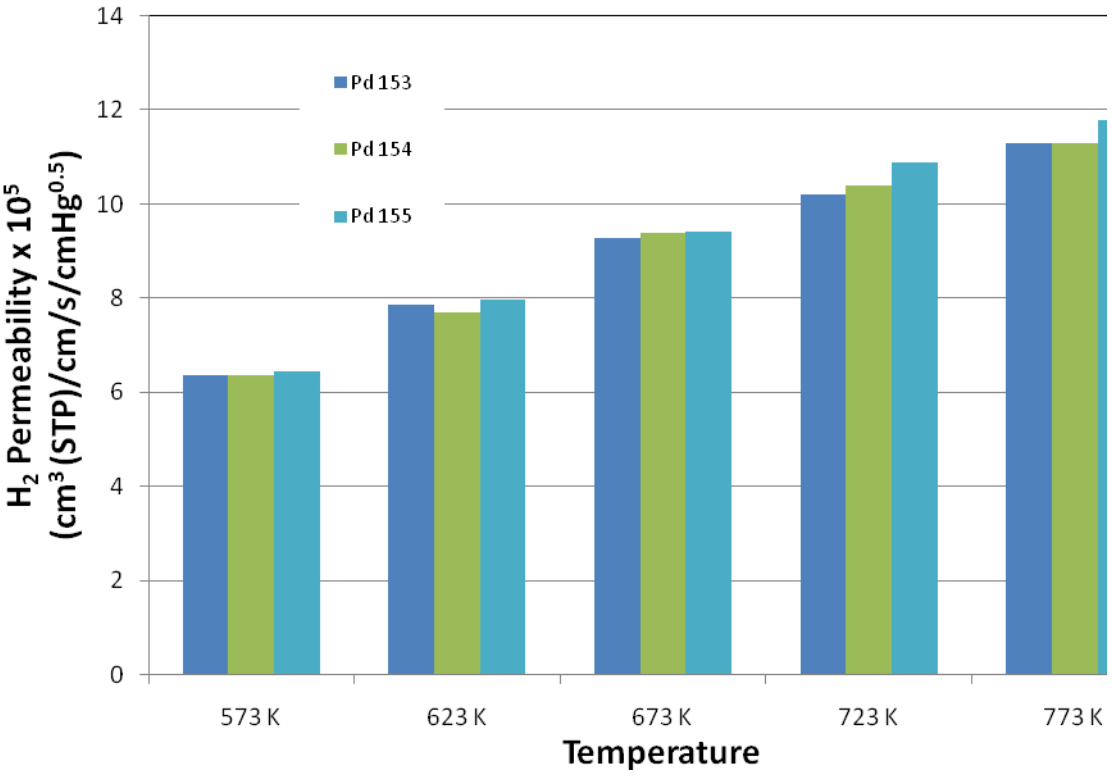

Figure 103. Comparison of hydrogen permeabilities for thicker Pd-Au-Pt alloys across a range of temperatures.

The pure hydrogen permeability data for the ~25 micron thick PdAuPt membranes are given in Figure 103. These thicker alloys showed almost equal permeability comparable to that of pure palladium with slight variation, perhaps due to non-uniform composition.

Another PdAuPt membrane, Pd-158, was characterized by SEM/EDS prior to testing, and the results are summarized in Table 36. Cross-sectional imaging showed that the gravimetric method of thickness calculation is accurate within measurement error.

Table 36. Membrane properties of SwRI Pd-158 as measured by SEM/EDS

Feed Side Composition (wt %)	Permeate Side Composition (wt %)	Thickness (µm, Gravimetric)	Thickness (µm, cross-sectional SEM)
$Pd_{72}Pt_9Au_{19}$	$Pd_{66}Au_{22}$ Pt_{11}	33.2	32.7

No detectable nitrogen leak was measured during permeation testing, which is summarized in Figure 104. The membrane had a hydrogen permeability of 8.5 x 10^{-5} cm^3 (STP)/cm/s/$cmHg^{0.5}$ at 673 K, approximately 78% that of pure Pd. Hydrogen flux had a linear dependence on the square root of pressure drop, suggesting that bulk diffusion was the rate limiting step in hydrogen transport across the membrane (Figure 104).

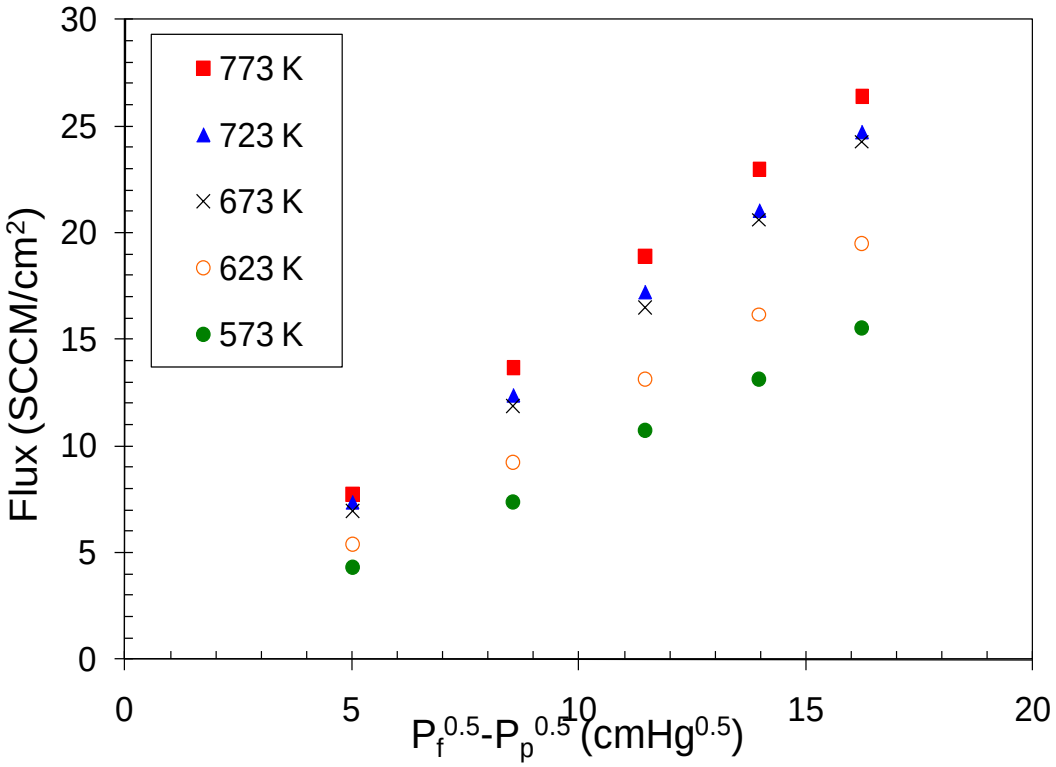

Figure 104. Hydrogen flux as a function of pressure gradient for SwRI Pd-158.

We have seen higher permeability of Pd-136 as compared to other alloys of the same composition due to pretreatment under air. In order to verify effect of air pretreatment on ternary alloys, we chose one Pd-Au-Ag alloy Pd-138 and two Pd-Au-Pt alloys. We heated these membranes under air to 300 ºC and found that permeability values for these membranes were higher than those heated under nitrogen. As shown in Figure 105, the effect was more pronounced at higher temperatures more than 400 ºC (permeabilities are almost doubled).

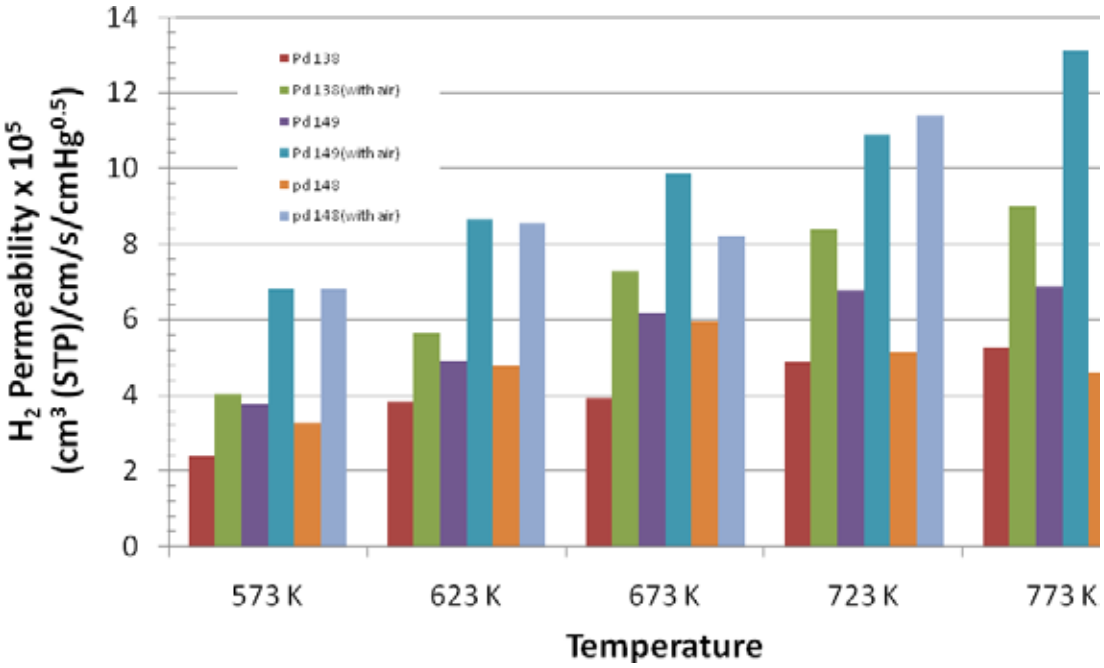

Figure 105. Comparison of hydrogen permeabilities for thinner ternary palladium alloys under different pretreatment.

Similar experiments were carried out with thicker PdAuPt alloys and they are summarized in Figure 106. The increase in permeability was less significant (10-20%). Therefore, we think that some surface properties of thinner foils might cause a boost in permeability.

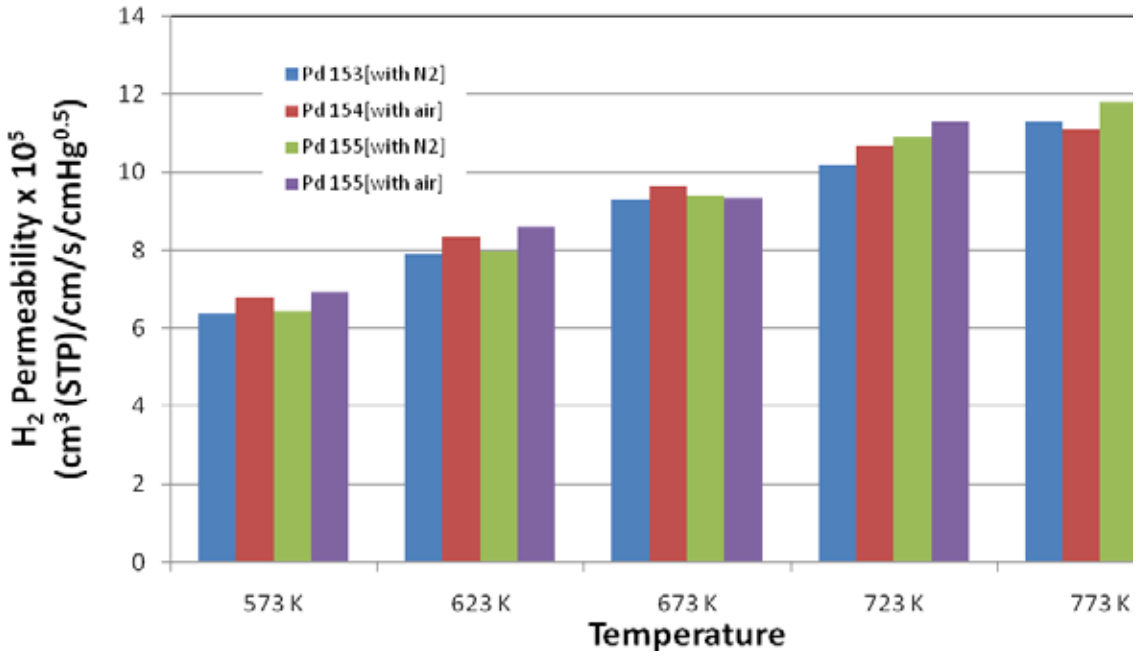

Figure 106. Comparison of hydrogen permeabilities for thinner PdAuPt alloys under different pretreatment.

In order to study effect of a reducing environment on thick PdAuPt alloys, we chose membrane Pd-155 which showed highest permeability under pure gas conditions. We heated the membrane up to 300 ºC in mild conditions, 3.5% H_2 in argon forming gas flowing over the membrane at very close to ambient pressure.

It failed as soon as we applied pressure at 300 ºC. When we analyzed it after removing it from the permeation cell, we found a large single split of 10-12 mm in length, near the edge of cut disk. The membrane appearance is metallic silver on the feed side and metallic silver with a slightly purple tint on the permeate side. After cooling a purple tint was seen which we attribute to hydride formation.

In another experiment, a membrane was cut from the same Pd-95 foil and mounted in the permeation cell. This membrane was heated under air to 573 K and then permeation measurements were performed in 50 K increments between 573 and 723 K with no air purge. In this case, the temperature increased between permeation experiments.

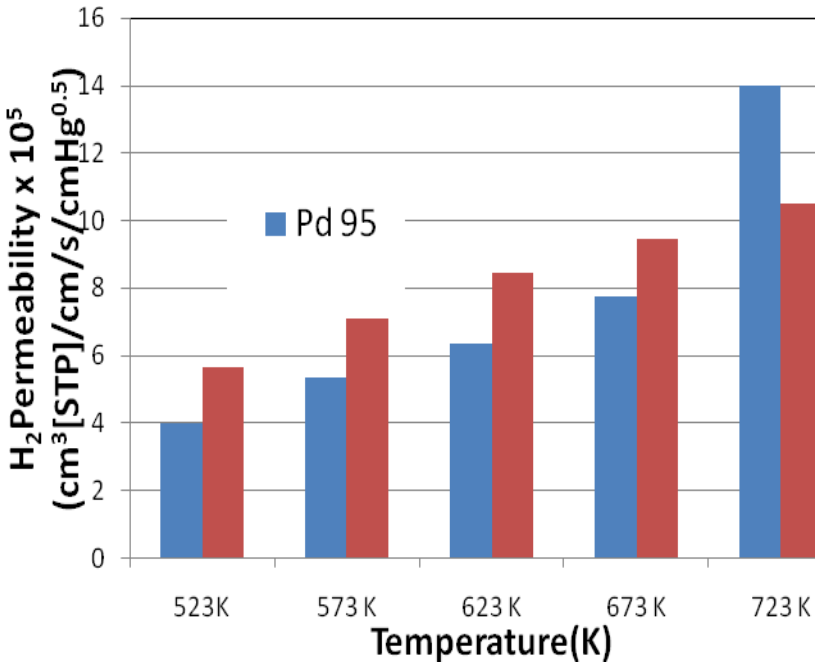

Figure 107. The effect of heating up in air to 300 ºC compared to a short (2 minute) air purge at 673 K on the pure hydrogen permeabilities of PdAuCu ternary alloy (membrane #Pd-95). The data marked Pd 95 (in air) refers to the sample that was heated up in air to 573 K.

As can be seen from Figure 107, pretreatment of a thin (13.5 µm) PdAuCu membrane under air to 573 K produced a slight increase (35%) in permeability at 623 K compared to the sample that was air purged only. This small permeability increase was seen in the thinner ternary alloy tested previously.

The air-purged membrane exhibited a higher permeability at 723 K than the air pretreated membrane. This observation is unusual and could be due to several factors, including the variability in composition across a foil sample. The air purged membrane was tested first at 723 K, immediately after the air purge. We have seen previously that the permeability increase due to an air purge can be transient. It can decrease to a new, lower, steady-state value over time.

Pure hydrogen permeation data for membrane Pd-161 are shown in Figure 108.

The composition of both membranes tested was determined by EDAX and they are given in Table 37.

Table 37. Foil compositions measured at CSM using EDAX for Pd-158 and Pd-161

Membrane	Pd-161	Pd-158
Side A	$Pd_{80}Au_{15}Ru_5$	$Pd_{72}Pt_9Au_{19}$
Side B	$Pd_{79}Au_{15}Ru_6$	$Pd_{66}Pt_{11}Au_{22}$
Mean composition	$Pd_{80}Au_{15}Ru_5$	$Pd_{69}Pt_{10}Au_{21}$
Thickness	26.5	32.7 (by SEM)

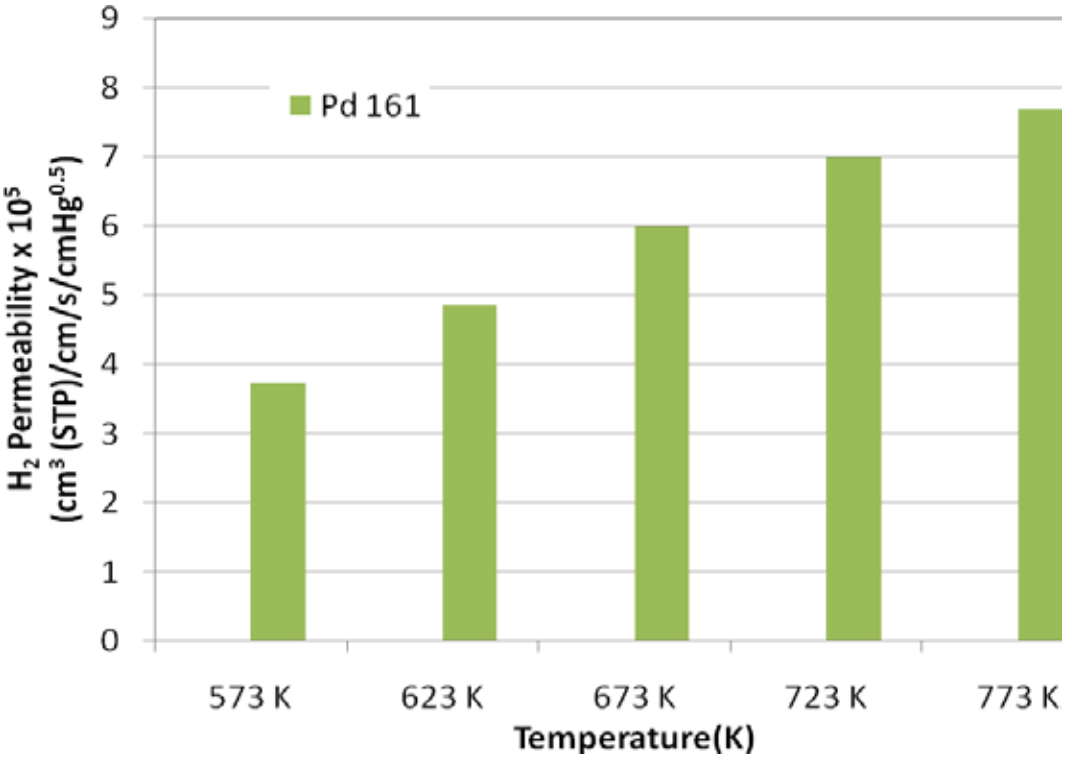

Figure 108. Comparison of pure hydrogen permeabilities for $Pd_{80}Au_{15}Ru_5$ ternary alloy and pure palladium.

As can be seen from Figure 108, the H_2 permeability for PdAuRu is 6 x 10^5 cm^3 (STP)/cm/s/$cmHg^{0.5}$ at 400 ºC; ~55% of pure palladium at similar conditions. Thus, this membrane has lower permeability as compared to other ternary alloys of Pd and Au.

Table 38. Composition by EDAX analysis

Membrane	Pd 158	Pd 165	Pd 168
Mean composition	$Pd_{69}Au_{10}Pt_{21}$	$Pd_{72}Au_{18}Pt_{10}$	$Pd_{65}Au_{21}Pt_{14}$
Thickness	33.2	30	29

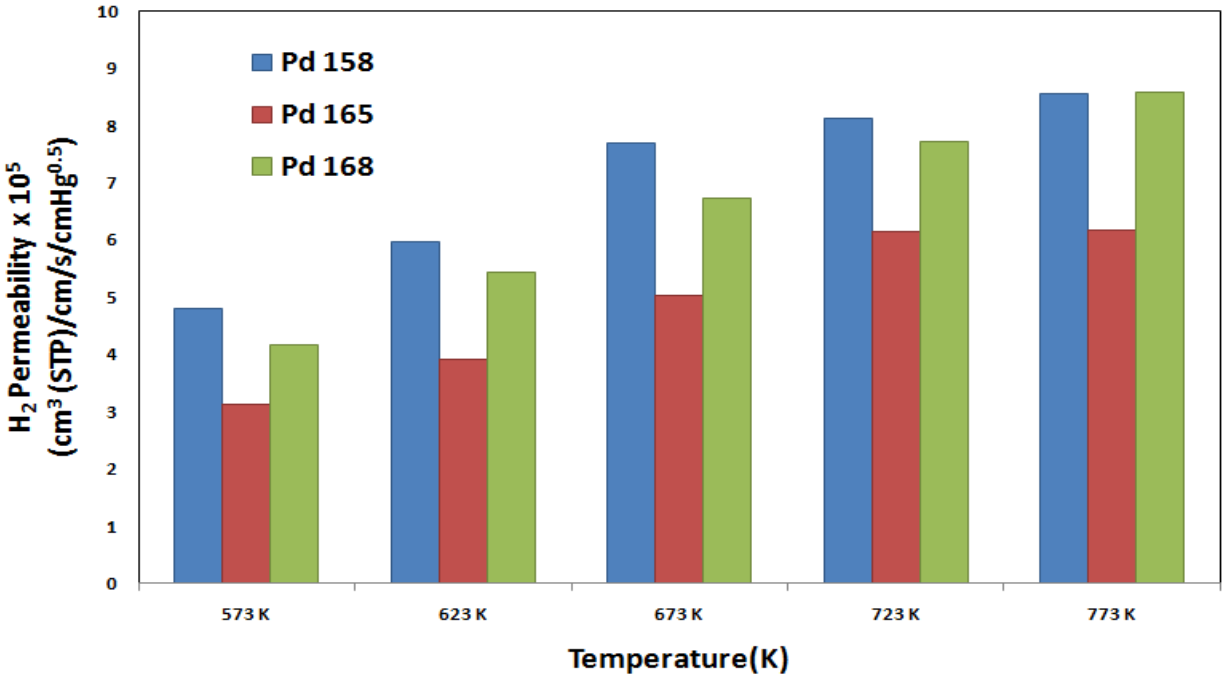

Figure 109. Comparison of hydrogen permeabilities for thicker Pd-Au-Pt alloys across a range of temperatures. Membranes 165 and 168 received the IBAD treatment.

As shown in Figure 109, both ion bombardment assisted deposition (IBAD) samples exhibited pure hydrogen permeability less than the foil #158, without IBAD treatment. As shown in Table 38, the composition of these three samples was not the same, therefore, composition variations are also likely to affect the pure H_2 permeability. For the IBAD membranes the pure H_2 permeability was 45-60% of pure palladium depending on temperature. Additionally, these membranes show a non-uniform surface structure, as expected due to angle of the ion beam with respect to target. X-ray diffraction was also performed in order to see whether these membranes had different orientation than membranes without IBAD.

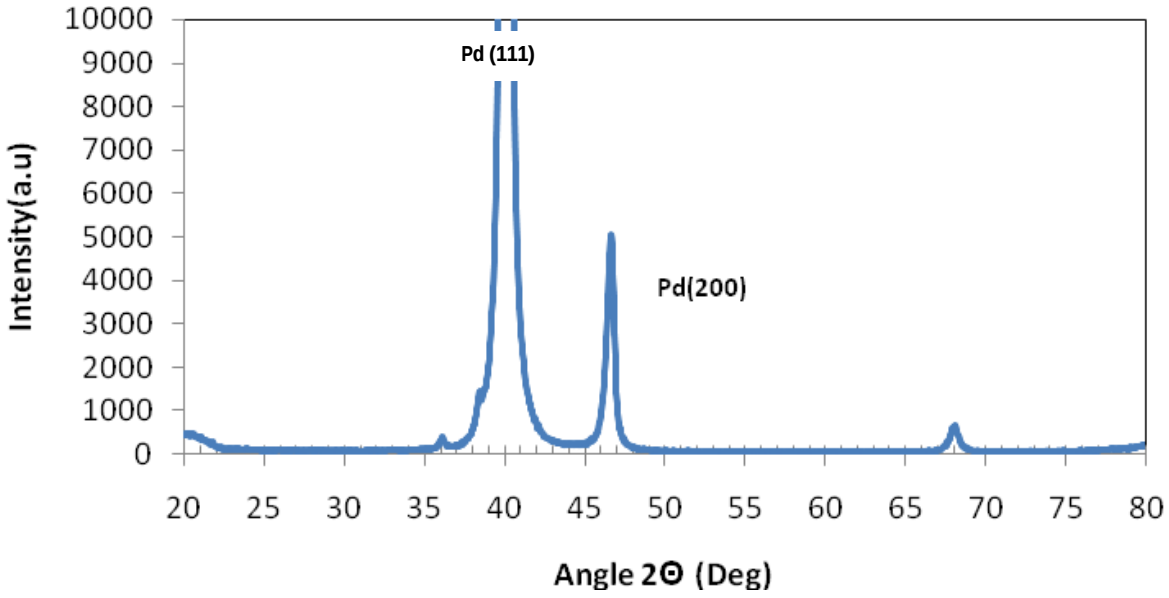

Figure 110. X-ray diffraction for Pd-168.

As can be seen from Figure 110, the large peak at 40.12^0 corresponds to Pd (111) while the other large peak for Pd (200) is seen at 46.65^0. The peaks are seen at the same 2q values as the PdAuPt foils that were not subjected to the IBAD treatment. Since there is no peak shifts, this suggests that IBAD doesn't change the orientation of the crystallites.

We heated Pd-168 membranes under air as it was heated to 300 ºC and found that a permeability value for this membrane was almost same as that of the nitrogen-pretreated membranes, as seen in the previous thick PdAuPt alloys, as shown in Figure 111. We would estimate that the permeability values are essentially the same, regardless of pretreatment.

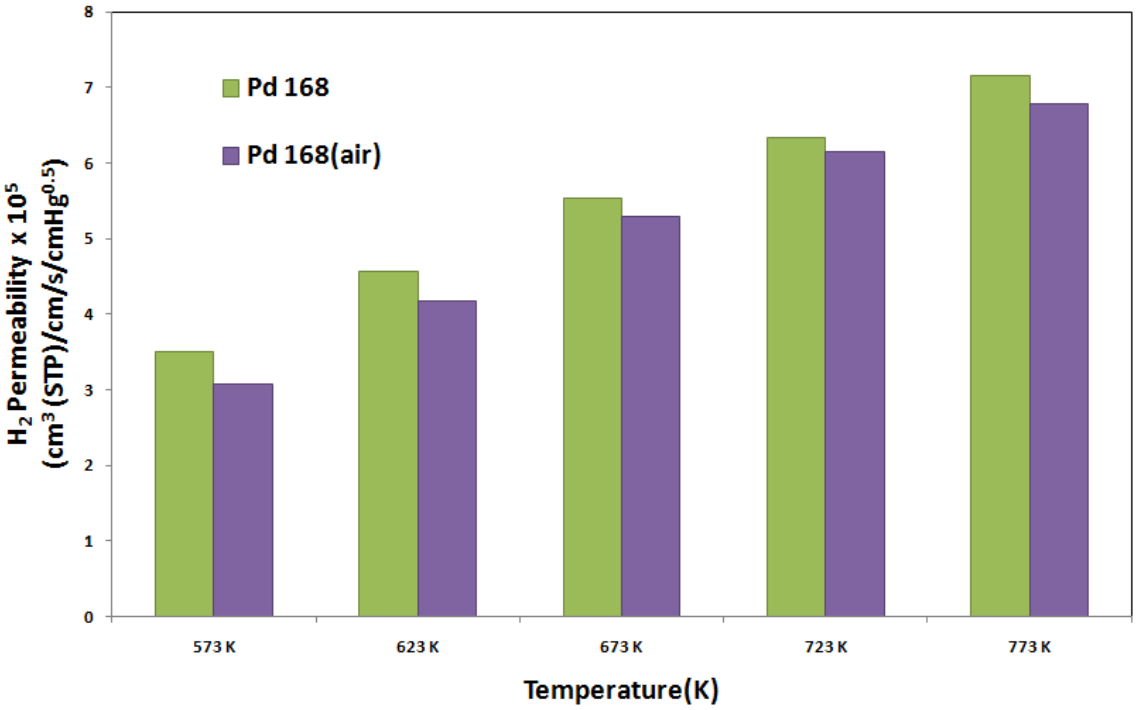

Figure 111. Comparison of hydrogen permeabilities for thicker PdAuPt alloy with IBAD under different pretreatments.

3.4 Mixed Gas Permeation Testing

TDA used an existing flow apparatus to evaluate the performance of the membranes under representative conditions (Figure 112). Electronic mass flow controllers were used to introduce the gas streams of H_2, CO, CO_2, and H_2S as well as N_2 used as an inert gas on the permeate side sweep gas. Water was introduced into the system using a high-pressure liquid pump. The feed gas mixture is either directed through the membrane module or through a by-pass loop for analysis. Prior to separation, these gases are heated to 185 ºC and mixed at the inlet of the test module. The system pressure was controlled with a Badger pressure control valve located downstream of the membrane module. The permeate flow was measured using an electronic mass flow meter. The gas stream exiting the module or by-pass loop is directed into two IR analyzers for continuous monitoring of CO, CO_2 and CH_4 concentrations both on the permeate and retentate streams. Control E/G software was used to control the apparatus and provided us unattended operation capability, including tests overnight. Safety precautions were in place for appropriate system shutdown, in the event of overheating, over pressurization or hazardous gas leak.

Figure 112. Picture of the test apparatus.

For these tests we cut the thin foils to the desired size and placed them into one of our reactors (Figure 113). Sections of the foil were cut into round disks and placed on a stainless steel frit with a layer of ceramic paper in between the layers. A graphite gasket was placed on top of the membrane and the module was assembled using screws to compress the graphite creating a seal around the membrane. The membrane loaded in the module with the graphite seal in place is shown in Figure 114. Both the top and the bottom of the module have two gas lines. The test gases enter through inlet line which is attached to the top of the module and the raffinate gases (the remaining gases that didn't permeate through the membrane) leave through a second line at the top of the cell. The inlet line at the bottom of the test cell was used to introduce a sweep gas (when desired), which was often used to purge the membrane during heating and cooling. The permeate flow (the gases that passed through the membrane) exits through an outlet line located at the bottom of the module.

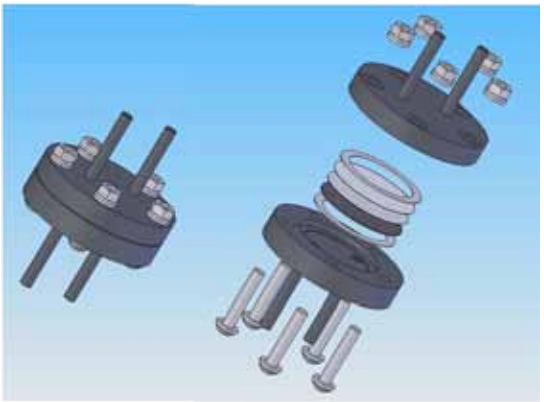

Figure 113. Membrane testing cell.

Figure 114. Membrane loaded into fixture.

The module fitted with the membrane foil was then placed into the testing apparatus. Before we began testing, the membranes were pressurized to 40 psi in nitrogen (N_2) to ensure that the membrane is intact and free of leaks before the testing begins. After this initial step, the membranes are purged on both sides with inert gas and heated up to the desired test temperature (400 ºC) at a rate of 0.5 ºC/min.

In a typical experiment, we first performed single-gas permeation measurements using the pure gas H_2 and N_2 to determine if the films were free of flaws to carry out the desired gas separation and to quantify permeance across the film. In these quick screening tests, the flow rate of gases permeated across the membrane was measured using an electronic flow meter.

Table 39. Membrane testing conditions specified in the DOE/NETL test protocol and methanol reforming conditions

Feed Gas Composition	DOE 1a (WGS)	DOE 2a (WGS w/H_2S)
H_2 (%)	50	50
CO (%)	1	1
CO_2 (%)	30	30
H_2O (%)	19	19
H_2S (%)	0	0.002 (20 vppm)†
Feed pressure	200 psia	200 psia
Sweep pressure	30 psia	30 psia
Temperature (ºC)	300-600	300-600
Duration (h)	100	100
Target H_2 purity	99.5%	99.5%

†vppm = volume parts per million

In the evaluation of the membranes, we maintained test conditions provided by DOE/NETL protocol. The composition of the gas mixtures used are summarized in Table 38. Once the initial screening was completed, the membranes were exposed to a mixture of H_2, CO, CO_2, H_2O, and H_2S. Almost all tests were carried out at 400 ºC and 170 psi on the feed side, while recovering permeate at ambient pressure on the sweep side. Although the protocol asked for 200 psia inlet pressure with 30 psia permeate gas recovery, because our unit did not have the capability of pressurizing the permeate gas, we maintained 170 psia inlet, while providing the same driving force requested in the protocol to provide a basis of comparison with other emerging membrane technologies. As per their guidelines, we typically ran our tests for 100 hours. If in the initial test (DOE 1a) membrane showed promise, we then introduced sulfur into the system for the second test (DOE 2A). The total flow gas for these tests was maintained at 1000 sccm.

The flux was calculated from the permeate gas flow and the known area of the membrane available for the transport process. The CO_2, CO and CH_4 concentrations were measured on our ZRE IR analyzer. We commonly observed CH_4 in the permeate stream at the beginning of most experiments, which then gradually dropped down to concentrations well below the detection range of the analyzer (less than 1 ppmv). We speculate that the permeate side of the membrane surface was catalyzing the formation of the CH_4 via CO and CO_2 methanation. Further into the test, the catalytic activity disappears (likely due to the reduction of the surface with hydrogen and CO). Once the membrane reaches its steady state operating conditions only CO and CO_2 impurities in the permeate are detected.

The TKK PdAu foils were supplied to TDA for testing under DOE conditions. The following plot shows the performance under DOE conditions #1 and 2a.

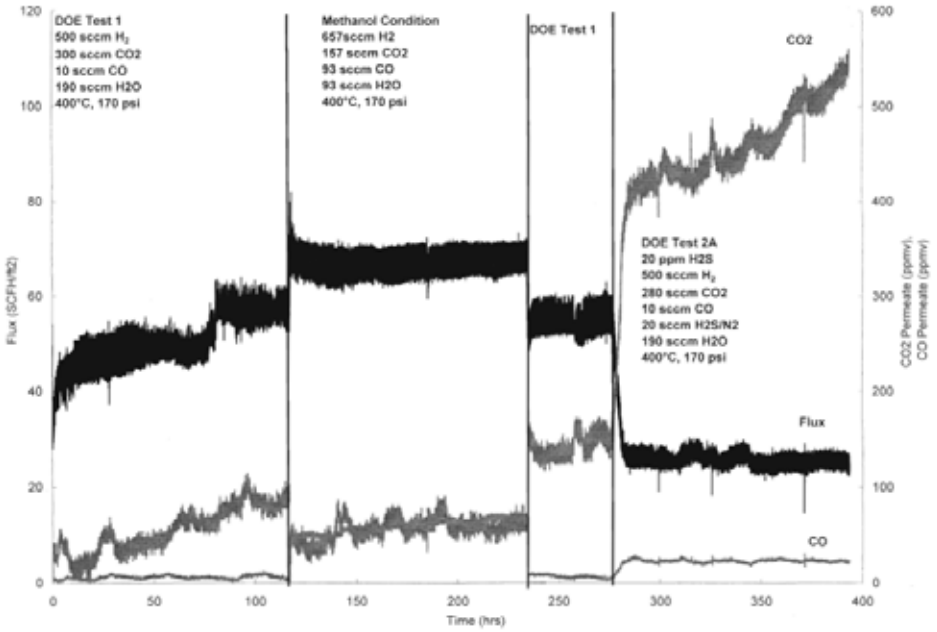

Figure 115. PdAu-10 tested under DOE test condition #1 & 2a.

Postmortem analysis by SEM/EDS, XRF, and XRD was performed on membrane Pd-48, which had been previously tested under mixture gas conditions at TDA Research. The membrane was stable under WGS mixtures, but failed rapidly when exposed to H_2S. No detectable surface sulfur was found on Pd-48, either by EDS or XRD, but at some point during or after the permeation testing, it had lost 70% of its thickness, and all but 0.8 wt% of its gold. A thicker cold-worked foil did have detectable surface sulfides after mixture testing, but did not lose any significant amount of its material. This result was confirmed by EDS and XRF.

The primary difference between Pd-48 and cold-worked PdAu is in the structure: the sputtered membrane had a columnar growth perpendicular to the surface, while the cold-worked membrane did not (Figure 116). The most plausible mechanism for this suggests that sulfides, which have significantly larger crystallite sizes than either palladium or gold, were allowed to penetrate deeply into the membrane bulk by the columnar structure, which then swelled and cracked, causing eventual disintegration and loss of metal.

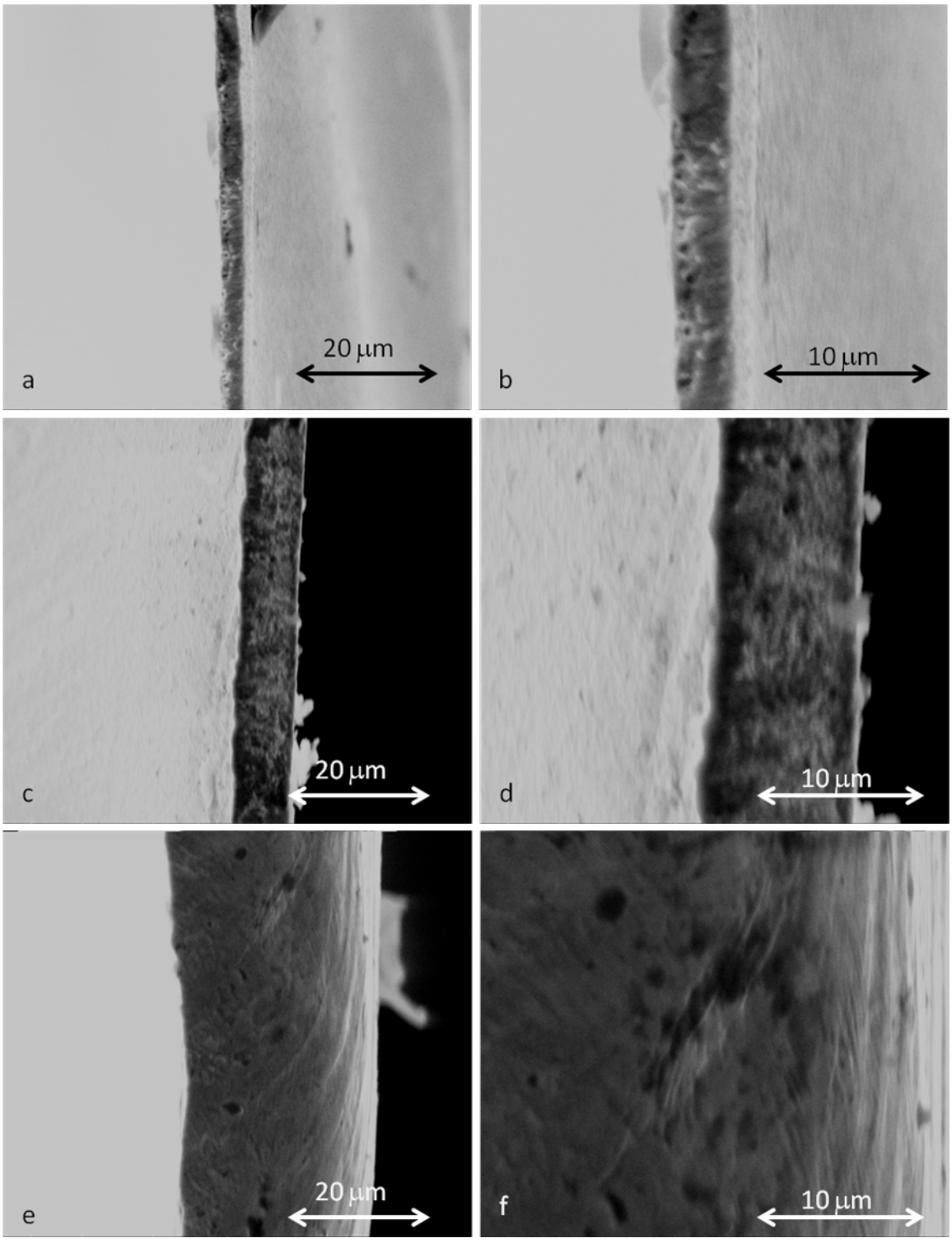

Figure 116. SEM images depicting torn cross-sections: a+b) SwRI Pd-48 after testing, b+c) SwRI Pd-48 before testing, and e+f) TKK 10% Au before testing.

IdaTech has tested 3 PdCuAu ternary foils but experienced foil ruptures upon exposure to the test gases following preconditioning. The following images demonstrate some of the issues they dealt with in trying to mount the foils.

Figure 117. Feed-side of membranes #1 and #2, shown with back-lighting to easily identify cracks.

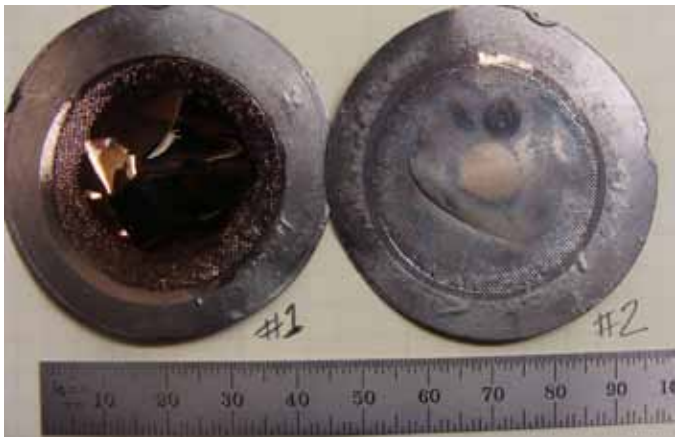

Figure 118. Supported-side of both membranes.

Figure 119. View of a possible defect along the crack edge, at 1000X, C-DIC, Membrane #1.

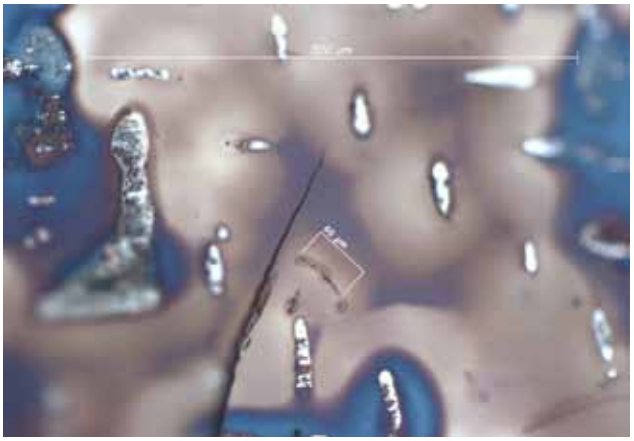

Figure 120. A view of the end of one crack, with two smaller ones nearby, 100X, BF, Membrane #1.

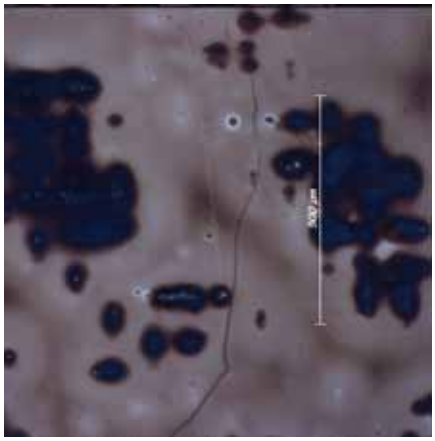

Figure 121. Crack observed between contact points. Other cracks were observed on top of contact areas. 100X, BF, Membrane #1.

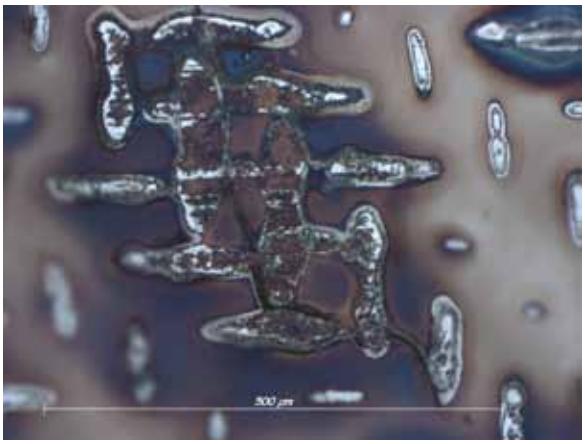

Figure 122. Crack running through supported region. 100X, BF, Membrane #1.

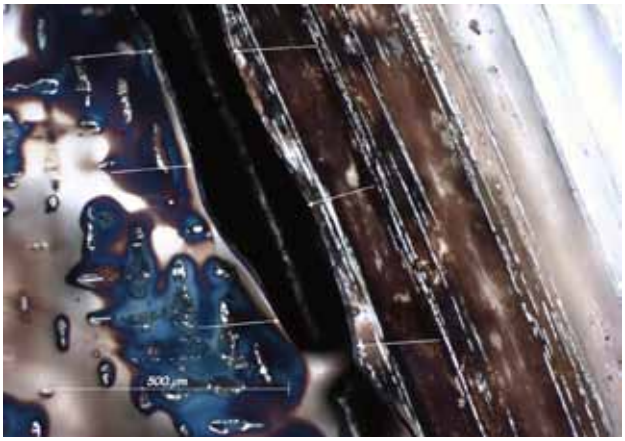

Figure 123. This is a view of the transition area between the screen-supported region and the clamped portion (between flanges), 100X, BF, Membrane #1.

The ridges shown in the image above are from the machined finish on the flanges. There is a "ditch" with cracks running along both sides (small arrows). Not sure how the inverted feature formed, since the other side was pressurized. Next slide shows membrane & gasket in the direction of the large arrow.

Figure 124. Another crack along the gasket.

The photo in Figure 123 was taken near the previous one, moving radially outward 1 to 2 mm, 100X, BF, Membrane #1. The ridges imposed by the machined finish indicate the membrane material has a certain amount of ductility, but not enough to accommodate the larger deformations in transition areas.

This is a view of the transition area between the screen-supported region and the clamped portion (between flanges), 100X, BF, Membrane #1. The ridges are from the machined finish on the flanges. There is a "ditch" with cracks running along both sides (small arrows). Not sure how the inverted feature formed, since the other side is pressurized.

Following are additional voids observed in the foils with the first three images taken following testing and the final image of a foil prior to loading it into the test cell. All of these voids appear to be some form of contamination that is either introduced in the handling or conditioning steps.

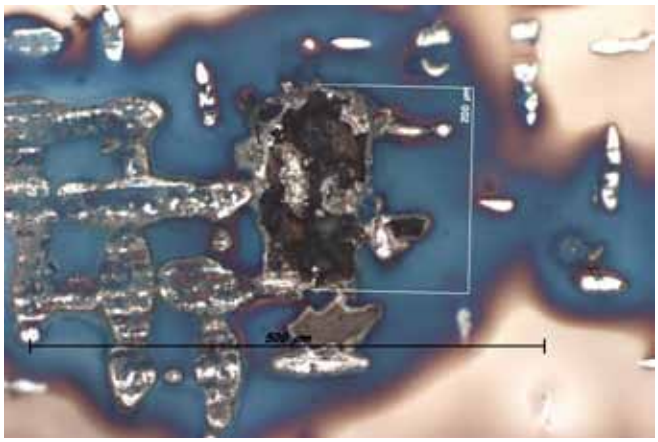

Figure 125. One of the larger voids observed. 200X, BF, Membrane #1.

Figure 126. Crack tip on supported side of the membrane, 500X, BF, Membrane #2. Software was used to capture and compile several images through multiple focal planes, resulting in some pixilated regions. The dark spots are voids.

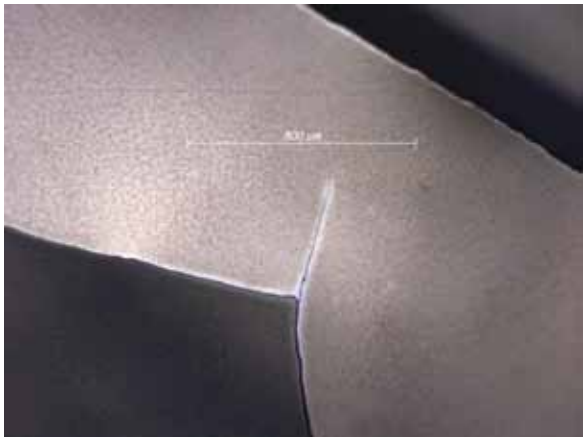

Figure 127. A star-pattern crack next to the main (open) crack, 100X, BF, Membrane #1.

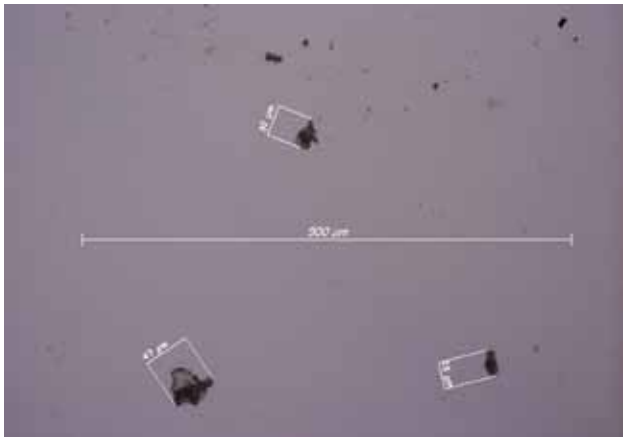

Figure 128. Cluster of pits in the new foil material. This is the highest density of pitting observed, 200X, BF.

Figure 129. An atypical pit with precipitate around the periphery, 500X, C-DIC, new foil sample.

The cold rolled foil performed well under test condition #1 but not as well upon exposure to test condition #2a.

The evaluation of Pd-93 under DOE condition #1 at TDA Research is shown below.

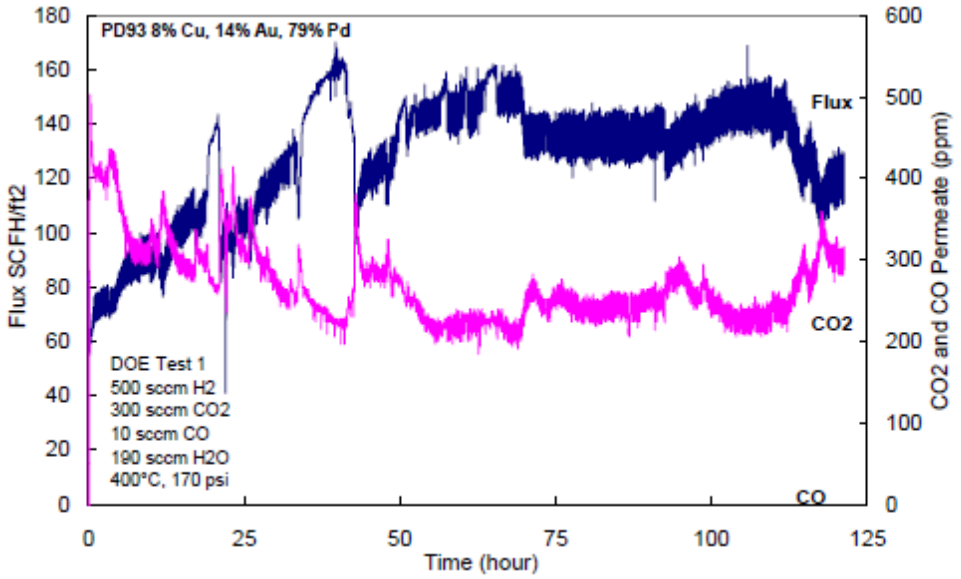

Figure 130. Pd-93 under DOE condition #1.

This sample showed increasing instability under high CO concentration.

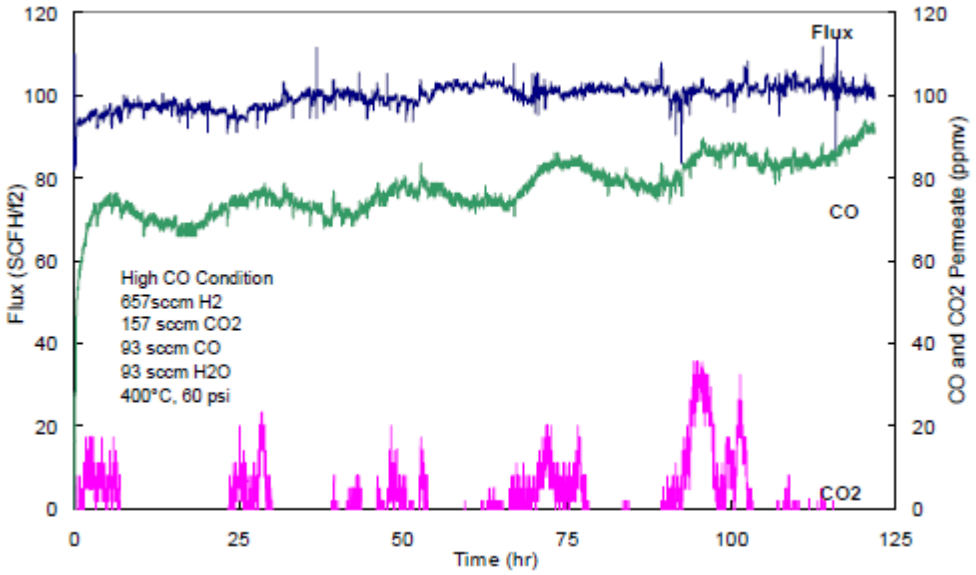

Figure 131. Pd-93 with an increased CO concentration.

The first Pd-93 sample was tested in a 20 ppmv H_2S conditions but the data was lost due to computer malfunction. There was only data for the first two hours showing good performance with the notebook showing that the permeate was 55 sccm with 4000 ppm CO_2 and 145 ppm CO over the 30 hour test. Following the fix, the flux through the membrane began to drop immediately followed by a rupture of the foil.

TDA tried to reproduce the results using another sample. The second sample failed almost immediately and showed much lower flux.

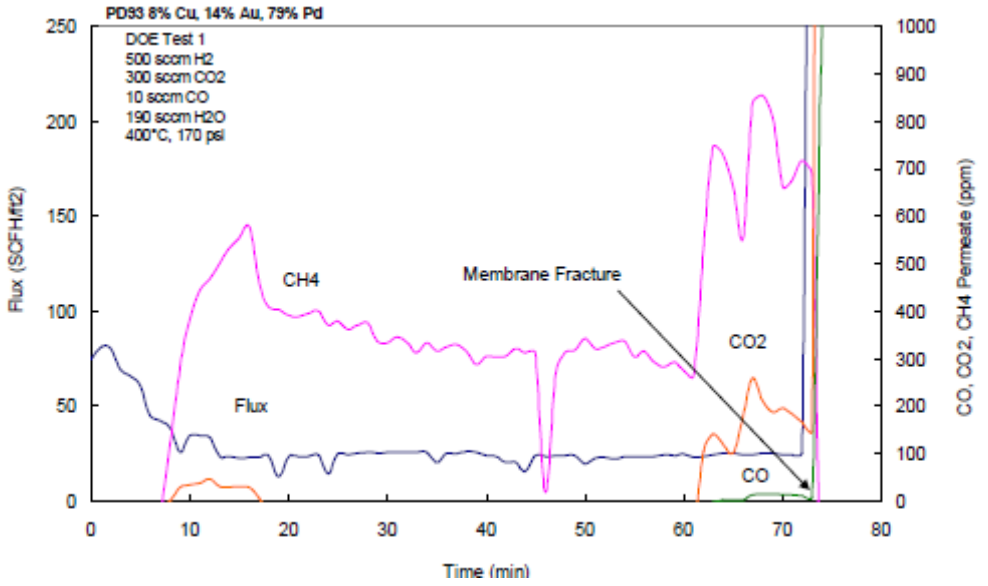

Figure 132. Second test of Pd-93.

A third sample showed results similar to the second, falling after about one hour of testing.

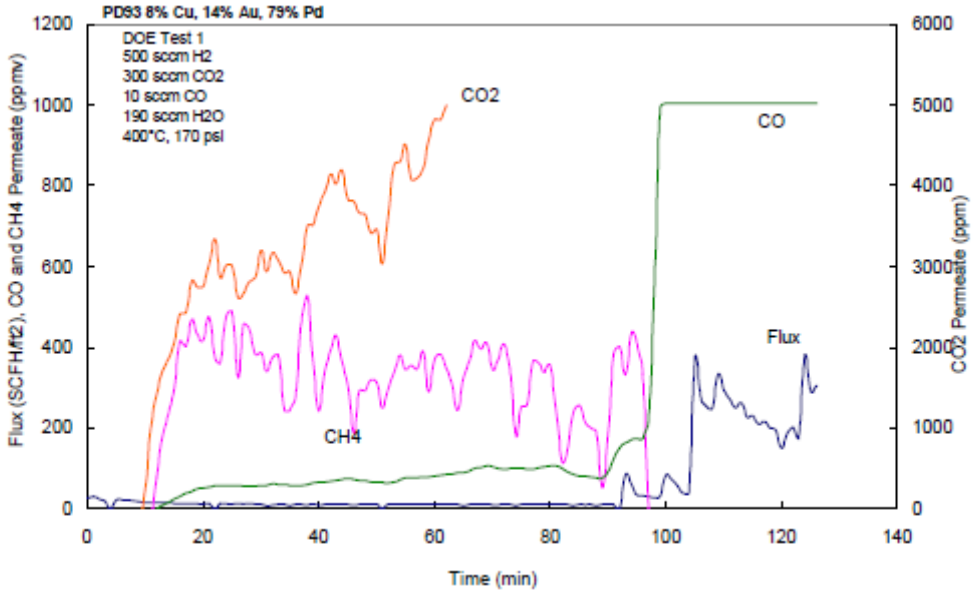

Figure 133. Third test of Pd-93.

A fourth sample showed similar results to the first under DOE1 with no CO or CO_2 detected.

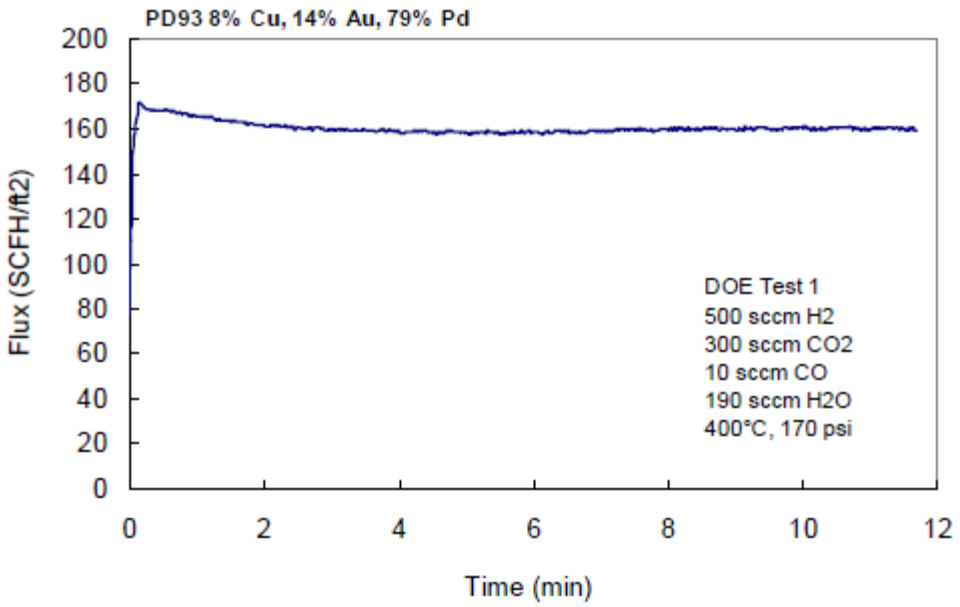

Figure 134. Fourth test of Pd-93.

The fourth test was restarted later and the permeate immediately declined. The pressure drop at around 0.4 hrs into the test was due to the analyzer re-calibration.

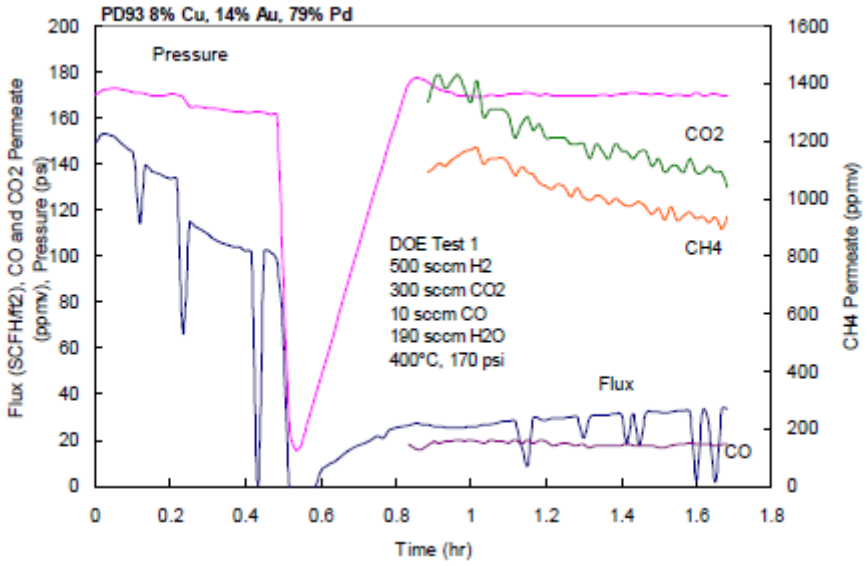

Figure 135. Fourth test re-start of Pd-93.

All of the data from the second DOE1 test for Pd -93 is plotted in Figure 136 and the foil was very sensitive to pressure change.

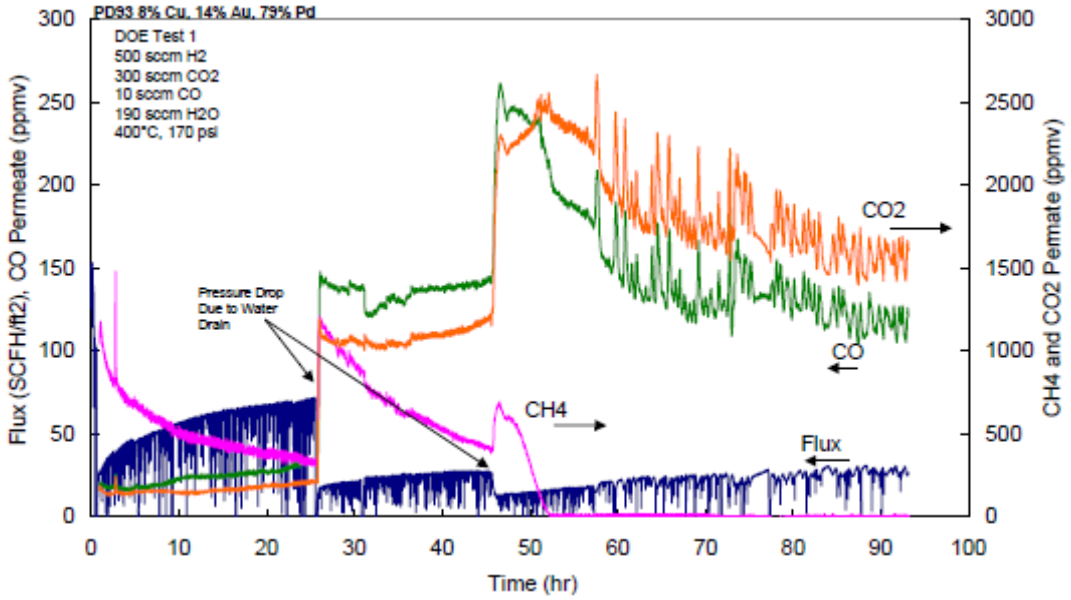

Figure 136. All of the Fourth test data for Pd-93.

The results from the DOE2A test (20 ppmv sulfur) for Pd-93 are shown in Figure 137.

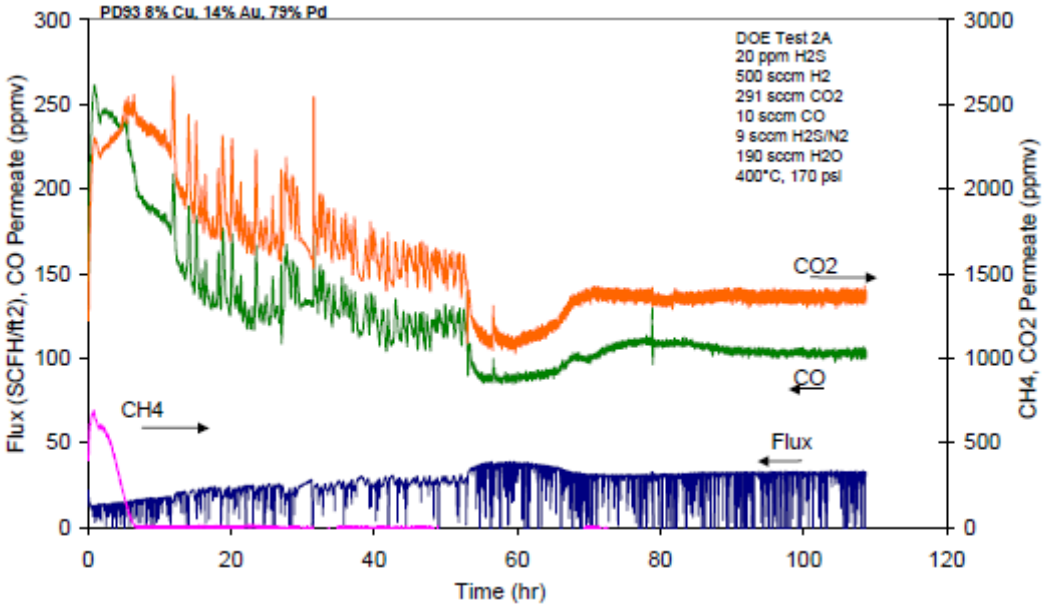

Figure 137. DOE Test 2A for Pd-93.

Two samples of membrane Pd-93 were characterized by SEM/EDS after WGS and WGS +H_2S experiments. Their compositions by EDS are reported below; post-mortem analyses on samples of membrane SwRI Pd-93 after mixture gas permeation experiments.

Table 40. PdCuAu composition following exposure

Membrane	Removed August 12		Removed August 19	
Side	**Feed**	**Reject**	**Feed (without contaminants)**	**Reject (without Al)**
Pd (wt %)	84.1	81.0	30.6 (76.8)	77.7 (82.5)
Au (wt %)	12.4	15.3	5.0 (12.5)	11.1 (11.8)
Cu (wt %)	2.0	3.0	.4 (1.0)	5.3 (5.7)
S (wt %)	1.5	0.7	3.7 (9.2)	-
O (wt %)	-	-	50.9	-
Si (wt %)	-	-	1.2	-
Mg (wt %)	-	-	4.5	-
Ca (wt %)	-	-	3.6	-
Al (wt %)	-	-	-	5.9

The most notable result is that the membrane sample was heavily oxidized, as well as being contaminated on its feed side with light elements (tentative peak assignments were given to silicon, magnesium, and calcium). Both whiskerlike and globular structures were observed under SEM, although EDS could not resolve compositional differences in them (Figure 138). The permeate side of this sample had a strong aluminum signal, presumably due to the aluminum oxide diffusion barrier paper adhering to the surface. Neither of these phenomena has been observed previously.

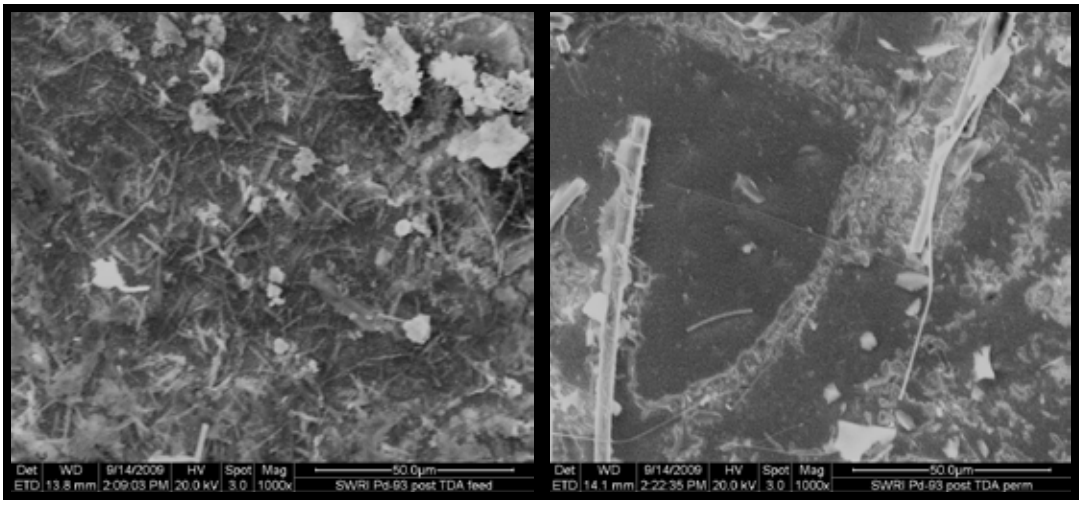

Figure 138. 1000x SEM micrographs of the feed and permeate sides of the August 19 sample of SwRI Pd-93.

Both membranes had distinctive sulfur signals on their feed surfaces. Previous EDS experiments on Pd-Au membranes have not shown any sulfur signal despite the presence of sulfide forms, due to the lack of sensitivity of the detector for such a light element. This suggests that the addition of copper may depress sulfur resistance in PdAu alloys. In addition, the feed sides of the membranes were copper-depleted. Initial membrane composition averaged $Pd_{82}Cu_6Au_{12}$ by weight, whereas the tested membrane feed sides ranged from 1-2 wt% Cu. No equivalent segregation has been observed for copper in pure-gas mixtures.

Following the DOE Test 2A, all of the membranes had lifted up off the support and the surfaces also appeared roughened and were no longer mirror-like. TDA continued testing with a binary Pd(90)Au(10) sample. The results of DOE test 1 conditions are shown below.

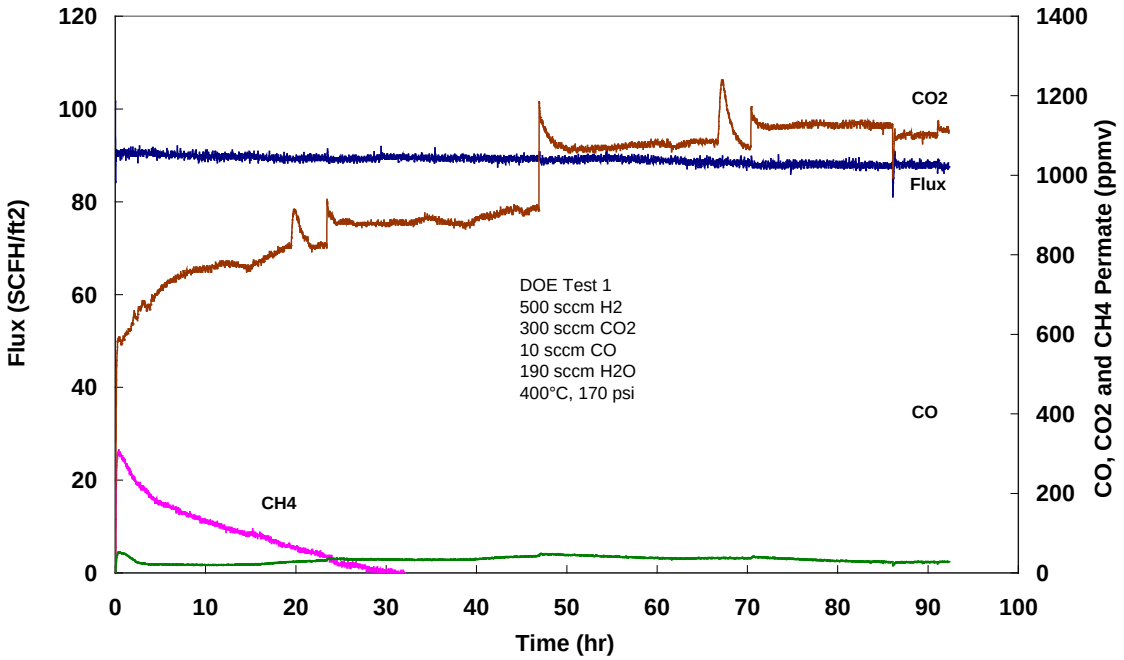

Figure 139. Evaluation of Pd-126 under DOE Test Condition #1.

While a relatively high flux was maintained the membrane appeared to degrade over time. The same sample was then exposed to test condition #2.

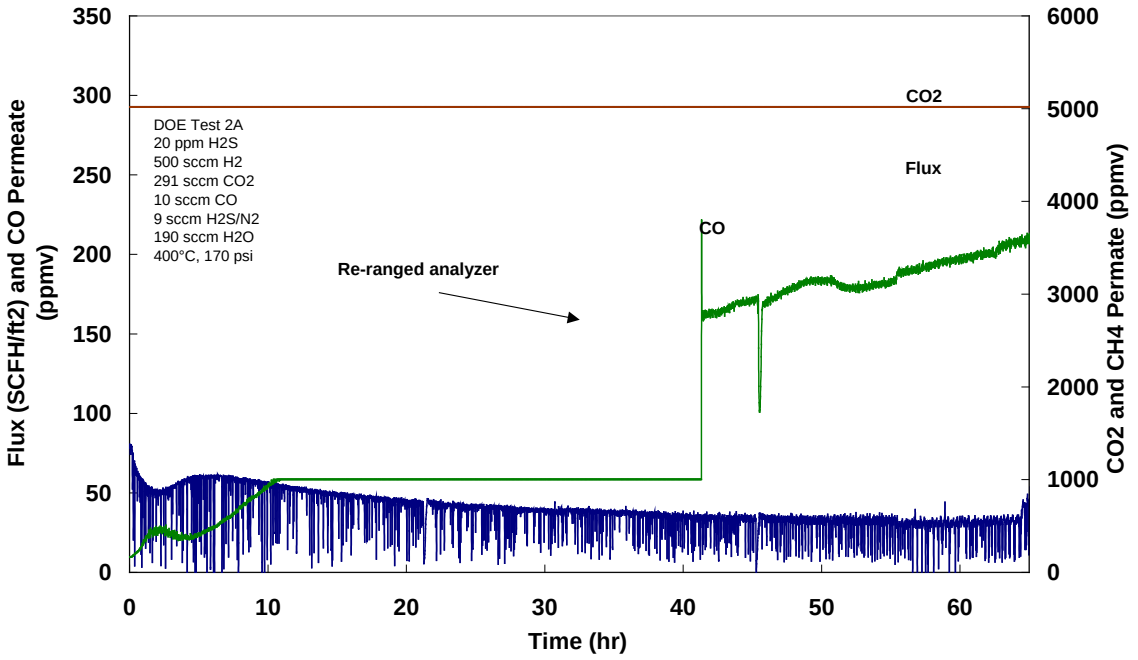

Figure 140. Evaluation of Pd-126 under DOE Test Condition #2.

IdaTech tested a sample from the Pd-127 lot following their conventional conditioning process; at the end of which there were no leaks. Started running on 100 psig hydrogen and observed twice the performance that CSM had observed in their testing. They shut down the furnace and restarted testing the following morning and discovered a massive leak after pressurizing with hydrogen. Not sure if the performance results IdaTech got were real or due to a leak. Pictures of the foil – before and after testing and a typical rolled foil test sample are shown below. Not sure what to make of the appearance of the foil - since it started out flat and was fully constrained, not sure where the excess material came from to form the ridges.

Figure 141. Pd-127 following testing and a standard cold rolled foil.

One observation IdaTech made is that SwRI deposited films are much more brittle than rolled materials. If IdaTech folded SwRI films, they cracked. If IdaTech folded rolled material they just formed a wrinkle. IdaTech tested Pd-128 following the same procedure used on Pd-127. The same high fluxes were obtained on Pd-137, but when a leak test was performed at the end of the test a big leak was found, so the performance is suspect. The appearance of the tested foil is different than Pd-128, but there is a crack in the foil on top of a ridge/wrinkle in the foil. General observation is that the deposited films are much more brittle than rolled foil.

Figure 142. Crack in Pd-128 following testing.

IdaTech tested another sample from Pd-127 and was able to get H_2 permeability measurements (with leak rate measurements), but the membrane failed when it was exposed to synthetic coal gas. Pictures of the foil after testing are shown below and the same orange peel appearance as the first sample. The foil had that appearance after the H_2 testing. Interestingly, the Pd-128 sample didn't have that degree of orange peel. Another Pd-128 was tested with a slower ramp rate on the heating (currently 500 ºC/hr – standard ramp rate) and IdaTech also tried applying pressure during the heat up to try and lock the foil down to the support. The hydrogen permeabilities these tested samples were: Pd-127 sample 1 = 1.58×10^{-4} $cm^3/cm/s/cmHg^{\wedge 0.5}$, Pd-128 sample 1 = 1.53×10^{-4} $cm^3/cm/s/cmHg^{\wedge 0.5}$ and Pd-127 sample 2 = 1.55×10^{-4} $cm^3/cm/s/cmHg^{\wedge 0.5}$.

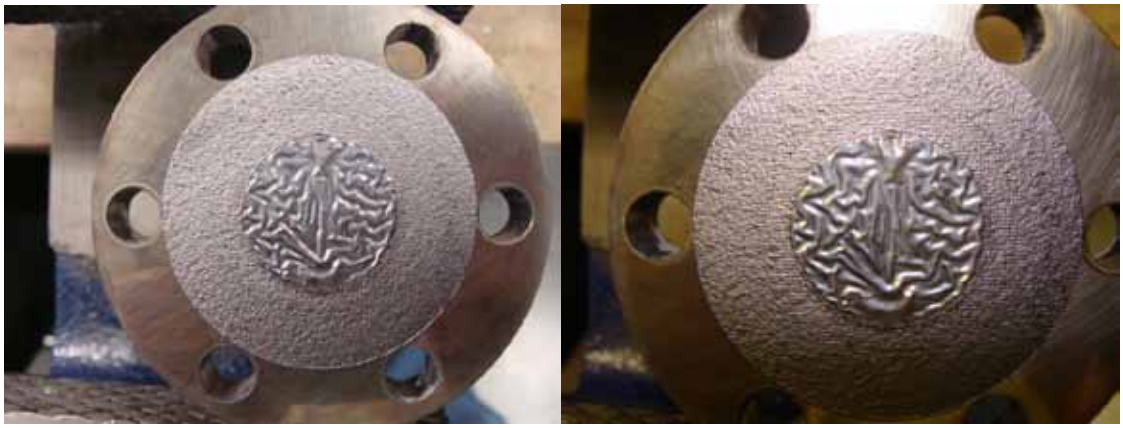

Figure 143. Pd-127 after testing.

The permeability was compared for the same Pd-126 membrane with data from CSM. The Pd-128 membrane data was collected at 80psig H_2 and the nominal composition was 89%Pd with the balance Au. The comparison is shown below.

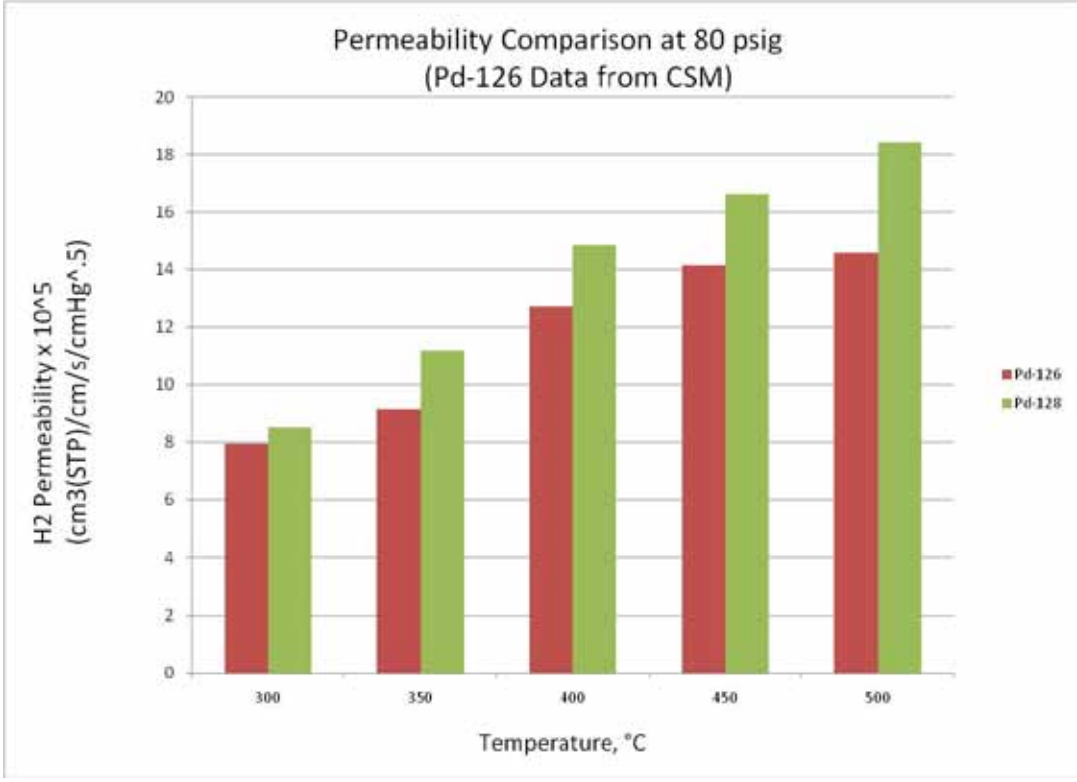

Figure 144. Permeability comparison of Pd-126 (CSM Data) and Pd-128.

Below is plotted the Pd-126 data from CSM, cold rolled foil data, and the Pd-128 H_2 permeability collected at 80 psig H_2. The nominal composition of Pd-128 is 89%Pd, with the balance Au and a nominal thickness of 33 µm. The standard temperature of 0 ºC was used for the calculations. The synthetic coal gas contained 50ppm H_2S and the Pd-128 H_2 purity during synthesis gas exposure ranged from 97% to 98% while the membrane was leak tested before and after testing (0.01cc/s – fluxes 0.85 to 1.4cc/s). The comparative performance of the membrane is shown below in Figure 145.

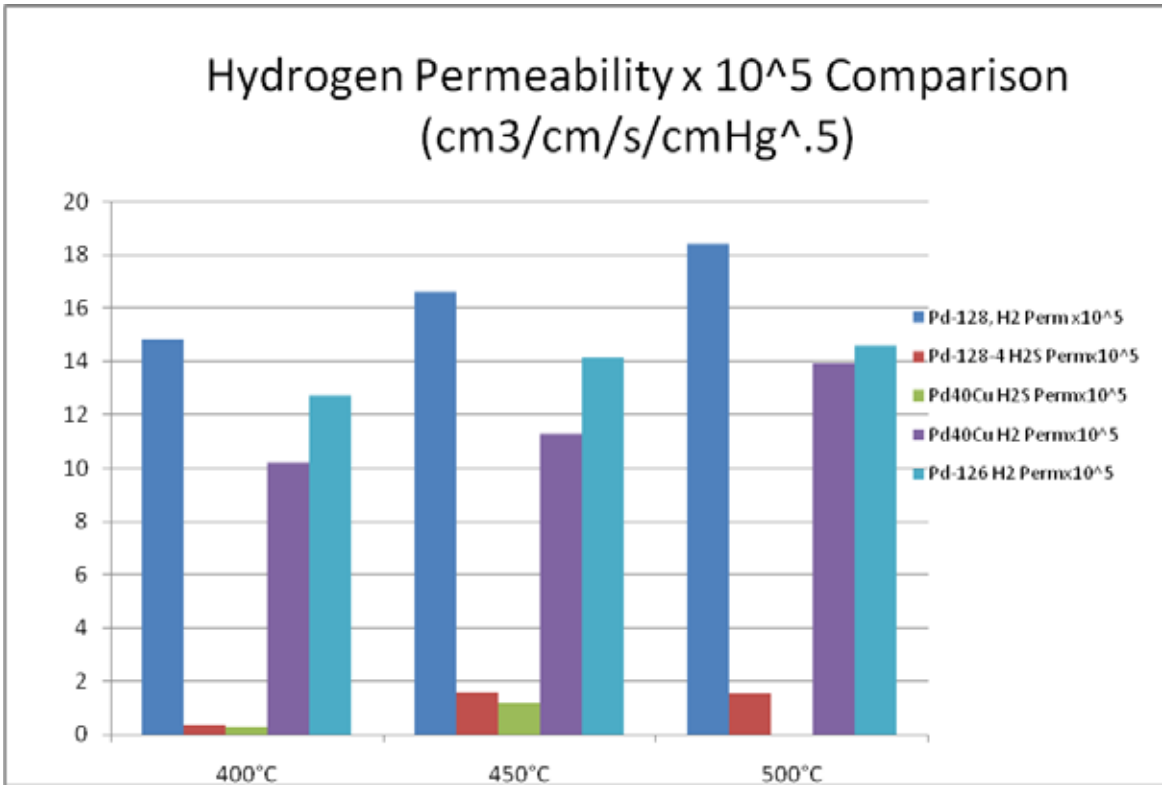

Figure 145. Pd-126 data from CSM and the Pd-128 H_2 permeability.

IdaTech tested membrane Pd-94, which appeared more durable than those previously tested – no wrinkles or cracks. The thickness of Pd-94 was 15 µm. The synthetic coal gas contained 50ppm H_2S. Membrane Pd-94 exhibited purity less than 96%; fluxes 0.28 to 0.08cc H_2/s at 400 ºC, 450 ºC and 500 ºC. Permeability decreased with increasing temperature as shown below.

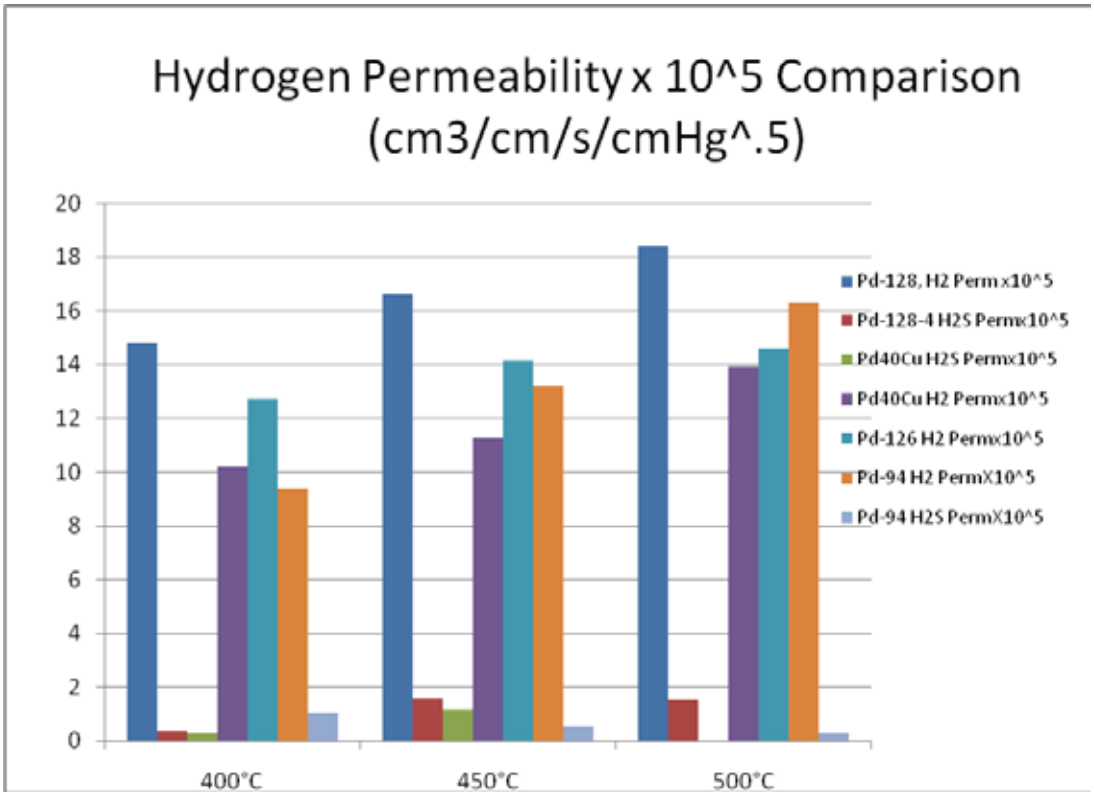

Figure 146. Pd-94 H_2 permeability collected at 100 psig H_2.

IdaTech tested Pd-69 with the first sample giving good results on H_2S with low air leak rate at end of test (4.3 cc/min vs 45 cc/min hydrogen flux although only 93% purity). The sample was retested and again got good results but the air leak test at the end of testing was high (72 cc/min vs 58 cc/min hydrogen flux). IdaTech tested a second sample which developed pinholes during heat up.

To establish a baseline, IdaTech tested multiple samples of TKK Pd40Au.

For the PdAuPt series, Pd-143 was tested and achieved stable hydrogen fluxes under pure hydrogen at 400 ºC and 450 ºC, but at 500 ºC the flux kept increasing. A comparison of the permeability for Pd-143 is shown below.

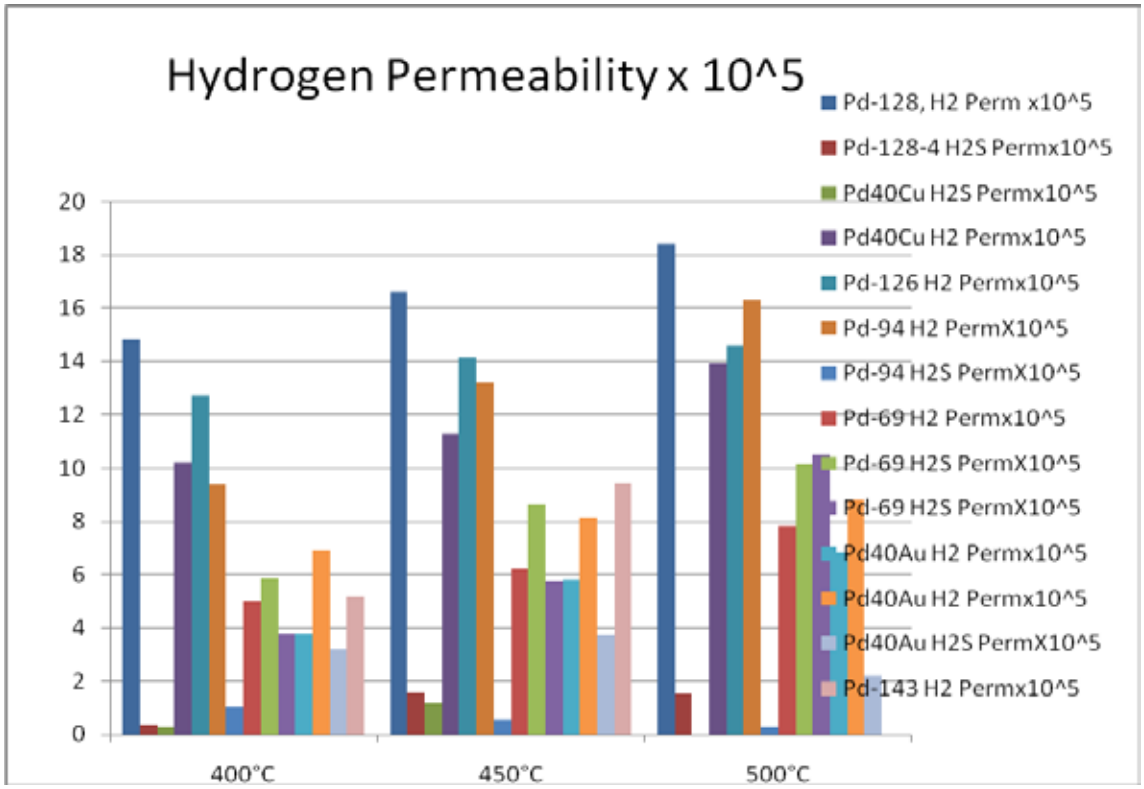

Figure 147. Permeability comparison for several foils of various compositions.

Conducted air leak test and found high leak rate. After test fixture disassembly found 12 pinholes.

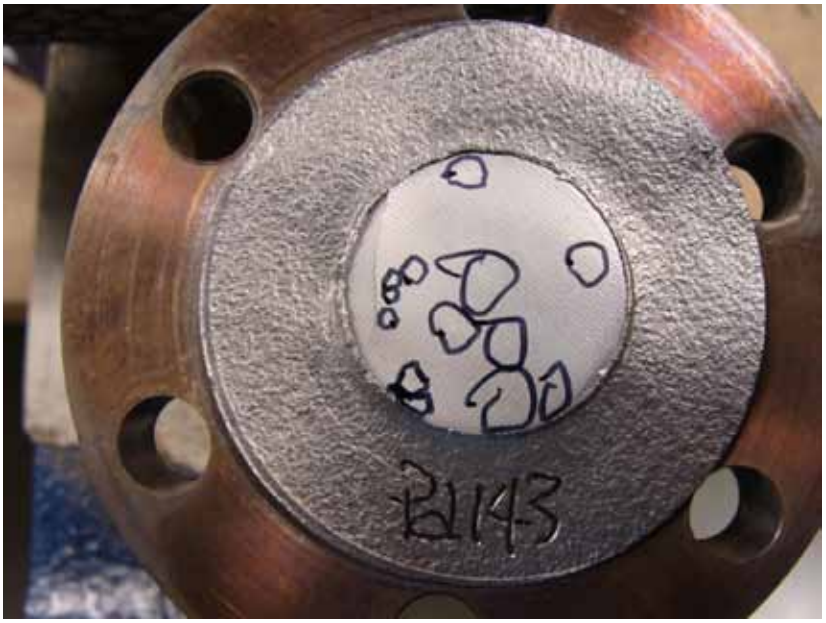

Figure 148. Pd-143 with visually identifiable pinholes circled.

The membrane was brittle after testing a crack formed during disassembly of the test fixture. There was concern that some of the test data was suspect because of measured N_2 leak rates at the end of testing. Not sure when the pinhole formation is occurring. Does order of testing impact results – i.e. increasing or decreasing temperature? The sample was returned to SwRI for SEM characterization of the identified pinholes. The following are images of 4 different types of defects identified in the foil.

Type 1

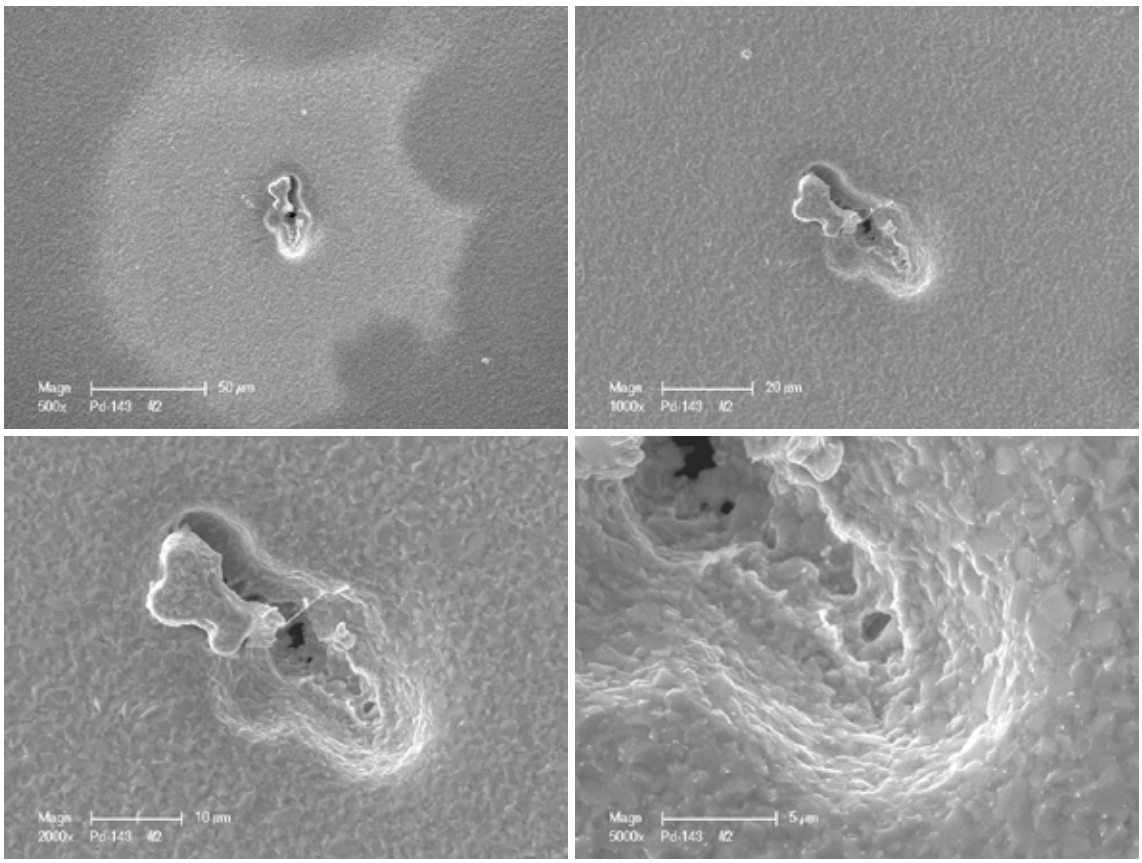

Figure 149. Type 1 defects at higher magnifications for Pd-143.

Type 2

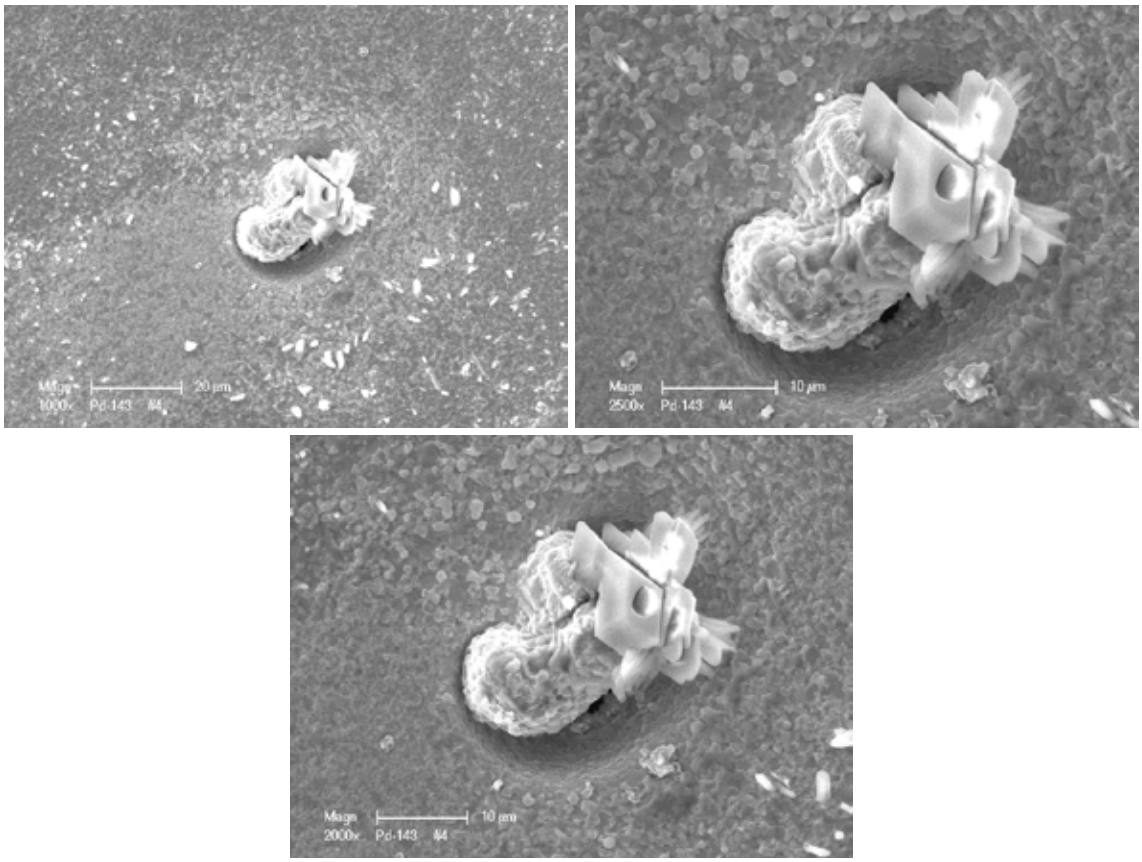

Figure 150. Type 2 defects at higher magnifications for Pd-143.

Type 3

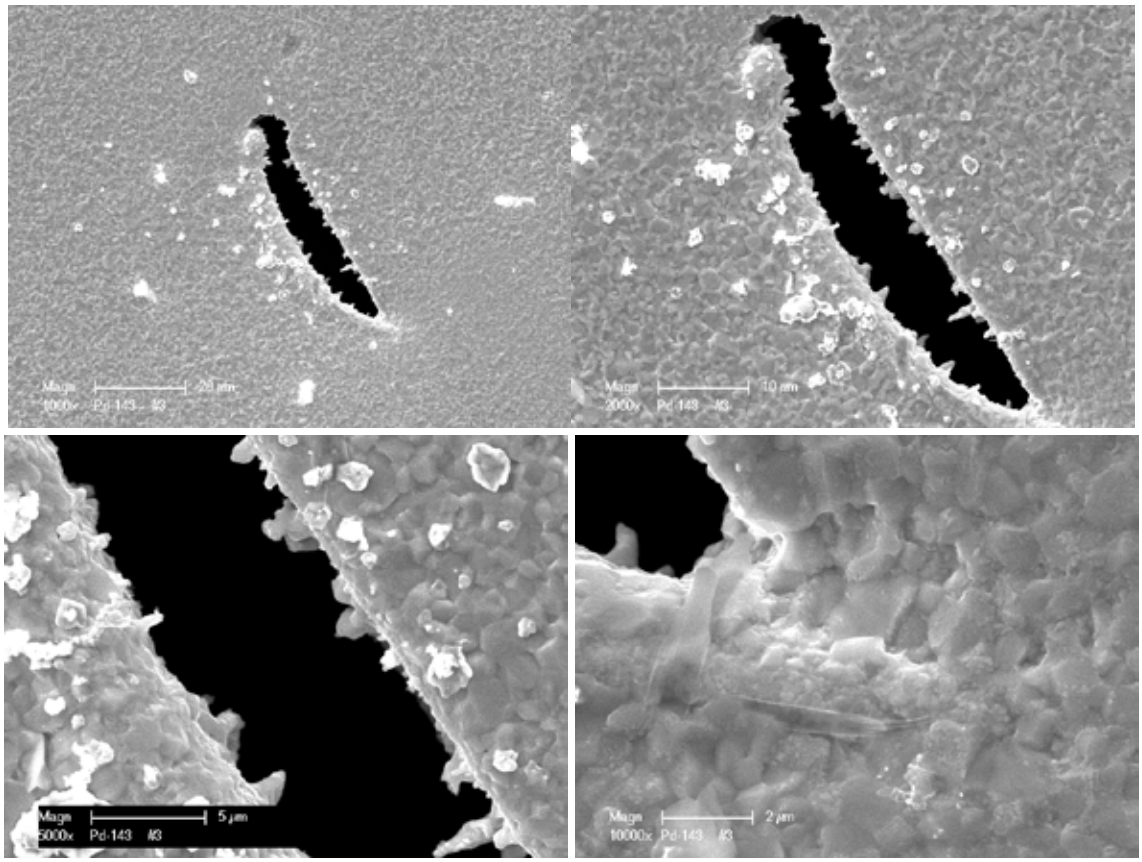

Figure 151. Type 3 defects at higher magnifications for Pd-143.

Type 4

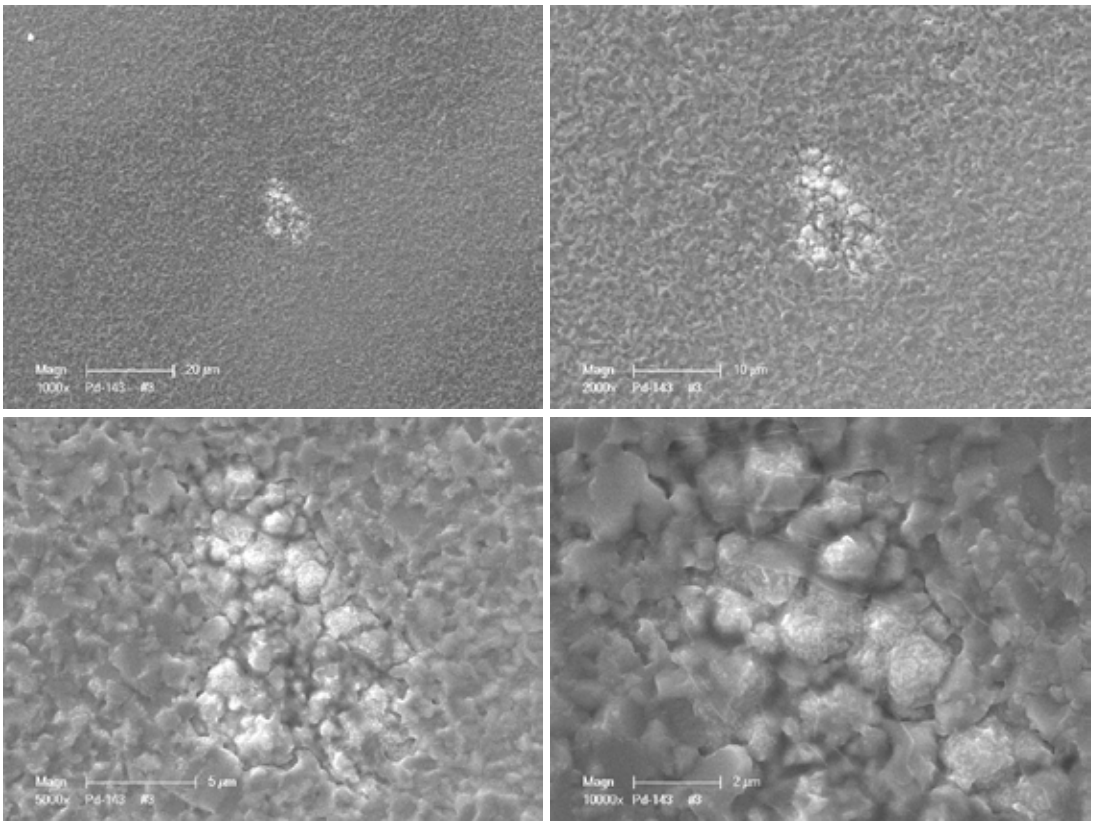

Figure 152. Type 4 defects at higher magnifications for Pd-143.

IdaTech attempted to run several foils and identified a significant formation of pinholes during the course of running. A good example is the cluster of pits in the foil material Pd-72. This is the highest density of pitting observed, magnified 200X.

IdaTech tested 2 samples from Pd – 152 and 2 from Pd – 157 has become good at making little pieces of membrane. Images of the fractured membranes are shown in Figure 154.

Figure 153. Pd-152 following heat up.

The first membrane from Pd-152 was ramped at 100 ºC/hr at 100psig air and fractured during heat up. The second membrane was ramped at 100 ºC/hr, exposed to air (ambient) after reaching 400 ºC and 100 psig air applied, which resulted in an immediate fracture.

Figure 154. Pd-157 following pressurization with hydrogen.

For Pd-157, the membrane was ramped at 100 ºC/hr under 100 psig air. After reaching 400 ºC the membrane exhibited a 5 sccm leak rate. Then 100 psig of H_2 was applied and the flux increased over the next 1.5 hours. The furnace was shut down, and the next day it was ramped at 100 ºC/hr ramp under ambient air. After reaching 400 ºC, 100 psig of H_2 was applied and the membrane fractured. The second sample was heated to 400 ºC (100 ºC/hr ramp) under ambient air but at 400 ºC the leak rate started at 20 sccm and increased to 70 sccm which was too high and the membrane was removed from testing.

Foil Pd-158, a $Pd_{69}Pt_{10}Au_{21}$ alloy of 33.2 microns in thickness was given to TDA for mixed gas permeation testing. The foil was mounted in the same style and type of housing in pure gas tests as described above. It was then tested under DOE-developed synthetic water gas shift mixtures, with and without sulfur, as described in Table 41.

Table 41. DOE mixed gas permeation test conditions

	DOE 1	DOE 2A
Temperature (K)	673	673
Pressure (kPa)	1253	1253
H_2S (ppm)	0	20/50
Feed gas compositions (at%)		
H_2	50.0	51.0
CO_2	30.0	29.0
H_2O	19.0	19.0
CO	1.0	1.0

The membrane was tested under mixed-gas conditions for a total of 160 hours, shown in Figure 155 below. The flux was allowed to stabilize under DOE condition 1 for 40 hours, at which time 50 ppm H_2S was incorporated into the feed stream. The membrane was kept at this condition (DOE 2A) for 100 hours, at which point the feed was returned to DOE condition 1 until the end of the experiment. The membrane maintained acceptable hydrogen selectivity for approximately 90 hours under sulfur conditions, thirty hours longer than any other sputtered membrane tested to this point. The average hydrogen permeate purity during the H_2S test was 99.7%.

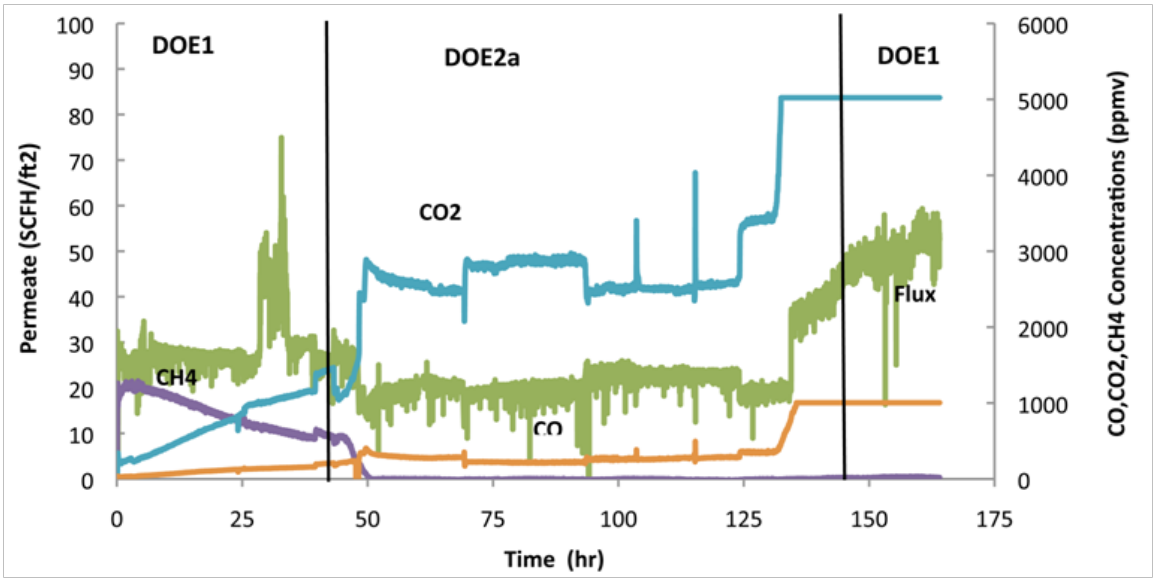

Figure 155. Mixed gas permeation test of a sputtered $Pd_{69}Pt_{10}Au_{21}$ 33 μm thick at 182 psia feed pressure and 400 °C.

The hydrogen permeability, as observed for other membranes, was depressed both by water-gas shift mixtures and by H_2S (Figure 156). However, the permeability under the water-gas mixture with sulfur was 49% of the pure-gas permeability, better than any previously tested sputtered membrane. From this it appears that either high quantities of gold or the presence of platinum, or both, are inhibiting sulfide formation, thereby improving both permeability and stability under mixture gas conditions.

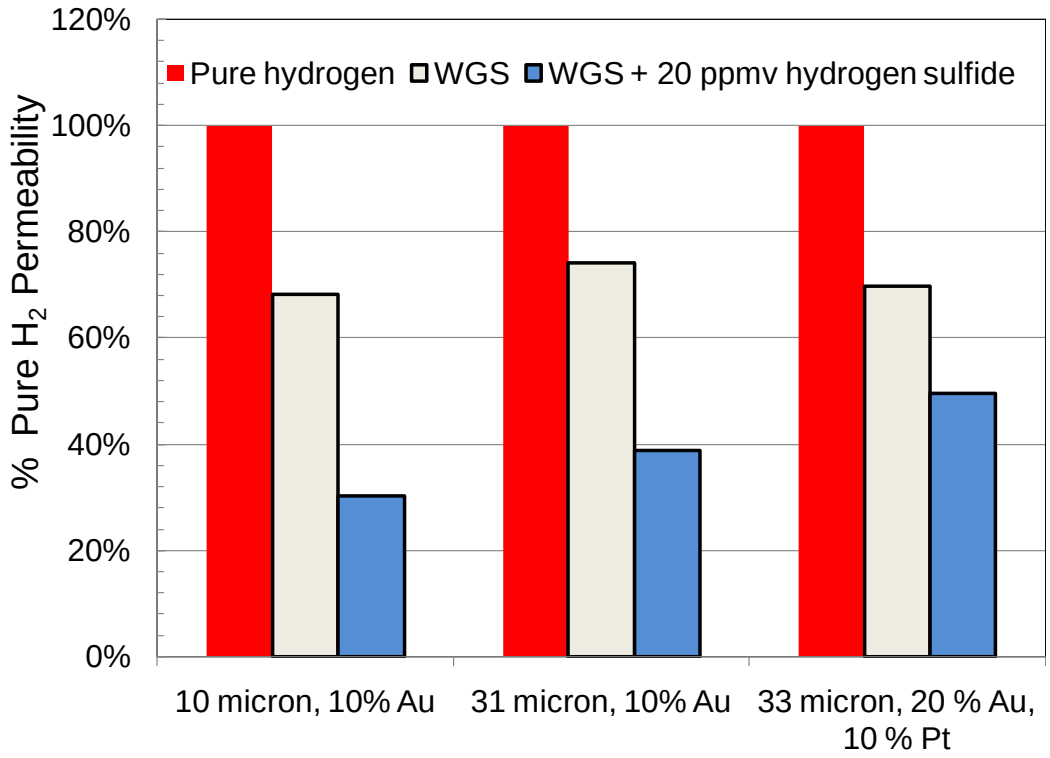

Figure 156. Inhibition of hydrogen permeability by water-gas shift mixtures with and without sulfur for sputtered membranes.

IdaTech continued to struggle with foil ruptures during heat up and conditioning. The following images show single and double layered foils that all cracked. Interestingly, the double layer foil crack was in the same location on both foils, suggesting a stress concentrator in the mounting seal.

Figure 157. Pd 67- 2 (Two layers of Pd-67 - After Heat-up and Initial Pressurization).

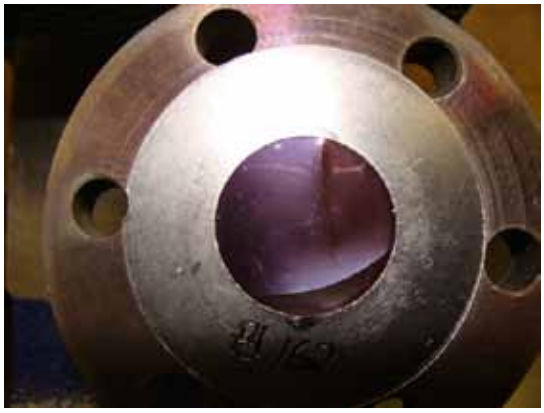

Figure 158. Pd 162-1 (After Heat-up and Initial Pressurization).

Figure 159. Pd 67 (After Heat-up and Initial Pressurization).

In addition, upon initial inspection of the foils that had been annealed at SwRI in a reducing atmosphere, these also showed cracks even prior to loading them into the pressurized cell apparatus. This suggests that the grain boundary defects are inherent in the film prior to being loaded into the cell.

Figure 160. Pd 162 (Cracks Observed Upon Initial Examination).

While IdaTech struggled with membranes breaking, the following table summarizes the measured permeabilities of several of the foils that were able to be successfully tested.

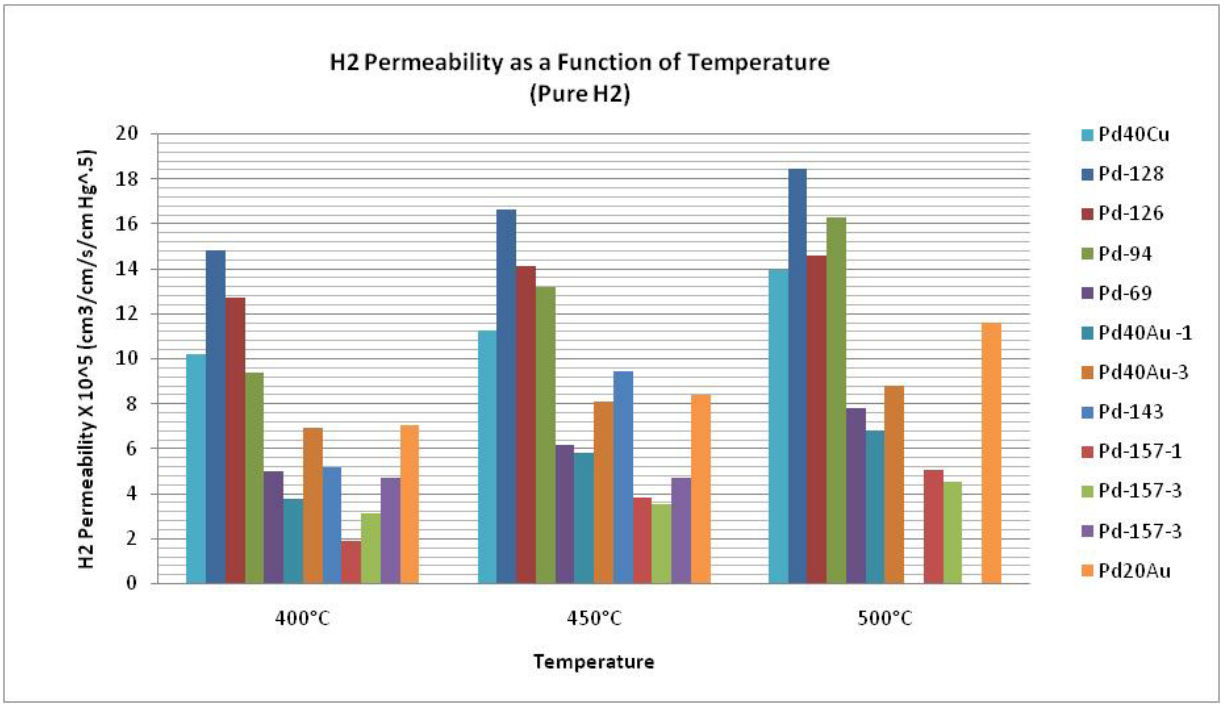

Figure 161. Summary of H_2 Testing.

In addition, per the year III program milestones, several foils were tested under H_2S and syngas environments. The year III milestone of producing a minimum of 5 sq. ft. of optimized membrane material for mixture permeation testing with H_2/CO and H_2/H_2S binary mixtures with the best three samples from the final optimization study was completed.

Over the course of the project, TDA received more than 15 different membrane foils from SwRI. Table 42 provides a summary of all tests we carried out during the project. The table shows the progress in quality of the membranes over the course of the project. There were 16 different foils tested, several of them multiple times. Several of the membranes proved to be too fragile to handle and to be loaded into the test module for testing. There were, however, several compositions that showed very good performance and high tolerance to the presence of sulfur. The details associated with the testing of these good membranes are provided below.

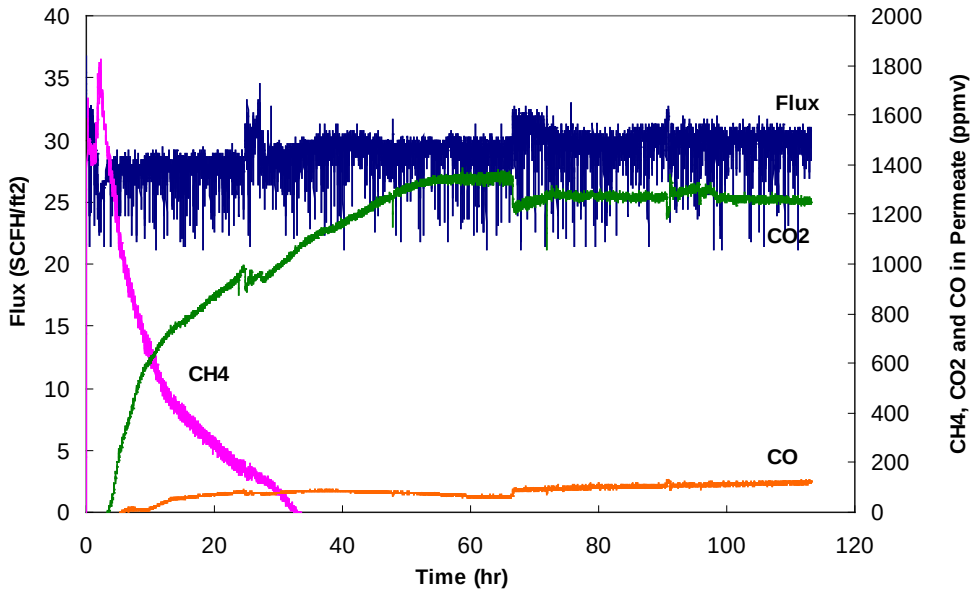

Figure 162. Results of testing Pd-158 under DOE1 conditions. Testing done at 400°C, 170 psi, 50% H_2, 30% CO_2 19% H_2O and 1%CO. Total inlet flow 1000 sccm.

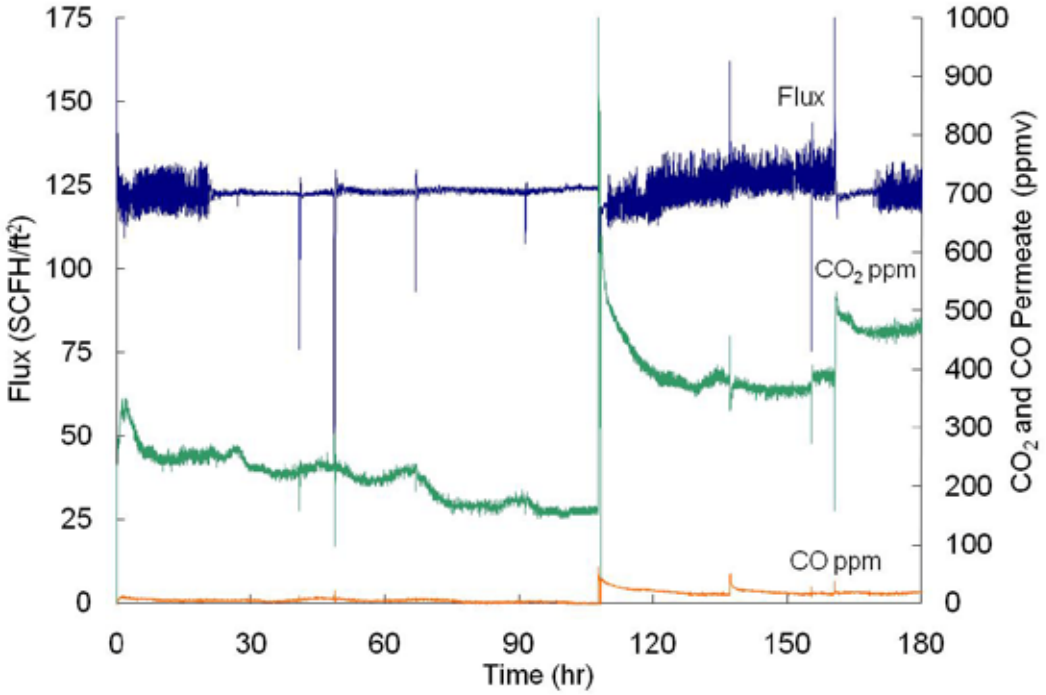

Figure 163. Flux and permeate gas purity profiles for membrane Pd-48, 10% Au, 90% Pd. Testing done at 400°C, 170 psi, 50% H_2, 30% CO_2 19% H_2O and 1%CO. Total inlet flow 1000 sccm.

The first foil that showed good separation performance in the DOE 1a mixture was the Pd-48 membrane (Figure 165). This membrane had a composition of 10% Au and 90% Pd, a composition usually considered for H_2 separation from sulfur containing synthesis gas due to its resistance to poisoning. The hydrogen flux and selectivity in the clean gas experiments were among the best in this series of tests. The flux remained consistent at 125 SCFH/ft^2 and the CO and CO_2 concentrations in the permeate remained at very low levels throughout the test (5 ppmv and 200 ppmv respectively). These performance characteristics were maintained for 100 hrs with no sign of degradation. However, about 100 hours into this test there was an unplanned shutdown. Both the CO and the CO_2 show a jump midway through the test, this was due to a computer malfunction that required the test to be very briefly shut down causing a loss of pressure and the test gases to be shut off. Even with this interruption, the CO and CO_2 concentrations in the permeate remained low, producing a purity that exceeded DOE/NETL's minimum purity requirements.

Another foil that showed good results in the DOE 1 gas mixture was the Pd-93 composition (85% Pd, 10%Au, 5% Cu). This foil (as shown in Figure 164) showed particularly good separation, the CO levels were undetectable in the permeate hydrogen and the CO_2 remained constantly low throughout the test at 200 ppmv. The flux through the membrane also remained high at an average of 120 SCFH/ft^2 throughout the 120 hour experiment, with no signs of degradation.

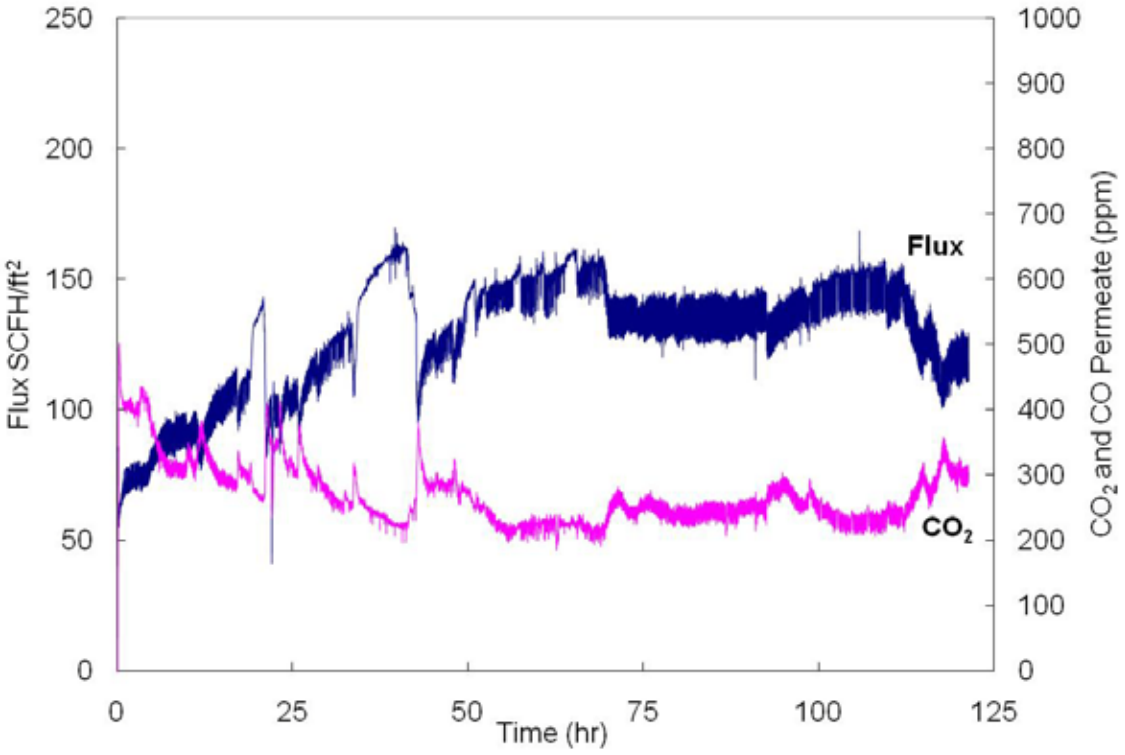

Figure 164. Flux and permeate gas purity profiles for membrane Pd-93, 85% Pd, 10% Au, 5%Cu. Testing done at 400ºC, 170 psi, 50% H_2, 30% CO_2 19% H_2O and 1%CO. Total inlet flow 1000 sccm.

Table 42. Summary of the tests done with the SwRI foils

Membrane	Composition	Dates Tested	Conditions Tested	Initial DOE1 Flux	Stable Selectivity	Comments
Pd-25	85% Pd, 14.6% Au	3/24/09-3/30/09	None	N/A	N/A	Install failed, foil crinkled, spider cracked when spread out
Pd-48	90% Pd, 10% Au	2/20/09-3/13/09	183 hrs DOE 1, 89 hrs DOE 2A	~125 scfh/f^2	~20 ppmv CO,~375 ppmv CO_2	Failed during test 2a
Pd-126	10% Au 90% Pd	9/11/2009-9/30/09	DOE1,DOE2A,	~88 scfh/ft^2	~40 ppmv CO, ~1125 ppmv CO_2	Pump problems during testing, membrane split during 2A
Pd-126	10% Au 90% Pd	10/09/09-10/23/09	DOE1,DOE2a	N/A	N/A	Lost Data, membrane broke DOE1 62 sccm perm, 382 ppmv CO_2, no CO
Pd-51	75% Pd, 17% Cu, 8% Au	2/2/09-2/10/09	None	N/A	N/A	Failed after 10 min on test 1
Pd-74	70% Pd, 13% Au, 17% Cu	4/2/09-4/14/09	50 hrs. DOE 1	~80 scfh/ft^2	~1628 ppmv CO, ~3000 ppmv CO_2	Failed during test 1
Pd-93	85% Pd, 10% Au, 5% Cu	7/10/09-8/5/09	DOE1, High CO, DOE 2A,	~140 scfh/ft^2	~250 ppmv CO_2	Rig problems during H_2S test, 1.5 hr testing
Pd-67	70%Pd, 17%Cu, 13%Pt	10/07/09-10/08/09	None	N/A	N/A	Membrane leaking at temperature
Pd-93	85% Pd, 10% Au, 5%Cu	8/7/2009-8/10/09	DOE1	~ 25 scfh/ft^2	~300 ppmv CH_4	Membrane broke during DOE1

Membrane	Composition	Dates Tested	Conditions Tested	Initial DOE1 Flux	Stable Selectivity	Comments
Pd-93	85% Pd, 10% Au, 5% Cu	8/12/2009-8/17/09	DOE1	~10 scfh/ft^2	~350 ppmv CH_4, 80 ppmv CO, CO_2 OOR	Membrane broke during DOE1
Pd-93	85% Pd, 10% Au, 5% Cu	8/19/2009-9/9/09	DOE1,DOE2a, DOE1	~ 70 scfh/ft^2	200 ppmv CO_2, 25 ppmv CO, 340 ppmv CH_4	Tested well, recovered some performance after DOE2a test
Pd-54	78.7% Pd, 17.6% Cu, 3.7% Pt	4/15/09-4/22/09	None	N/A	N/A	Reactor leaking
Pd-67	70%Pd, 17%Cu, 13%Pt	10/02/09-10/05/09	None	N/A	N/A	Membrane leaking at temperature
Pd-67	70%Pd, 17%Cu, 13%Pt	10/5/2009-10/07/09	None	N/A	N/A	Membrane leaking at temperature
Pd-68	70%Pd, 17%Cu, 13%Pt	10/23/2009-11/02/09	DOE1,DOE2A	~55 scfh/ft^2	~690 ppmv CO_2, ~100 ppmv CO	Rig shut down, shorting out furnace.
Pd-68	70%Pd, 17%Cu, 13%Pt	11/02/06-11/06/09	none	N/A	N/A	Module shorting out furnace
Pd-68	70%Pd, 17%Cu, 13%Pt	11/06/09-11/11/09	DOE1	~60 scfh/ft^2	~625 ppmv CO_2, ~100 ppmv CO	Broken quickconnect causes overpressurization
Pd-68	70%Pd, 17%Cu, 13%Pt	12/28/09-12/30/09	None	N/A	N/A	Membrane broke during ramp,

Membrane	Composition	Dates Tested	Conditions Tested	Initial DOE1 Flux	Stable Selectivity	Comments
Pd-68	70%Pd, 17%Cu, 13%Pt	12/30/09-01/01/10	None	N/A	N/A	Oven TC off, temps too high, reactor leaking, preventing pressurization.
Pd-141	90% Pd, 5% Pt, 5% Au	12/16/09-12/21/09	DOE1	~100 scfh/ft^2	~41 ppmv CO_2	Membrane broke during DOE1 after about 32 hrs
Pd-142	90% Pd, 5% Pt, 5% Au	12/21/09-12/28/09	DOE1	~80 scfh/f^2	~180 ppmv CO_2	Membrane broke during DOE1 test after about 72 hrs.
Pd-147	Pd/Au/Pt	1/15/10-1/22/10	DOE1,DOE2A	~45 scfh/ft^2	~2000 ppmv CO_2	Steady decline in performance under DOE1, broke under DOE2a after a few hours
Pd-158	70% Pd, 20% Au, 10% Pt	4/21/10-4/28/2010	DOE1	~30 scfh/ft^2	~1250 ppmv CO_2, ~120 ppmv CO	
Pd-158	70% Pd, 20% Au, 10% Pt	5/24/10-06/02/10	DOE1, DOE2A	~28 scfh/ft^2	~1250 ppmv CO_2, ~154 ppmv CO,600 ppmv CH_4	Membrane developed a hole during DOE2a testing.
Pd-165	Pd/Au/Pt	10/25/10-11/02/10	DOE1, DOE2A	~55 scfh/ft^2	~450 ppmv CO_2, ~50 ppmv CO,270 ppmv CH_4	Membrane broke during safety shutdown
Pd-165	Pd/Au/Pt	11/3/10-11/4/10	None	N/A	N/A	Membrane broke while being brought to temperature
Pd-165	Pd/Au/Pt	11/5/10-11/19/10	DOE1, DOE2A	~65 scfh/ft^2	~650 ppmv CO_2, ~120 ppmv CO	Membrane recovered flux levels after H_2S testing, CO, CO_2 levels rose during H_2S, but didn't decrease after.

Membrane	Composition	Dates Tested	Conditions Tested	Initial DOE1 Flux	Stable Selectivity	Comments
Not given	70%Pd, 15%Cu, 15%Au	12/10/10-12/12/10	None	N/A	N/A	Membrane broke while being brought to temperature
Not given	70%Pd, 15%Cu, 15%Au	12/13/10-12/14/10	None	N/A	N/A	Membrane broke while being brought to temperature
Not given	70%Pd, 15%Cu, 15%Au	12/14/10-12/15/10	None	N/A	N/A	Membrane broke while being brought to temperature

The membrane foils that exhibited desirable flux and purity in the clean synthesis gas were then evaluated by using the sulfur-laden gas following the second test protocol (DOE Condition 2a). The best foils were exposed to a gas mixture identical to that of the earlier DOE 1a tests except that it contained 20 ppmv H_2S. A summary of the sulfur tests are given in Table 43. Ideally, due to the selected composition, the hydrogen permeation through the membrane would not be inhibited by the sulfur. However if the sulfur did inhibit the permeability of the membrane, we then followed up the sulfur exposure experiment with another test under DOE1 conditions (i.e. clean synthesis gas) to see if the membrane recovered its initial activity and whether the sulfur inhibition was reversible.

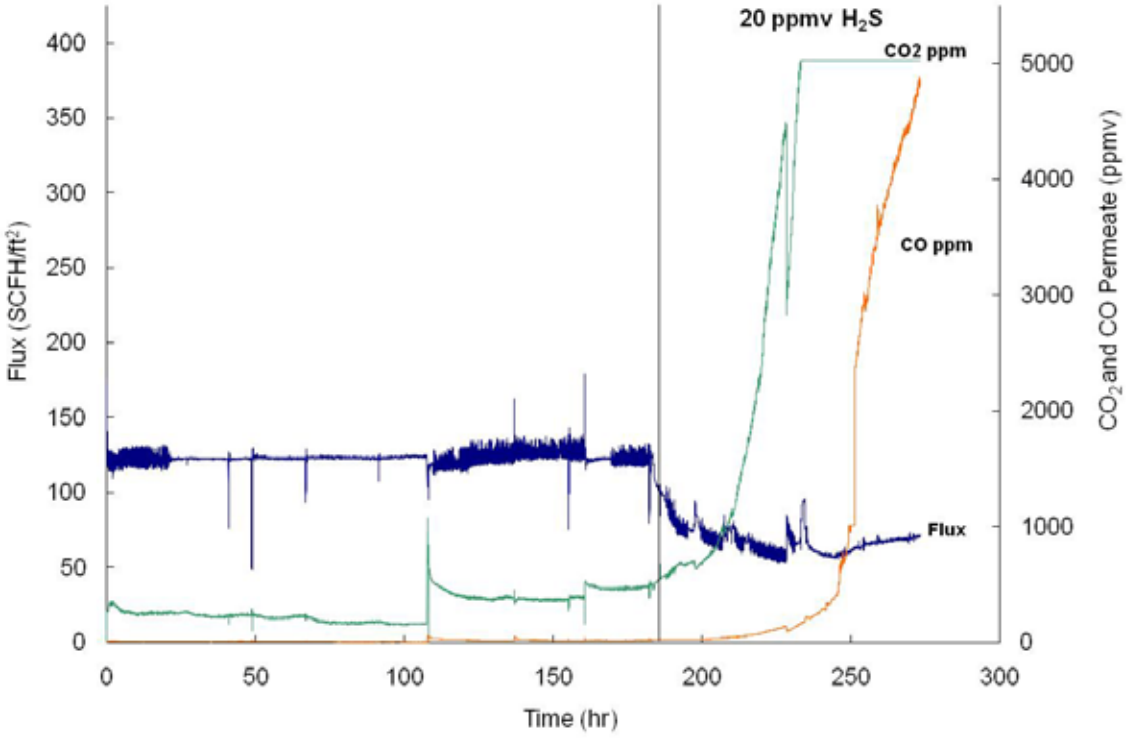

Figure 165. Flux and permeate gas purity profiles for membrane Pd-48, 10% Au, 90% Pd. Testing done at 400 °C, 170 psi, 50% H_2, 30% CO_2 19% H_2O and 1%CO. The second part of the testing added 20 ppmv H_2S into the gas mixture as noted on the figure. Total inlet flow 1000 sccm.

Figure 165 compares the results of the clean gas testing (DOE condition 1) with the sulfur condition (DOE condition 2a) for Pd-48 membrane. We observed a decline in flux when we introduced 20 ppmv sulfur into the feed gas at 170 hours into the test. The drop in the flux was 40-50%, reducing the flux from 125 SCFH/ft^2 to 70 SCFH/ft^2. Worse than the decrease in the flux, we also observed a gradual increase in CO and CO_2 concentration in the permeate gas. CO and CO_2 impurities in the permeate gas suggests that the membrane integrity was compromised.

The results of the sulfur testing on the Pd-93 membrane are shown in Figure 166. The flux observed using the clean gas flux in this test was not as high as observed for the same foil used in an earlier experiment (Figure 155). We speculate that this was because this sample was taken from a different section of the foil that has different film thickness and perhaps composition.

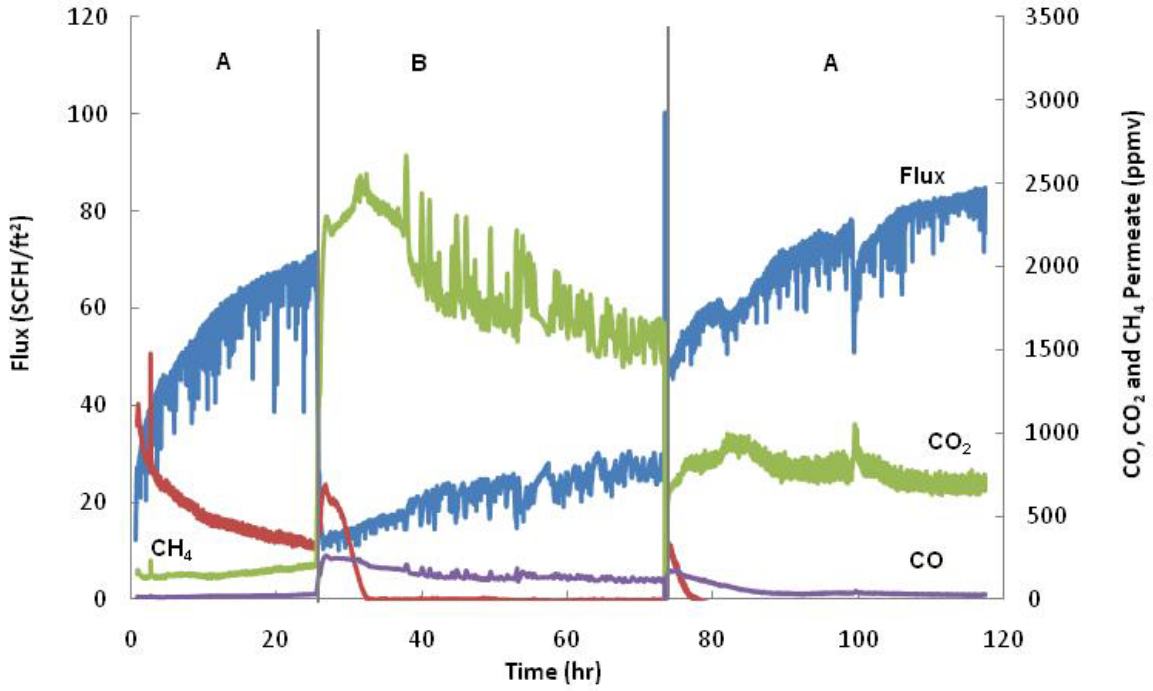

Figure 166. Flux and permeate gas purity profiles for membrane Pd-93. 85% Pd, 10% Au, 5%Cu. In sections marked with an A testing done at 400 ºC, 170 psi, 50% H_2, 30% CO_2 19% H_2O and 1% CO. 20 ppmv H_2S was added to the gas mixture in sections marked with a B. Total inlet flow 1000 sccm.

In this test, while there was a drop in the permeate when the membrane was exposed to sulfur, as well as an increase in carbon levels (CO, CH_4 and CO_2) in the permeate, the foil shows excellent recovery, with the permeate rising from 25 SCFH/ft^2 under sulfur to 83 SCFH/ft^2 in the clean gas (where the initial testing in sulfur free gas gave a permeate of 70 SCFH/ft^2). The rise of the CO and CO_2 concentrations in the permeate hydrogen are partly a reflection of the decrease in hydrogen permeation rate (as the amount of hydrogen passing through the membrane decreases and the levels of CO, CO_2 and CH_4 permeation remain constant, the concentration of the

impurities rises). Once the sulfur is removed, the flux rises to approximately the same level as previously observed with the clean gas. As a result, the CO and CO_2 levels decreased and stabilize, (although not quite as low as their original values), but to low enough levels to indicate that the membrane integrity has remained intact (no major pores or pinholes were formed).

The final foil evaluated under the DOE conditions (Pd-165), showed good recovery in flux after exposure to sulfur. The flux dropped from 65 SCFH/ft^2 to 50 SCFH/ft^2 when sulfur was added to the gas mixture. When the sulfur was removed from the gas mixture the flux returned to its original flux of 65 SCFH/ft^2. However, in the presence of H_2S the selectivity of the membrane somewhat degraded. After the sulfur was shut off, the CO_2 level in the permeate hydrogen dropped, likely due to the increase in H_2 permeating through the membrane. The CO concentration showed a similar decrease, indicating that minimal damage occurred to the membrane. However, the carbon levels were far higher than they were originally, indicating that while the sulfur didn't have a permanent effect on the flux, it did cause some damage to the membrane and decrease its selectivity.

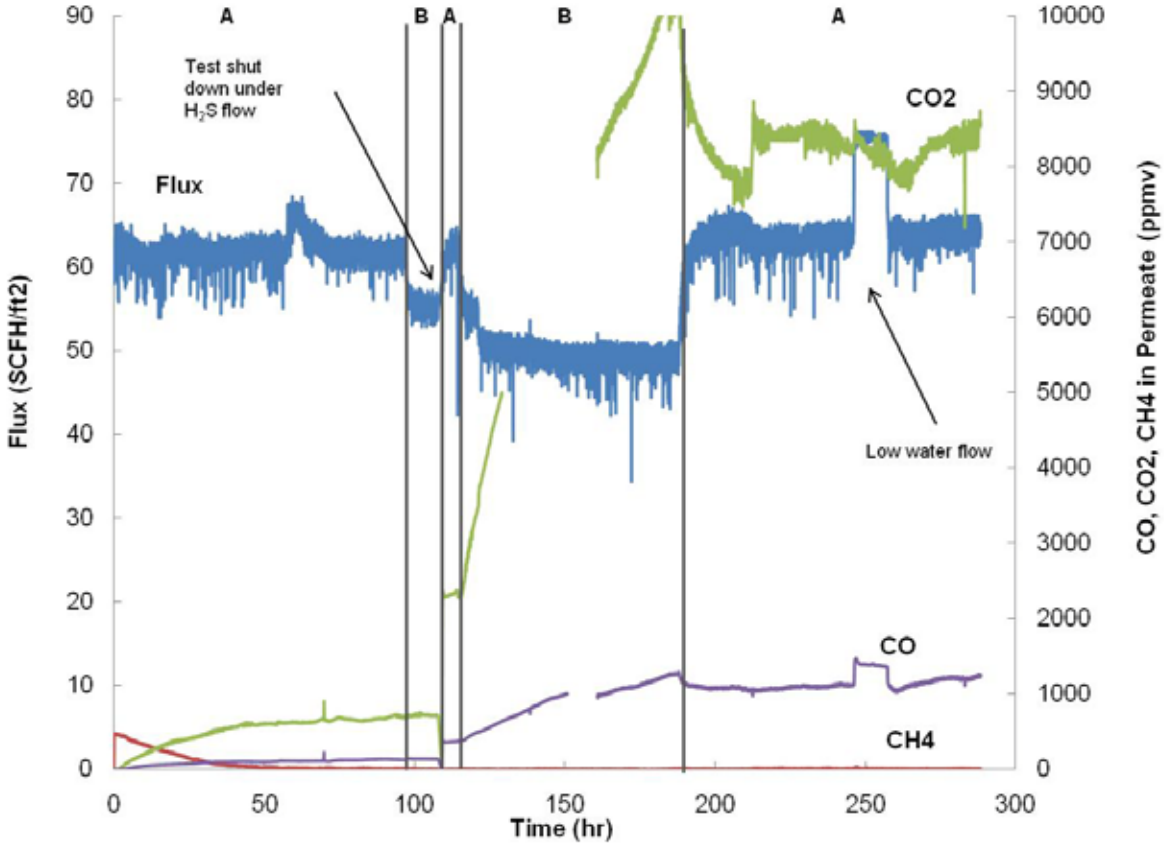

Figure 167. Flux and permeate gas purity profiles for membrane Pd-165. Pd/Au/Pt. In sections marked with an A testing done at 400ºC, 170 psi, 50% H_2, 30% CO_2 19% H_2O and 1%CO. 20 ppmv H_2S was added to the gas mixture in sections marked with a B. Total inlet flow 1000 sccm.

Table 43. Summary of DOE2a H_2S Tests.

Membrane	Composition	Dates Tested	Initial DOE1 Flux	Initial DOE1 Selectivity	DOE2a Flux	DOE2a Selectivity	Second DOE1 Flux	Second DOE 1 Selectivity
Pd-48	90% Pd, 10% Au	2/20/09-3/13/09	~125 scfh/ft^2	~20 ppmv CO, ~375 ppmv CO_2	~70 scfh/ft^2	CO, CO_2 rose above analyzer limits (5000 ppmv)	N/A	N/A
Pd-126	10% Au 90% Pd	9/11/09-9/30/09	~88 scfh/ft^2	~40 ppmv CO, ~1125 ppmv CO_2	~32 scfh/ft^2	CO above analyzer limit(5000 ppmv), CO_2 up to 3550 ppmv and still rising	N/A	N/A
Pd-93	85% Pd, 10% Au, 5% Cu	8/19/2009-9/9/09	~70 scfh/ft^2	200 ppmv CO_2, 25 ppmv CO, 340 ppmv CH_4	~25 scfh/ft^2	1600 ppmv CO_2, 120 ppmv CO	~83 scfh/ft^2	700 ppmv CO_2, 30 ppmv CO
Pd-147	Pd/Au/Pt	1/15/10-1/22/10	~45 scfh/ft^2	~2000 ppmv CO_2	~28 scfh/ft^2	3000 ppmv CO_2 until membrane broke, 5 hours into test	N/A	N/A
Pd-158	70% Pd, 20% Au, 10% Pt	5/24/10-06/02/10	~28 scfh/ft^2	~1250 ppmv CO_2, ~154 ppmv CO,600 ppmv CH_4	~20 scfh/ft^2	3000 ppmv CO_2, 250 ppmv CO, hole developed, then above analyzer range	~55 scfh/ft^2	Above analyzer range
Pd-165	Pd/Au/Pt	10/25/10 - 11/02/10	~55 scfh/ft^2	~450 ppmv CO_2, ~50 ppmv CO, 270 ppmv CH_4	~45 scfh/ft^2	1450 ppmv CO_2, 400 ppmv CO	N/A	N/A
Pd-165	Pd/Au/Pt	11/5/10-11/19/10	~65 scfh/ft^2	~650 ppmv CO_2, ~120 ppmv CO	~50 scfh/ft^2	10,000 ppmv CO_2, 1200 ppmv CO	~65 scfh/ft^2	8400 ppmv CO_2, 1000 ppmv CO

3.5 TDA Test Results

Under a subcontract from Southwest Research Institute (SwRI), TDA Research, Inc. (TDA) carried out evaluation of a variety of binary and ternary Pd alloy membrane films for separation of hydrogen from simulated synthesis gas. These membrane films were developed at SwRI as self-standing foils, which were installed into a test module at TDA where we carried out performance and stability evaluations under representative conditions provided by the U.S. Department of Energy (DOE) National Energy and Technology Laboratory (NETL). The primary objectives of these experiments were: 1) to assess the hydrogen permeation and selectivity of the membrane foils provided by SwRI first under a clean simulated synthesis gas at the desired operating temperature range, and 2) to test the foils which had high flux and selectivity for stability in the presence of sulfur.

Through the course of the project, TDA received 16 foils from SwRI. These foils were formulated following the guidelines provided by a molecular simulation model developed by the Georgia Technology of Institute. Before submission to TDA, foil integrity and preliminary permeation characteristics (e.g., pure gas H_2 permeation) were also evaluated at Colorado School of Mines to ensure that only the best formulations were selected for further, more comprehensive (and expensive) tests at TDA. Small sections of the foil were sealed in a test cell and heated it to the desired testing temperature. Some of the foils formed cracks, caused by the thermal stress generated during this heating process, and could not be tested further. A fair amount of the samples were evaluated using clean (i.e., sulfur-free) simulated synthesis gas (50% H_2, 30% CO_2, 19% H_2O and 1% CO) at 400 ºC and a 170 psi pressure drop across the membrane; DOE condition #1. Most of the foils showed favorable H_2 transport properties with the clean gas. A particular foil of interest was Pd-93, which consisted of 85% Pd, 10% Au and 5% Cu. Pd-93 achieved up to 140 SCFH/ft2 flux, while meeting DOE's purity requirements, with less than 250 ppmv CO_2 detected in the permeate (CO levels were below the 1 ppmv detection limit of our analyzers). The Pd-93 foil also maintained these superior transport properties over long duration tests (for over 120 hr) with no signs of degradation in performance. A 90% Pd, 10% Au foil also showed good performance as well, with a flux of 125 SCFH/ft^2 with 20 ppmv CO and 1125 ppmv CO_2 in the permeate.

The foils that achieved the best performance in the clean synthesis gas were then exposed to 20 ppmv H_2S (H_2S was metered into the same gas mixture without changing $CO/CO_2/H_2/H_2O$ concentrations, the testing temperature was the same, 400 ºC and the pressure drop across the membrane was 170 psi). The addition of sulfur caused some amount of degradation to all foils (with different alloy compositions). In addition to reducing the H_2 flux across the membrane film, sulfur also degraded most of the foils, causing the formation of pinholes and other defects in the film and leading to a significant increase in the CO and CO_2 impurity concentrations in the permeate gas.

Several of the foils, however, showed considerable resilience to sulfur poisoning and high stability. Of particular interest is the Pd-165 preparation which consisted of Pd/Pt/Au. We observed only a 20% drop in flux through this membrane when sulfur was added to the gas mixture. The flux was completely recovered when the sulfur flow was stopped, restoring the foil to the original flux that it had at the DOE 1 conditions before sulfur exposure. However, with this membrane we observed an increase in CO and CO_2 impurities in the permeate gas following sulfur exposure, which raises concerns about the long-term stability of the foil. A different foil, Pd-93 (85% Pd, 10% Au, 5% Cu) showed a more significant drop in flux (approximately 65%) but showed excellent recovery when the sulfur was removed.

4.0 BUDGET

The program was completed on budget. All the financial documentation has been submitted separately.

5.0 DELIVERABLES

All the original milestones identified have been completed. Following is the listed of completed milestones.

Year 1

1. Use DFT methods to predict H_2 flux through Pd96M4 for M = Ni, Rh, Pt, Nb, Ta, V, Mg and Y. Use same methods to predict H_2 flux Pd74Cu22M4 for at least 3 of the same M.
2. Screening of initial set (• 6) of ternary alloys by pure gas (H_2 and N_2) permeation experiments.

Year 2

1. A minimum of 20 membrane specimens with different copper concentrations based on GT hydrogen transport predictions for the 2-3 most promising ternary elements will be fabricated.
2. Four to five preliminary membrane samples will be tested at TDA and IdaTech with clean syngas and single impurity additions of H_2S and COs.

Year 3

1. Produce a minimum of 5 sq. ft. of optimized membrane material for use at CSM and TDA and for independent third-party evaluation by IdaTech.
2. CSM will complete mixture permeation testing with H_2/CO and H_2/H_2S binary mixtures with best three samples from the final optimization study.

6.0 CONCLUSION

The project team consisting of Southwest Research Institute® (SwRI®), Georgia Institute of Technology (GT), the Colorado School of Mines (CSM), TDA Research, and IdaTech LLC was focused on developing a robust, poison-tolerant, hydrogen selective free standing membrane to produce clean hydrogen. The project completed on schedule and on budget with SwRI, GT, CSM, TDA and IdaTech all operating independently and concurrently. GT has developed a robust platform for performing extensive DFT calculations for H in the bulk of palladium (Pd), binary alloys, and ternary alloys of Pd. Binary alloys investigated included $Pd_{96}Ag_4$, $Pd_{96}Au_4$, $Pd_{96}Cu_4$, $Pd_{74}Cu_{26}$, $Pd_{70}Cu_{30}$, $Pd_{96}Ni_4$, $Pd_{96}Pt_4$, $Pd_{96}Rh_4$, and $Pd_{96}Y_4$. They have also performed a series of calculations on, $Pd_{70}Cu_{26}Ag_4$, $Pd_{70}Cu_{26}Au_4$, $Pd_{70}Cu_{26}Ni_4$, $Pd_{70}Cu_{26}Pt_4$, and $Pd_{70}Cu_{26}Y_4$. SwRI deposited and released over 160 foils of binary and ternary Pd alloys. There was considerable work on characterizing and improving the durability of the deposited foils using new alloy compositions, post annealing and ion bombardment. The 10 and 25µm thick films were sent to CSM, TDA and IdaTech for characterization and permeation testing. CSM conducted over 60 pure gas permeation tests with a SwRI binary and ternary alloy membranes. To date the PdAu and PdAuPt membranes have exhibited the best performance at temperatures in the range of 423-773 K and their performance correlates well with the predictions from GT. TDA completed testing under the Department of Energy (DOE) prescribed water-gas shift conditions on over 16 membranes. Of particular interest is the PdAuPt alloy that exhibited only a 20% drop in flux when sulfur was added to the gas mixture and the flux was completely recovered when the sulfur flow was stopped. IdaTech tested binary and ternary membranes on a simulated flue gas stream and experienced significant difficulty in mounting and testing the sputter deposited membranes. IdaTech was able to successfully test PdAu and PdAuPt membranes and saw similar sulfur tolerance to what TDA found. The Program met all the deliverables on schedule and on budget. Over ten presentations at national and international conferences were made, four papers were published (two in progress) in technical journals, and three students (2 at GT and 1 at CSM) completed their Ph.D.s using results generated during the course of the program. The three major findings of program were; 1) the DFT modeling was verified as a predictive tool for estimating the permeability of Pd based ternary alloys, 2) while magnetron sputtering is useful in precisely fabricating binary and ternary alloys, the mechanical durability of membranes fabricated using this technique are inferior compared to cold rolled membranes and they are currently not ready for industrial environments, 3) based on both modeling and experimental verification in pure gas and mixed gas environments, PdAu and PdAuPt alloys were found to have the combination of the highest permeability and tolerance to sulfur.

7.0 REFERENCES

1. G. L. Holleck J. Phys. Chem. 74, 503 (1970) 5.
2. F. Berger, M. Varga, G. Mulas, A. Molnar, and I. Dekany, Langmuir 19, 9 (2003), 3692-3697.
3. H. Yukawa, T. Nambu, Y. Matsumoto, N. Watanabe, G.X. Zhang, and M. Morinaga, Mater. Trans 49, 10 (2008) 2202-2207.
4. G. X. Zhang, H.Yukawa, N. Watanabe, Y. Saito, H. Fukaya, M. Morinaga, T. Nambu, Y. Matsumoto, Int. J Hydrogen Energy 33, 16 (2008) 4419-4423.
5. R.E. Buxbaum and A.B. Kinney, Ind. Eng. Chem. Res. 35, 2 (1996) 530-537.
6. T. Pawluk, Y. Hirata, and L.C. Wang, J Phys Chem B 109, 44 (2005) 20817-20823.
7. S.K. Gade, M.K. Keeling, A.P. Davidson, O. Hatlevik, and J.D. Way, Int J Hydrogen Energy 34, 15 (2009) 6484-6491.
8. M. Hansen, McGraw-Hill: New York, 1958.
9. M. Yoshihara and R.B. Mclellan, Acta Metall Mater 31, 1 (1983) 61-68.
10. L. Semidey-Flecha, First-Principles Approach To Screening Multi-Component Metal Alloys For Hydrogen Purification Membranes. Georgia Institute of Technology, Atlanta, 2009.
11. T. B. Flanagan, Platinum Metals Rev. 37, l (1993) 26-37.
12. Y. Sakamoto, K. Kajihara, T. Kikumura, and T.B. Flanagan, J Chem Soc Faraday Trans 86, 2 (1990) 377-383.
13. H. Uchikawa, T. Okazaki, and K. Sato, Jpn. J. Appl. Phys., 32, 11A (1993) 5095-5096.
14. Subramanian P.R., H-Tm (Hydrogen-Thulium), Binary Alloy Phase Diagrams, 2nd Ed., Ed. T.B. Massalski, 2 (1990) 2069-2070.